The PHENIX Experiment at RHIC

Decadal Plan 2011–2020

Brookhaven National Laboratory

Relativistic Heavy Ion Collider

October, 2010

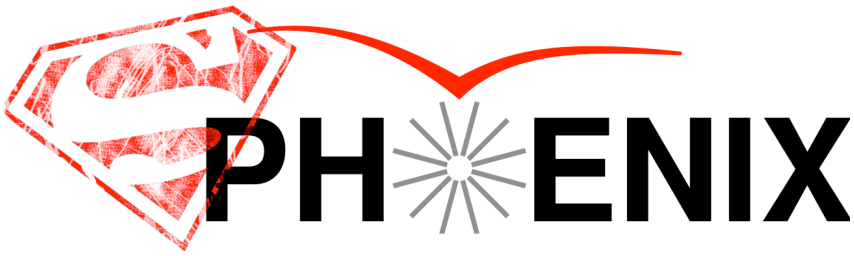

Spokesperson	Barbara Jacak *Stony Brook University*
Deputy Spokesperson	Jamie Nagle *University of Colorado*
Deputy Spokesperson	Yasuyuki Akiba *RIKEN Nishina Center for Accelerator-Based Science*
Operations Director	Ed O'Brien *Brookhaven National Laboratory*
Deputy Operations Director for Upgrades	Mike Leitch *Los Alamos National Laboratory*
Deputy Operations Director for Operations	John Haggerty *Brookhaven National Laboratory*

Executive Summary

The first decade of operations at the Relativistic Heavy Ion Collider (RHIC) has provided striking new insights into Quantum Chromodynamics (QCD) and has revealed new and surprising connections to other disciplines of physics. The PHENIX experiment has been at the forefront of these advances, while at the same time training the next generation of scientists. PHENIX has published over 90 refereed journal articles with nearly ten thousand citations and granted over 100 Ph.D's. The measurements described in those articles, together with theoretical modeling, are converging towards a coherent picture of a strongly coupled quark-gluon plasma (sQGP) at temperatures of order (2–3)$\times T_c$. New questions about the nature of the sQGP, its quasi-particle content, and its relation to other nearly perfect fluids have emerged. Parallel to these developments, the RHIC spin program now dominates the world constraints on the gluon contribution to the proton spin, and we have begun an exciting program of W physics aimed at constraining the flavor dependence of the quark spin contribution and entering the rapidly developing area of transverse spin physics and parton dynamics in hadrons.

As we look forward with anticipation to the next decade of physics, Associate Laboratory Director (ALD) Steve Vigdor has charged the RHIC experiments PHENIX and STAR to produce Decadal Plans. We have been asked to articulate what physics results are anticipated from the PHENIX detector incorporating the Midterm Upgrades currently nearing completion, and to identify compelling areas of physics that would be opened with further upgrades of PHENIX. The charge is given in Appendix A. This charge comes at an opportune time as exciting questions emerge that help us refine our understanding of the sQGP. Additionally, towards the end of this next decade, the potential upgrade to the RHIC accelerator complex that would produce electron-ion collisions presents a scientifically compelling opportunity to utilize an upgraded PHENIX detector as a first-generation Electron-Ion Collider (EIC) experiment, while pursuing inherently new quark-gluon plasma and spin studies.

The Decadal Plan builds upon the vision for the next five years (2010–2015) that maps out a set of Midterm Upgrades to address a targeted set of physics questions. This Midterm Physics Plan, which has been developed in consultation with the ALD and endorsed by the Program Advisory Committee (PAC), is highlighted in Figure 1 in terms of the physics topics addressed and the associated detector upgrades. The suite of currently funded upgrades (including the HBD, VTX, FVTX, DAQTRIG2010, MuTrig) addresses key physics

questions related to the sQGP (e.g. chiral symmetry restoration, heavy flavor flow), fundamental cold nuclear matter physics, and spin physics (e.g. quark flavor contributions to the proton spin via parity-violating W decays). Additionally, we see a need during this time frame for a new forward calorimeter (FOCAL) to address low-x gluon saturation physics (targeted for 2014) and an upgraded data acquisition referred to as Super-DAQ (targeted for 2013–2014) to fully utilize the increased luminosity of the collider. As demonstrated in the draft run plan (see Appendix B), these key physics questions will be addressed on the five-year time scale.

Beyond these five years, after the completion and full exploitation of the Midterm Upgrades and RHIC luminosity increases, and after the turn on of the LHC heavy ion program, we have identified new areas of investigation related to the fundamental properties of the sQGP, and to transverse spin physics, that require major new detector capabilities. These new opportunities to address fundamental properties of QCD lead to an evolution of the detector towards a configuration that can simultaneously address fundamental questions in heavy ions, cold nuclear matter, nucleon structure, and highly energetic electron probes of nucleons and nuclei.

A key theme in all of these areas is the interplay between perturbative and nonperturbative physics in QCD. By exploring hot QCD matter over a very broad range of collision energies (and also informed by results at the LHC), we can vary the relative importance of *strong and weak coupling*, critically extended by studying high-energy partons and their interaction with the quark-gluon plasma via jets. The question of strong coupling also directly relates to the quasi-particle nature of the sQGP, the color screening scale in the sQGP, the issue of rapid equilibration, and the connections of QGP physics with other perfect fluids, offering the exciting prospect of further exploring the gauge-gravity duality that has been so transformative.

Recent theoretical ideas stemming from the intense activity surrounding single-spin asymmetries have raised new questions regarding basic assumptions in pQCD of factorization and universality, which play a fundamental role in our understanding of the partonic structure of hadrons. Key measurements to test these ideas have been proposed, with one particularly clear example being the transverse single-spin asymmetry in Drell-Yan pair production at forward rapidity. Observation of the sign change in the asymmetry with respect to semi-inclusive deep-inelastic scattering would confirm the predicted modified universality for T-odd transverse-momentum-dependent (TMD) distribution functions. Exploration of TMD distribution and fragmentation functions will be a central focus of the future nucleon structure program, opening up a window to parton dynamics inside hadrons and in the hadronization process, thus advancing one of the frontiers in understanding QCD.

The tools for answering these questions rely on a major evolution in the configuration of the PHENIX detector, while still building upon core detectors and data acquisition, infrastructure, and collaboration personnel strength. Studying the coupling of quarks to the medium and exploring the mechanisms of fast parton interactions demands precision

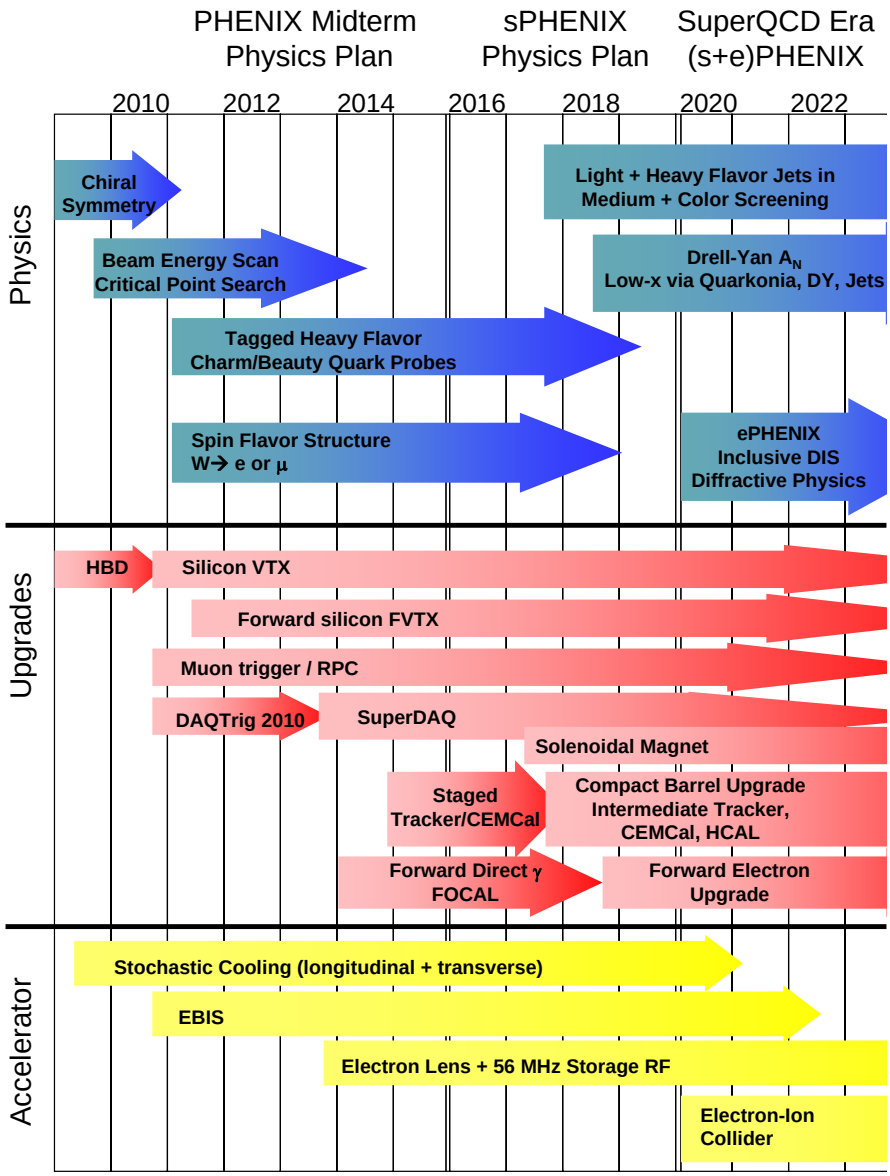

Figure 1: Timeline indicating the physics topics, detector upgrades, and accelerator upgrades over the next decade.

measurements of jets, dijets, heavy flavor jets, and direct photon-jet correlations. Substantially more sophisticated and differential measurements beyond those presently accessible are needed, with an emphasis on reconstructing jets from their fragments rather than reliance upon one or two hadrons from each jet. Determination of heavy quarkonia production and survival, as a function of p_T at various colliding energies, is another key observable for interactions with the sQGP. Precision spectroscopy of J/ψ, ψ', and the

Υ states is needed to determine the relevant color screening length in the sQGP. In order to make these and other exciting measurements, we must supplement the high rate, sensitive triggering, and electron and photon identification capabilities of PHENIX with larger detector acceptance—an increase by two orders of magnitude for many key measurements. The new goals that drive detailed jet reconstruction drive the need to add, for the first time, large acceptance hadronic calorimetry at RHIC.

RHIC is a powerful and flexible facility that allows us to vary the medium properties by colliding different nuclear species at different energies, and that also provides timely comparisons with critical baseline p+p and proton(deuteron)-nucleus collisions at the same $\sqrt{s_{NN}}$. The very large luminosities now available at RHIC enable a new generation of jet studies up to 50 GeV, spanning a range of energies that provides maximum sensitivity to parton-sQGP interactions. Current-day and an upgraded PHENIX can sample a very large luminosity with minimum bias triggers, thereby exploring the entire dynamical range of jets provided by RHIC. Furthermore, leveraging the current PHENIX Collaboration strength and interests in addition to the infrastructure will make an upgraded detector extremely and rapidly productive.

The PHENIX upgrade plan is envisioned for the 2016–2018 time frame, and involves replacing the PHENIX central magnet with a new compact solenoid. The limited aperture provided by the outer central arm detectors would be replaced with a compact EMCal and an Hadronic Calorimeter covering two units in pseudorapidity and full azimuth, complemented by the existing VTX and FVTX inner silicon tracking. Two additional tracking layers would be added. We highlight that the large acceptance and excellent detector capability is combined with high rate and bandwidth, allowing the accumulation of 25 billion Au+Au collisions recorded and 50 billion Au+Au collisions sampled with spectrometer triggers in a single 20-week run period—an increase by an order of magnitude over current data samples. The limited forward coverage of the current PHENIX detector does not allow us to adequately address the questions driving the nucleon structure and cold nuclear matter community, nor does it provide any capabilities for e+p or e+A collisions. Hence, we are considering an upgrade where one muon arm would be replaced by a new large-acceptance forward spectrometer with excellent PID for hadrons, electrons, and photons and full jet reconstruction capability. The modified detector layout is shown schematically in Figure 2. The new compact barrel component at midrapidity is designed for excellent jet reconstruction and PID for photons, electrons, and π^0 in p+p, proton-nucleus, through central nucleus-nucleus collisions. The forward upgrade design is driven by nucleon structure physics, cold nuclear matter physics, and the capability to study first collisions at the EIC.

The upgraded PHENIX detector as proposed would enable a number of measurements in e+A and e+p collisions if an electron beam became available at the PHENIX intersection region. Specifically, the proposed detector would be well suited to measure inclusive structure functions in e+p, such as g_1 and F_L, and inclusive structure functions in e+A. It would also allow us to improve our knowledge of nuclear PDFs and diffractive vector meson production in e+A, and permit probing low-x gluons in nuclei as well as allowing

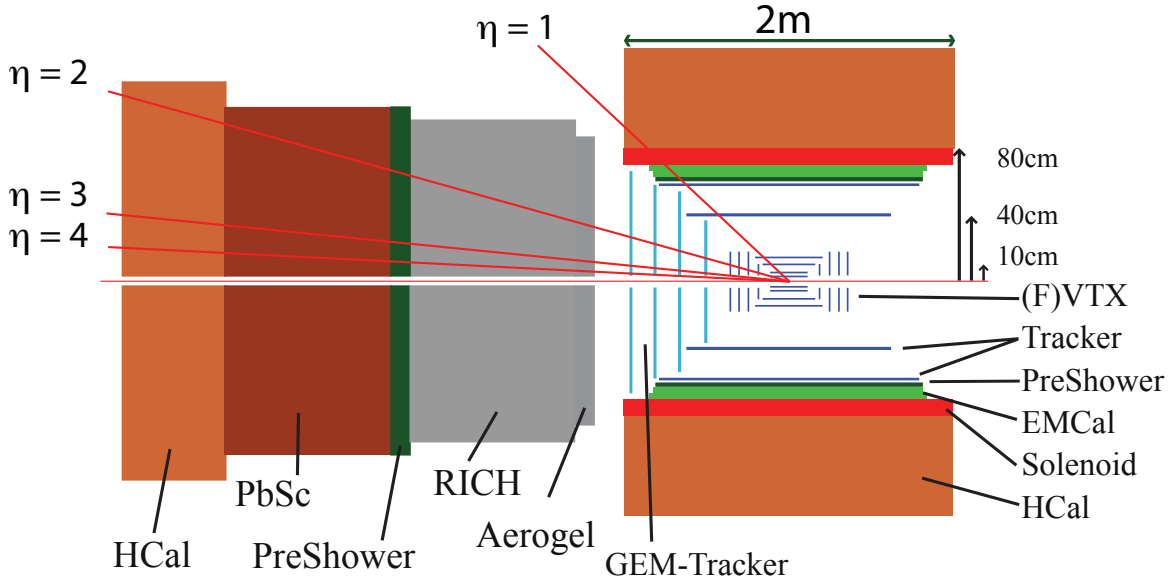

Figure 2: Layout of the upgraded PHENIX detector (sPHENIX).

spatial tomography of partons within nuclei.

Our plan is to carry out the Midterm Physics Plan while simultaneously aggressively pursuing a targeted R&D program and detailed physics simulations to move this new detector concept to the proposal stage. Critical R&D is necessary to optimize the radius of the compact detector and its implications for jet capabilities and maintaining electron and photon PID. This R&D work will enable optimized technology choices and the development of a full detector proposal. We note that development work for the proposed forward spectrometer has significant overlap with work towards a dedicated EIC detector. We then envision a staged approach where some components are available for physics, as indicated in Figure 1, and then over a two-year period the solenoid and two new spectrometers would be installed. This new detector is referred to as sPHENIX and would then be ready at the start of EIC physics (referred to as ePHENIX). At this time a SuperQCD era at RHIC would begin, with the power of this truly formidable facility.

This document is organized as follows. We use a parallel structure where we describe separately for heavy ion physics and for nucleon structure physics: A) the current status of the field and the RHIC program therein, B) the key physics questions and measurements to address them over the next five years – the Midterm Physics Plan, and C) the key physics questions and measurements to address them over the decade beyond that – the sPHENIX Physics and Upgrade Plan. Then in Chapter 7, we describe the detector plans and required R&D for the sPHENIX upgrade, and in Chapter 8 we discuss the physics for

PHENIX enabled by $e+p$ and $e+$A collisions in the Electron-Ion Collider era (ePHENIX). In the Appendices we include the charge from ALD Steve Vigdor (Appendix A), the input for the five-year run plan (Appendix B), a brief description and status of each of the Midterm Upgrade projects in (Appendix C), the status of the collaboration (Appendix D), and the PHENIX collaboration list (Appendix E).

Contents

Chapter 1

Heavy Ion Physics: Current Understanding

The first decade of the RHIC experimental program has produced a deep body of results that have dramatically improved our understanding of QCD under conditions of extreme temperature and energy density. The qualitative features of QCD under these conditions are now understood to be quite different from the preRHIC conception widely held on the eve of the first collisions on June 12, 2000. Detailed reviews of the early progress in these investigations are contained in the white papers [48, 25, 105, 116] of the four day-1 experiments BRAHMS, PHENIX, PHOBOS and STAR. Subsequent progress has culminated in what might be called a "standard model" of heavy ion physics: the rapid thermalization of an energy-dense initial state into a QCD plasma which evolves as a nearly ideal hydrodynamic system, followed by a freeze-out into final-state hadrons. The precise nature of the plasma remains an open question both experimentally and theoretically, motivating a broad range program of study in the next decade of RHIC physics.

The fact that hydrodynamics has been so successful in describing the behavior of the bulk in RHIC heavy-ion collisions has been enormously useful. In particular, it has meant that one can study in a sensible way the modification in the medium of a full range of familiar observables: single particle spectra; two- and three-particle correlations; electromagnetic probes; direct photons; and even full jet reconstruction. The systematic study of the modifications of these signals has been a significant tool for understanding the nature of the medium.

The RHIC discoveries have garnered deep interest across many other fields of physics. It was exciting to see that the hottest matter in the laboratory shares characteristic flow patterns with the coldest matter – lithium atoms captured in magneto-optical traps at temperatures $T \approx 10^{-7}$ K. There are also strongly coupled electromagnetic plasmas that exhibit similar properties. It has been surprising that these diverse systems can be described by string theory with calculations in the limit of infinitely strong coupling. This

connection with string theory has been particularly fruitful, often with nuclear theorists leading the way for new insights within the string community.

Section 1.1 summarizes the evidence for quark-gluon plasma formation and the description of the collectively expanding plasma at RHIC as being strongly coupled. Section 1.2 discusses the properties of this novel matter. Section 1.3 reviews our current understanding of QCD in cold nuclear matter in the low-x region, which represents the initial state for heavy ion collisions.

1.1 The success of the sQGP paradigm

One of the primary goals of the RHIC program was to establish whether or not a *quark-gluon plasma* (QGP) was being created in very high energy heavy ion collisions. While some important discoveries in particle physics, such as the observation of the J/ψ, can be made clear in a single histogram [111, 112], the discovery of this state of strongly-interacting nuclear matter did not emerge from a single observable. In large part, it has been the success of hydrodynamics in describing the overall evolution of the system that has allowed many disparate observations to be related and which has led the community to adopt the paradigm of a strongly-coupled system, which acts much more like a fluid (or liquid) than a gas. This "perfect fluid" is often called the "sQGP" or "strongly-coupled quark-gluon plasma", to distinguish it from the weakly-coupled deconfined state predicted before the RHIC program began.

A depiction of the space-time evolution of a heavy-ion collision is shown in the left panel of Figure 1.1. After the initial collision, the resulting high energy density state rapidly thermalizes into a quark-gluon fluid that evolves hydrodynamically. As the temperature and density fall with proper time, this fluid breaks down and hadronizes into final-state particles. The success of nearly ideal hydrodynamics in describing the bulk evolution of the system has provided a single physics scenario that has successfully reconciled a wide array of theoretical and experimental inputs with a wide array of RHIC experimental observations (diagrammatically shown in the right panel of Figure 1.1).

The initial high energy density is obtained via measurements of transverse energy distributions ($dE_T/d\eta$) in heavy ion collisions. This was one of the earliest results from RHIC and one which provided evidence that the energy density of the created medium is extremely high, higher than the energy density – determined by lattice QCD calculations – required for a transition from a hadron gas to a plasma state. Figure 1.2 shows the product of energy density times formation time as calculated in a Bjorken-like boost invariant picture in Au+Au collisions at $\sqrt{s_{\rm NN}} = 19.6$, 130, and 200 GeV [54]. The formation time, τ, is the earliest time at which one can regard the system as a collective state of "matter" and is conventionally thought to be $\tau \sim 1$ fm/c. The experimental points are compared to a relatively narrow range for the critical energy density, ϵ_c, as generally expected from lattice calculations. In the most central collisions the achieved energy density sits well

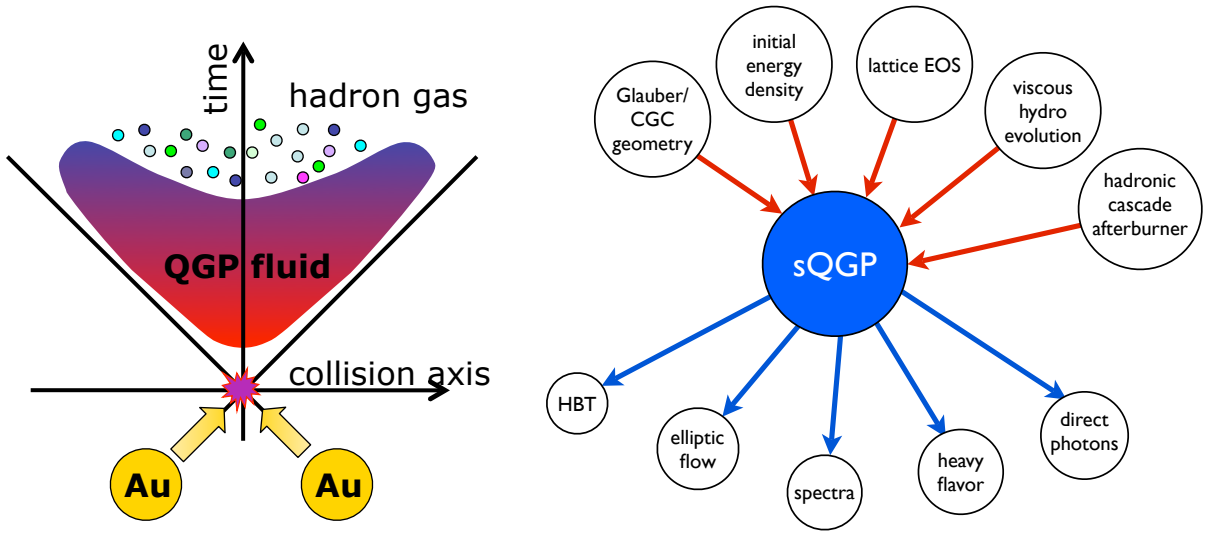

Figure 1.1: (left) Space-time evolution diagram for heavy ion collisions at RHIC. (right) Diagram displaying the various inputs for the sQGP picture and the outputs as predictions to compare with experimental data.

above the range of QCD phase transition values, and the medium is difficult to describe via the propagation of distinct hadronic states.

The system that is created initially has a large central pressure and steep pressure gradients that cause the system to expand explosively. For heavy-ion collisions at RHIC energies, this expansion is successfully described using nearly ideal hydrodynamics, which was not the case at lower collision energies. The transverse momentum (p_T) spectra of final state hadrons is well reproduced up to moderate values of p_T by ideal hydrodynamic models that include a hadronic cascade afterburner. In Figure 1.3, we show recent calculations from Hirano *et al.* [202] using a 3+1-dimensional ideal hydrodynamics followed by a hadronic cascade. These include fluctuating initial conditions for the hydrodynamic calculations, a realistic equation-of-state from lattice QCD, and zero shear and bulk viscosity (i.e., ideal hydrodynamics). The results show good agreement with both hadron spectra (π, k, p) up to $p_T \approx 2.0 - 2.5$ GeV/c, and with elliptic flow v_2 as measured by the PHENIX experiment in Au+Au collisions at $\sqrt{s_{\rm NN}} = 200$ GeV.

Despite the impressive agreement of ideal hydrodynamics for the early time stage (i.e., with zero shear viscosity η), there is a conjectured low bound to the ratio of the shear viscosity to entropy density η/s. This conjecture was originally motivated from simple arguments based on the quantum mechanical uncertainty principle, and has since been shown to be rigorously true for a broad class of gauge theories within the string theory duality referred to as AdS/CFT [227]. This is a result with relevance far outside the field of nuclear physics. For one thing, relativistic viscous hydrodynamics calculations have only recently advanced sufficiently to be compared against RHIC results. This has ultimately been beneficial for hydrodynamics experts in general, but was pushed in part by

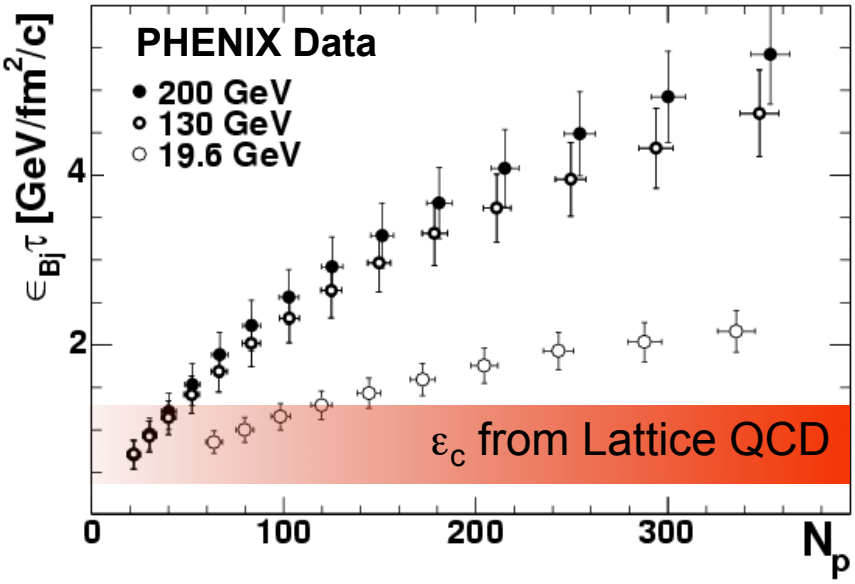

Figure 1.2: The product of energy density, ϵ_{Bj} and formation time, τ, as a function of centrality (as measured by the number of participants N_p) for Au+Au collisions at three different energies. This has been calculated in a Bjorken-like boost invariant scenario, where one conventionally takes $\tau \sim 1\,\mathrm{fm}/c$. The band shows the critical energy density, $\epsilon_c \sim 1\,\mathrm{GeV/fm}^3$, assuming a formation time of $1\,\mathrm{fm}/c$, as determined using lattice QCD.

the needs of the RHIC analyses. There is also a connection to strongly coupled systems of Fermi gases at μKelvin temperatures. Figure 1.4 shows the measurement of η/s for helium, nitrogen, and water in comparison to the conjectured quantum lower limit. And of course, the connections between RHIC physics and string theory, by way of the AdS/CFT conjecture, have led to striking developments in both fields.

Figure 1.5 shows a comparison of a viscous hydrodynamic calculation [243] and PHENIX experimental data for v_2 as a function of p_T. These initial results indicate that the quark-gluon plasma may have a η/s ratio near the "perfect fluid" bound of $1/4\pi$. However, calculations of viscous hydrodynamics with fluctuating initial geometry and the full hadron cascade afterburner are needed to obtain systematically reliable values for η/s. We expect this to be an area of great theoretical progress in the next couple of years. Additionally, different methods of constraining η/s via the flow of heavy quarks have been made [30], and will reach a precision era over the next five years with the PHENIX upgrades described in Section 2.2.

While the viscosity to entropy density ratio is found to be small, the detailed dependence of the flow on centrality and p_T suggests that it is not zero, potentially reflecting the influence of microscopic degrees of freedom, which tend to inhibit flow due to dissipative effects. Shown in the left panel of Figure 1.6 are the v_2 dependencies on p_T for multiple hadronic final states compared with an ideal hydrodynamic calculation. One observes significant disagreement between data and the calculation for $p_T > 2\,\mathrm{GeV}/c$. In the right

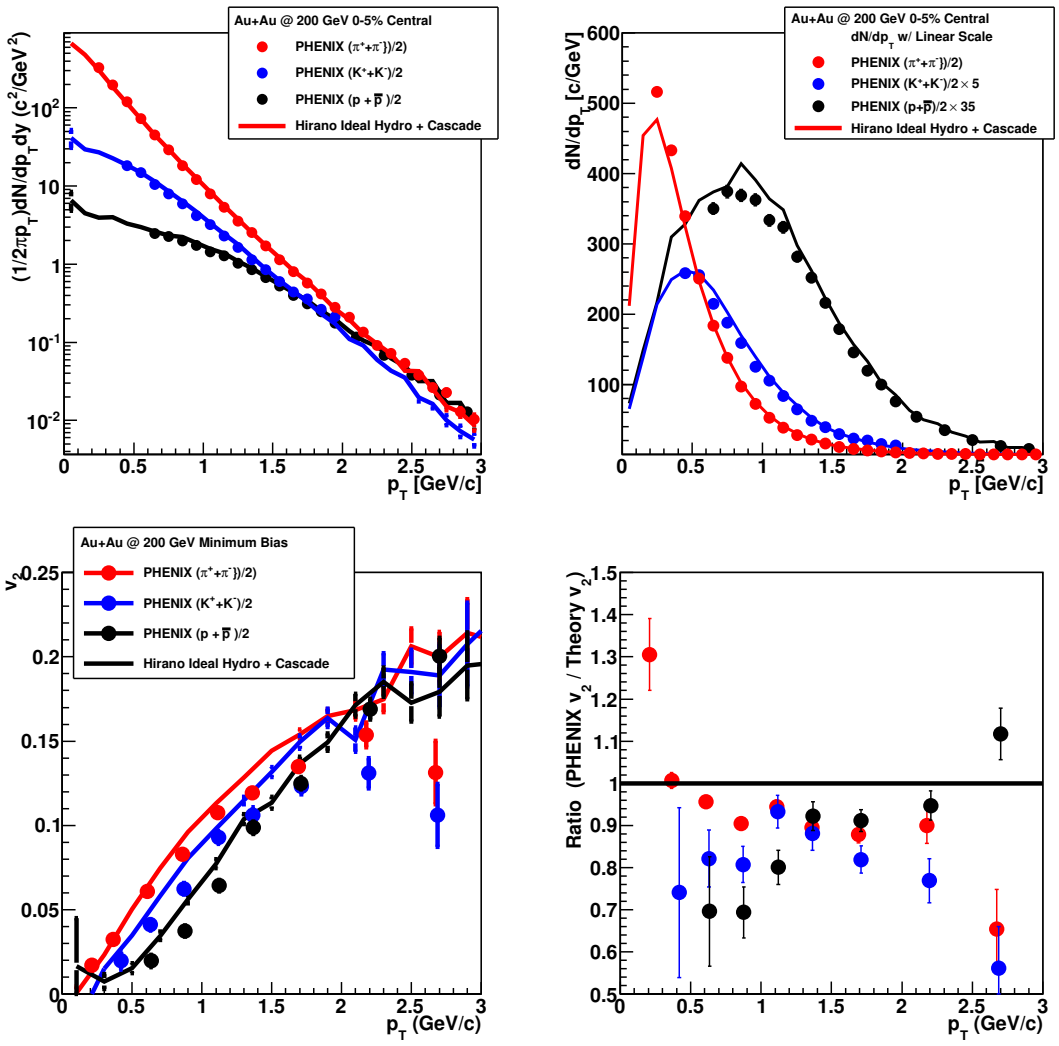

Figure 1.3: Spectra and flow for identified hadrons compared to the ideal hydrodynamic + hadronic cascade calculation of Hirano *et al.* [202]. (upper) p_T invariant yield for π, k, p on (left) log and (right) linear scales. (lower left) v_2 vs p_T. (lower right) ratio of PHENIX v_2 to theory v_2 vs p_T.

panel of Figure 1.6 is the same experimental data plotted as v_2/n_q versus the transverse kinetic energy KE_T/n_q, where n_q is the number of valence (anti)quarks in the hadron. This observation has been interpreted by some to mean that quasi-particles with the quantum numbers of quarks are the relevant degrees of freedom when these hadrons are formed. This potential answer raises other very interesting questions – what are the masses and widths of these quasi-particles? Also, if they are well defined quasi-particles and they exist in the early time stages, they should create significant viscous effects which are not observed [238]. Extending these measurements to other hadronic states and higher flow moments [42], along with improved theoretical modeling of the hadronization process

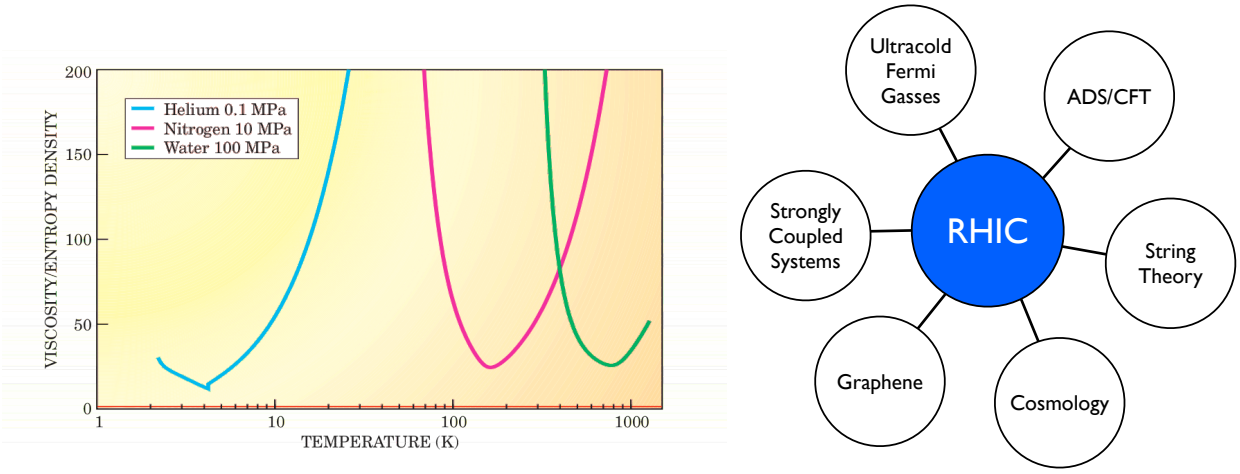

Figure 1.4: (left) Shear viscosity to entropy density ratio (η/s) near the conjectured lower limit for helium, nitrogen, and water [227]. (right) Surprising connections involving RHI physics that have emerged over the last decade.

are needed.

The success of a hydrodynamic description indicates that the system is close to local equilibrium, and thus one can calculate the emission of electromagnetic radiation from the scattering of its charged constituents. In particular, the system should radiate real and virtual photons, with the highest rate of radiation at the earliest times when the temperature is at its highest. It is difficult to access the dynamical processes which characterize the system at these early times, but PHENIX has opened a window into this physics by the measurement of direct virtual photons, radiated off of the hot charged constituents of the plasma [43, 41]. Figure 1.7 shows the spectrum converted to real direct photons in Au+Au central collisions. The solid line in the plot is an NLO pQCD calculation of the expected rate in p+p appropriately scaled up in order to provide a baseline comparison for the Au+Au results. There is a clear excess below $p_T = 3\,\mathrm{GeV}/c$. These dielectrons stem largely from the internal conversion of virtual photons. At low virtuality, the flux of virtual photons is nearly the same as the flux of real photons. The flux of these photons in Au+Au collisions provides an estimate of the temperature achieved in the early stage of the collision. The excess observed above the spectrum expected from p+p collisions has been modeled by hydrodynamic calculations coupled to EM radiation, and imply early temperatures from $T = 300$–$600\,\mathrm{MeV}$, depending on the initialization time used in the calculations. This clearly demonstrates that a hot, thermal system was created, with an initial temperature well above the Hagedorn temperature (i.e., the temperature limit predicted for a hadronic resonance gas [198]). This would not be possible if the system was purely hadronic.

In conclusion, the RHIC data show that a hot, dense system is formed – well beyond the transition temperature suggested by the lattice. It flows with a low viscosity, indicative of strong coupling between the constituents, building up substantial elliptic flow, and freez-

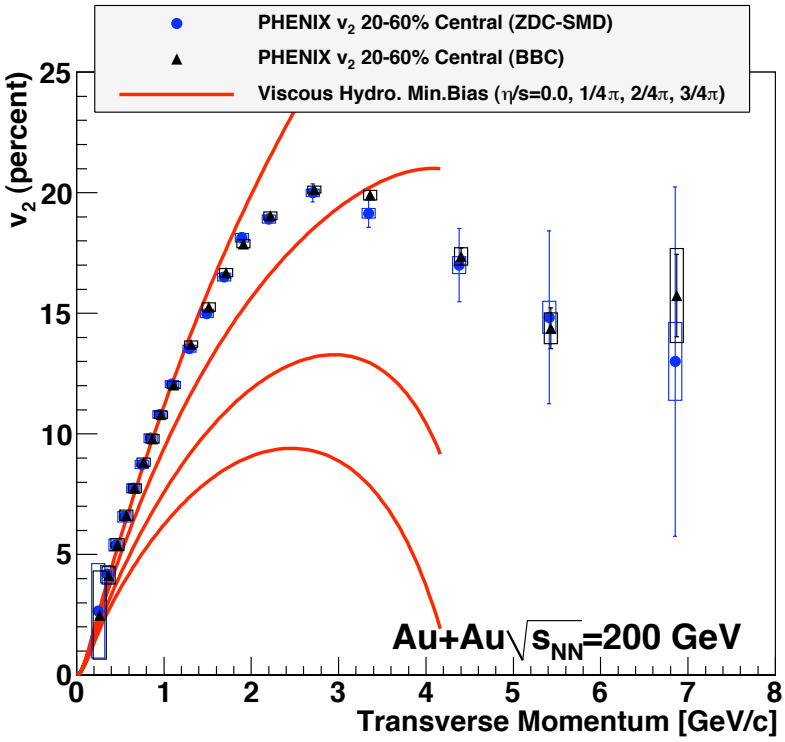

Figure 1.5: Elliptic flow of charged hadrons, compared to relativistic hydrodynamic calculations that includes viscosity [243].

ing out into hadrons at or near the Hagedorn temperature. Thus, from a decade of results from RHIC we have established the creation of a nearly equilibrated strongly-coupled quark-gluon plasma. We also have some experimental insight into the bulk properties of this matter (in particular its viscosity), although we still do not yet know its microscopic degrees of freedom. This is the focus of the next phase of the RHIC program.

1.2 Properties of the sQGP

Beyond establishing the creation of a quark-gluon plasma, the RHIC program is working to quantify the detailed properties of the created medium. This includes transport properties, such as the previously discussed viscosity-to-entropy ratio, as well as looking for the restoration of chiral symmetry, effects of color screening, and jet quenching.

The measurement of low mass dileptons for the purpose of understanding the modification of spectral functions in the quark-gluon plasma, and the relation of these measurements to the restoration of approximate chiral symmetry, have provided some exciting hints from the experimental data [41], but the fundamental answers will come in the next five years utilizing the PHENIX upgrades. These issues are discussed in detail in Sec-

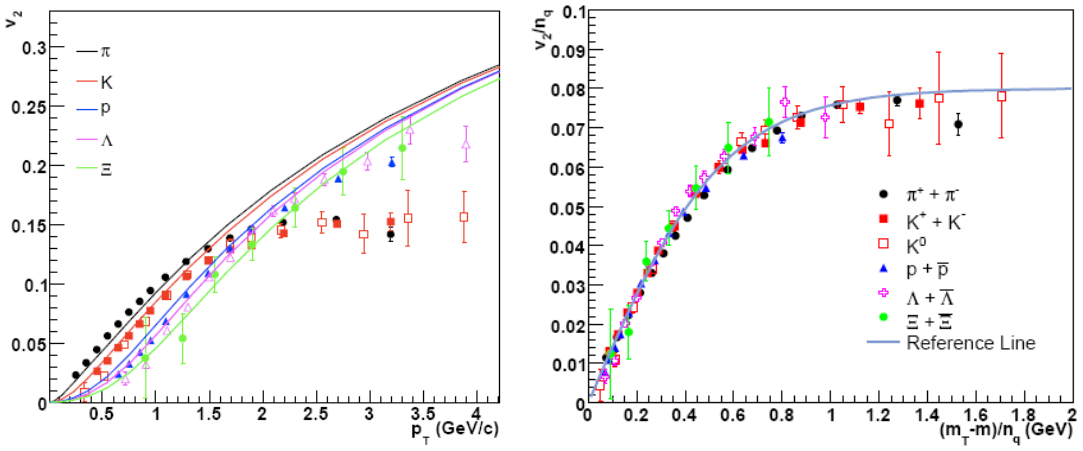

Figure 1.6: (left) Elliptic flow v_2 versus p_T in midcentral Au+Au collisions at $\sqrt{s_{\rm NN}} = 200\,\text{GeV}$ [33] for various hadrons compared with an ideal hydrodynamic calculation. (right) Elliptic flow v_2/n_q versus KE_T/n_q where n_q is the number of valence (anti)quarks in the hadron.

tion 2.1 on chiral symmetry.

In addition, the measurement of heavy quarkonia states (to date most measurements include only the J/ψ state) is expected to encode information about color screening in the quark-gluon plasma. Significant progress has been made, but there remain more questions than answers [32, 35]. We discuss key measurements designed to unravel this puzzle and answer detailed questions about color screening with PHENIX upgrades in Section 3.4.

Jet quenching has proven to be one of the richest areas of experimental and theoretical results in the first decade at RHIC. Jet quenching refers to the interactions of fast partons (quarks, gluons, heavy quarks) with the surrounding color charges and possibly quasiparticles in the quark-gluon plasma. Two keys sets of experimental observables have been published to date.

One set is from high p_T single particle yields. The modification of their spectra are characterized by the nuclear modification factor $R_{\rm AA}$, which is defined at the ratio of yields in Au+Au collisions divided by the yield in p+p collisions scaled up by the expected number of binary collisions $\langle N_{\rm coll}\rangle$. Deviations from unity are expected to arise from a variety of nuclear effects, both in the initial and final state. We have measured $R_{\rm AA}$ for a variety of hadrons and have compiled representative results in Figure 1.8. Direct photons are not suppressed up to about $p_T \sim 13\,\text{GeV}/c$, showing that there is no depletion of partons in the initial state. At the highest p_T there is a hint of suppression which may be related to isospin or the EMC effect. At the lowest values of p_T, the photons are enhanced, which corresponds to the enhancement seen in the internal conversion measurement in Figure 1.7. The light quarks are represented here by the π^0s; they show a strong suppression up to the highest values of p_T. It is particularly interesting that the heavy quarks,

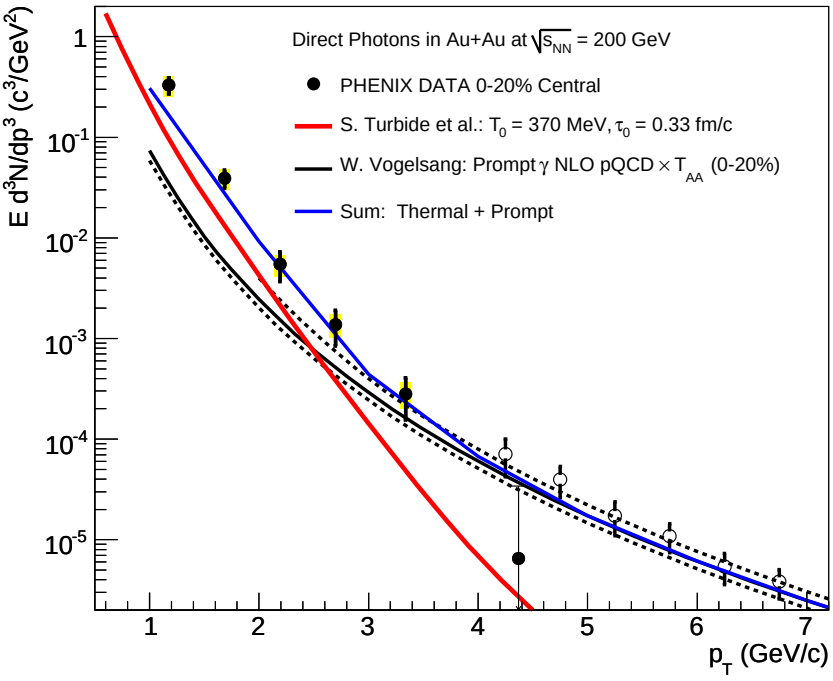

Figure 1.7: The spectrum of direct photons in central Au+Au collisions measured (open points) as direct real photons and (closed points) as virtual photons via e^+e^- pairs and converted to the real photon yield. (black line) NLO pQCD calculation in p+p multiplied by $T_{\rm AA}$ to provide an estimate for the yield in Au+Au of photons coming from hard initial collisions (*prompt photons*). (black dashed line) Results from variations in the scale uncertainties. (red line) Calculation by Turbide *et al.* [303] estimating the yield of photons emitted thermally by the hot system. (blue line) Sum of thermal plus prompt. The Au+Au results show a clear excess above the prompt photon yield for $p_T < 3\,{\rm GeV}/c$. This excess, attributed to photons emitted in the early stage of the collision, leads to an estimate of the initial temperature of 300–600 MeV [41].

represented here by the nonphotonic electron results, also show a significant suppression. The medium is so opaque that even heavy quarks seem to be strongly quenched, indicating that heavy quarks lose substantial energy in traversing the medium.

Perhaps more striking is the azimuthal dependence of these hadron yields, as encoded by the v_2 variable as shown in Figure 1.9 [46]. Note that for these high p_T values, the v_2 is not expected to result from hydrodynamic flow, but rather the difference in path length of material encountered by fast partons going in different orientations through the medium. The data are compared to several different jet quenching calculations. While some of the models can correctly reproduce the magnitude of quenching, all of them under-predict the v_2 found in the data. Whether this is due to an incomplete description of the quenching, the medium dynamics, or other effects remains a crucial unanswered question.

The second set of observables comes from two and three-particle hadron correlations. We

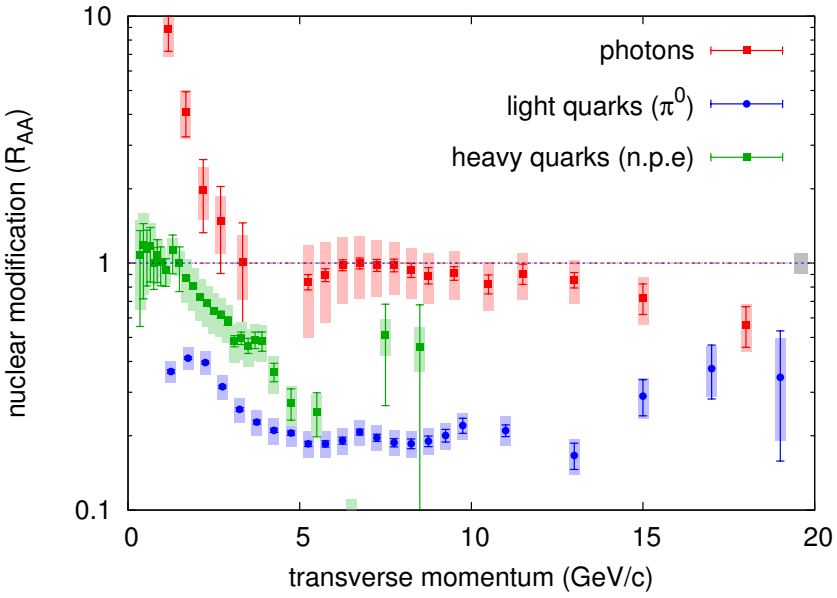

Figure 1.8: Nuclear modification factor for direct photons [260], neutral pions (predominantly from light quark jet fragmentation), and nonphotonic electrons (n.p.e.) from heavy flavor meson decay.

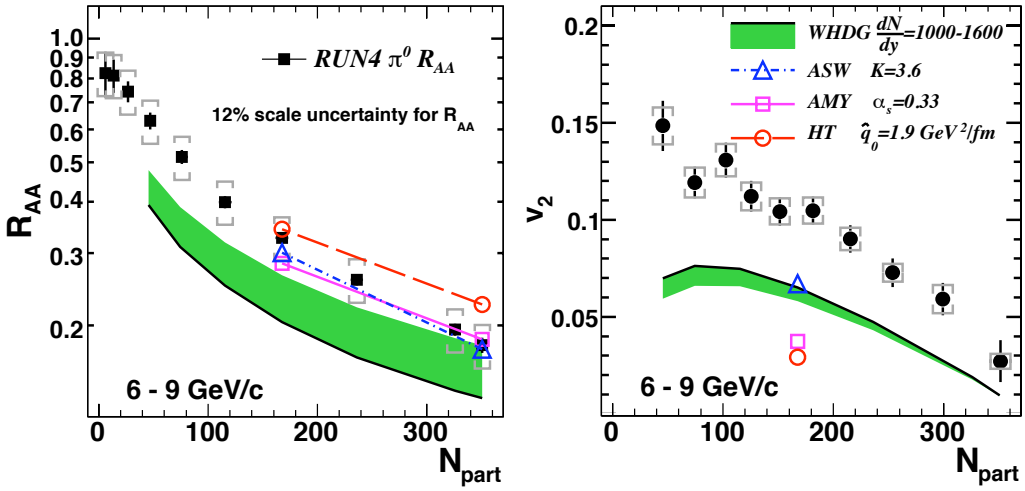

Figure 1.9: (left) The nuclear modification factor R_{AA}, and (right) elliptic flow v_2, versus centrality for neutral pions in Au+Au collisions at $\sqrt{s_{\mathrm{NN}}} = 200\,\mathrm{GeV}$. The data are compared to several different jet quenching calculations.

use a high p_T hadron as a stand-in for a jet, which at leading order is itself a proxy for a hard scattered parton. Figure 1.10 shows the correlation function in Au+Au collisions of two hadrons, each of which has p_T between 2 and 3 GeV/c. On the near-side ($\Delta\phi \sim 0$), there is a strong peak which looks similar to what one sees in p+p collisions. On the away-side ($\Delta\phi \sim \pi$), one sees a bifurcated peak quite unlike the single broad peak seen

in p+p collisions.

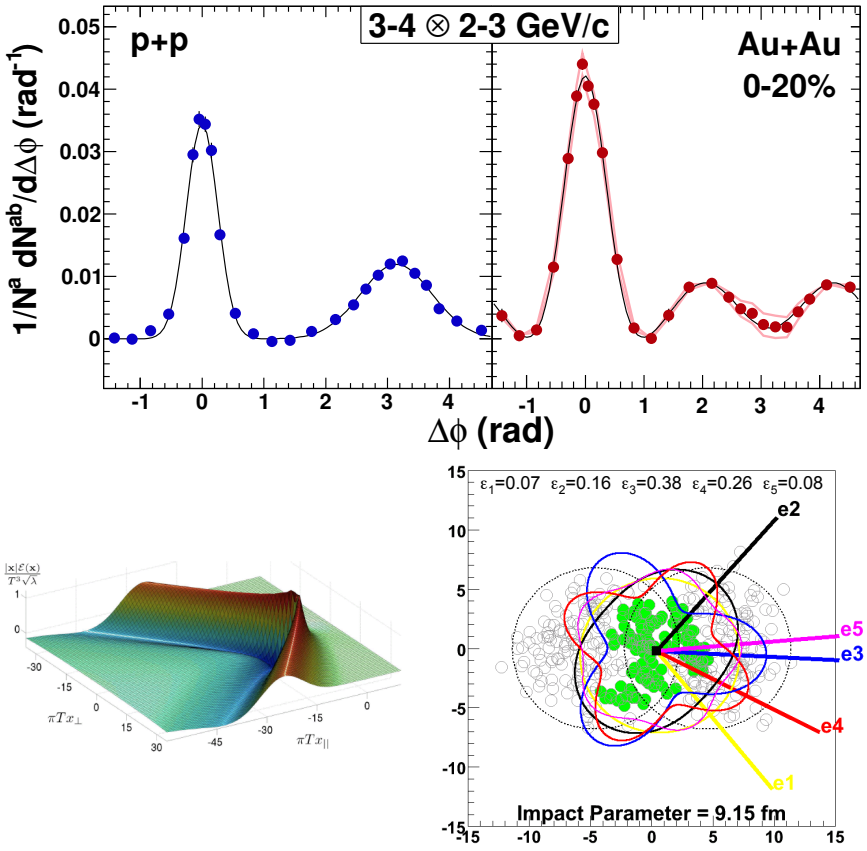

Figure 1.10: (upper) Two-particle azimuthal angle correlation for (upper left) p+p and (upper right) heavy ion collisions. In the heavy ion case, the near-side peak is similar to that seen in p+p collisions; the away-side distribution is broad and bifurcated. (lower) Theoretical representations of two different interpretations of the existing jet correlation measurements. (lower left) A shock wave simulation in AdS/CFT [157]. (lower right) A diagram for fluctuating initial conditions in a Glauber calculation leading to a large ϵ_3 moment.

It turns out that there are several possible (and possibly competing) interpretations for this observed modification, as shown in Figure 1.10. The left panel shows a depiction of a Mach cone arising from the supersonic propagation of a fast parton through the medium. This is expected to arise both in the context of QCD calculations as well as AdS/CFT-based ones [157]. The right panel shows the location in the transverse plane of individual nucleons. These positions fluctuate from event to event and it is possible to generate a significant *triangular* component [87, 292]. Particle emission from such an arrangement could produce a pattern in the final state similar to that seen in the data, after the dominant v_2 modulation is subtracted. Within the next year this important issue is likely to be resolved both experimentally and theoretically, which is very important for understanding a future jet physics program.

Figure 1.11 shows two examples of the sort of jet correlation measurements possible with

the current PHENIX detector. Both of these correlations rely on single particle proxies as a stand-in for the jet. The panel on the left of Figure 1.11 shows the strength of the away-side correlation (I_{AA}) between a π^0 trigger and an opposite side hadron [46]. The correlation shown in the right panel is similar, but for direct photon triggers correlated with away-side hadrons [164]. A direct photon trigger provides a calibrated measure of the jet energy (neglecting the contribution of photons stemming from jet-medium interactions), so the yield can be plotted in terms of the fractional momentum z_T. As informative as these results are, it is not currently possible to reconcile the full set of results on R_{AA}, I_{AA}, and v_2 within any current theoretical model.

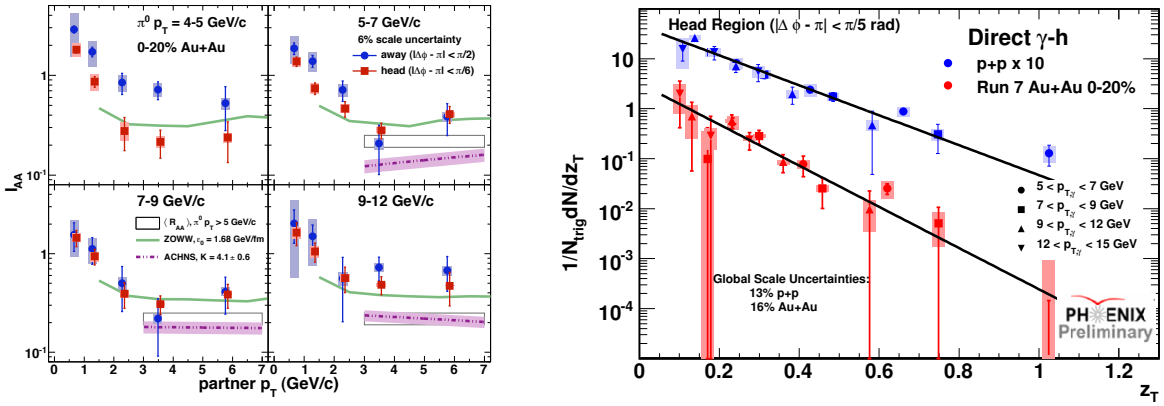

Figure 1.11: Examples of the jet correlation measurements possible with the current PHENIX detector. Both of these correlations rely on proxies for the jet. (left) The strength of the away-side correlation (I_{AA}) between a π^0 trigger and an opposite side hadron [46]. (right) A similar correlation, but for direct photon triggers correlated with away-side hadrons [164]. A direct photon trigger provides a calibrated measure of the jet energy (neglecting the contribution of photons stemming from jet-medium interactions), so the yield can be plotted in terms of the fractional momentum z_T.

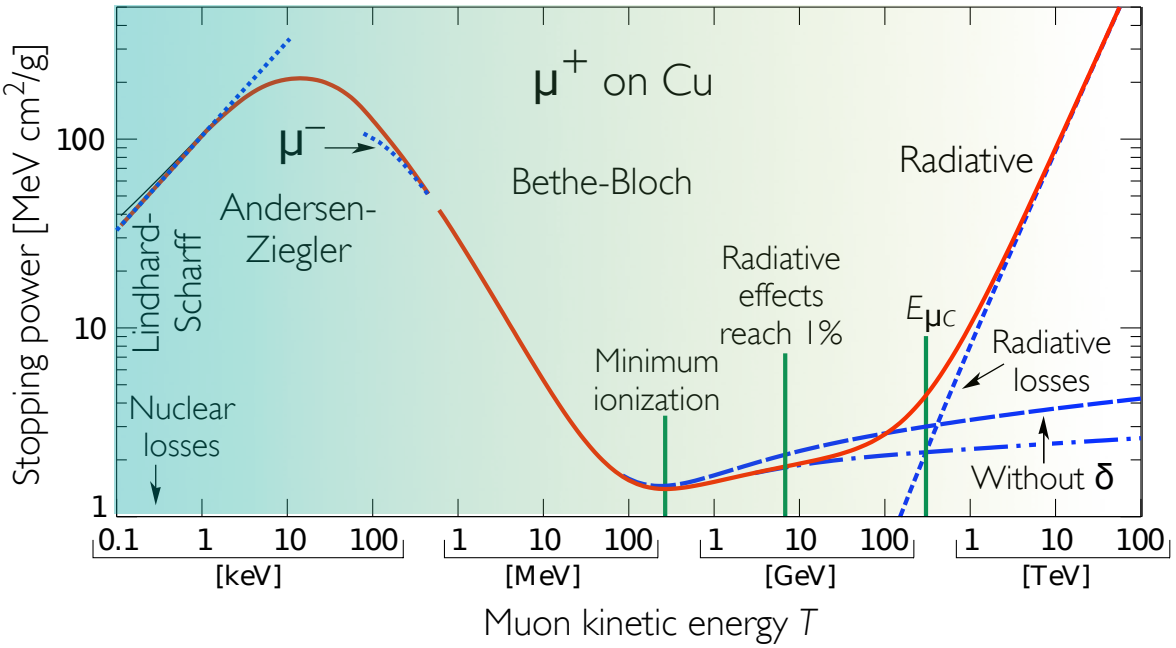

Figure 1.12: The muon stopping power in copper [88] demonstrates a comprehensive understanding of the interaction of a fundamental particle with matter over an enormous range of scales.

Figure 1.12 shows the stopping power of a muon incident on copper as a function of incident kinetic energy from 0.1 keV to 100 TeV, annotated along the way by the physical processes responsible for that stopping power. This diagram represents a comprehensive understanding in QED of the interaction of a fundamental particle with a medium over an enormous range of scales. We are striving toward a similar understanding of interactions in QCD (i.e., the interaction of a parton with the sQGP). PHENIX and STAR, with their current and planned capabilities, are yielding valuable results that will improve over the next five years. However, we believe that major advances in our understanding—the sort of developments that will move us materially toward a QCD version of Figure 1.12—will require a detector specifically designed to measure jets well. This is a major focus of the PHENIX upgrade effort beyond 2015 and both its physics rationale and a description of the required detector capabilities are discussed in detail in Section 3.1.

1.3 Cold Nuclear Matter and low-x Physics

Our quest to understand QCD processes in Cold Nuclear Matter (CNM) centers on the following fundamental questions:

- What are the dynamics of partons at very small and very large momentum fraction (x) in nuclei, and at high gluon density what are the nonlinear evolution effects (i.e., saturation)?
- What are the pQCD mechanisms that cause energy loss of partons in CNM, and is this intimately related to transverse momentum broadening?
- What are the detailed hadronization mechanisms and time scales and how are they modified in the nuclear environment?

These questions are being attacked by numerous experiments and facilities around the world. Deep inelastic scattering on nuclei address many of these questions with results from HERMES at DESY [73, 64], CLAS at Jlab [142], and in the future at the Jlab 12 GeV upgrade and eventually an Electron-Ion Collider [141]. This program is complemented with hadron-nuclei reactions in fixed target p+A experiments at Fermilab (E772, E886, and soon E906) [305] and at the CERN-SPS. RHIC has significantly extended this program to d+A reactions at much higher colliding energies, and also with the key augmentation of being able to tag impact-parameter categories of the collisions.

The RHIC program has already played a major role in addressing the fundamental question of low-x partons in nuclei. It has been known for many years that the population of small momentum fraction (small x) partons in a nucleon embedded in a nucleus is depleted compared to that for a free nucleon. Evidence for this phenomena has come largely from deep-inelastic scattering (DIS) measurements [191, 123] and from Drell-Yan [75, 305] measurements. Quarks and anti-quarks are both depleted for $x < 10^{-2}$. For gluons the evidence is mostly indirect and relies on the Q^2 scaling violations observed in lepton DIS measurements. The state of the art for gluons is embodied in the EPS09 gluon nuclear parton distribution functions (nPDF's) of Eskola *et al* [184], which are shown in the left panel of Figure 1.13. These modifications are extremely uncertain, with depletion factors ranging from $\simeq 10\%$ to nearly no gluons at $x \simeq 5 \times 10^{-3}$.

A more fundamental approach to the depletion of low-x gluons, often called nuclear shadowing, involves coherence models where production from the multiple scattering centers in a nucleus can be coherent at high enough incident parton momenta, and these multiple scatterings can interfere such that the net amplitude for production is reduced [222]. In such pictures, the interior nucleons in a nucleus are "shadowed" and only production from the surface is important. In some models, higher-twist contributions also play a role [268]. Another fundamental picture involves changes in the dynamics of gluons in the very crowded realm of gluons at small x, resulting in saturation effects [262]. At

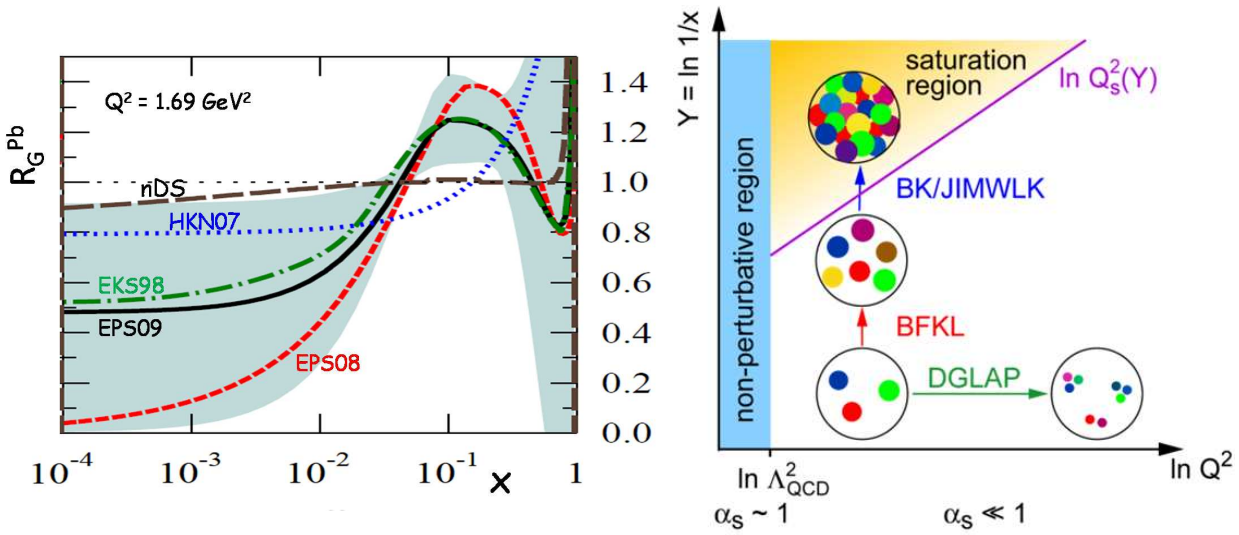

Figure 1.13: (left) Nuclear modification of gluons from a global analysis of Deep Inelastic Scattering (DIS), Drell-Yan data, and PHENIX hadron data by the EPS09 group [184]. (right) Schematic diagram of the different regions in the momentum transfer (Q^2) vs momentum fraction (x) space, showing the gluon saturation region at large $\ln 1/x$ and small $\ln Q^2$.

these very high gluon densities, gluon diagrams where two low-momentum gluons fuse into one higher momentum gluon—thus depleting the low-momentum gluons—become dominant. These effects are present in a nucleon, but become much stronger ($\simeq A^{1/3}$) in a nucleus. Recent saturation models, assert that a novel semiclassical state—the color glass condensate (CGC)—is formed above a critical saturation scale, Q^2, at low enough momentum [192]. Figure 1.13 (right) shows a conceptual diagram of the CGC picture, and indicates the region at small x and large Q^2. However, the boundary where saturation physics is dominant in x and Q^2 is not yet well constrained.

Here we highlight two recent areas where PHENIX measurements at RHIC have started to provide data to address these fundamental questions, while also attempting to provide a reliable baseline of CNM effects to extrapolate to heavy ion collisions, and thus more clearly isolate final state effects from the hot quark-gluon plasma.

The first set of highlighted measurements are of heavy quarkonia J/ψ over a wide range of rapidity and for different centrality classes in d+Au reactions at $\sqrt{s_{NN}} = 200$ GeV [34]. Figure 1.14 shows that for different colliding energies the nuclear modification factor has a very different behavior as a function of the parton momentum fraction in the heavy nucleus x_2. There is better scaling of the results with center-of-mass rapidity y_{CM}, although deviations are already seen. PHENIX has collected ≈ 50 times more statistics in 2008 and expects to submit new results for publication soon. We expect the data will help discriminate between pictures of traditional gluon shadowing, gluon saturation, and possible initial state energy loss of the incoming parton before the hard scattering.

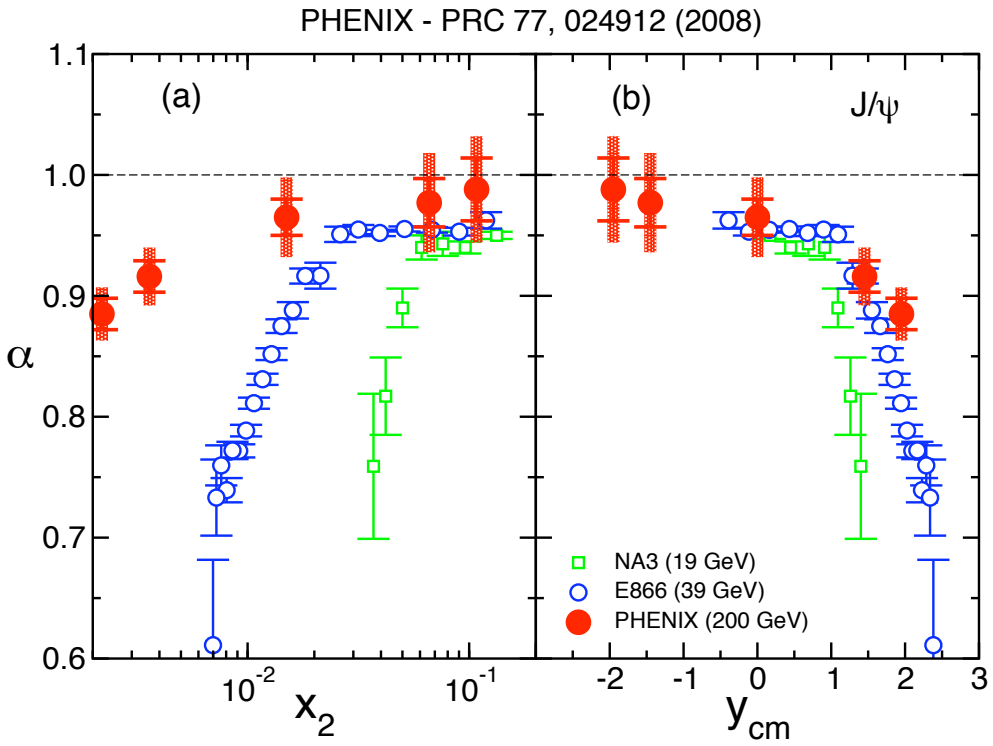

Figure 1.14: Nuclear suppression of J/ψ production for measurements at three different energies (a) vs the momentum fraction of the gluon in the nucleus, x_2 and (b) vs the rapidity (y_{cm}) of the J/ψ. α is a representation of the nuclear dependence in terms of a power law, i.e. $\sigma_A = \sigma_N A^{\alpha}$.

The second set of measurements involve correlated pairs of hadrons at forward rapidity that probe the small-x gluon distributions, and for nuclear targets the modification of these gluon distributions in nuclei. For pairs of hadrons, where one is forward and the other at midrapidity, the x range probed is very broad. However, when both hadrons are detected at forward rapidity, the x distribution is relatively narrow and at fairly small x. Gluon saturation models have predicted that in the nuclear environment probed by d+A collisions the correlation will be broadened and the away-side peak will be weakened compared to p+p collisions. For this phenomena, usually called mono-jets, one observes (triggers on) a hadron from one parton jet and the opposing jet vanishes (for d+Au compared to p+p) with the momentum of the trigger jet balanced on the other side by many gluons associated with the saturated gluon field. Recent data using the Muon Piston Calorimeter, which covers pseudorapidity $|\eta|$ =3.1–3.8, does show broadening and weakening of the away-side particles, as shown in Figure 1.15. However, the theoretical interpretation of this phenomena remains unclear, since pQCD model calculations including higher twist may also be able to produce such effects, particularly at the rather low momenta of the hadrons measured so far.

Extending the set of measured probes of CNM effects to include open heavy flavor, Drell-Yan, and direct photons and over a much broader kinematic range is essential to the world wide effort to address these key questions. As part of the PHENIX upgrade program we address measuring open heavy flavor ($D \rightarrow e$ or μ and $B \rightarrow e$ or μ) including at forward rapidity $\eta = 1.2$–2.2 in Section 2.4.1 and with direct photons over a similar rapidity range in Section 2.4.2. However, extending the kinematic reach to much larger rapidities and x_F requires a new forward rapidity spectrometer that is discussed in Section 7.2. We believe this complete program, in addition to other DIS experiments, hadron-nucleus fixed target experiments, and eventually a proton-nucleus program at the Large Hadron Collider and the Electron-Ion Collider will give the community the full tool set needed to answer these questions.

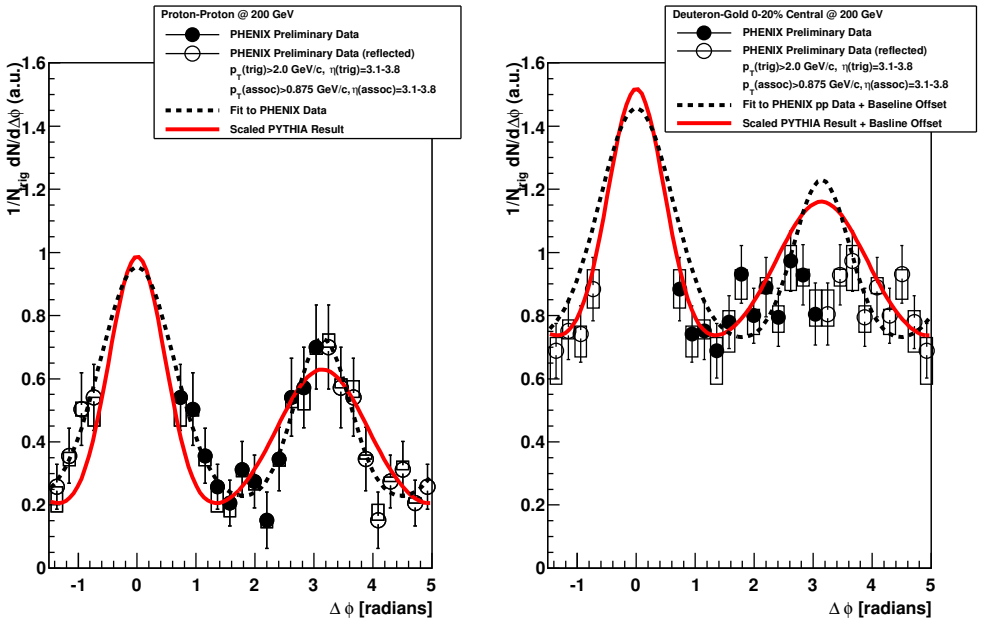

Figure 1.15: Conditional yield vs azimuthal angle ($\Delta\phi$) in (left) p+p and (right) d+Au collisions for two π^0s at forward rapidity.

Chapter 2

Heavy Ion Physics: Midterm Plan

PHENIX has an ambitious plan for addressing topics of current interest in RHIC physics in the next five years. Here we highlight four key physics questions that our targeted midterm upgrades and year-by-year run plans will answer. Details on the detector upgrades and status are given in Chapter 7, and the 5-year proposed run plan is given in Section B.2.

We plan to carry out the following program:

- We will investigate the restoration of approximate chiral symmetry and its impact on vector meson spectral functions via dielectron measurements with the Hadron Blind Detector.
- We will explore the mechanisms of parton energy loss for heavy quarks (charm and beauty) and their coupling to the medium with the new silicon vertex detectors (the VTX and FVTX).
- We will search for a QCD critical point with a continued systematic low energy scan.
- We will look for further evidence of gluon saturation at low x with the FVTX and potentially with new forward calorimetry, referred to as the FOCAL.

These physics lines of investigation are directly connected to the PHENIX midterm upgrades as shown schematically in Figure 2.1. In this Chapter we focus on these four key areas, but we note that there are many other areas where larger data samples and new detector performance will also be beneficial. For example, we want to extend the bulk matter dynamics measurements described in Section 1.1 to U+U collisions with larger energy densities and to asymmetric heavy ion collisions (e.g. Cu+Au) in order to study higher flow moments – as detailed in the 5-year run plan in Table B.1. Also in the 5-year run plan, we foresee an increase in Au+Au data sample a factor of 4–5 over the run-10 Au+Au data set. This increased data sample, combined with the larger acceptance in the

VTX for low momentum charged hadrons, will improve our direct γ-hadron correlations. The improved momentum vector resolution from the VTX and FVTX we will improve our J/ψ measurements (including the separation of the ψ').

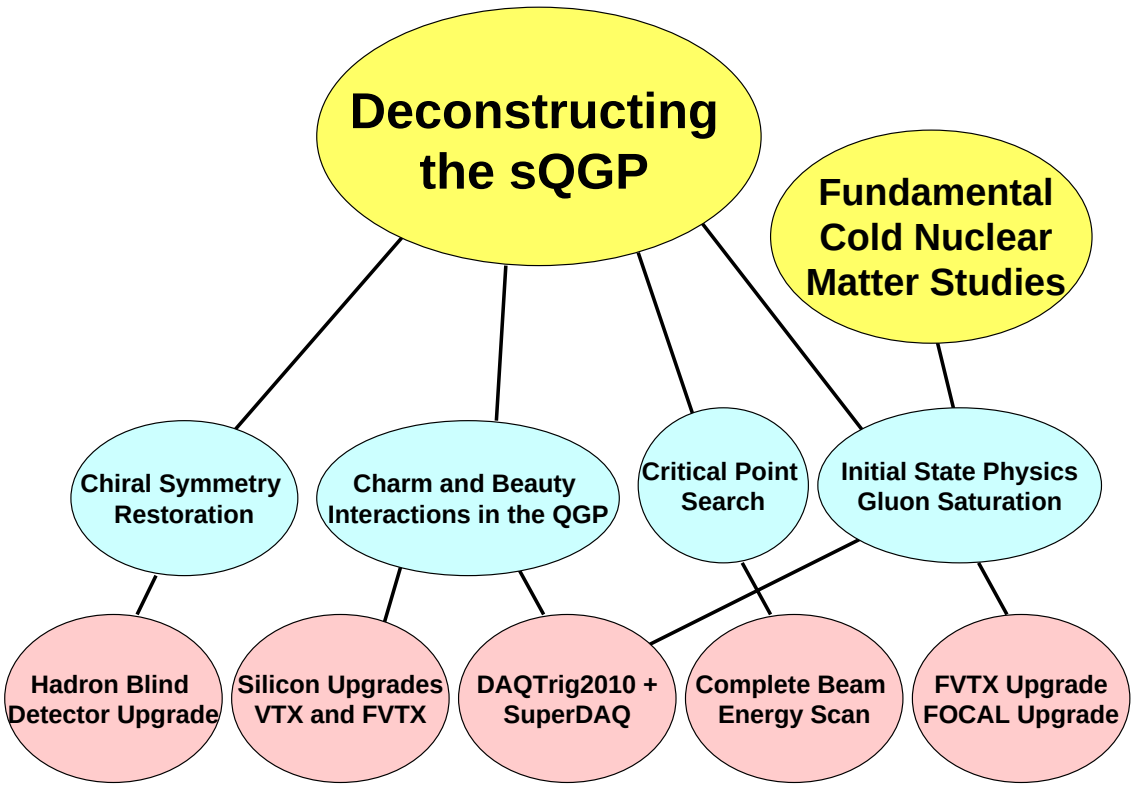

Figure 2.1: Schematic outline of key physics lines of investigation and the detector upgrades needed.

2.1 Modified Spectral Functions and Chiral Symmetry

A key property of the phase transition from a hadron gas to the Quark Gluon Plasma is that lattice QCD calculations at $\mu_B = 0$ indicate that the deconfinement transition temperature is close to the temperature for the restoration of approximate chiral symmetry. Although it is true that this symmetry is not fully restored, as the light quarks still retain 5–15 MeV current masses due to electroweak symmetry breaking (i.e. the Higgs mechanism), these masses are very small compared to Λ_{QCD} and the residual chiral symmetry breaking is only very slight. The breaking of chiral symmetry in the QCD vacuum accounts for almost all of the mass of hadrons (including baryonic matter in the universe). As such, it is of utmost importance to understand in detail the manner in which the quark masses evolve from their current-quark values at very high temperatures to the constituent masses which appear in "dressed" hadrons. As detailed in Chapter 1, we have strong experimental evidence that heavy ion collisions at RHIC create a nearly equilibrated Quark Gluon Plasma with temperatures well above the transition value. However, we have no direct experimental evidence that chiral symmetry is restored.

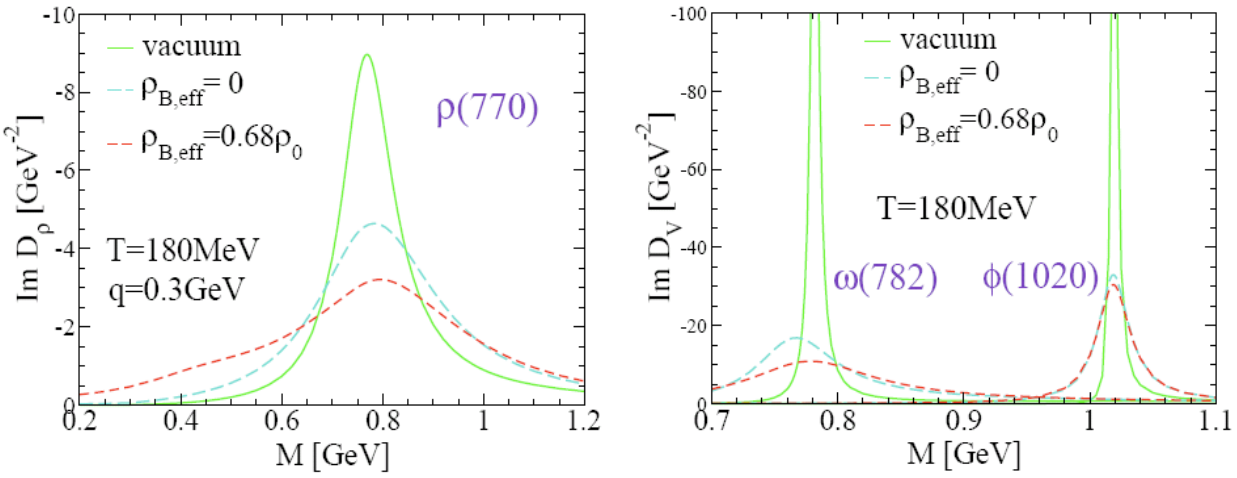

Figure 2.2: Spectral functions of the light vector mesons ρ (left) and ω and ϕ (right) in vacuum (solid lines) as well as in hot nuclear matter (dashed lines).

Calculations within effective chiral theory indicate that near and above the phase transition temperature, the spectral functions of vector mesons including the ρ, ω and ϕ are substantially modified (see [274] for example). Shown in Figure 2.2 is one calculation of the spectral function modifications as a function of temperature. Measuring the modification of vector meson states is challenging for a number of reasons. First, any of the decay products of a modified vector meson will reflect the complex time evolution of the vector meson states as they themselves evolve and then decay in the medium. And, second, any strongly interacting decay products will scatter in the medium, weakening or destroying their correlations. This is why it is crucial to measure the leptonic decay of these states, since the leptonic decay products do not interact with the medium via the

color force and thus exit essentially undisturbed. In this regard the measurement of dileptons in the invariant mass region 0.2–1.1 GeV/c^2 are very interesting, specifically for the ρ state because of the short lifetime ($\tau \approx 1$ fm/c) allowing it to decay in the hot and dense matter.

Key measurements were done at the CERN-SPS with heavy ions for colliding energies $\sqrt{s_{NN}}$ = 17–20 GeV to address this issue, including measurements by the CERES experiment [58] and more recently by the NA60 experiment [102]. Figure 2.3 shows results from In+In collisions at $\sqrt{s_{\mathrm{NN}}} = 17\,\mathrm{GeV}$ from NA60, after subtracting the contributions expected in the absence of any modifications. Substantial modifications are observed. Also shown are various competing theories about the nature of the evolution of these spectral functions in addition to other hadronic contributions. The calculation of Rapp and Wambach with a modified ρ state and contributions from $\pi\pi$ annihilation shows reasonable agreement with the experimental data, except for masses greater than $0.9\,\mathrm{GeV}/c^2$. For a detailed review of the measurements and alternative theoretical explanations see [300].

The PHENIX experiment has demonstrated excellent electron identification and tracking capabilities and has published results not only regarding low-mass dielectrons at low p_T, where the process discussed above is believed to be most prominent, but also for higher p_T dielectrons where contributions from nearly-real virtual photons are significant [57]. The right panel of Figure 2.3 shows that the PHENIX published result (integrated over all p_T) indicates a significant enhancement below the vacuum value for the ρ meson. Interestingly, this disagrees with a model of ρ modified spectral function and $\pi\pi$ annihila-

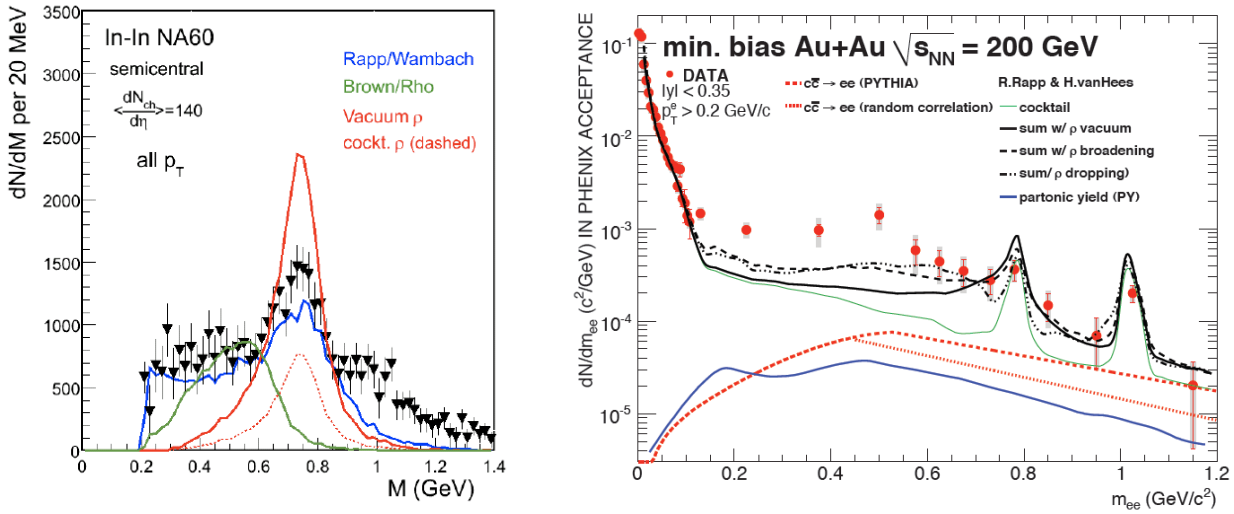

Figure 2.3: (left) Results from the NA60 experiment for low-mass dimuon pairs produced in In+In collisions. Various theoretical model calculations are shown for comparison. (right) PHENIX results for the invariant mass spectra of e^+e^- pairs in Au+Au collisions in the low-mass region. The calculation is by Rapp and van Hees [274]

tion that reasonably described the NA60 data at lower colliding energies. However, the enhancement is seen in only three data points, which is insufficient to make a detailed determination of the shape of the modification. Also, since there seems to be a significant disagreement between theory and measurements taken at colliding energies $\sqrt{s_{\rm NN}}$ that are an order of magnitude apart, it is crucial to map out the full energy span more thoroughly.

The key limitation in the current PHENIX measurements is the very large combinatorial background in central Au+Au collisions that must be subtracted before accessing the correlated electron pairs of interest. Additionally, a low signal-to-background ratio results in a systematic uncertainty from the detailed understanding of the combinatorial background and its normalization. Exhaustive analysis of the PHENIX Au+Au data taken at $\sqrt{s_{\rm NN}}$ = 200 GeV has allowed control of the dielectron background normalization at a level of 0.25%. Such precision is required in order to obtain our published true dielectron signal via subtraction since the signal to background below 1 GeV/c^2 was approximately 1:200. The combinatorial background is mainly a result of associating uncorrelated electron-positron pairs in the mass spectrum. The problem is exacerbated by a high multiplicity of beampipe conversions and π^0 Dalitz decays in conjunction with the limited acceptance of PHENIX. In dielectron reconstruction, typically one of the two pair partners is lost. An upgrade of the PHENIX detector was necessary to considerably reduce the resulting combinatorial background.

For the express purpose of answering in detail the questions regarding modified spectral functions in the medium, PHENIX started a very ambitious research and development project back in 2003. This detector project was a significant part of the last PHENIX Decadal Plan (2004–2013) [4] which has now come to fruition.

In order to differentiate between γ conversions, π^0 Dalitz decays and light vector meson decays, the opening angle of the decay pair must be measured. Since Dalitz decays and photon conversions typically produce pairs with very small opening angles, the direction of the momentum is sufficient to tag electrons originating from these sources. The inner coil of the PHENIX central magnet was designed to be able to cancel the field within a 60 cm radius of the beampipe and provide the zero-field region required for this type of measurement to work. Thus a Hadron Blind Detector (i.e. one that is only sensitive to electrons and not hadrons) that can operate in this field-free region, can make this differentiation. The main Hadron Blind Detector (HBD) specifications are: electron identification with a very high efficiency ($> 90\%$), double hit recognition at a comparable level and a moderate hadron rejection factor of 100. Details on the detector design and hardware performance are given in Appendix C.

The HBD was installed for an engineering run in 2007, and significant operating problems were encountered. The detector was removed and was refurbished to improve its ability to hold high voltage stably. The HBD was then reinstalled for $p+p$ data taking during the 2009 run. The HBD operated stably during the entire duration of the 2009 and 2010 runs. First analysis of Hadron Blind Detector data in full energy Au+Au collisions indicates

that the HBD performed in run-10 as well as in run-9.

The superb performance of RHIC in run-10 allowed PHENIX to collect over 8 billion events at 200 GeV and 700 million events in 62.4 GeV Au+Au collisions. This will lead to an excellent measurement of the low-mass dilepton spectrum, and allow us to determine whether the large dilepton excess observed by PHENIX at 200 GeV also appears at lower $\sqrt{s_{\rm NN}}$. In the 39 GeV Au+Au run, PHENIX collected 250 million events. With such a data sample, which is substantially larger than initially anticipated, it should be feasible to measure the low-mass dielectron spectrum at a third energy.

Optimization of the analysis algorithms for high multiplicity events is underway at the time of this writing, with a particular focus on effective rejection of photon conversions in the HBD back plane. We anticipate an improvement in the effective signal by at least an order of magnitude over our published Au+Au 200 GeV results. Lowering the background to be subtracted also substantially decreases systematic uncertainties in the extracted signal. The improved data set will allow a detailed examination of the low-mass enhancement and ρ modification as a function of both p_T and centrality, similar to that shown at lower energies from NA60 in Figure 2.3. Measurements from the large data set at 62 GeV, using the HBD background rejection, will have twice the statistical significance of the existing result at 200 GeV. It becomes more difficult to predict the measurement

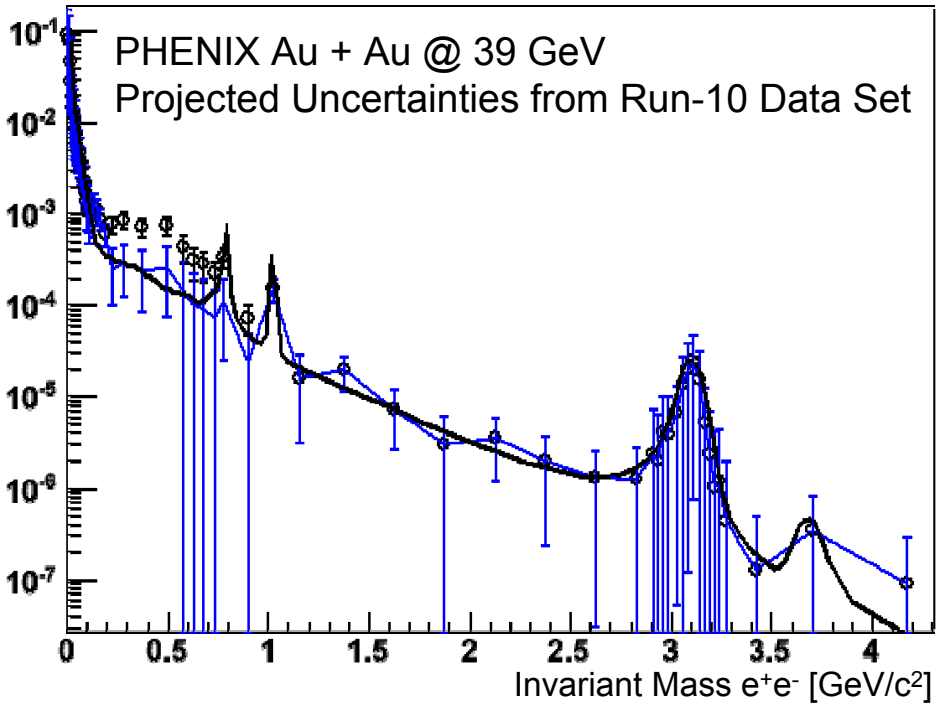

Figure 2.4: Projected yields and uncertainties for e^+e^- pair invariant mass measurements in Au+Au at 39 GeV data after background subtraction. Details on the projection are given in the text.

significance in the 39 GeV data set, as we do not yet know the $\sqrt{s_{NN}}$ dependence of the low-mass enhancement. Figure 2.4 shows the invariant mass distribution predicted for 200 million minimum bias events with vertex inside $\pm$ 20 cm, under two assumptions about the magnitude of the enhancement. The solid line shows the mass spectrum of dielectrons calculated with the hadronic decay cocktail. The black points show the expected measurement should the enhancement be the same at 39 GeV as measured at 200 GeV. The uncertainties are rather small because the combinatorial background falls as the square of the hadron multiplicity, and the HBD further reduces the background that must be subtracted. The blue points show the mass spectrum that results if the excess at 39 GeV is 30% of that observed at 200 GeV. This illustrates the limit of measurable enhancement at this energy.

These three excellent data sets span the region of interest, and they are under very active analysis. We expect this to be a focus within the collaboration over the next two years, and to result in high quality measurements to answer key physics questions. The HBD detector has now been removed from the PHENIX hall to make space for the inner silicon detectors, discussed in the next Section.

2.2 Heavy Flavor Lepton Physics

The PHENIX experiment was specifically designed to have exceptional electron particle identification, even in the high multiplicity environment of central Au+Au reactions. PHENIX has published [30] Au+Au results from the 2004 run on nonphotonic electrons, which are predominantly from charm and bottom meson decays. Figure 2.5 shows the measurements of the nuclear modification factor R_{AA} out to $p_T \approx 10$ GeV/c and elliptic flow v_2, which indicate a dramatic change in the momentum distribution of heavy quarks in the medium. If the heavy quarks were unaffected by the surrounding Quark Gluon Plasma, the R_{AA} value would be close to one (excepting modest initial state effects) and v_2 would be zero. This Letter has been cited 200 times in the last three years which is a simple indicator of the strong interest in the field in these results. In a recent manuscript submission we have extensively documented the entire analysis procedure for nonphotonic electrons, including systematic uncertainty estimation, and theoretical model comparisons [44].

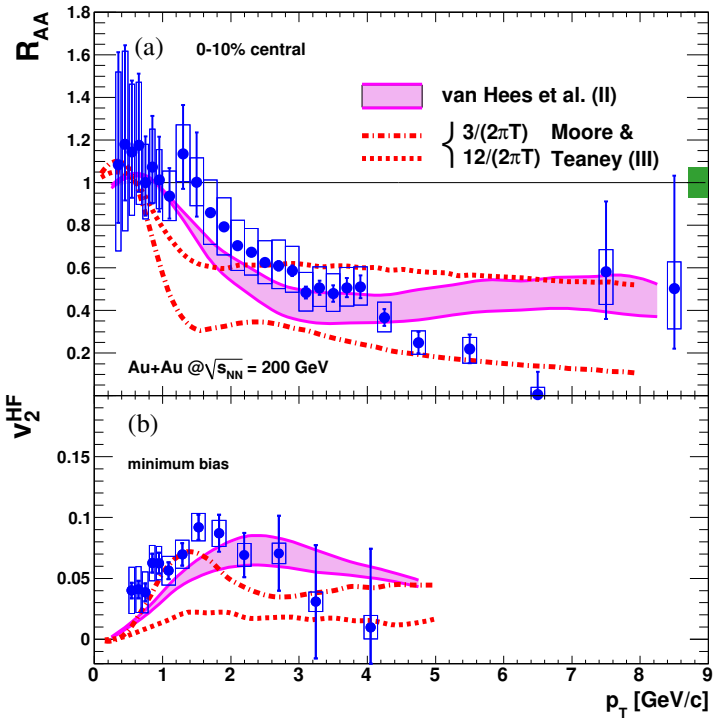

Figure 2.5: (a) Nuclear modification factor R_{AA} of heavy-flavor electrons in 0–10% central collisions compared with PHENIX π^0 data and various model calculations. The box at $R_{AA} = 1$ shows the uncertainty in the number of binary collision estimate. (b) v_2 of heavy-flavor electrons in minimum bias collisions compared with PHENIX π^0 data and the same models.

As shown in Figure 2.6, these results present a challenge for the perturbative (weak coupled expansion approximation) picture of partonic energy loss. However, a fundamen-

tal complication is that the nonphotonic electrons have contributions from both charm hadron (e.g. D meson) and bottom hadron (e.g. B meson) decays. It is expected that charm hadrons dominate the electron contribution for $p_T < 5$ GeV/c and bottom hadrons for $p_T > 5$ GeV/c. This is roughly confirmed by examining nonphotonic electron-hadron angular correlations in p+p reactions [38]. However, the statistical uncertainties are large and the current perturbative QCD FONNL calculations have an uncertainty in the ratio of $b \rightarrow e/c \rightarrow e$ ratio from approximately 0.3 to 0.7 at $p_T = 5$ GeV/c.

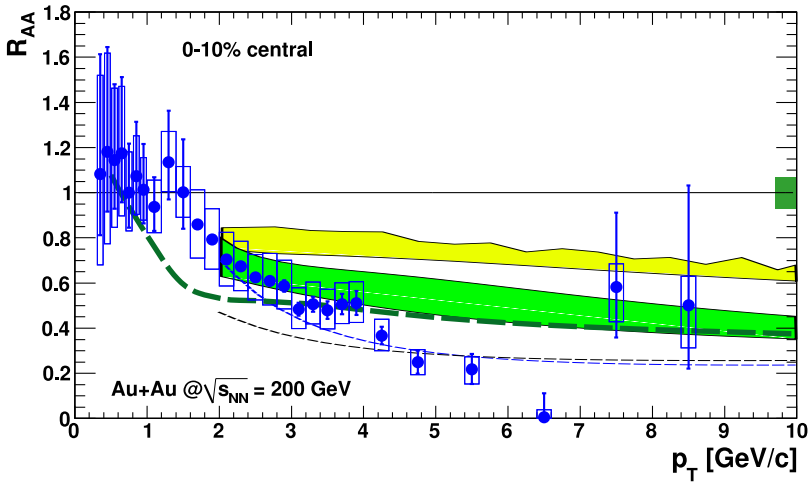

Figure 2.6: R_{AA} in the 0–10% centrality class compared with energy loss models. The thick dashed curve is the BDMPS calculation for electrons from D and B decays. The bands are DGLV calculations for electrons from D and B decays. The lower band contains collisional energy loss as well as radiative energy loss. The thin dashed curves are DGLV calculations for electrons from D decays only.

Figure 2.7 shows a number of calculations of charm quark flow in the Quark Gluon Plasma. At $p_T = 5$ GeV/c, some calculations of v_2 range as high as 15%. The data do not support a monotonic increase of v_2 with p_T, despite large statistical uncertainties. The trend seen in the data could be the result of reduced charm quark flow, or it could be due to a predominance of bottom quark contributions at higher p_T.

Diffusion calculations show that bottom quarks are so heavy that they are difficult to move around, and thus exhibit minimal flow. In the perturbative energy loss framework, radiative energy loss of heavy quarks via gluon bremsstrahlung is suppressed due to the "dead cone" effect, where forward radiation for heavy quarks, traveling at velocities much less than the speed of light, is limited. If, contrary to expectations, the bottom quarks exhibit strong flow in the medium, this would challenge the entire paradigm of perturbative energy loss as the proper framework for understanding jet quenching. Additionally, a measurement of charm flow (separated from bottom flow) out to higher p_T may well provide one of the best constraints on the η/s ratio via the diffusion approach. This method for constraining η/s is an excellent alternative to the current method which compares the bulk flow of light hadrons to viscous hydrodynamic models. It would help

us answer the question of how close η/s in the quark-gluon plasma is to the conjectured minimum bound.

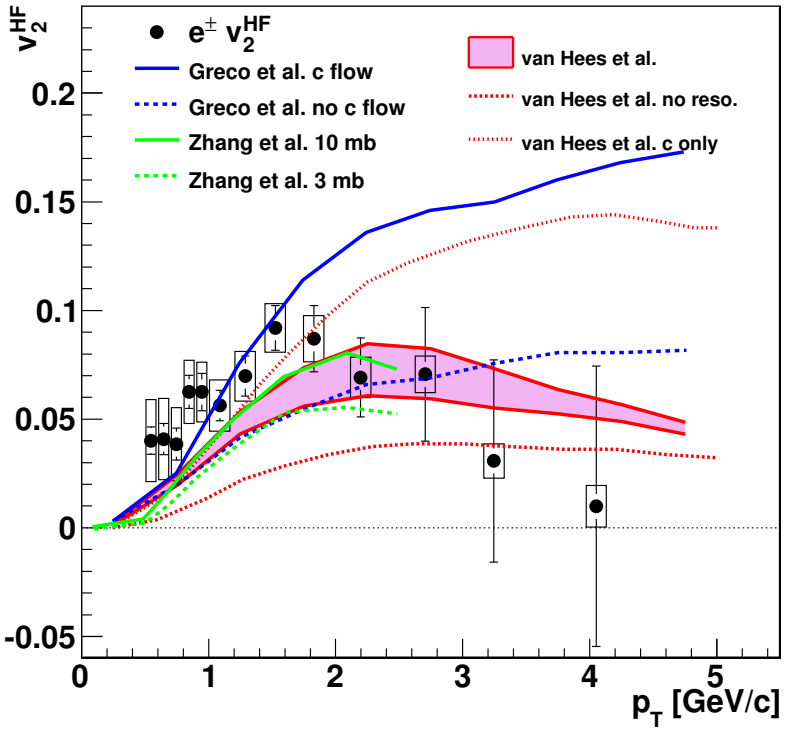

Figure 2.7: Nonphotonic electron (HF) elliptic flow (v_2) as a function of transverse momentum compared with theoretical models from Greco *et al.*, Zhang *et al.*, and van Hees *et al.*

In the last Decadal Plan (2004–2013) [4], the PHENIX collaboration proposed to develop and build a set of inner silicon vertex detectors specifically to unambiguously resolve these heavy quark puzzles. These detectors will enable us to measure the displaced vertices of leptons from the decay of charm and bottom mesons, and separate the charm and bottom contributions with high precision. As described in Appendix C, excellent progress on the construction of the midrapidity barrel vertex detector (VTX) and forward rapidity (FVTX) has been made, and installation of the VTX is on schedule for the fall of 2010, and will be followed by the installation of the FVTX in the fall of 2011. The Appendix also describes a data acquisition upgrade (referred to as DAQTrig2010) that is being implemented for reading out these new detectors. This important set of physics measurements are a driving factor in our expected beam use request for the next five year period. As shown in Table B.1, we project two initial Au+Au runs in 2010/11 and 2011/12 for commissioning the silicon detectors and to obtain initial physics results, and later a longer run when full accelerator stochastic cooling becomes available, and additional data acquisition bandwidth via the SuperDAQ upgrade is installed (see detailed in Appendix C.2.6).

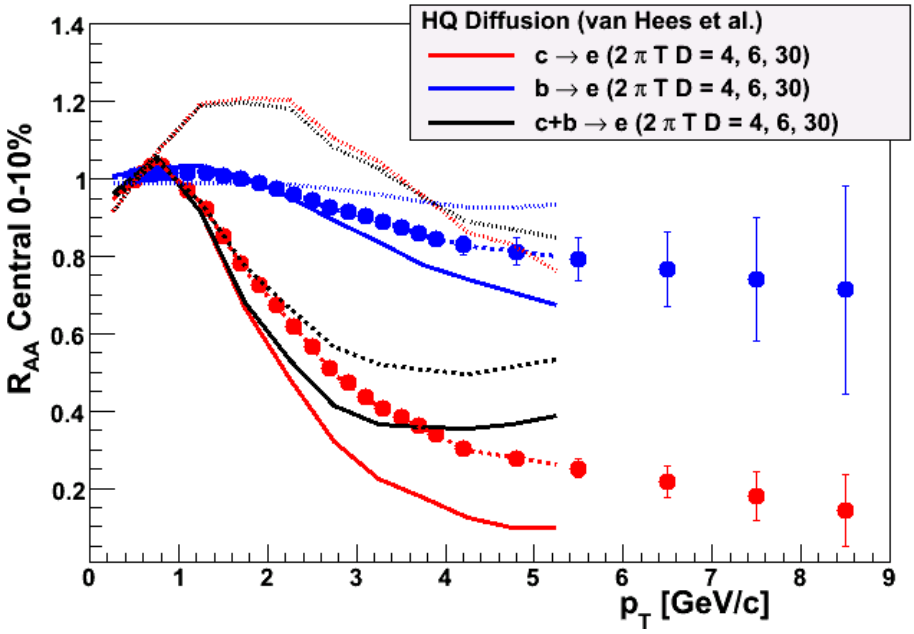

Figure 2.8: Projected uncertainties for the nuclear modification factor (R_{AA}) as a function of transverse momentum for heavy flavor electrons tagged with a displaced vertex from D meson decay (red) and B meson decay (blue). The uncertainties are for the 10% most central Au+Au collisions—a subset of a total of 29 billion Au+Au minimum bias events and 14.8 pb^{-1} p+p events at 200 GeV. Also shown are calculations by van Hees *et al.* [304] assuming different diffusion coefficients.

In total this will yield 4.3 (3.6) nb^{-1} or equivalently 29 (24) billion recorded Au+Au interactions for the VTX (FVTX). All of these event number projections take into account the smaller z-vertex acceptance (i.e. ± 10 cm) of the silicon detectors. For comparison p+p measurements at 200 GeV, we project an integrated luminosity over two years of running of 15 pb^{-1} sampled within the same z-vertex acceptance.

We show the projected physics performance we expect to achieve by 2015, using the above integrated luminosities over multiple year running periods. Shown in Figure 2.8 are the Au+Au p_T distributions of electrons from charm and bottom hadron decays (left) and the corresponding nuclear modification factors R_{AA} (right). Figure 2.9 shows the projected uncertainties for minimum bias Au+Au collisions for the elliptic flow v_2 observables. For the elliptic flow projections, we have assumed a reaction plane resolution comparable to that from the reaction plane detector that was installed prior to 2007. This detector was removed after the 2010 running period due to conflicting space requirements with the VTX, but studies indicate that the VTX and FVTX can be similarly utilized with a comparable resolution. These results will provide great insight into the puzzles of the behavior and interaction of heavy flavor quarks in the medium.

The FVTX provides an excellent opportunity to measure the open heavy flavor suppres-

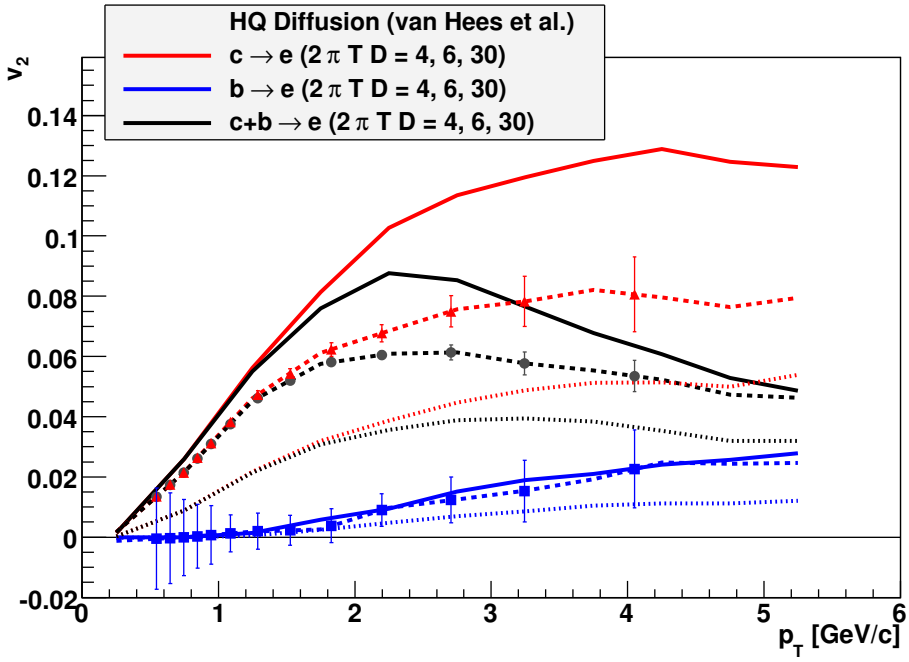

Figure 2.9: Shown are the projected uncertainties for the elliptical flow (v_2) as a function of transverse momentum for heavy flavor electrons tagged with a displaced vertex from charm hadron decay (red) and bottom hadron decay (blue) and the combination of the two (black). The uncertainties are for 10% central Au+Au reaction as a subset of a total of 29.0 billion Au+Au minimum bias events as projected to be accumulated by 2015. Also shown are calculations from van Hees *et al.* [304] in a heavy quark diffusion calculations assuming different diffusion coefficients. Note that the largest flow magnitude case corresponds to nearly zero shear viscosity.

sion and flow at forward rapidity. Here the measurement is also sensitive to low-x gluons in the gold nucleus, and will provide a baseline measurement for comparison with the J/ψ suppression seen in the same kinematic range. Shown in Figure 2.10 are the projected measurement uncertainties on $R_{\rm AA}$ for heavy flavors, using muons that are tagged by the FVTX as originating from heavy meson decays. This displays a very clear discriminating power between different energy loss scenarios: 'DGLV' including perturbatively calculated radiative energy loss only [175], 'DGLV Rad + El' which includes additional elastic energy loss [316], and collisional dissociation of the mesonic state in the medium [52]. These measurements will provide excellent discriminating power between these different scenarios.

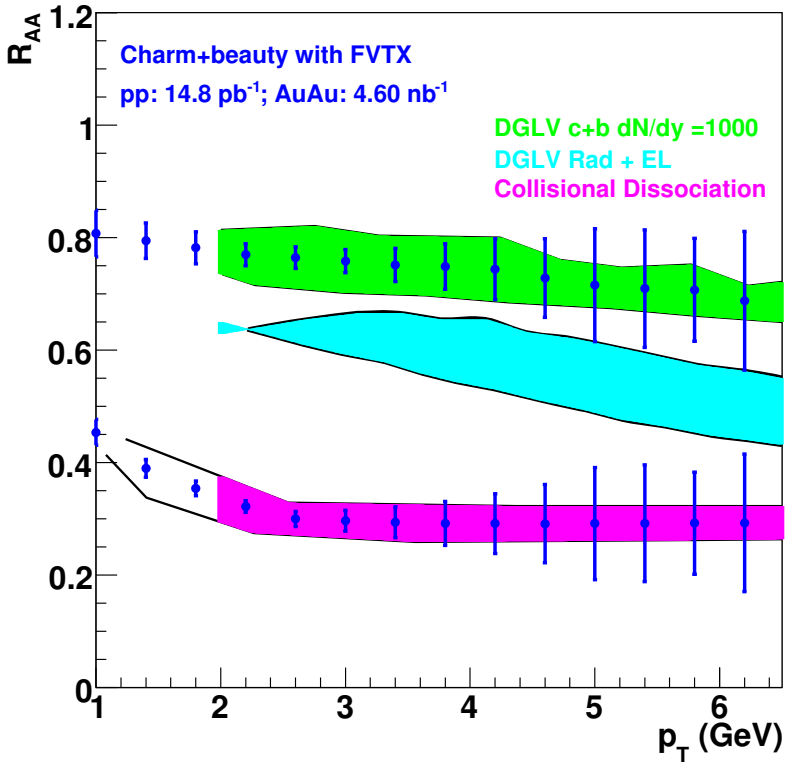

Figure 2.10: Projected heavy flavor R_{AA} measurement with the FVTX versus transverse momentum p_T, compared with three different theoretical expectations.

2.3 Beam Energy Scan and Search for the Critical Point

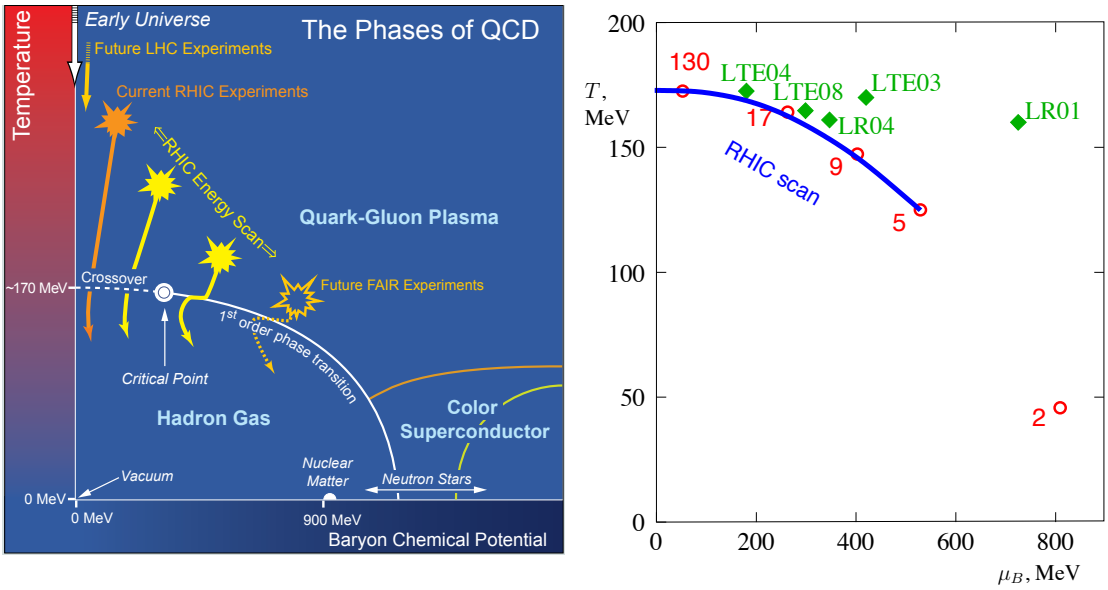

Figure 2.11: (left) Schematic diagram for the phases of QCD matter. Note the hypothesized Critical Point connecting the first order phase transition line down to the region of Color Superconductivity. (right) Similar diagram with various theoretical estimates for the position (in particular μ_B,T) for the critical point and the range of μ_B values accessed through the RHIC beam energy scan.

There are several compelling reasons for performing a beam energy scan at RHIC. The measurement of excitation functions for many important observables at RHIC, like quark-number scaling of elliptic flow or parton energy loss, can serve as powerful constraints and discriminators between various theoretical models of the quark-gluon plasma and its eventual hadronization. In addition, a beam energy scan serves to map a large region of the QCD phase diagram, Figure 2.11. In particular, the region of higher baryon chemical potential (large net baryon density) is predicted to be one of the more feature-rich parts of the QCD phase diagram. At the center of the discussion is the possibility that a critical end point to a first order phase boundary may be located at finite μ_B. Whether such a point exists and at which value of μ_B it is located is currently unknown. Lattice calculations at finite μ_B are challenging, and make a number of as yet untested assumptions. Recent results are shown in the right panel of Figure 2.11. One can argue for the existence of a critical point on general grounds, since current lattice QCD calculations indicate that there is a smooth crossover at $\mu_B = 0$, and there is a first order transition at very low temperatures, in the domain of color superconductivity. However, it is possible that this first order phase transition line could be moved all the way back to the color superconductor boundary. These arguments only underscore the high priority for experimentally investigating this part of the phase diagram. Locating the critical point by experiment would

significantly expand our knowledge of the QCD phase diagram.

There are a number of observables within reach for the existing PHENIX detector that are sensitive to this physics problem.

- The measurement of fluctuation observables is expected to provide the most direct evidence that the system has approached a critical point. Simultaneous observation of an increase in fluctuations in $\langle p_T \rangle$ and multiplicity, along with the observation of an increase of correlation lengths has the potential to identify the critical point location. Using the latest Collider-Accelerator Division rate estimates, we can make statistically significant measurements of multiplicity, $\langle p_T \rangle$ and $\langle E_T \rangle$ fluctuations for collision energies above $\sqrt{s_{NN}}$ = 10 GeV. Additional fluctuation measurements of correlation functions at low p_T and longitudinal density fluctuations should be possible. For event-by-event measurements of the K/π ratio, we will be near the statistical limit for energies below 39 GeV.

- Density fluctuations at the critical point may inhibit momentum transport over large distances, thereby effectively decreasing the shear viscosity (and hence the η/s ratio). Data from a variety of substances near the critical point suggest that the minimum of the η/s ratio may be reached [165]. An excitation function of flow observables (including elliptic flow v_2) is important for mapping out the energy dependence of the shear viscosity. Additional measurement of quark-number scaling as a function of energy should also prove elucidating in this regard.

- The measurement of identified particle ratios, including K/π, π/p and $\overline{p}/p$ are important for determining the degree of chemical equilibration and the location at freeze-out in the $\mu_B - T$ plane. These measurements are a strength of the PHENIX spectrometer with its excellent collision start time and particle time-of-flight detectors.

- Parton energy loss as a function of collision energy is another key handle on the properties of the medium as it evolves. The exact conditional dependence (energy, system size) of the parton energy loss will have major constraining power on different theoretical frameworks for understanding parton-medium interactions. While we do not expect moderate to high p_T nuclear modification factors $R_{\rm AA}$ to be directly sensitive to the critical point, there should be a dependence in terms of the relevant quasi-particles and excitation modes of the medium that the parton scatters from.

- Femotoscopy (HBT correlations) provides a number of experimental control tools to measure the space-time dimensions of the medium created by these heavy ion reactions. Measurements at the higher RHIC energies reveal extended nonGaussian tails in the source function [55]. These tails are sensitive to the emission time duration of the fireball, and thus may be significantly modified near the critical point.

The RHIC program had a very successful start to the beam energy scan program in 2010, and as shown in Appendix B, Table B.2. PHENIX has already recorded substantial Au+Au minimum bias data sets at $\sqrt{s_{NN}}$ = 7.7 (1.6M events), 39 (250M events), and 62.4 GeV (700M events). We are proposing to run at $\sqrt{s_{NN}}$ = 18 and 27 GeV over the 2010–2012 period to collect comparable data sets and thus complete the first pass energy scan. The PHENIX detector has shown the ability to trigger and analyze data below RHIC injection during the 7.7 GeV running. However, the finite acceptance of the central arm spectrometers and the finite z-vertex acceptance ($|z| < 30$ cm for accepting produced particles from collisions without striking the magnet pole tips) limits the PHENIX physics reach for energies below 15 GeV. The introduction of the silicon VTX detector increases our overall acceptance, but at the same time only has optimal acceptance for collisions with $|z| < 10$ cm. Thus, we do not project requesting additional sub-injection energy running at this time.

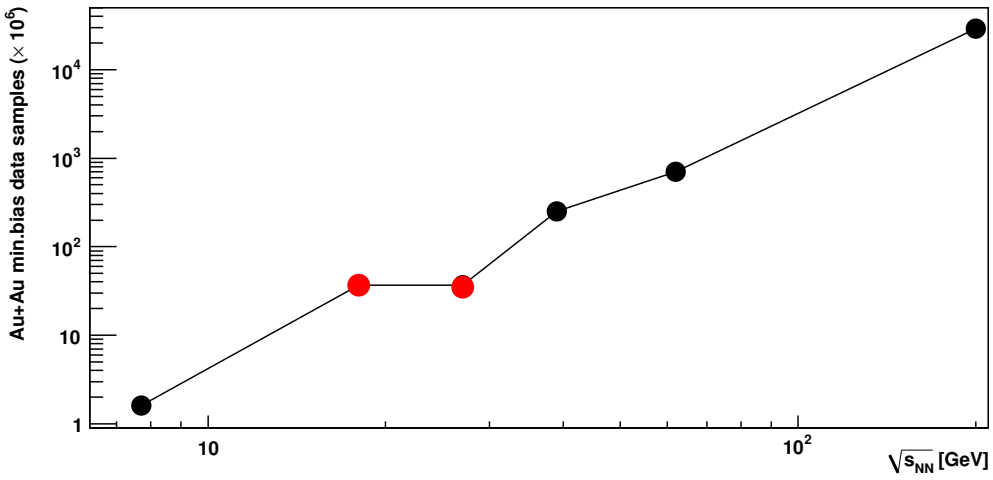

Figure 2.12: The number of events ($\times 10^6$) of Au+Au minimum bias data that can be recorded as a function of beam energy $\sqrt{s_{NN}}$. The black points are at energies where data has already been taken, and the red points are projected future runs to complete the scan.

We are very excited to carry out this program and analyze the experimental data. We show the data sets already on tape and the projected data sets in Figure 2.12. We also show in Table 2.1 the breadth of observations possible with various sized data sets. One can see that for energies greater than 15 GeV, a wide suite of analyses are possible. It is also clear that other observations, such as three-dimensional source imaging via pion HBT is not possible at the lower energies. Although there are prospects for upgrades to the accelerator for higher luminosity at lower energies, we do not currently anticipate that they make these observations possible within PHENIX. We note that the beam energy scan program is one with great discovery potential. There is a possibility that, based on the analysis of the experimental data, additional requests for running at an intermediate energy (between those already requested) or for additional run time to follow up

Physics Topic	Collision Energy $\sqrt{s_{NN}}$			
	7.7	18	27	39
$\langle n \rangle$ fluctuations	0.01	0.01	0.01	0.01
$\langle p_T \rangle$ fluctuations	0.03	0.03	0.03	0.03
PID spectra, ratios	0.02	0.01	0.01	0.01
longitudinal density correlations critical exponent η	2	2	2	2
1D imaging of pions source Lévy exponent α pion 3D Gaussian HBT $R_i(m_T)$ HBT intercept parameter $\lambda(m_T)$	33	19	16	14
dielectron spectra $\langle K/\pi \rangle$ fluctuations	50	50	50	50
dihadron correlations	246	109	68	48
nuclear modification factor R_{AA} optical opacity κ		157	24	6.3
heavy flavor electrons				700
1D imaging of kaon source 3D imaging of pion source kaon 3D Gaussian HBT $R_i(m_T)$	586	340	276	239

Table 2.1: Table of physics topics versus colliding Au+Au energy. The numbers represent the number of events ($\times 10^6$) required to make a precision measurement in this particular channel. The values in red represent measurements that require significantly more statistics than PHENIX can record (c.f. Figure 2.12).

interesting signals might be made.

2.4 Cold Nuclear Matter and low-x Physics

As detailed in Section 1.2, we are interested in cold nuclear matter (CNM) physics to answer fundamental questions about parton distributions in nuclei (nPDFs) and interactions of partons and hadrons in nuclei, as well as to have a controlled baseline for quark-gluon plasma studies in heavy ion collisions. Particularly interesting are the forward rapidity measurements in d+Au collisions that are sensitive to low-x gluons in the nuclear wave function and to possible gluon saturation effects. In the next five years, we expect to make significant progress on this front with two projects. First, the forward silicon tracker (FVTX) is on schedule to be installed in 2011. The detector will enable detailed measurements of open heavy flavor, multiple quarkonia states, and a first look at Drell-Yan at forward rapidity ($1.2 < y < 2.4$). The detector design and status are given in Appendix C. Second, we want to extend the study of forward rapidity hadron and dihadron production that is hinting at gluon saturation effects to the cleaner direct photon channel. To this end, we are preparing a proposal for a forward compact electromagnetic calorimeter (referred to as FOCAL and described in Appendix C.2.5) that would measure direct photons at $1.0 < \eta < 3.0$ and thus be sensitive to gluons with $x \approx 3 \times 10^{-3}$–$10^{-2}$, in addition to other complementary observables.

2.4.1 Open and Closed Heavy Flavor with the FVTX

Currently, the suppression in $p(d)$+Au reactions of forward rapidity J/ψ over a broad range of colliding energies ($\sqrt{s_{NN}} = 18$–$200\,\mathrm{GeV}$) is not well understood. At RHIC energies, part of the large suppression may be the result of gluon saturation at low-x but these effects should be much smaller at the lower energies. The most recent measurements of J/ψ suppression in d+Au collisions in 2008 by PHENIX have been analyzed using a simple two-component model with nuclear modified PDFs that include gluon shadowing, and an *ad hoc* effective breakup cross section σ_{br} that is allowed to vary with rapidity in order to obtain the best agreement with the data. The latter is unphysical in the sense that realistic breakup cross sections should not have a substantial variation with rapidity. The results of this phenomenological analysis are shown in Figure 2.13. What is striking is that data from lower energies follows the same pattern with a steeply rising suppression (i.e. larger σ_{br}) at the most forward rapidity. This may indicate that initial state energy loss for the high-x parton in the proton (deuteron) is responsible for the suppression.

The path to follow for disentangling these different physics is through the comparison of other final states that have very different sensitivities to the physics. Shown in the right panel of Figure 2.13 is the nuclear modification factor α (where $\sigma_{pA} = \sigma_{pp} \times A^{\alpha}$) as a function of center-of-mass rapidity for J/ψ and open charm from the E866 and E789 experiment at $\sqrt{s_{NN}}$ = 38 GeV. Any nuclear modifications to the initial gluon density in the nucleus or initial state effects (including parton energy loss and/or multiple scattering) should affect the open and closed charm similarly. In contrast, final state breakup of the

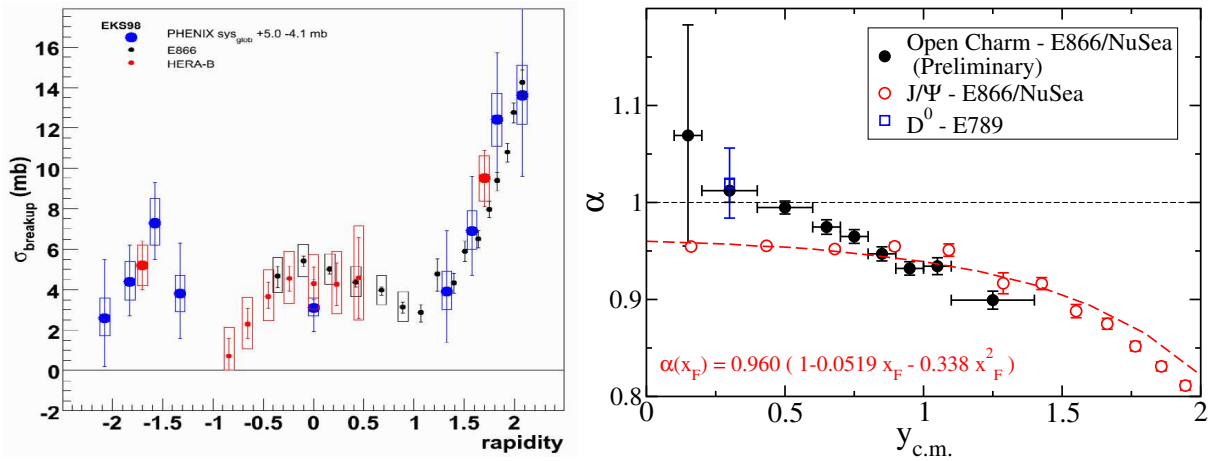

Figure 2.13: (left) Effective breakup cross section $\sigma_{\rm br}$ versus center-of-mass rapidity from theoretical model fit to the preliminary 2008 data from PHENIX (blue), FNAL E866/NuSea (black) and HERA-B (red). (right) Nuclear suppression (α) vs rapidity ($y_{c.m.}$) for open charm production (closed black circles, and open blue boxes) and for J/ψ (open red circles) from FNAL E866/NuSea and E789.

J/ψ will have different effects from open charm. There are also data from E866 for the ψ' [235] that show a similar suppression to the J/ψ at forward rapidity indicating that the modification occurs before the physical state is manifest, in contrast to backward rapidity where the ψ' has a larger suppression possibly due to its larger physical size (and thus larger expected cross section for breakup). Key new measurements in the next five years will also be done in E906 in proton-nucleus collisions with the Fermilab 120 GeV Main Injector beam. Measurements of Drell-Yan and quarkonia states at this even lower energy will be crucial for helping to separate and constrain the different physics effects.

Extending this suite of observables to RHIC energies is a primary goal of the FVTX program. The FVTX and increases in d+Au statistical data sets will enable measurements of:

- Open charm and beauty tagged via $D \rightarrow \mu X$, $B \rightarrow \mu X$, and $B \rightarrow J/\psi X$.
- J/ψ and ψ' separation and nuclear modification.
- Drell-Yan first measurements at forward rapidity.

The forward silicon tracker (FVTX) will be installed during the 2011 shutdown and will be available for physics starting in run-12. It covers pseudorapidity $1.2 < |\eta| < 2.4$ using four planes of silicon mini-strips with their precision coordinate in the radial direction. Using it will allow reconstruction of a precision vertex that will enable selection of detached vertices to select charm and beauty mesons, to reject long-lived decays of pions and kaons, and also will provide precision tracking of muons before the large effect of multiple scattering from the thick absorber in the front of the muon arms. This will

enable higher precision quarkonia measurements, provide the ability to tag open heavy flavor (charm and beauty), and give a first look at Drell-Yan yields at forward rapidity.

The expected coverage in x_2 and x_1, momentum fractions in the target nucleus and projectile deuteron (or proton) respectively, are shown in Figure 2.14. For charm one is sensitive down to $\langle x_2 \rangle \approx 5 \times 10^{-3}$ while for beauty the minimum x_2 is higher, at about 4×10^{-2}. The small x_2 values make these measurements quite sensitive to gluon saturation effects, and the large x_1 values also make these measurements sensitive to initial state parton energy loss effects—assuming precision measurements.

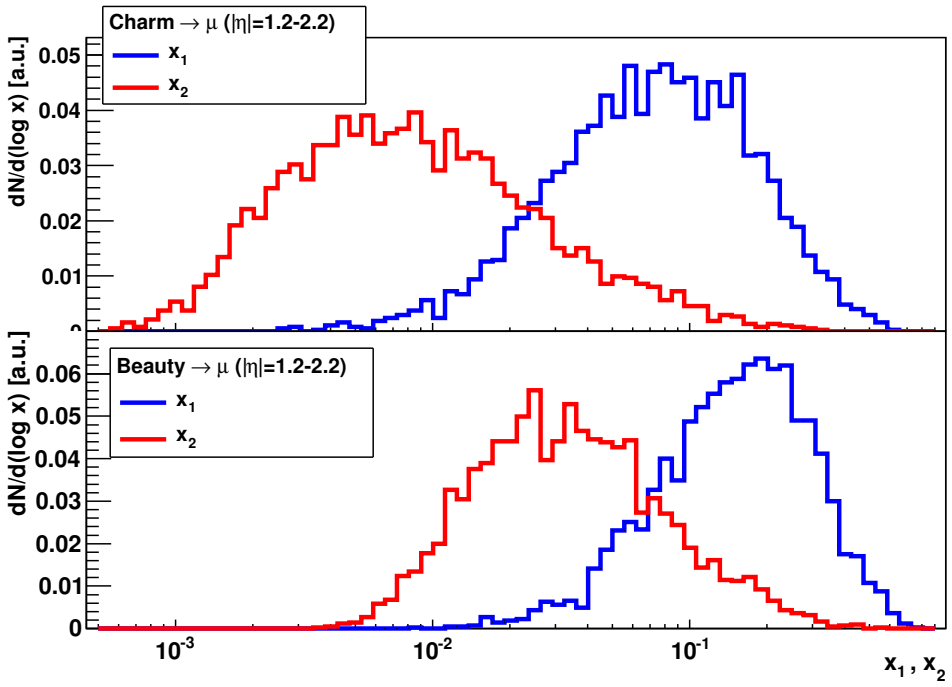

Figure 2.14: Coverage in x_2 and x_1 for detection of charm and beauty with the Forward Vertex detector (FVTX).

At PHENIX, existing open-charm and open-beauty measurements rely largely on observation of the lepton (electron or muon) from the semileptonic decay of the heavy mesons, and on statistical subtraction of a large amount of background—e.g. π^0, η, Dalitz and quarkonia decays for electrons, and light hadron and quarkonia decays for muons [29, 56]. This results in significant systematic and statistical uncertainties from the background subtraction. The tagging of D and B decays to single muons will change this to a precision picture.

The FVTX also improves the mass resolution for dimuon pairs and will allow separate measurements of the small ψ' peak in the mass spectra even though it is next to a much larger J/ψ peak. This will provide the first measurements of the cold nuclear matter effects on the ψ' at forward rapidity with dimuons at RHIC. The most recent d+Au run

allowed us to make the first measurement of the nuclear suppression of Υ's in CNM, shown in Figure 2.15. Increasing luminosities of the machine will allow correspondingly higher statistics measurements of these most rare processes in the future.

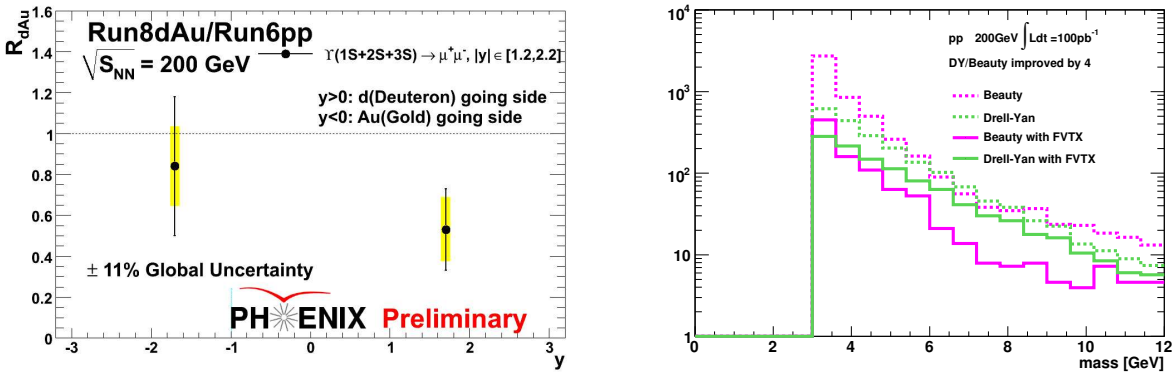

Figure 2.15: (left) Upsilon nuclear modification factor in d+Au collisions vs rapidity from the 2008 d+Au data. (right) Projected dimuon counts as a function of invariant mass from correlated beauty and Drell-Yan pairs shown as dashed lines. An anti-displaced vertex cut using the FVTX results in an improved Drell-Yan to beauty ratio by a factor of four as shown by the solid lines.

Lastly, the extension of these measurements to Drell-Yan (with no final state effects) is a very important control. To date it has not been possible to extract Drell-Yan yields at RHIC energies due to the larger yield of dilepton pairs from correlated open heavy flavor decays in the invariant mass region above the J/ψ. Only for invariant masses above the Υ states does the Drell-Yan yield become dominant. The introduction of the new silicon vertex detector upgrades in PHENIX will allow (via an anti-displaced vertex cut) a suppression of the open heavy flavor contributions and potentially the extraction of Drell-Yan yields. A initial simulation of the expected improvement in signal to background for Drell-Yan into dimuons at forward rapidity is shown in Figure 2.15. The relative Drell-Yan contribution increases as one moves to more forward rapidity and higher invariant masses, and thus the kinematic range of the measurement needs to be determined. It is expected that for the rapidity coverage of the FVTX, even with an anti-displaced vertex cut to improve the Drell-Yan to open heavy flavor contributions (charm and beauty), a statistical subtraction of the remaining backgrounds will be necessary.

2.4.2 Direct Photons at Forward Rapidity (FOCAL)

There are multiple channels at forward rapidity that give one experimental sensitivity to low-x gluon dynamics, including open and closed heavy flavor, as discussed above. Direct photons, produced predominantly via the gluon-Compton process ($q + g \rightarrow q + \gamma$), are a theoretically clean way to access the gluon distribution in nuclei and to determine

how those gluons are modified in the nuclear environment. The direct photon is a clean final state independent of fragmentation where the leading order diagram described above is expected to be dominant. Thus, the extension of this program to include the direct photon channel in $p(d)$+Au collisions at forward rapidity is essential.

Figure 2.16 shows the results of a recent NLO analysis of nuclear parton distribution functions and their uncertainties [185]. It is clear that while the valence and sea quark distributions are well constrained, there is a high degree of uncertainty in the gluon nuclear parton distribution function (nPDF). There are existing measurements of forward rapidity hadrons that in principle can help reduce this uncertainty. However, the ambiguity about the fragmentation process and diagram contributions have resulted in substantial debate about their inclusion in global nPDF fits. Direct photon measurements in the same forward kinematics have the potential to resolve this debate, in addition to allowing a global analysis of multiple channels (including heavy flavor).

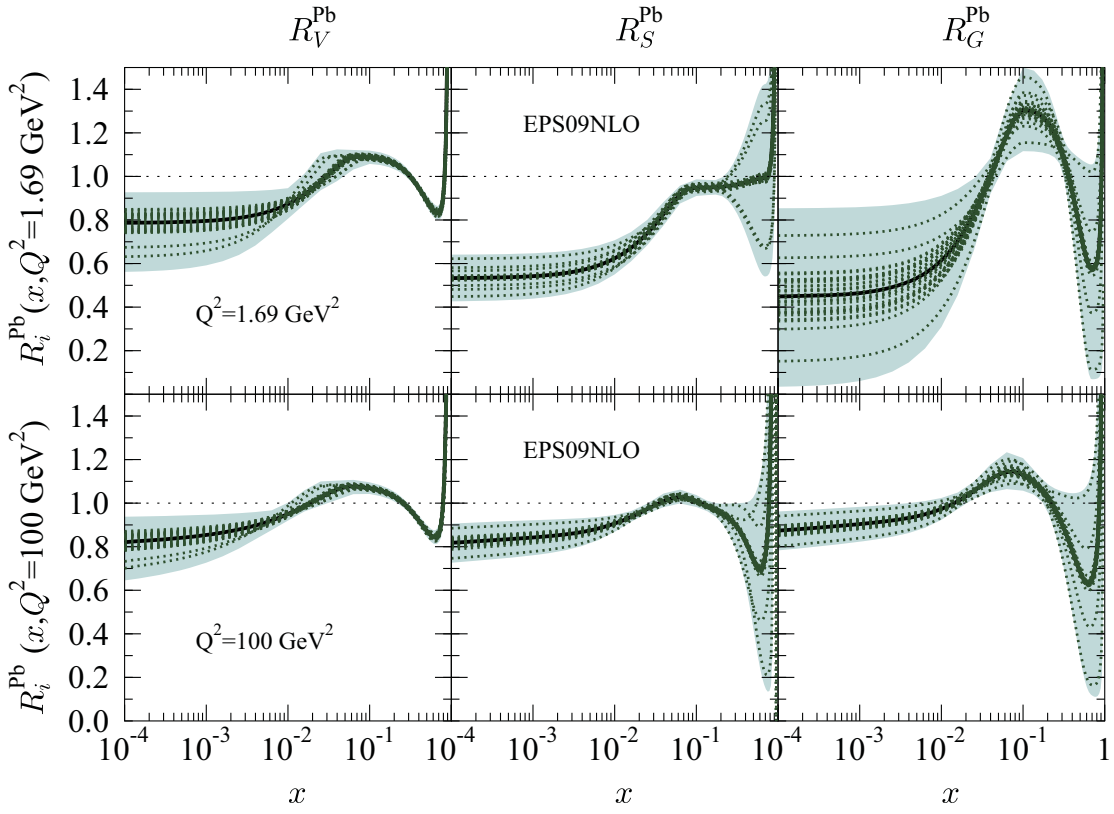

Figure 2.16: The nuclear modification factors for valence quarks R_V, sea quarks R_S and gluons R_G in Pb nuclei. The thick black lines indicate the best-fit results, whereas the dotted green curves denote the PDF error sets. The shaded bands correspond to the 90% confidence level range of the nPDFs.

As noted in Section 1.2, the depletion of low-x gluons can be interpreted in terms of coherence models. These models effectively "shadow" the interior nucleons in the nucleus

due to coherence effects that arise from parton multiple scattering. There is also the exciting possibility that at small x gluon recombination dominates and the gluons can be described as classical fields. McLerran and his collaborators [249, 250, 251] have used a classical approximation to describe the initial stages of heavy ion collisions, referred to as the color glass condensate (CGC). The CGC may be a universal description of the QCD vacuum that is relevant to hadrons as well as nuclei. This universal description is consistent with observations made in electron-proton collisions at HERA [228]. In a heavy ion collision, the nucleus acts as an amplifier of the effect because the gluon wave functions extend across the entire thickness of the nucleus. Saturation effects which in a proton would be at $x \sim 10^{-4}$, would be at an x about 6 times larger in a $(p)d$+Au collision, making the measurement accessible at a lower collision energy.

It is notable that not only are these measurements important for understanding CNM, but also for constraining the initial state in heavy ion reactions that transitions to the sQGP. As a specific relevant example, calculations in the CGC framework indicate a smaller concentration of the initial deposited energy with a larger eccentricity than traditional Glauber calculations without gluon saturation effects [179]. Hydrodynamic descriptions of the sQGP have to have as input the initial energy density and spatial profile. In order to have precision measurements of the shear viscosity and constraints on the equation of state, these ambiguities in the initial spatial profile need to be resolved. Tests of the gluon saturation picture and the dependence of these effects on the nuclear density are of the utmost importance for having precision answers to many of the questions in heavy ion physics.

One of the important early results from RHIC was the suppression of high p_T particles in central collisions at midrapidity. One explanation of this effect was that it was not due to the produced medium (i.e. jet quenching), but due to the initial state (i.e. gluon shadowing or color glass condensate effects). Results from all of the RHIC detectors saw no suppression of high-p_T particles in the central rapidity region ($|\eta| < 1$) in d+Au collisions, implying that at midrapidity, RHIC experiments lie outside the saturation region and that suppression was due to energy loss of the parton through the medium.

Unlike high p_T particles at midrapidity, data from d+Au collisions at *higher* rapidity show that high momentum particles are suppressed, indicating a suppression of the gluon nPDF at RHIC. It becomes important therefore, to explore the region of x between 10^{-2} and 10^{-3} in cold nuclear matter. This can be accomplished by making complimentary measurements in d+Au collisions with different theoretical and experimental strengths. For experiments at the LHC, at even higher collision energies, the lower x-data will lie almost entirely within the saturation region at central rapidity. The RHIC energy range is unique in that measurements made at midrapidity lie outside the saturation region, but measurements at forward rapidity are within the saturation regime. Hence, the *onset* of saturation can be studied at RHIC.

Exploring the suppression of the gluon structure function directly via the study of direct photons is more difficult experimentally, but much cleaner theoretically. A proposed up-

grade to the PHENIX detector, the Forward Calorimeter (FOCAL) (see Appendix C.2.5 for details) is being developed to be directly sensitive to the gluon distribution function over a region of x between $x \approx 3 \times 10^{-3}$–$10^{-2}$ through a variety of measurements. By charting out the suppression in a variety of observables versus centrality and rapidity the FOCAL will be able to map out the gluon nPDF and provide critical input to models of gluon suppression in cold nuclear matter. We show in Figure 2.17 the EPS09 nPDFs as a function of x (left) and the corresponding calculation for the direct photon yield as a function of pseudorapidity η in central 0–20% d+Au events. Sufficiently precise measurements of this nuclear modification factor can provide strong constraints on R_G. We are currently evaluating the full performance of the FOCAL measurement in terms of statistical and systematic uncertainties.

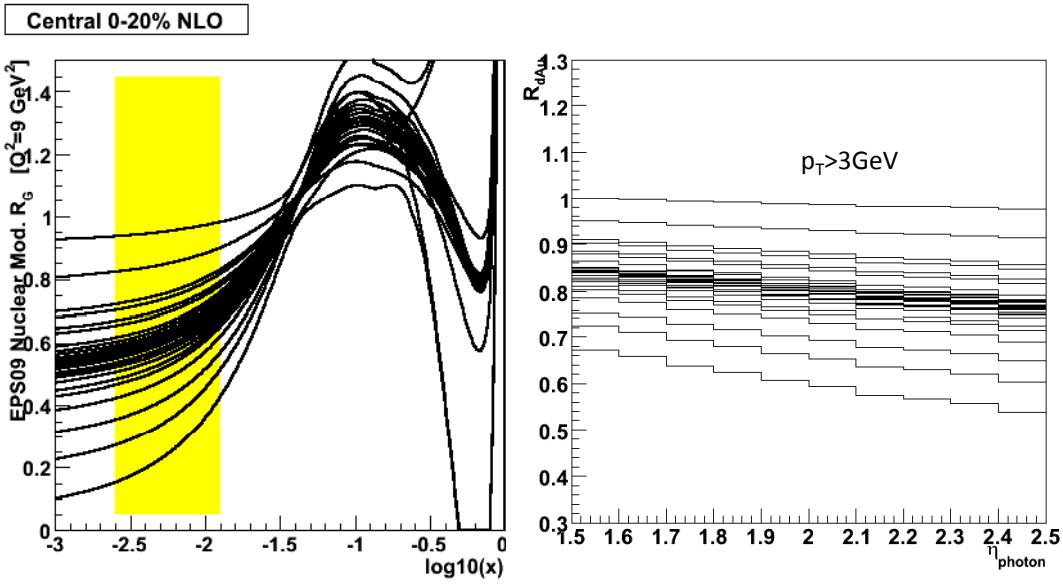

Figure 2.17: (left) The nuclear modification factors for gluons R_G as a function of x from EPS09 with the uncertainty bands from variations in the global analysis. (right) Calculation of the nuclear modification factor R_{dAu} for direct photon yields as a function of pseudorapidity for the corresponding set of EPS09 nPDFs in central 0–20% d+Au events.

While we consider direct photon production to be a critically important channel, it is one of many interesting channels in the forward rapidity region that are sensitive to the gluon nPDF which are accessible to the FOCAL. The FOCAL combined with tracking from the FVTX in front of the FOCAL should allow measurements of not only the direct photon, but also the jet axis from the associated quark fragmentation in the quark-gluon Compton process. The additional jet axis information will allow a narrow range of x that contributes, thus providing better constraints.

In addition to γ+jet axis measurements, the FOCAL also provides measurements of single and dihadrons (i.e. π^0 and η). Energetic dihadrons would correspond to leading particles from dijet events, which give an estimate of the jet direction and provide inde-

pendent information on the gluon distribution in nuclei at small x [129].

There is an intriguing signature of the CGC suggested by Kharzeev, Levin, and McLerran [217]. Monojets reflect the fact that the recoiling medium (presumably a CGC) reacts as a whole coherently. Such a phenomenon would be manifest as a suppression of back-to-back jets (seen as correlated particles) even in d+Au collisions at forward rapidity. In contrast, one recent theoretical work suggests that this possibility is unlikely even in the context of the CGC [135]. Additionally, Jalilian-Marian has made predictions about the correlations between direct photons and hadrons [210]. Theoretical calculations for the CGC are not as extensive and available as compared to calculations using a pQCD inspired parton distribution function framework, hence we have chosen to concentrate on the more standard viewpoint of measuring parton distribution functions. However, this is a measurement which is essentially identical to the one we concentrate on here, and the FOCAL will certainly be sensitive to any such signals. Our approach is that we will design and plan for the task of measuring the gluon distribution functions. We will analyze the data in both the Color Glass framework and the gluon distribution function framework.

Chapter 3

Heavy Ion Physics: sPHENIX Plan

We are excited about the expected state of the field and advanced knowledge that we project to acquire by 2015 (as described in the previous chapter), but beyond 2015 we foresee facing critical unanswered questions that will only be addressable through an upgraded RHIC program operating in conjunction with the LHC heavy ion program. These questions include:

- Are quarks strongly coupled to the quark-gluon plasma at all interaction distance scales?
- What are the detailed mechanisms for parton-QGP interactions and responses? Are the interactions coherent over the entire medium length scale, what are the dominant energy loss mechanisms?
- Are there quasi-particles in the medium? What are their masses (m) and widths (Γ)?
- Is there a relevant color screening length in the quark-gluon plasma?
- How is rapid equilibration and entropy production achieved?
- What is the nature of color charge in large nuclei? What role does gluon saturation and the EMC effect play in nucleus-nucleus collisions? How do these modifications evolve?

The answers to these questions are related to the very nature of the quark-gluon plasma (QGP) and the fundamentals of the interactions between high energy partons and the QGP in nucleus-nucleus collisions. In Figure 3.1, we illustrate the relations between the question we seek to answer, the observables carrying the answers, and the detector capabilities required to measure those observables. In this Chapter, we will focus on the connections between the questions and observables. Later, in Chapter 7, we will shift focus to the connections between observables and needs by describing a specific detector and technological approach to realize these observables in experiment.

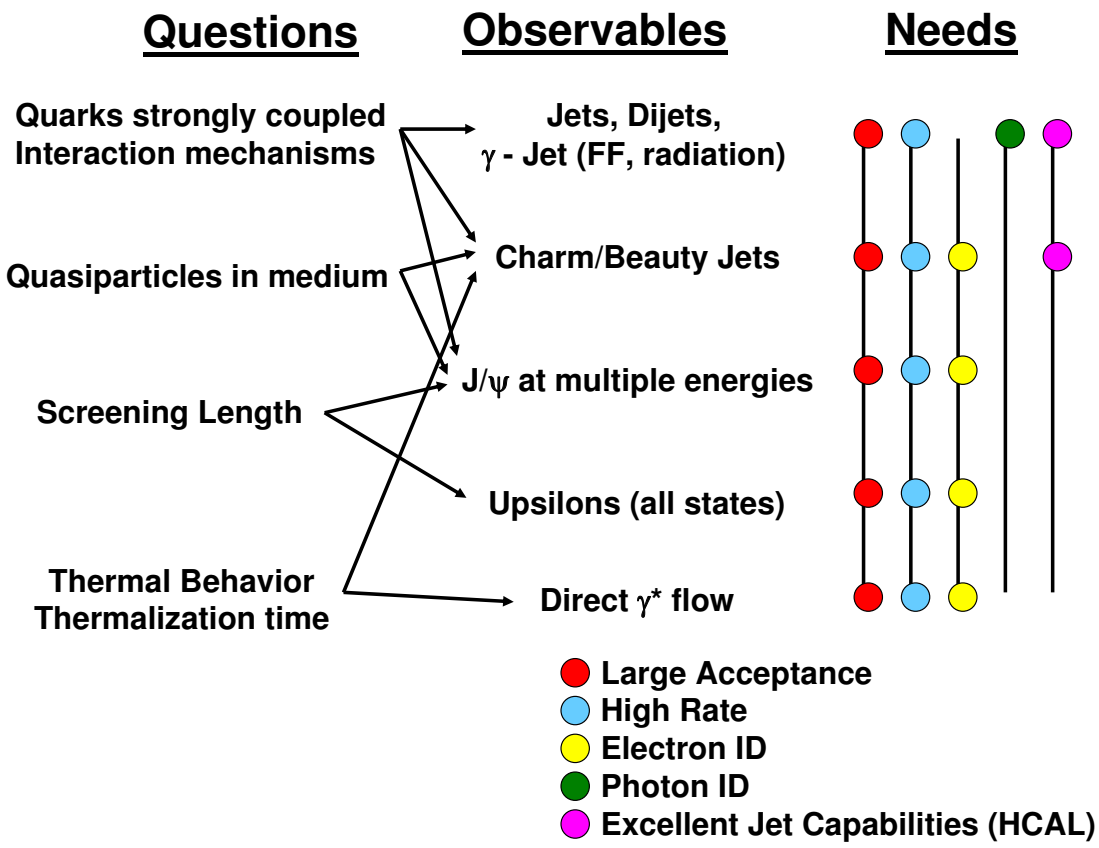

Figure 3.1: A chart illustrating the interesting physics questions after 2015, their relationship to final-state observables, and the detector requirements needed for these measurements.

Figure 3.1 is a pictorial representation of the aim of this Chapter, but putting that picture into words, we find that the most promising approach to answering questions in RHIC physics that are fundamental, compelling, and unanswered by 2015, is through precision measurements as detailed in the following Sections.

- Section 3.1: Jet and Photon-Jet Physics
- Section 3.2: Heavy Flavor Jet Physics
- Section 3.3: RHIC and LHC Complementary Roles
- Section 3.4: Quarkonia and Color Screening
- Section 3.5: Early Time Dynamics
- Section 3.6: Cold Nuclear Matter Physics

3.1 Jet and Photon-Jet Physics

Studies of hard scattering processes and jet quenching in ultra-relativistic heavy ion collisions attempt to answer the fundamental question: **How does a high energy colored parton interact with the quark-gluon plasma (QGP)?** The familiar cartoon of the physics embodied by this question is shown in Figure 3.2 which depicts jet quenching in a very simple fashion, showing individual outgoing partons from the hard scattering losing energy by interacting with the medium and then fragmenting in the vacuum. A more complete and rigorous understanding of hard-scattering processes views the final-state as containing two or more parton showers generated by the outgoing quarks and gluons. With that in mind, we can re-phrase the question above in a more precise way: **How is the final-state parton shower initiated by a hard scattering process modified by the presence of the quark-gluon plasma?** The answer to this question not only addresses a fundamental problem in QCD, but through the interaction between the partons in the shower and the medium, it also provides insight into the properties of the medium itself and into the physical process by which thermalization is achieved.

Nearly a decade after the first publications demonstrating jet quenching via single-particle jet-proxy measurements in Au+Au collisions at RHIC [47], there is still no unique interpretation of the experimental data or understanding of the underlying physics. Most descriptions of jet quenching have relied on weakly coupled techniques [246] to calculate both radiative and collisional energy losses.

Given the sQGP paradigm for the bulk interactions detailed in Section 1.1, it would be surprising if the physics of jet quenching did not contain some features of strong coupling. Other physical mechanisms may contribute to observed jet quenching including synchrotron radiation from strong chromomagnetic fields [285, 323] and even turbulent chromomagnetic fields [245] generated by plasma instabilities [276]. Sufficiently detailed and precise measurements of jet quenching, pursued via reconstruction of the medium-modified parton showers, combined with controlled theoretical calculations should provide direct sensitivity to the mechanisms of parton-medium interactions and, thus, to the properties of the medium. With currently available data and theoretical calculations we cannot even determine the most basic quenching parameter, $\hat{q}$, to better than a factor of four [36, 119]. A comprehensive approach to a full suite of jet measurements (including dijet and γ-jet) will answer many fundamental questions about the properties of the quark-gluon plasma.

3.1.1 What do jets teach us about the medium?

The products of hard scattering processes are not simply massless quarks and gluons but highly virtual, "undressed" quarks and gluons whose virtuality evolves with time. That virtuality evolution includes the development of a parton shower that ultimately results in final-state hadrons with their vacuum properties.

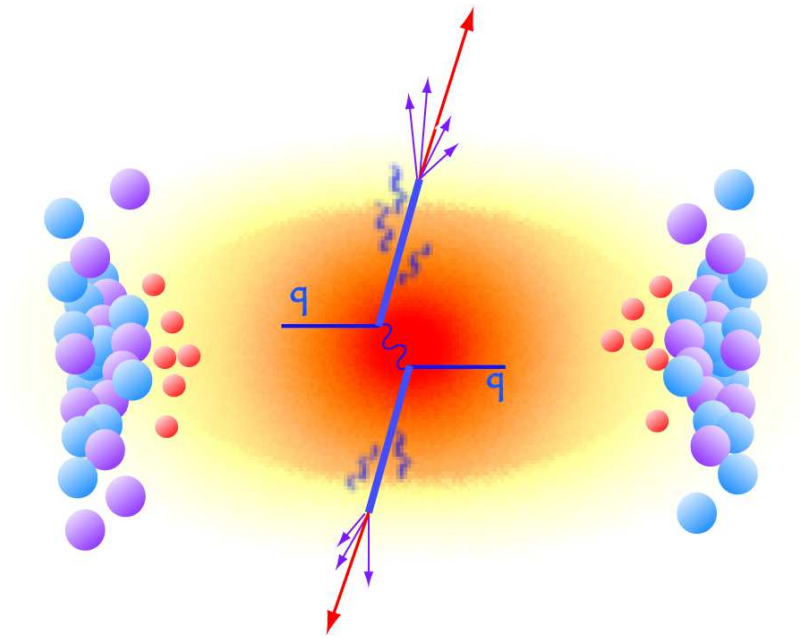

Figure 3.2: A familiar depiction of jet quenching at leading order and without virtuality evolution. After an initial hard scattering the partons lose energy in the medium and eventually fragment in the vacuum into final-state hadrons.

The properties of the medium probed by a high energy quark or gluon necessarily depend on the virtuality of that quark and gluon. This is illustrated in Figure 3.3. A high p_T parton interacts with the medium over a full range of Q^2 scales with a maximum $Q_{\max}$ set by the p_T^2 of the parton. For the very highest values of Q^2, the parton probes the medium on short distance scales where the constituents of the medium are bare color-charge point-like quarks and gluons and pQCD descriptions of resulting interactions should be applicable. At intermediate scales we expect the probe to see a medium composed of quark and gluon quasi-particles with thermal masses and associated dispersion relations. At still lower Q^2 the probe samples the medium across longer distance scales where the strong coupling physics is manifest. At these length scales, weakly coupled pQCD and strongly coupled string dual (AdS/CFT) descriptions of the quark-gluon plasma offer different and competing models of the interaction of the probe with the medium [240, 206, 195]. Note that in the string dual case (as shown at the lower right of Figure 3.3) there are no quasi-particles to absorb locally any collisional energy loss.

Because the virtuality of a hard-scattered quark or gluon evolves with time, jet measurements provide a doubly "integrated", or time-averaged, view of the medium. That averaging includes both the virtuality evolution of the probe and also the time evolution of the medium properties. Because the upper limit on virtuality of the quarks and gluons, $Q_{\max}$, is determined by the momentum transfer in the hard scattering process, by varying that momentum transfer we can **dial the range of distance scales and structure** with which a quark or gluon probes the medium. Figure 3.4 shows the pQCD yields [309] for vari-

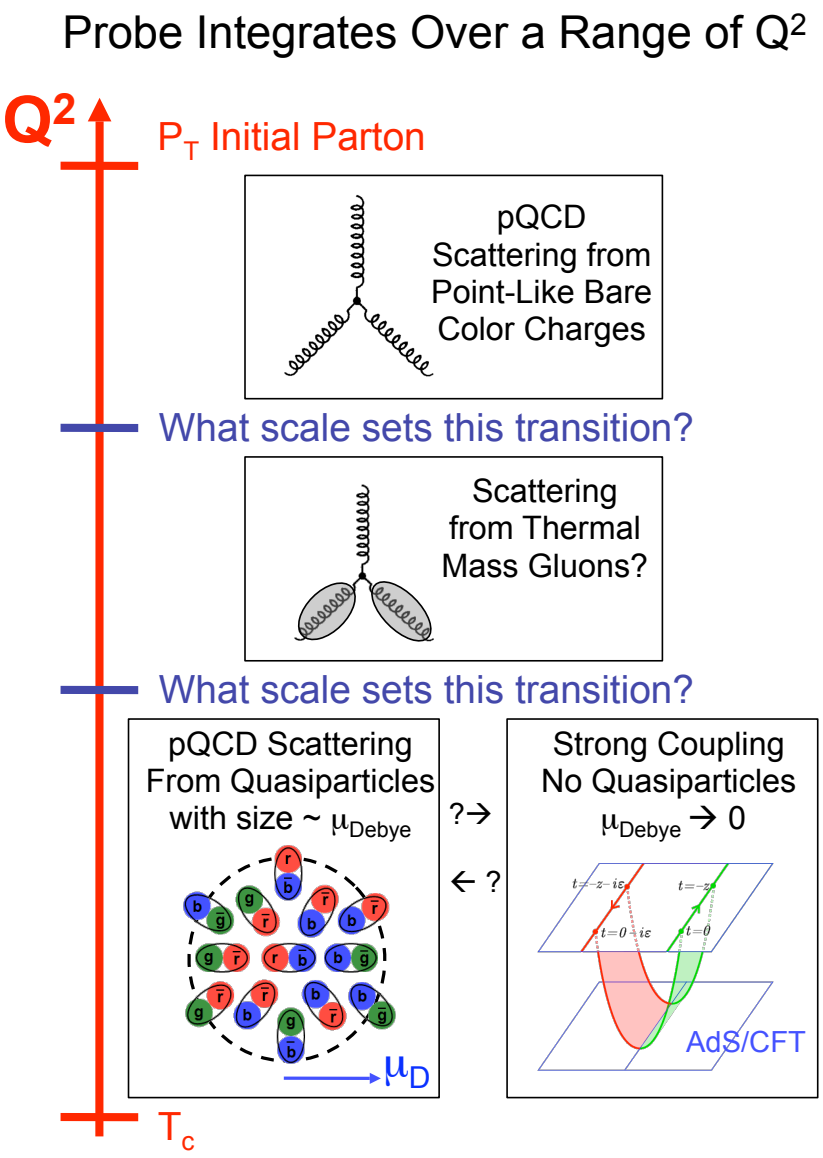

Figure 3.3: Schematic Diagram of the Parton Probe Sensitivity to Different Physics and QGP Structure [204].

ous hard scattering final states scaled for Au+Au central 0–20% collisions. As detailed in Chapter 7, with an upgraded PHENIX detector and increased RHIC luminosities, we can sample ten billion Au+Au central collisions—corresponding to one count at 10^{-10} at the bottom of the y-axis range. We would be able to measure light quark jets with 10^5 counts above 40 GeV and 10^3 counts above 60 GeV. Approximately 50% of all single jet events also have their away-side partner jet contained within the acceptance of the upgraded detector. A similar fraction of direct γ events also contain the away-side jet. Therefore the γ-jet count rates can be determined from Figure 3.4 by dividing the direct γ rate by two. While these estimates for jet yields do not account for detector and reconstruction

efficiencies, we expect those reductions to be more than offset by additional increases in luminosity or running time not included in the estimate of 10^{10} central events. Through a combination of single jet, dijet, and γ-jet measurements we will be able to extend the jet measurements down to 15 GeV, we would be able to measure jet final states with a factor of 3–4 variation in $Q_{\max}$. RHIC is an ideal place to carry out this jet program and to substantially extend the measurements over a broader range of $Q_{\max}$at the LHC.

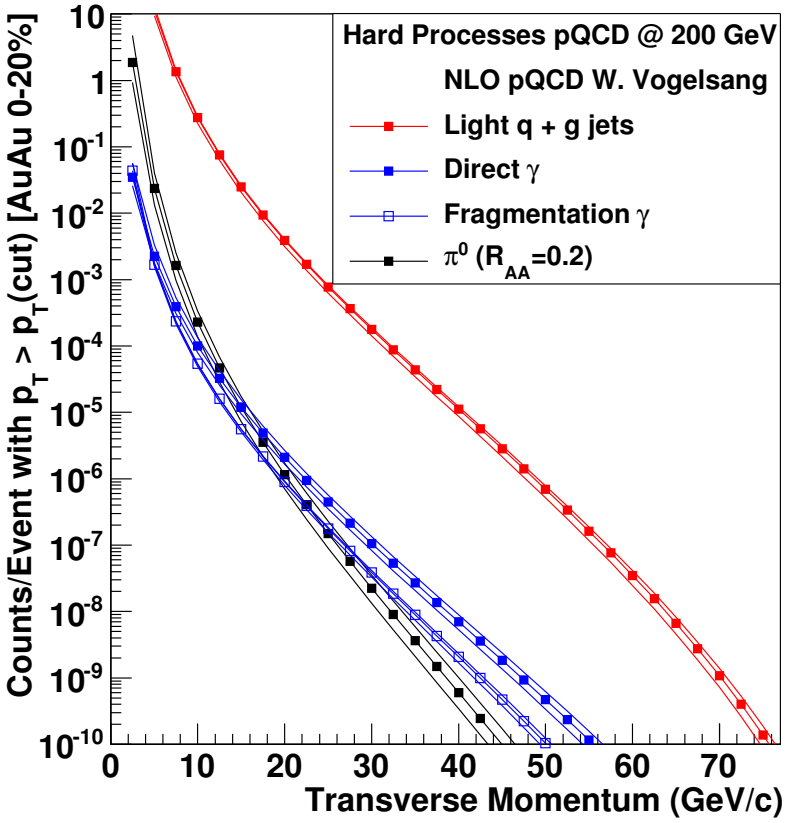

Figure 3.4: Jet, photon and π^0 rates within $|\eta| < 1.0$ from NLO pQCD [309] calculations scaled to Au+Au central collisions. Ten billion Au+Au central collisions corresponds to one count at 10^{-10} at the bottom of the y-axis range. With that data sample, we would measure light quark jets with 10^5 counts above 40 GeV and 10^3 counts above 60 GeV.

For the highest jet energies that we anticipate to be available at RHIC, we have access to quark and gluon virtualities so large that the initial stages of the parton shower develop prior to the formation of a medium, and the quenching of the resulting jets should proceed through the independent quenching of the sub-jets. Such "premedium" development of the parton shower generated by hard-scattering processes will be more important in jet measurements at the LHC, but with the range of jet energies accessible at RHIC we will be able to study the evolution of jet quenching from relatively low initial virtuality probes to very high virtuality probes. The capability to select jets of both high and low virtuality

will be essential for understanding of the medium properties and also for understanding energy loss itself. The ability to "dial" the $Q_{\max}$ needs to go along with the ability to "dial" the path length via collisions of lighter ions, asymmetric ion collisions, centrality selection, and reaction plane angle dependence. These essential tools allow one to tune the effects from virtuality evaluation and the coherence of the radiation.

The use of "full" jet measurements provides much more insight into the physics of the interaction of high-p_T quarks and gluons with the medium than current single- and dihadron measurements (as previously described in Chapter 1). The angular distribution, transverse momentum distribution, and longitudinal momentum distribution of partons produced in a medium-modified parton shower encode the physics of the parton-medium interaction. For example, we show in Figure 3.5 a comparison by Iancu *et al* of a dijet parton shower in a strongly-coupled Super Yang-Mills (SYM) theory with a cartoon of the collimated jets produced in pQCD hard processes. The angular distribution of the strongly coupled parton showers will be very different from that of typical pQCD parton shower due to the difference in the kinematics of the splitting process [200]. Such a picture represents an extreme case of the modification of a jet parton shower by the medium. It is even possible that the modification of the parton shower at very strong coupling may be so severe that the products of the hard scattering process become effectively thermalized in medium.

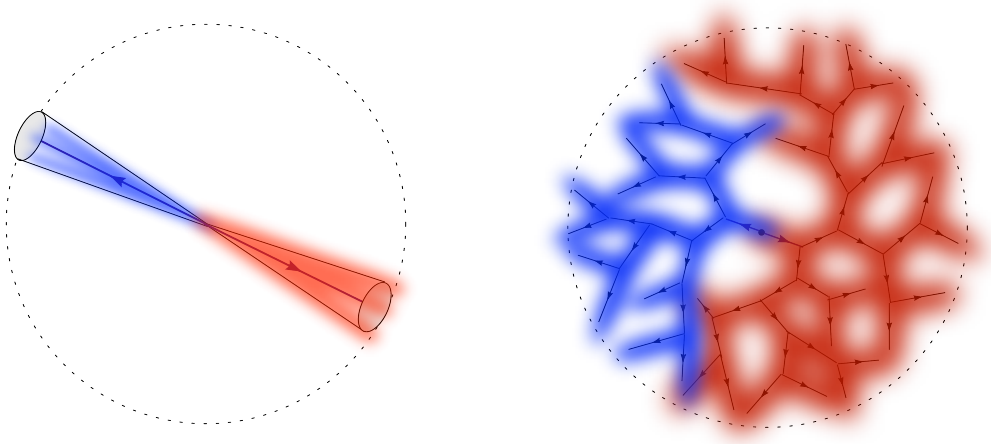

Figure 3.5: Comparison for the collimated back-to-back jets in pQCD (left) and the parton showers for a pair of strongly coupled jets in a Super-Yang Mills theory (right).

To demonstrate the sensitivity of the gluon transverse momentum distribution to this screening scale we show in Figure 3.6 the distribution of gluon transverse momenta obtained from WHDG calculations [315] for quarks of 20 GeV and 40 GeV in a static medium with a length of 5 fm for three different values of the screening scale used in the WHDG formalism. The results in Figure 3.6 demonstrate that the gluon k_T distribution for fixed medium density is sensitive to the screening length in the medium.

There is a wealth of fundamental information about the parton interaction and the basic

composition of the sQGP that can be determined from these measurements. Simple questions arise, such as when the parton suffers collisional energy loss, what are the quanta (if any) that absorb the recoil energy and momentum? In order to answer these questions, we now detail the experimental observables that can be realized in the laboratory.

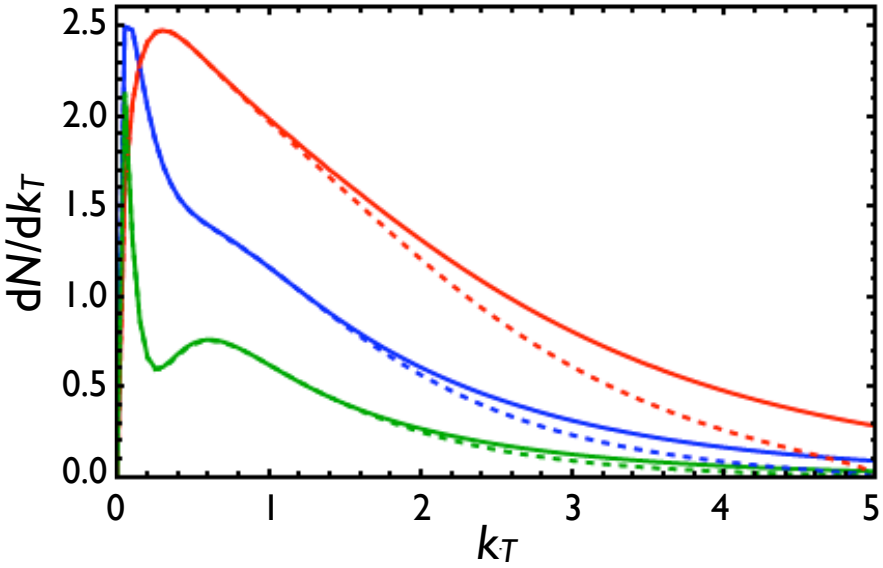

Figure 3.6: Distributions of radiated gluon transverse momentum (k_T) obtained from the leading order in opacity DGLV energy loss formalism for jets of energy 40 GeV (solid) and 20 GeV (dashed) in a medium of path length $L = 5$ fm. Results are shown for three screening scales: $\mu = 0.25$ GeV (green), $\mu = 0.5$ GeV (blue) and $\mu = 1$ GeV (red).

3.1.2 Jet Observables

To study the properties of the parton shower generated by hard-scattered quarks and gluons we must first be able to find the events in which hard scatterings took place, reconstruct the nominal direction of the outgoing parton showers and separate the products of those showers from the background either event-by-event, statistically, or both. We will discuss the issues with carrying out such a program below, but assuming that we can successfully measure jets, we list here a set of measurements that will address the physics issues raised above and provide insight on the mechanism of jet quenching, and, in turn, on the medium itself. We defer a discussion of heavy flavor jet observables and the opportunities that they provide to Section 3.2. Key experimental observables include:

- Single jet spectrum and jet R_{AA} for different jet sizes and different jet algorithms.
- Single jet fragment z, J_T, and angular distribution for different jet sizes.
- Statistical measurement of hadron $\Delta\phi$ and $\Delta\eta$

- Di-jet I_{AA}, ΔE, and $\Delta\phi$ distribution
- γ-jet energy balance, and $\Delta\phi$ distribution, γ-tagged fragment z distribution
- Jet fragmentation/bremsstrahlung photon spectrum
- Centrality, A, and reaction plane angle ($\phi - \Psi$) dependence of all the above.

Ideally we would reconstruct and separate from the background of the underlying event every hadron produced in the parton shower generated by a hard-scattered quark or gluon, but such a separation is not possible even in p+p collisions due to the fact that the hard-scattered partons can emit radiation over all angles including in their backward hemispheres, though that radiation is typically quite soft. Because the large angle and backward radiation from dijets or multi jets are necessarily entangled, "vacuum" jet reconstruction algorithms impose constraints on the angular region included in the jet. If the jet algorithm is both collinear and infrared safe, the direction and number of reconstructed jets is insensitive to the presence of the soft, large angle radiation and pQCD calculations of the jet cross section corresponding to the jet definition can be performed [125]. While many of the cone algorithms that have been used for jet reconstruction are not collinear or infrared safe, we will nonetheless use the concept of a cone jet definition with a radius R illustrated in Figure 3.7 as a conceptual proxy for the angular constraint imposed by a generic jet algorithm.

As discussed earlier, the medium is expected to broaden the parton showers—by different amounts in the presence of strong chromomagnetic fields and through the influence of the collective motion of the sQGP on the quenching process. That broadening reduces the energy contained within a cone of given radius and shifts the reconstructed jet to lower energy. For example, a calculation of the angular distribution of medium-induced radiation by Vitev and Zhang [308] is shown in Figure 3.7 compared to the in-vacuum fragmentation of an unmodified jet. In Au+Au or Cu+Cu (the red or the blue curve, respectively, in Figure 3.7), one can see the striking effect of the medium on the angular shape of the jet. The forward gluon intensity is suppressed by coherent interactions with the medium, the parton splittings are strongly modified, and the jet acquires a much broader angular shape as a consequence. One could test this picture of jet modification by looking at the details of energy flow around the direction of a reconstructed jet.

Figure 3.8 shows the results of a theoretical calculation [308] of the jet suppression (R_{AA}) in Au+Au collisions at $\sqrt{s_{NN}} = 200\,\text{GeV}$ as a function of jet energy and for different cone radii. This calculation includes the effects of nuclear PDFs and initial state energy loss. It shows substantial suppression even for large jet energies and large cone radii where the effects of "out of cone" radiation are expected to be small. The predicted value of R_{AA} depends strongly on the cone radius, varying from a value similar to that of the π^0 ($R_{AA} \sim 0.2$) for a narrow cone ($R \sim 0.2$), up to $R_{AA} \sim 0.7$ for a large cone ($R \sim 1.0$). There are a number of effects at work here. One is the outright loss of jets because they are so strongly modified in the medium that they are not reconstructed. This will deplete

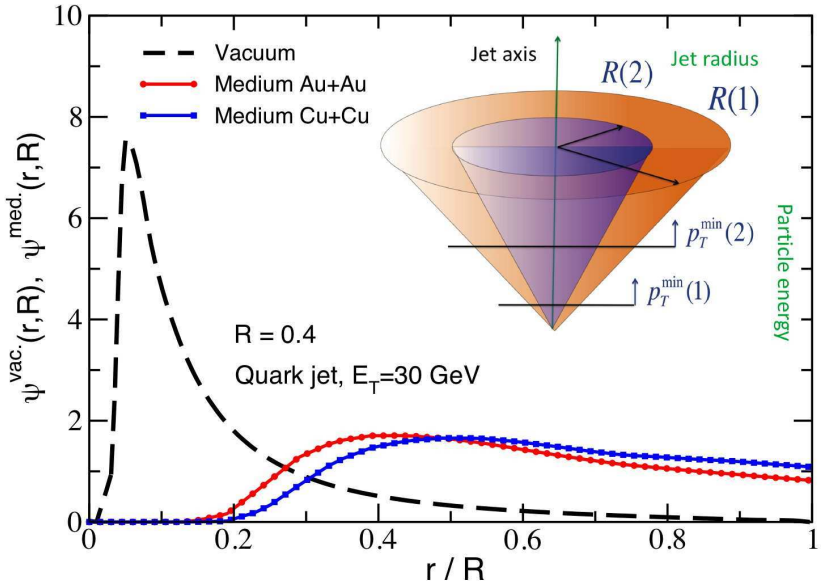

Figure 3.7: The differential jet shape variable, $\psi(r, R)$, for 30 GeV quark jets, from Vitev and Zhang [308], shows how the energy of a jet is distributed in angle relative to the direction of the jet as a whole. In vacuum (black dashed curve), the jet has a very focused angular distribution. In Au+Au or Cu+Cu (red or blue curve, respectively), one can see the striking effect of the medium on the angular shape of the jet. The forward gluon intensity is suppressed by coherent interactions with the medium, the parton splittings are strongly modified, and the jet acquires a much broader shape as a consequence.

the yield at a given E_T. Another effect is the shift downward in energy of jets that are reconstructed successfully.

Vitev [308] argues that for pure radiative energy loss, the jet R_{AA} provides sensitivity to the medium-induced angular broadening of the jet, but collisional energy loss and quenching due to strong coupling effects can also contribute to the observed jet suppression. The energy lost due to the recoil of medium constituents will be rapidly thermalized in the sQGP and will contribute to a reduction in the jet energy which, in turn, will reduce the yield of jets at a given (transverse) energy. It is also possible that quenching strong enough to "isotropize" the energy of a jet will cause the jet to become unobservable, leading to a suppression of the jet yield. The effects of broadening can be separated from suppression due to collisional energy loss or strong coupled quenching. If the suppression is due to the broadening of jets, the jets will nonetheless be reconstructed. The inset in Figure 3.8 shows the ratio of measured R_{AA} values for different cone radii. Those ratios are insensitive to the initial-state effects and reflect the effects of the angular broadening of the parton shower.

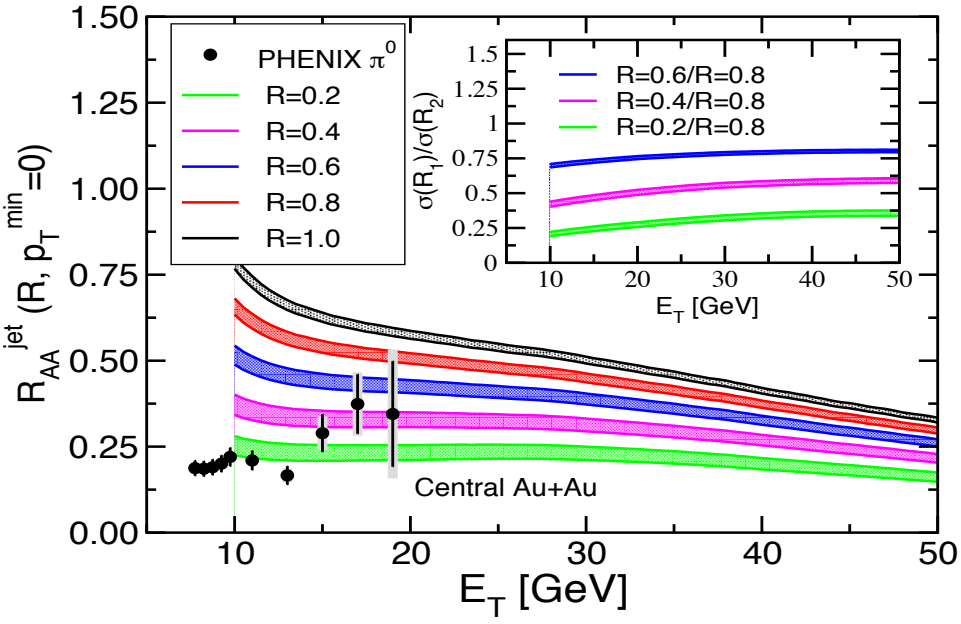

Figure 3.8: Plot of jet R_{AA} calculated by Vitev and Zhang [308] in 200 GeV Au+Au collisions as a function of jet energy for different jet cone radii. The calculations include effects of quenching, nuclear PDFs, and initial state energy loss. Jets reconstructed using a narrow cone ($R \sim 0.2$) show a strong suppression as the angular spread of their energy is broadened by the effects of parton-medium interactions. The inset shows ratios of jet R_{AA} for different jet cone radii.

A statistical measurement of the angular distributions and k_T distribution of hadrons with respect to the jet axis with an appropriate subtraction of the underlying event should indicate if the jet is broadened or not. Distinguishing between suppression due to collisional energy loss and strongly coupled quenching may be more difficult. However, the relative contribution of collisional energy loss ($\Delta E/E$) is expected to decrease with increasing jet energy while the strongly coupled modifications of the parton shower may persist to large jet energies [200]. Also, the dramatic modification of the parton shower suggested in Figure 3.5 may not be achieved for short path lengths, so it should still be possible to detect modifications of jets that propagate over relatively short lengths in the sQGP.

A new set of theoretical tools for understanding parton showers are available as Monte Carlo codes. These tools are still under active development. For illustration, we show in Figure 3.9 and Figure 3.10 results obtained from the QPYTHIA Monte-Carlo simulation of medium-induced modifications of parton showers [99] generated by light (quark and gluon) partons, charm quarks and bottom quarks for a $\hat{q} = 0$ (i.e. no quenching) and for $\hat{q} = 10$ GeV^2/fm and average path length $L = 3$ fm. The modified fragmentation function (top) and the modified J_T distribution (bottom) yield direct information about the parton shower and angular ordering.

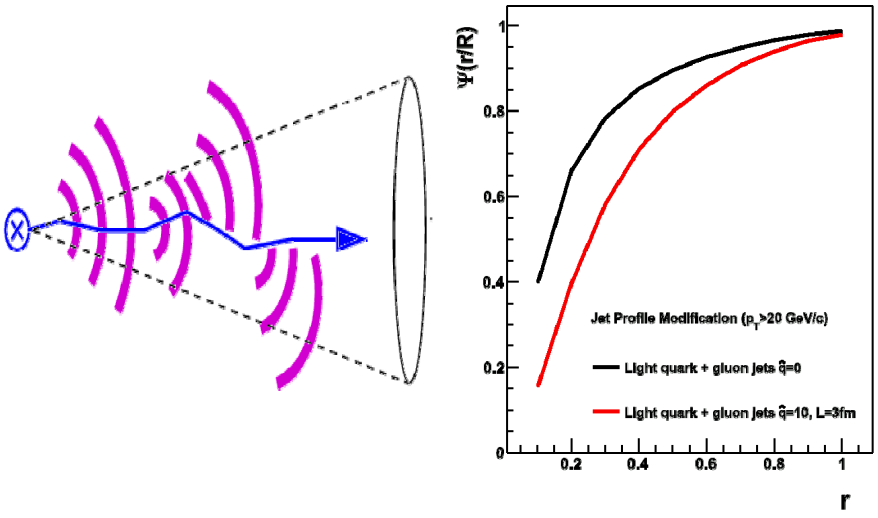

Figure 3.9: QPYTHIA simulations of the fraction of jet energy within a certain radial size $\Psi(r/R)$. Results are shown for $\hat{q} = 0$ (i.e. PYTHIA with no quenching) and $\hat{q} = 10$ GeV^2/fm with $L = 3$ fm. The jets were reconstructed from the QPYTHIA generated hadrons using the anti-k_T algorithm with $R = 0.4$ and results are shown here for jets with energy > 20 GeV.

The benefits of full jet reconstruction can be combined with direct photon measurements to yield significant additional insight on jet quenching. At leading order the direct photon and opposing quark have balanced transverse energy, giving an event-by-event calibration of the quark E_T. Shown in Figure 3.11 are the results of a QPYTHIA simulation for direct photons with $p_T > 20$ GeV/c and the reconstructed jet energy on the opposing side ($|\Delta\phi_{\gamma-jet}| < 0.2$ radians). The results are shown for jet reconstruction with the anti-k$_T$ algorithm with radius parameter $R = 1.0, 0.4, 0.2$ and for unquenched and quenched jets. One observes a dramatic shift in the quenched scenario for the reconstructed jet energy in jets with smaller radius values, which we will be able to measure experimentally. It is worth emphasizing that the rate of background or "fake" jets in this type of analysis is dramatically reduced because only the rate of "fake" jets in events with high p_T photons is relevant. As shown in Figure 3.4, a large acceptance, high rate detector can measure of order 10^4 direct photons with $p_T > 20$ GeV/c and with a 50% acceptance for the partner jet.

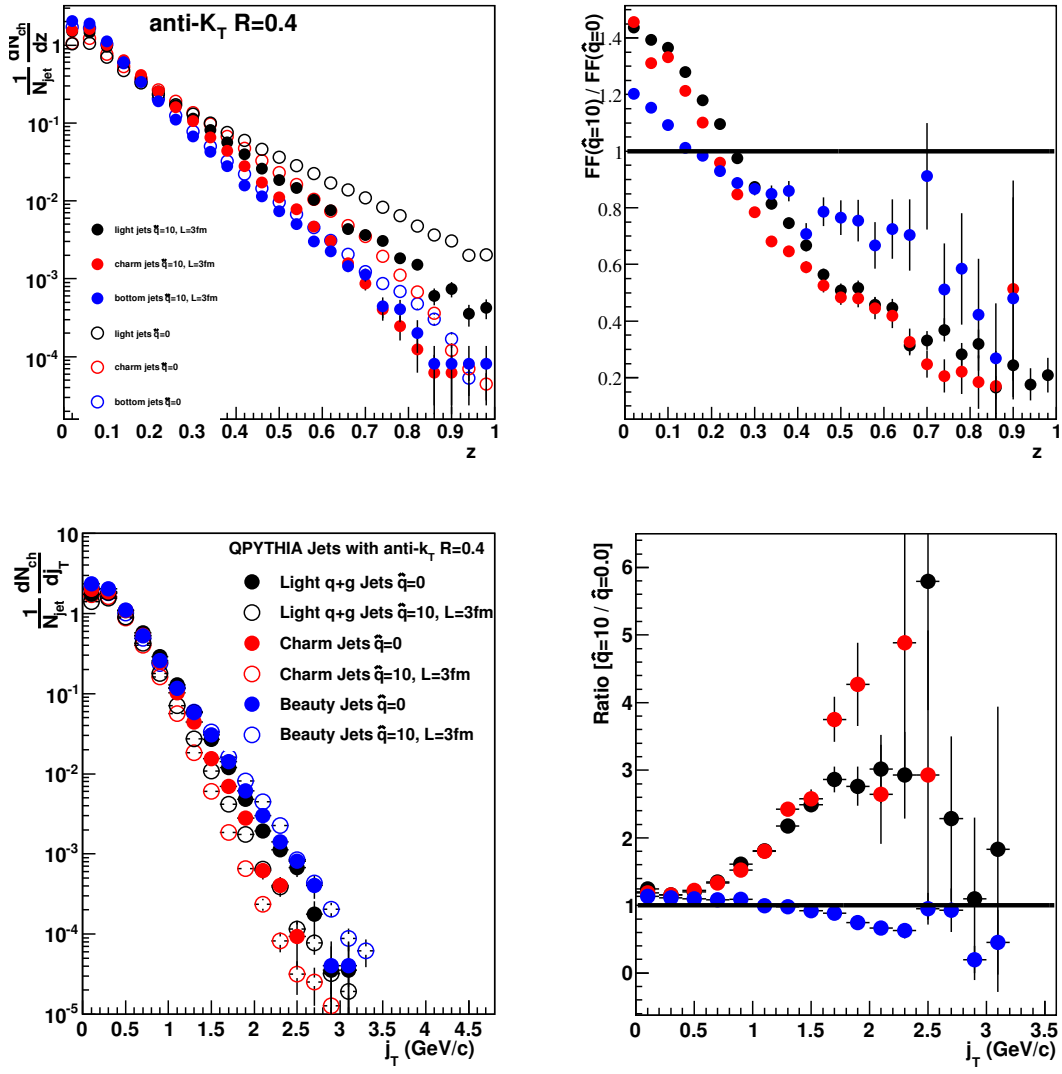

Figure 3.10: QPYTHIA simulations of the momentum distributions longitudinal (top) and transverse (bottom) to the jet axis of light charged hadrons ($\pi^{\pm}$, $K^{\pm}$, p and $\overline{p}$) produced in light and heavy flavor jets. Results are shown on the left for $\hat{q} = 0$ (i.e. PYTHIA) and $\hat{q} = 10$ GeV^2/fm with $L = 3$ fm. The ratios of the distributions obtained from $\hat{q} = 10$ GeV^2/fm to $\hat{q} = 0$ are shown on the right. The longitudinal momentum distributions are expressed in terms of fraction of the jet energy, $z = p_l/p_{\text{jet}}$. The jets were reconstructed from the QPYTHIA-generated hadrons using the anti-k_T algorithm with $R = 0.4$ and results are shown here for jets with energy 20 GeV.

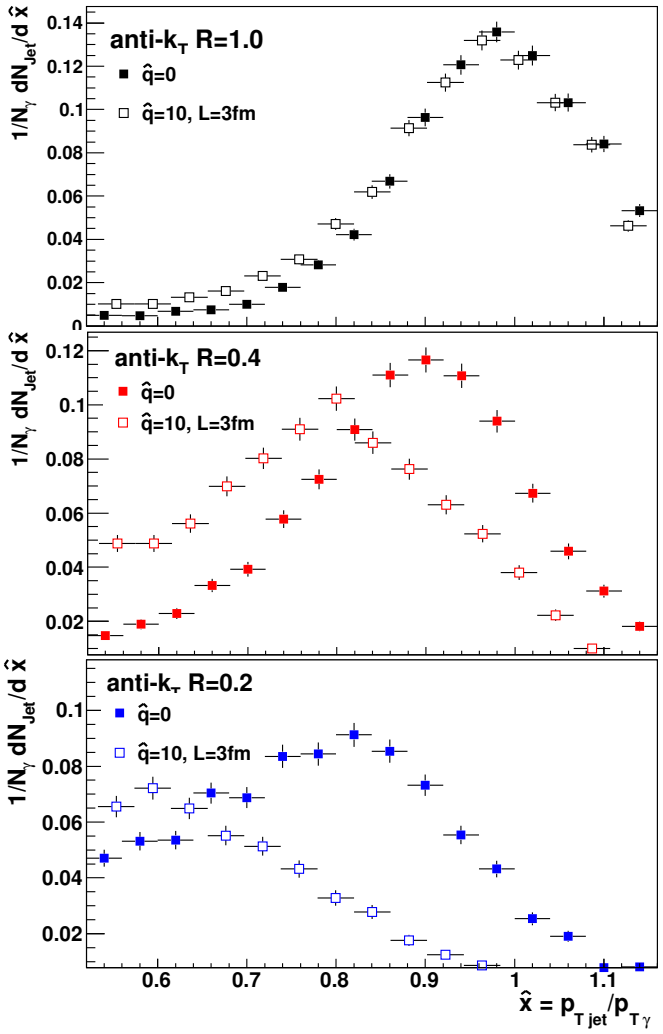

Figure 3.11: QPYTHIA simulations of the $\hat{x}$ distribution (i.e. the ratio of reconstructed jet transverse momentum to the direct photon transverse momentum) for three different jet algorithms—all anti-k$_T$ with $R = 1.0$ (top), $R = 0.4$ (middle), and $R = 0.2$ (bottom)—and two different jet quenching parameters $\hat{q} = 0, 10\ \mathrm{GeV}^2/\mathrm{fm}$.

3.1.3 Experimental challenges

In heavy ion collisions, the underlying event will prevent clean separation of low momentum hadrons from the parton shower and hadrons from the underlying event. The fluctuations in the particle and transverse energy density in the underlying event can also present difficulties by distorting the direction of a reconstructed jet and/or by generating false jets. Currently there are preliminary results from both the PHENIX and STAR experiments on jet reconstruction in heavy ion reactions as shown in Figure 3.12. These results lead to very different conclusions regarding the "fake" jet contribution and intense studies within the field are working to reconcile these differences. There are no published jet reconstruction results in heavy ion reactions at any energies.

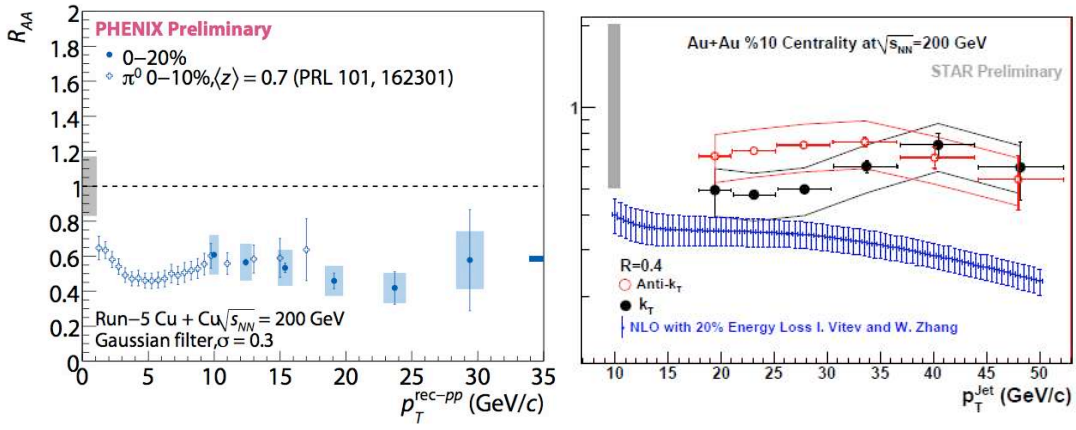

Figure 3.12: (left) Preliminary PHENIX reconstructed jet R_{AA} in Cu+Cu collisions utilizing a Gaussian Filter algorithm with $\sigma = 0.3$ [233]. (right) Preliminary STAR reconstructed jet R_{AA} in central Au+Au collisions with the k_T and anti-k_T algorithms [281].

To illustrate the status of our evaluation of the jet measurement, we have utilized the HIJING model [197] for the underlying Au+Au event. Shown in Figure 3.13 is the reconstructed jet p_T from the PYTHIA jet Monte Carlo truth information at the particle level (i.e. no detector response is included) compared with the reconstructed jet p_T when the PYTHIA jet is embedded in a central HIJING event. The (left) right panel shows the results for the anti-k_T algorithm with R = (0.2) 0.4. The lower panels indicate the average baseline shift in the reconstructed jet energy (blue curves) and the RMS jet resolution blurring from the subtraction of the average underlying event. For jets with true $p_T > 20$ GeV, the relative resolutions are quite modest (4–8 GeV/c) and correctable via standard jet unfolding techniques. In order to study the "fake" jet contribution, we have run HIJING central Au+Au events where hard processes are turned off above $p_T > 5$ GeV/c, where processes below that p_T are not possible to include accurately in the unfolding matrix.

We run the standard anti-k_T jet finder on these events to produce a "fake" jet distribution (where the baseline average energy is subtracted), as shown in Figure 3.14. We compare this distribution to the scaled pQCD [309] jet distribution. Additional detailed studies are

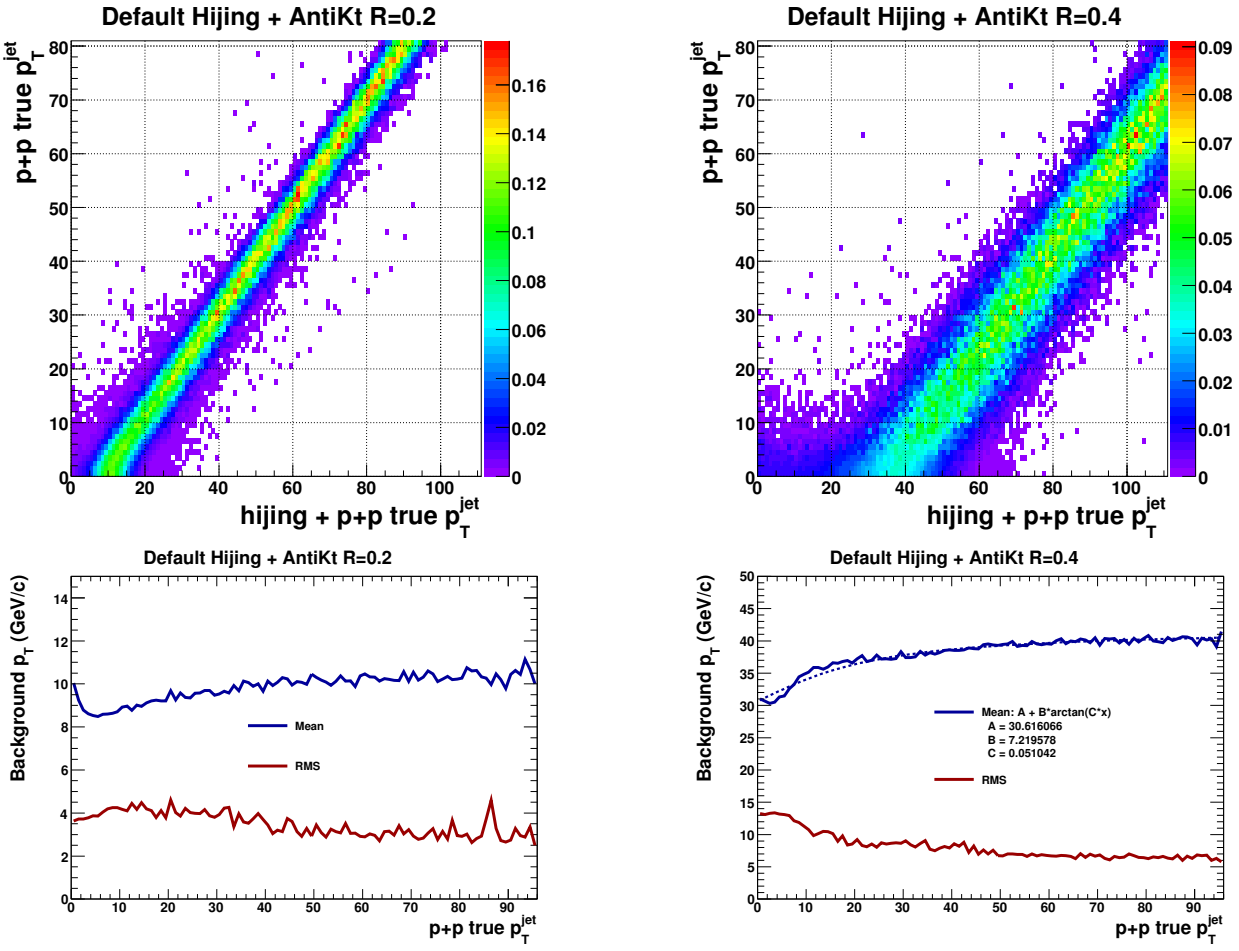

Figure 3.13: A summary of jet response functions obtained using a fast simulation and the anti-k_T jet finding algorithm. The plots on the left use a "cone" size parameter, $R = 0.2$, the ones on the right use a larger value, $R = 0.4$.

needed to fully understand the "fake" jet contribution, but this *work in progress* indicates that for jet $p_T > 25$ GeV one can start to reliably find full jets. We believe that with additional studies and "fake" jet rejection algorithms, this threshold can be pushed down further.

Dealing with jet radii greater than 0.4 will be more challenging, but one can also utilize a narrow jet cone algorithm and then measure broader radiation contributions statistically. It is very important to note that as seen in Figure 3.4, we have sufficient event rate for direct photons out to $p_T \approx 50$ GeV/c and for these events one can study the opposing quark jet with a dramatically reduced "fake" jet rate. The reduced rate is due to the fact that one is only encountering fluctuations within the small subset of Au+Au events with very high p_T photons, and not with fluctuations in the multibillion Au+Au event sample when trying to measure inclusive single jets. This reduction of "fake" jet contributions is also realized for tagged heavy flavor jets.

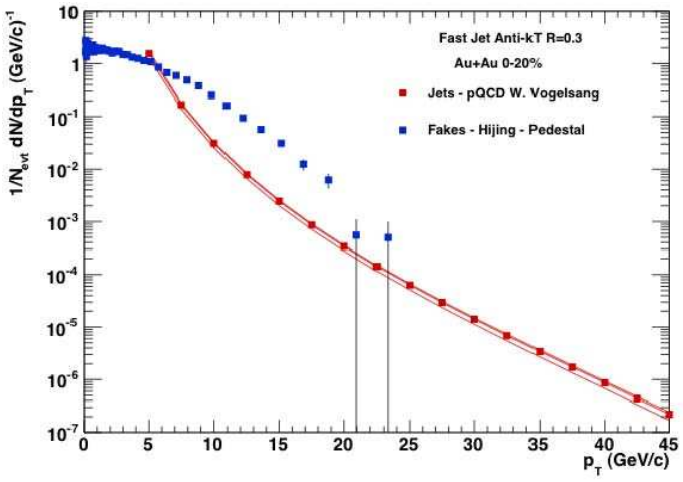

Figure 3.14: HIJING events with hard processes above a cut-off scale turned off to generate "fake" background events, compared with the scaled pQCD jet cross section.

If jet quenching is due to strong coupling, or proceeds through a mechanism that produces a much stronger angular broadening than that predicted by weakly coupled calculations, then narrow jet definitions may be largely insensitive to the jet modifications. That situation will be experimentally identifiable since the jets would be strongly suppressed while the detected jets (e.g. from the corona) might appear completely unmodified. In that situation, broader jet definitions may recover the missing jets at the cost of larger backgrounds and fake rates.

3.2 Heavy Flavor Jet Physics

The main motivation for studying heavy flavor jets in heavy ion collisions is to understand the mechanism for parton-medium interactions and to further explore the issue of *strong versus weak* coupling [205]. Light quarks and gluons interact with the medium and were originally thought to lose energy by radiating gluons. However, measurements of electrons from the decay of heavy mesons also show suppression out to $\approx$10 GeV/c (see Figure 2.5(a)). Gluon radiation from heavy quarks was expected to be suppressed via the dead cone effect [176]. However, the measured $R_{\rm AA}$ fell below pQCD based calculations for both charm and bottom suppression and set off a theoretical search for an energy loss mechanism which can provide better agreement with the data. Recent measurements of the contribution of electrons from B decays to the nonphotonic electrons [39] have contributed to the disagreement as the data suggest that electrons from B and D decays are equally suppressed.

Our knowledge of the mechanisms heavy quark energy loss and its dependence on quark masses should be substantially improved by the new results that will be provided by the VTX and FVTX in the next five years (2010–2015), as described in the previous chapter. However, there are two areas of heavy flavor measurements that will still be limited by detector capabilities, even with the VTX and FVTX upgrades.

- Full reconstruction of D and B mesons.
- Full jet reconstruction with c and b flavor tag

These are measurements that are limited by the small acceptance of PHENIX central arms. Large acceptance tracking and calorimetry would make these measurements possible and would extend the study of heavy flavor jets into new areas.

3.2.1 High statistics measurement of Heavy mesons

Although the VTX has sufficiently good secondary vertex resolution (50–100μm) to separate the D decay vertex from the primary vertex, the reconstruction efficiency of D decays is small due to the small acceptance of the PHENIX central arms. The long flight path ($>$ 5 m) from the beam to the EMCal or TOF further reduces the acceptance due to the decay-in-flight of kaons from $D \rightarrow K\pi$ and $D \rightarrow K\pi\pi$ decays. The VTX covers a large acceptance ($|\eta| < 1$), but its stand-alone tracking momentum resolution is approximately $\sigma_p/p \simeq 10\% \oplus 5\%p$, which is not adequate for D meson reconstruction.

A large acceptance tracking system that covers $\pm$1 unit of rapidity with high momentum resolution will increase the reconstruction efficiency of D mesons by almost two orders of magnitude compared to the present PHENIX detectors. A high statistics measurement of fully reconstructed D mesons will enable much more detailed studies of the energy loss

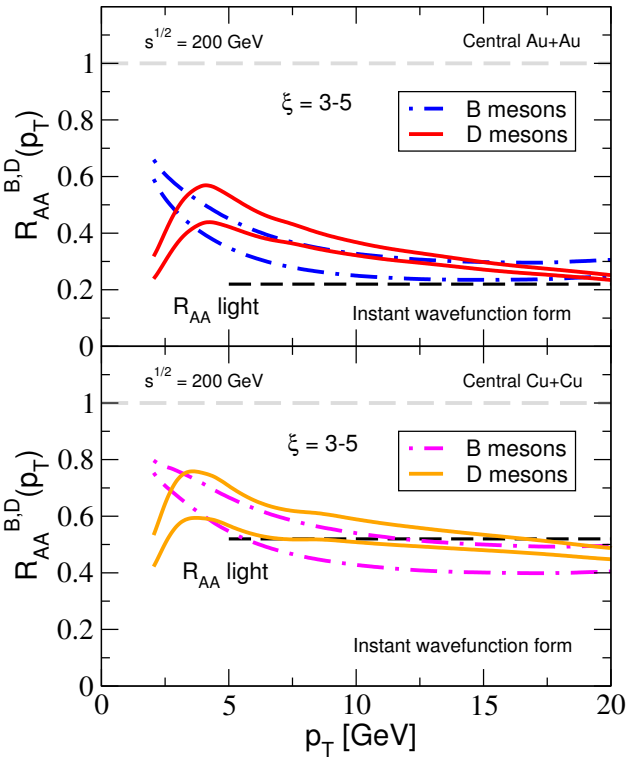

Figure 3.15: $R_{\rm AA}$ of D and B mesons in Au+Au (top) and Cu+Cu (bottom) collisions at $\sqrt{s_{NN}}$ =200 GeV from collisional dissociative processes. Figure from Ref. [284].

and flow of charm. Correlation measurements involving D mesons and other hadrons are useful tools to study the fragmentation of charm quarks in the medium.

The expected yield of fully reconstructed D mesons is quite substantial, primarily because the acceptance of the tracking system is so large. For minimum bias Au+Au collisions at $\sqrt{s_{NN}}$ =200 GeV, the number of $c\bar{c}$ pairs per event is approximately 0.7 per unit of rapidity. Since about half of the c quarks fragment to D^0, the number of D^0s plus $\overline{D^0}$s is also approximately 0.7 per event. A tracking system covering ± 1 unit of rapidity has a geometrical acceptance close to 100% of dN/dy for $D \rightarrow K\pi$. Thus the number of $D \rightarrow K\pi$ accepted by such a tracking system is 2.7×10^{-2} per event. The actual yield is much smaller than this since we would need to apply very tight secondary vertex cuts to remove a large combinatorial background. For D mesons at low p_T, the vertex cut efficiency can be less than 10% and still achieve a good S/B ratio. But even taking into account the small efficiency of the vertex cut, approximately 100 million reconstructed $D \rightarrow K\pi$ can be expected for 50 billion Au+Au minimum bias collisions. Similar or even larger data samples can be obtained in the other decay channels of D^0, D^+ and D_s mesons. A measurement of Λ_c should also be possible although the yield after the vertex cut should be modest due to its small $c\tau$ of 59μm.

A high statistics measurement of D mesons will allow the extension of $R_{\rm AA}$ measure-

ments to a very high p_T. Figure 3.15 shows the expected R_{AA} of D and B mesons calculated by Vitev[284]. In this particular calculation, the strong suppression of both D and B mesons due to collisional dissociation persists to a very high p_T—at least up to 20 GeV/c. Thus it is important to measure R_{AA} of D at very high p_T. It is interesting to see out to what p_T the strong suppression persists. If R_{AA} measurements of charm and bottom quarks begin to rise at some p_T, the measurements of D and B mesons via tagging will be more sensitive to the effect than measurements of their decay electrons.

High p_T D^0 mesons can be reconstructed from $D^0 \to K^-\pi^+$ with a relatively high vertex cut efficiency. For a D^0 with momentum of 15 GeV/c, the flight distance is about 1 mm, and the typical decay opening angle is about 0.2 radian. At such an opening angle, the secondary vertex resolution along the flight direction is approximately 250 μm. For such a high p_T, the combinatorial background is also much smaller than in the low p_T region. A 0.5 mm cut would eliminate virtually all the background while keeping approximately 60% of the signal. A similar argument can be made for the $D^0 \to K^-\pi^+\pi^0$ channel, where the π^0 is not tracked to a secondary vertex but is used in the mass reconstruction. The expected yields of charm and bottom hadrons are shown in Figure 3.16 for 20% central Au+Au collisions. For $p_T > 20$ GeV/c, the yield of charm hadrons is approximately 2×10^{-7} per event, and the yield of $D^0 \to K\pi$ is approximately 1% of charm hadrons after the D/c ratio ($\simeq 0.5$), the branching ratio (3.9%), and vertex efficiency ($\simeq 60\%$) are taken into account. Thus the yield of $D^0 \to K\pi$ for $p_T > 20$ GeV/c is approximately 2×10^{-9} per event or 20 per 10 billion central Au+Au collisions.

High statistics measurements of charm hadrons will also enable a detailed study of v_2 of charm. We can investigate whether the quark number scaling observed in the light hadron sector also holds in the charm sector. We can also investigate whether there is a difference in the v_2 of the D^0 and the D_s due to its mass difference or quark content. The large D meson sample can also be used for a detailed study of D-hadron correlations. Correlation studies can also reveal modification of charm fragmentation inside the medium.

3.2.2 Heavy Flavor tagged Jet

The most direct way to understand the energy loss mechanism is to study the modification of jets as a function of the type of jet: light quark or gluon jets (which together dominate the inclusive jet spectrum), charm jets and bottom jets.

Unlike one- and two-particle observables, full jet measurements provide a complete picture of the modifications of hard processes from $p+p$ to heavy ion collisions. One- and two-particle observables which require a high p_T particle are also biased toward those jets which have undergone less interaction with the medium (e.g. by having been created near the surface). Since the goal is to study the interactions between the medium and the hard partons, less biased observables are needed.

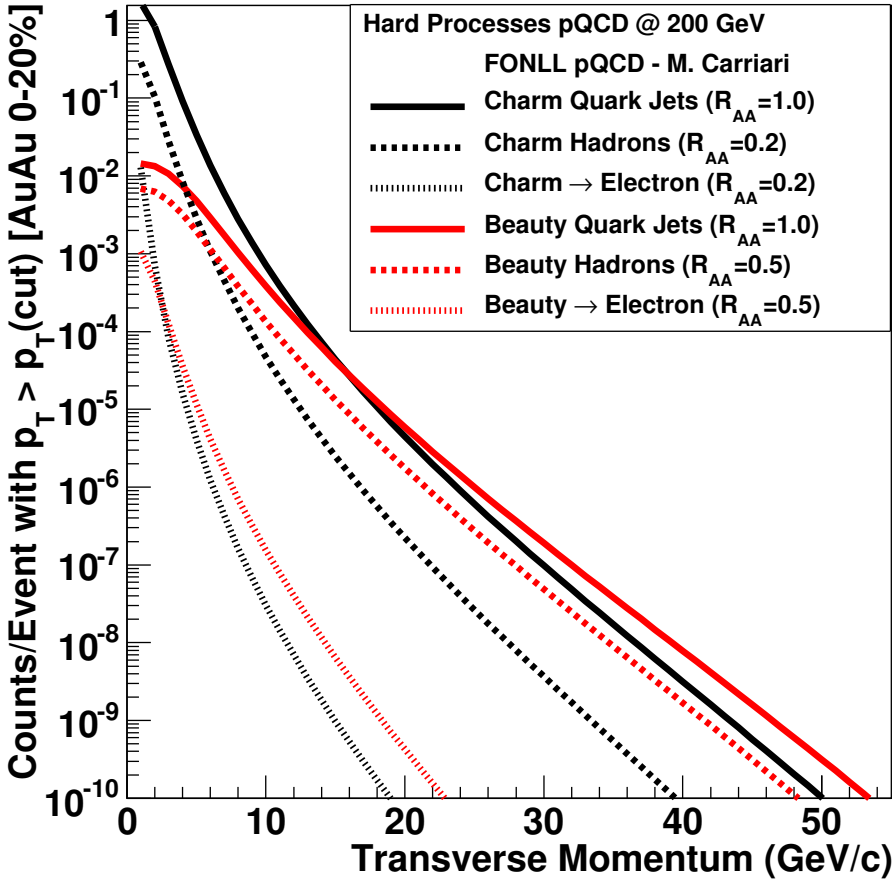

Figure 3.16: FONLL calculations [146] for heavy flavor (charm and bottom) jets, fragmentation hadrons (D,B mesons primarily), and decay electrons as a function of transverse momentum.

By significantly expanding the experimental acceptance and having the ability to reconstruct full jets with a heavy flavor tag, the kinematic reach of our measurements is substantially extended. The rates of heavy flavor production from perturbative QCD calculations [146] are shown in Figure 3.16. The calculations are then scaled for central 20% Au+Au collisions at $\sqrt{s_{NN}} = 200$ GeV with the assumed nuclear suppression factors ($R_{\rm AA}$) shown in the legend. These are the counts per Au+Au event with $p_T > p_T(cut)$ and within pseudorapidity $|\eta| < 1.0$.

One promising tool is the study of jet-shape modification in nucleus-nucleus events compared to p+p collisions. Different mechanisms of energy loss would be expected to lead to different redistributions of the jet energy. Figure 3.17 shows $\Psi(r/R)$, the fraction of the total jet energy inside a sub-cone of radius r, as a function of r in QPYTHIA and PYTHIA. QPYTHIA, which incorporates energy loss via radiation only, broadens the jet in nucleus-

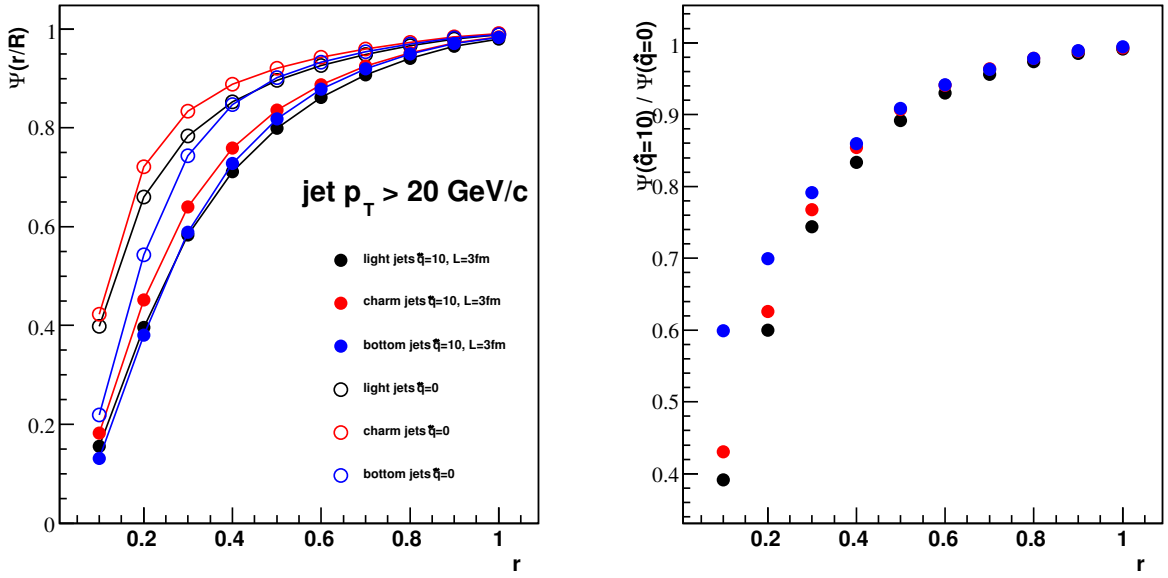

Figure 3.17: $\Psi(r/R)$ as a function of r, the radius of the sub-cone, for $R = 1$ jets reconstructed with the anti-k_T algorithm. The jets are from PYTHIA and QPYTHIA with jet p_T >20 GeV/c. In all cases the jets are broadened in QPYTHIA compared to PYTHIA however the degree of broadening depends on the parton type.

nucleus collisions compared to $p+p$ collisions. Collisional energy loss might be expected to broaden the jet further. Collisional dissociation processes, in which the meson forms and is dissociated in the matter [284], would lead to a nearly unmodified jet shape from $p+p$ collisions. Comparisons of the shape modifications from light and heavy jets would provide insight into the dominant mechanisms of energy loss for the different jet types. These measurements are very similar to those in which the jet $R_{\rm AA}$ is measured as a function of the jet size (see for example Ref. [308]).

There are three methods to tag heavy flavor jets. All of these methods can be used to study heavy flavor jets.

Lepton Tagging The simplest method of tagging heavy flavor jets is to select events with a high p_T electron. In the current PHENIX setup, for p_T >1.5 GeV/c the number of electrons from heavy meson decay exceeds that from nonheavy flavor sources. With the addition of the VTX the rejection power of electron tagging will be increased because of the ability to select on displaced tracks, separating charm from bottom and rejecting electrons from Dalitz decays at the vertex. Since semileptonic branching ratio of both c and b is approximately 10%, this method provides a reasonable tagging efficiency of heavy flavor jets for a wide p_T range.

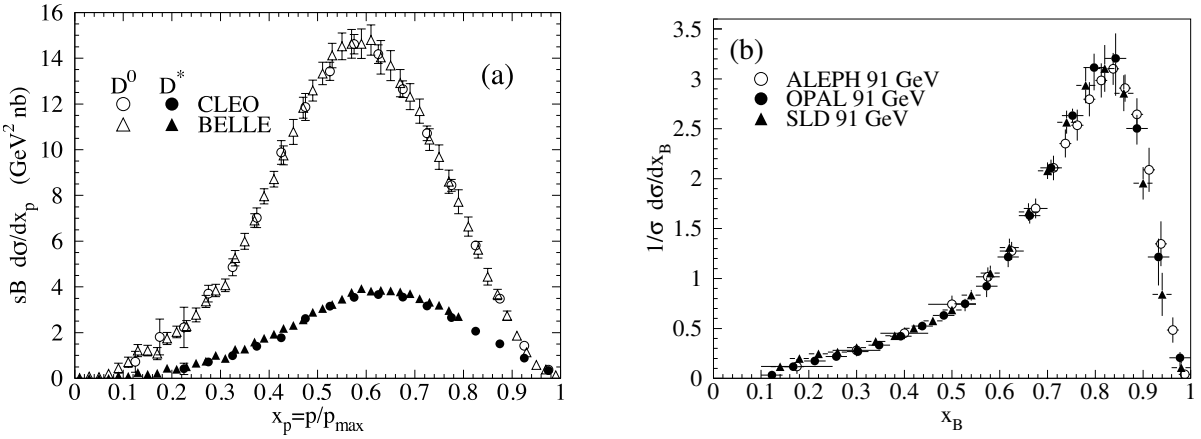

Figure 3.18: D and B fragmentation functions as measured in e^+e^- collisions from Ref. [88].

Reconstruction of Heavy Mesons Tagging heavy flavor jets by reconstructing the heavy meson has a number of advantages. In vacuum fragmentation, the D and B mesons carry a large fraction of the heavy jet energy, z, see Figure 3.18. In-medium fragmentation function modifications are a sensitive probe of energy loss, especially for heavy flavor where so much of the jet energy ends up in the heavy meson. This is especially true if collisional dissociation is significant, which would change the heavy meson z without changing the overall jet $R_{\rm AA}$ or energy distribution[284]. Figure 3.19 shows the D meson fragmentation function in PYTHIA and QPYTHIA for 20 GeV/c jets. The peak of the fragmentation function is shifted from $z \simeq 0.7$ to $z \simeq 0.5$. Thus for a given p_T, D mesons are more suppressed than charm jets. Jet tagging with reconstructed D mesons allows direct measurement of the modification of the D meson fragmentation function and can disentangle the causes of the large suppression of charm.

Tracks from Secondary Vertices Another possible method for tagging charm and bottom jets is to look for jets with many tracks which do not point back to the collision vertex. Heavy jets typically fragment into a heavy hadron which contains a large fraction of the jet momentum. This method looks for evidence of a decay displaced from the primary collision vertex. It does not require the heavy hadron itself to be reconstructed, but rather tags the jet as containing a heavy hadron. This in principle allows higher efficiency because it eliminates the need to isolate specific decay modes as in the previous methods. This technique is used by the D0 collaboration to identify b-jets at the Tevatron [15]. This method exploits the fact that most b-hadron decays lead to multiple charged particles originating at the b-hadron's decay point, and thus it is particularly effective to tag b jets.

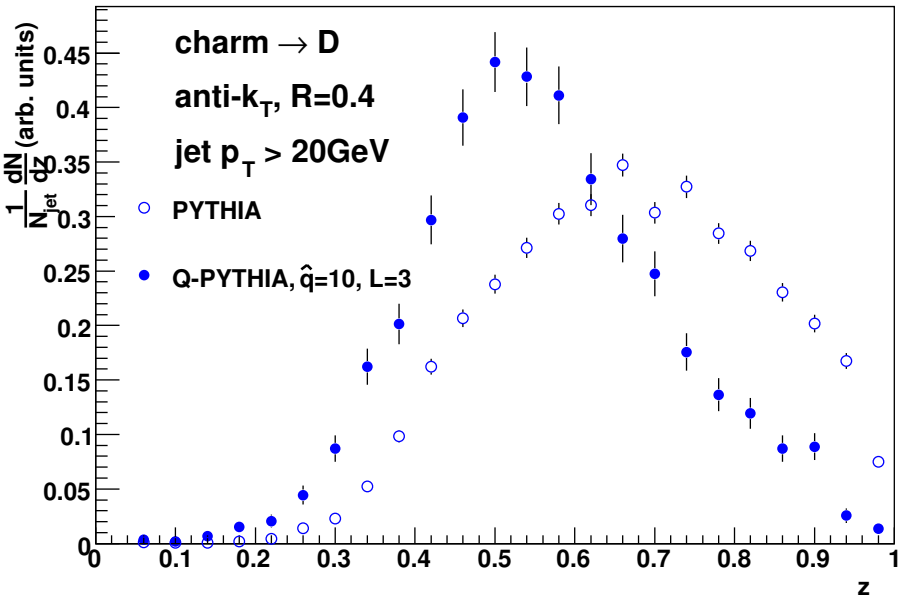

Figure 3.19: D meson fragmentation function in PYTHIA (open points) and QPYTHIA (solid points) for anti-k_T jets with $R = 0.4$ with $p_{T,jet}$ >20 GeV/c.

3.3 RHIC and LHC Jet Physics

Within the next year the LHC will provide Pb+Pb collisions at 2.75 TeV that will expand the excitation function for heavy ion studies by more than an order of magnitude in colliding energy. One of the most exciting questions is whether the quark-gluon plasma properties will be strikingly different in collisions at these higher energies. Calculations from lattice QCD shown in Figure 3.20 indicate a rather dramatic spike in the nonconformality $(\epsilon - 3p)/T^4$ just above the transition temperature to the quark-gluon plasma, and then a steep decline towards zero. While temperatures in the early stages at RHIC are of order $2 \times T_c$, the initial temperatures achieved at the LHC may be $4 - 5 \times T_c$ [98]. As illustrated in Figure 3.21, the fundamental properties of the quark-gluon plasma are expected to evolve with temperature, and the relevant range of temperatures for sQGP (i.e. nearly perfect fluid) properties is potentially quite narrow.

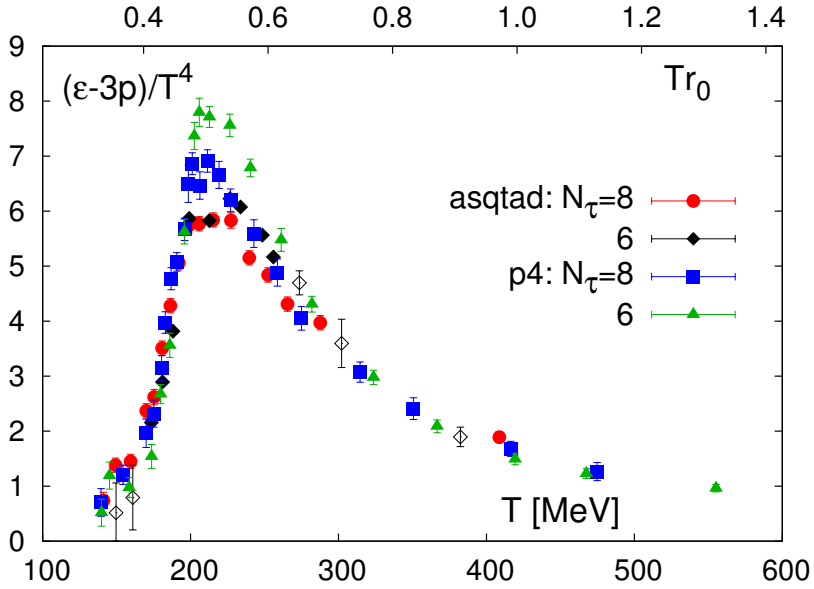

Figure 3.20: Lattice QCD calculation for the trace anomaly $(\epsilon - 3p)/T^4$ versus temperature [122].

Early data at low luminosities at the LHC will already be quite revealing in terms of the bulk dynamics. A fundamental question is whether the shear viscosity to entropy ratio is small only very near the transition temperature, as speculated in [201], or remains small over the entire range of bulk dynamics explored at the LHC. The answer to this question will shape many of the future investigations at both RHIC and the LHC.

If the LHC probes an initially weakly-coupled quark-gluon plasma (wQGP), then RHIC will remain the unique world facility for studying and dissecting the properties of the strongly-coupled sQGP. However, if the increased temperature range for the QGP at the LHC still resides within the strongly-coupled domain, the complementary program of

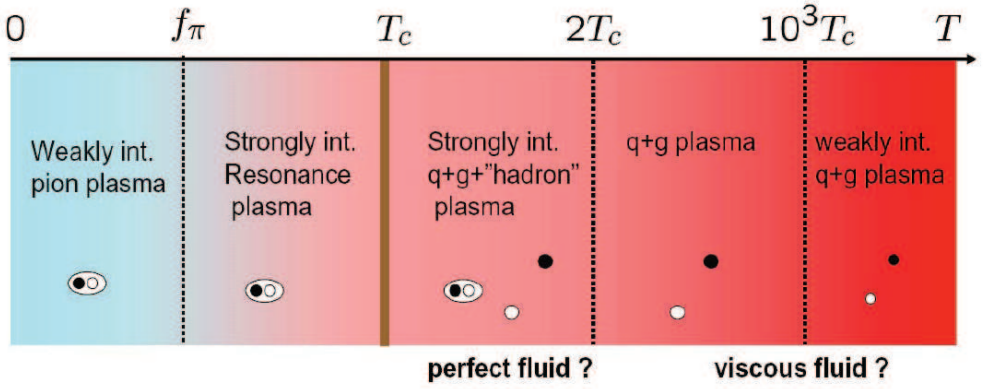

Figure 3.21: An illustration of the characteristics of QCD matter as a function of temperature.

RHIC and the LHC will have unprecedented tools to gain a complete understanding of hot QCD in this domain.

A number of strengths of the RHIC physics program and the complementary role of the LHC are itemized here and then a detailed discussion of each follows.

- sQGP created at RHIC is optimal for *strongly coupled* studies. Whether the medium at the LHC is strongly or weakly coupled remains to be determined experimentally.
- RHIC is a powerful and flexible facility that will allow us to *dial* the medium properties via colliding different nuclear species, colliding at different energies, and comparison with critical baseline p+p and proton(deuteron)-nucleus collisions at the same $\sqrt{s_{NN}}$.
- RHIC experiments will measure jets with energies $15 < E_T < 60$ GeV thus spanning a large range of scales in the medium as shown in Figure 3.3.
- RHIC collisions are dominated by quark jets over a wide E_T range. In a complementary way, LHC has a majority contribution from gluon jets.
- RHIC experiments have shown that cold nuclear matter initial state effects are modest at midrapidity for $p_T > 2$ GeV/c and can be separated from jet quenching effects.
- PHENIX and an upgraded PHENIX can sample a very large Au+Au luminosity with minimum bias triggers, which is crucial for lower energy jet studies and understanding calorimeter trigger biases for higher energy jet studies.

The LHC will study the medium with probes at much higher Q^2 with jet energies in excess of 100 GeV. At such energies, the underlying event from the Pb+Pb collisions will have little impact on jet reconstruction if the jets are modified as expected from weakly coupled calculations. Measurements at the LHC will produce significant advances in

the understanding of jet quenching by answering basic questions about the nature of the medium-modified final-state parton showers generated in very high energy hard-scattering processes. However, we believe that jet measurements at RHIC, in conjunction with LHC measurements, will be *essential* for the development of a unique answer to the "big picture" question posed at the beginning of this section—namely an understanding of the modification of the parton shower generated by hard scattering processes and the physics of the interactions of the partons in that shower with the medium at all resolution (virtuality) scales and as a function of medium temperature and density.

Also, there is a significant difference in the flavor composition of the final-state parton spectrum at high E_T between RHIC and the LHC. As shown in Figure 3.22, for $E_T > 50$ GeV more than 90% of the jets at RHIC are quark jets. At the LHC there is a more even balance of quark and gluon jets, though the majority of jets are still due to the fragmentation of gluons. The difference in the strength of the quenching for quarks and gluons needs to be disentangled, particularly when the role of flavor changing $g \rightarrow q\bar{q}$ splitting processes in the parton shower are included. The purity of the sample of high energy quark jets at RHIC provides an advantage in a program whose goal is a precise understanding of the mechanism of jet quenching.

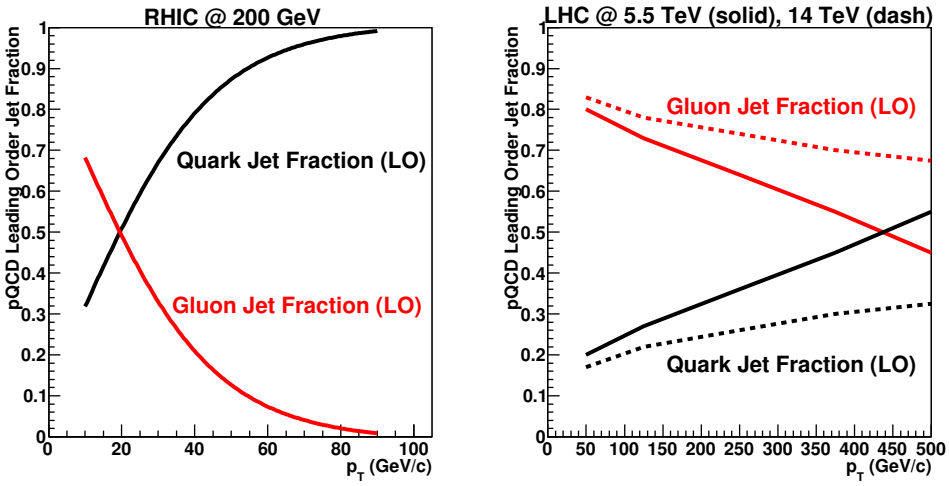

Figure 3.22: Comparison of fraction of quark and gluon jets from LO pQCD calculations for RHIC (200 GeV) and the LHC (5.5 and 2.75 TeV) [306].

Hard scattering processes at the LHC will provide the opportunity to study jet quenching at very high outgoing parton virtualities, but those high virtualities also present a challenge. The interpretation of the quenching of multijet (i.e. more than 2 jet) final states—predominantly from hard radiation of one of the outgoing jets—must account for the interplay of the time-scale for the emission of that radiation in the parton shower and the time-scale for the evolution of the medium. Underlying event studies of jet substructure will be necessary to measure split jets which are nominally isolated but where one of the jets is below 50 GeV. Ultimately, the understanding of the substructure of very

high energy jets will be a valuable tool for probing the quark-gluon plasma, but it is likely that understanding the additional physics introduced by the presence of hard radiation will take some time to understand. At RHIC, the radiation from the highest energy jets will be suppressed since those jets are mostly quark jets. Radiation from heavy flavor jets, discussed in the next section, will be further suppressed by the quark mass, so the measurement of quenching for those jets will be even more "clean".

As we have discussed above, the underlying event in heavy ion collisions provides a challenge for jet reconstruction for jet energies below some E_T, determined by the level of and fluctuations in the underlying event and by the jet algorithm. Studies of the performance of jet reconstruction by ALICE, ATLAS and CMS [172] suggest that jet measurements below 50 GeV are challenging. Evaluations of jet finding efficiency indicate that the efficiency reaches 50% near 50 GeV for cone sizes of 0.4–0.5. Additionally, triggering on lower energy jets has a low efficiency in current LHC experiment studies for heavy ion reactions. In contrast, in current-day PHENIX and an upgraded PHENIX, we have the ability to sample a very large luminosity with minimum bias triggers which enable lower energy jet studies and understanding calorimeter trigger biases for higher energy jet studies.

In the physics discussion above we have stressed the need to understand the influence of the virtuality evolution on quenching, and more generally, the value in understanding the evolution of quenching phenomena using jet reconstruction over a wide range of jet energies. Even if the medium properties at the LHC and RHIC turn out to be similar, a jet measurement program at RHIC will provide a unique window for jet energies E_T ∼10–20 GeV where the virtualities of outgoing partons are limited and the picture in Figure 3.2 represents a reasonable approximation to the physics. Additionally, it is important to have an overlap in measured jet energies between RHIC and the LHC around E_T ∼50 GeV where partons showers are more fully developed and the virtuality evolution discussed above is most relevant. The experimental study of that evolution will likely turn out to be essential to developing a rigorous understanding of the influence of the medium on the virtuality evolution.

RHIC data taken in 2003 from d+Au collisions indicate rather modest initial state effects at midrapidity for particles with $p_T > 2$ GeV/c. In contrast, initial state effects at the LHC are potentially quite large. These initial state effects guarantee a robust proton-nucleus program at the LHC, and at the same time indicate the necessity of careful experimental and theoretical work to disentangle final state quark-gluon plasma jet quenching effects. Figure 3.23 shows a comparison of two different calculations of the nuclear modification factor for single hadrons in p+Pb collisions. One calculation is based on the EPS09 parton distribution functions [184] which have only modest nuclear modifications at large Q^2. The other result is obtained from a saturation calculation based on the dipole model [74]. The dramatic difference between these results indicates the large theoretical uncertainties in the initial state physics relevant for predictions of hard scattering rates for the very high collision energy at the LHC. Clearly, p+Pb measurements at the LHC will substantially reduce the theoretical uncertainties. Such large saturation effects at the LHC would be

very exciting, even if it means extrapolation to Pb+Pb collisions is then more complicated. There is also uncertainty in the possible influence of BFKL physics on hard scattering processes at moderate E_T, particularly for processes producing jets with large rapidity separation. In contrast to the situation at the LHC, at RHIC for high p_T processes the dominant initial-state effects are EMC suppression in the nuclear parton distributions and initial-state energy loss. Existing d+Au jet measurements currently being carried out by PHENIX will provide a calibration of these effects out to jet E_T ~30–40 GeV so that theoretical calculations of jet rates in Au+Au collisions have initial-state effects fully constrained within the next few years.

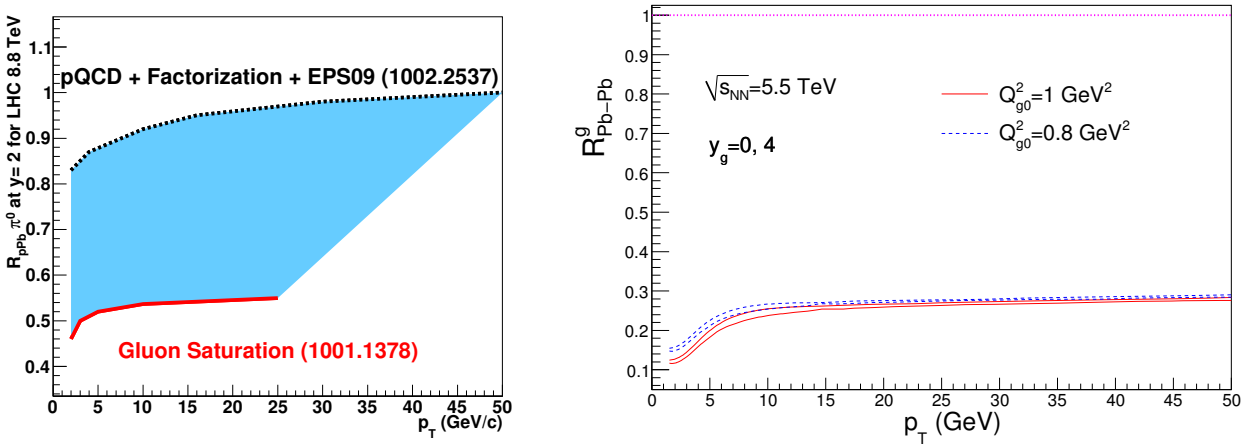

Figure 3.23: (left) The calculated nuclear modification factor R_{pPb} (for p+Pb collisions) at the LHC at $\sqrt{s_{NN}} = 8$ TeV from a pQCD + factorization picture with EPS09 nuclear modified Parton Distribution Functions (PDFs) [269]. The red curve is the same quantity calculated in a nonfactorized picture of gluon saturation [74]. Note that their calculation assumes an $N_{\rm coll}$ numerical factor of 3.6, and would be re-scaled after this is determined at the LHC. (right) Results from the same gluon saturation calculation for the outgoing gluon nuclear modification factor R_{PbPb} at LHC energy.

Lastly, the flexibility and running time at RHIC has been an essential component of the success of the program. Crucial information regarding initial state effects from cold nuclear matter have been highlighted. Additionally the running of smaller systems provided breakthrough information regarding initial state fluctuations and also a controlled path length dependence study. New large acceptance upgrades combined with accelerator luminosity improvements will allow RHIC to study many physics probes over a broad range in energy – including jet and heavy flavor studies down below $\sqrt{s_{NN}}$= 62 GeV. It is notable that key comparisons between RHIC and the lower energy CERN-SPS have been very insightful, and we fully expect an even more prominent interplay between RHIC and LHC data analysis and theoretical understanding.

3.4 Quarkonia and Color Screening

Color screening in the quark-gluon plasma directly relates to the issue of *strong versus weak* coupling. Measurements of heavy quarkonia provide the best access to information about color screening. We detail here a set of measurements of multiple quarkonia states and at multiple colliding energies to answer this question.

The proposal for directly observing the effects of color screening in the QGP by measuring the reduction in yield of heavy quarkonia in nuclear collisions dates back over twenty years [248]. Results from Pb+Pb collisions at $\sqrt{s_{NN}} = 17\,\text{GeV}$ at the CERN SPS fixed target program gave tantalizing hints of such effects [81]. Multiple theoretical calculations predicted significant further J/ψ suppression at RHIC energies due to the higher temperatures achieved and the longer lifetime of the QGP stage. PHENIX has recorded and published high statistics heavy quarkonia data from the J/ψ channel in $\sqrt{s_{NN}}$=200 GeV p+p [31], d+Au [34], Cu+Cu [35] and Au+Au [32] collisions to test this prediction. The resulting measurements from the PHENIX experiment, shown in the left panel of Figure 3.24, revealed that the J/ψ nuclear modification factor (R_{AA}) at midrapidity was in fact in agreement with that measured at the lower energies $\sqrt{s_{NN}}$=17 GeV (and in disagreement with simple expectations of increased screening effects). Additionally, with the PHENIX forward spectrometers, we observed that the suppression was even larger at forward rapidity, in contrast to expectations based on lower energy densities in this region. A number of theoretical proposals have been put forward in the last five years to explain this surprising result, and many of these proposals also highlight exciting potential uses of quarkonia as tools for probing the sQGP.

The first of these proposals relates to what are referred to as initial state or cold nuclear matter effects. It is known that parton distribution functions are modified in heavy nuclei. In particular the modification of low-x (small momentum fraction) gluons is not well constrained by experimental measurements (for details see [184] for example). Predictions of nonlinear evolution for low-x gluons, referred to as gluon saturation or color glass condensate effects, may be even more dramatic [218]. A smaller population of gluons in the incoming nuclei results in a reduced number of hard-scattering reactions that can produce $c\bar{c}$ pairs and thus eventually J/ψ states. Additionally, once the heavy $c\bar{c}$ pair is produced it may be scattered or its correlation broken up in traversing the back-side of the incoming nucleus (which is often parameterized as a simple σ_{breakup}). Recently, new data from the CERN SPS at lower energies [103] and precision d+Au data from PHENIX [166] indicate that this σ_{breakup} may be significantly smaller as one goes to larger collision energies. In a calculation incorporating these two effects [101, 187], one finds that if one accounts for the different initial state modifications as a function of energy and rapidity, the suppression from the QGP medium is in fact larger at RHIC (see the right panel of Figure 3.24). It is important to note that the recent PHENIX d+Au data do not seem to be consistent with existing models of a modified gluon distribution and a constant σ_{breakup}—see Section 2.4 on Cold Nuclear Matter effects for details. The data require a much stronger suppression at forward rapidity. The physics behind this observation must be understood before one

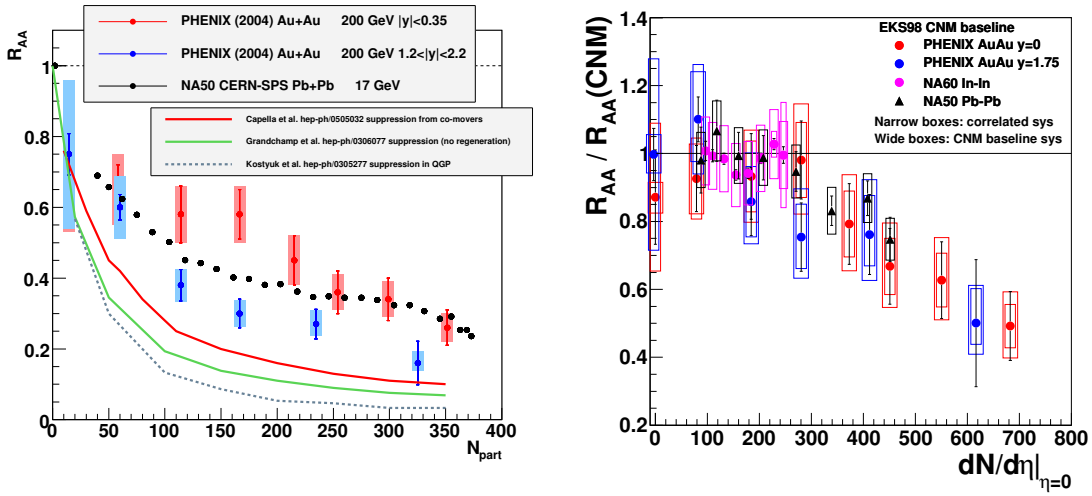

Figure 3.24: (left) J/ψ nuclear modification factor R_{AA} as a function of collision centrality (characterized via $N_{\rm part}$) from the PHENIX experiment in Au+Au and the NA50 experiment in Pb+Pb. Also shown are several theoretical calculations that predicted larger suppression at RHIC energies. (right) PHENIX and CERN SPS midrapidity nuclear modification factors with the estimated cold nuclear matter contribution divided out [187], plotted versus particle multiplicity.

can claim to have accounted properly for initial-state effects.

The second class of these proposals is that recombination (also referred to as coalescence) of previously unbound heavy quark pairs into quarkonia cancels any additional suppression at RHIC energies [298, 275]. There are large uncertainties associated with the dynamics and basic cross sections involved in this process. In Figure 3.25, we schematically show three competing production mechanisms. Case 1 shows the traditional production mechanism where the $c\bar{c}$ are produced together and bind. Case 2 is where the $c\bar{c}$ are produced together but with relative momentum such that they would normally not produce a quarkonium state. However, due to scattering in the medium (and even focusing by the hydrodynamic flow of the medium), they are able to coalesce. Case 3 is where one has the recombination of a c and $\bar{c}$ quark produced from two separate hard-scattering reactions at different spatial locations in the medium. These recombination cases are particularly interesting since they might be specific indicators of the distance scale over which heavy quarks travel in the QGP prior to hadronization (thus yielding information on the time evolution of deconfinement - see [298] for example). Also, we know that approximately 10 $c\bar{c}$ pairs are produced per central collision at RHIC, and expect about 115 pairs at the LHC. Case 3 has a rate that is roughly proportional to the square of the density of $c\bar{c}$ pairs, and thus would have virtually no contribution at CERN SPS energies, but would produce enormous J/ψ enhancement effects at the LHC in Pb+Pb collisions. A comparison of the RHIC and LHC J/ψ data could therefore resolve the contribution of off-diagonal pair coalescence (Case 3). Also, this last scenario might help explain the larger suppression of J/ψ

at forward rapidity at RHIC, due to the lower density of $c\bar{c}$ pairs in that rapidity region.

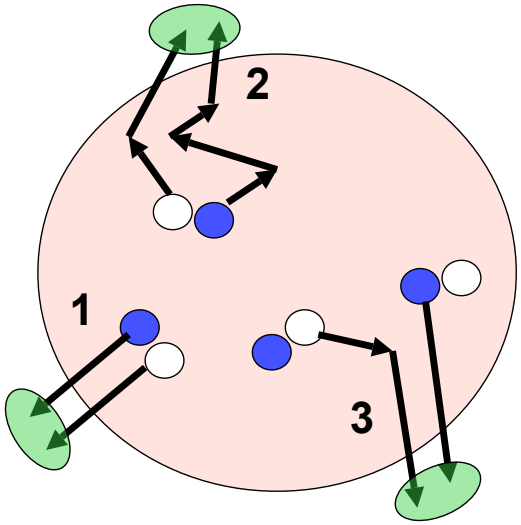

Figure 3.25: Cartoon of three quarkonia production mechanisms, including two recombination schemes.

These effects need to be understood to be able to answer the key original question of color screening in the QGP, and could potentially reveal other very interesting physics of heavy quark mobility and/or gluon saturation effects. The critical aspect of this program is the ability to systematically study these effects in a number of different heavy quarkonia states with precision (critically including the three $\Upsilon(1s, 2s, 3s)$ states), study them as a function of collision energy and geometry, and study their effects in cold nuclear matter (in $p(d) + A$ reactions) over a broad kinematic reach. We need to:

- Vary the temperature and lifetime of the QGP medium by changing the collision energy between $\sqrt{s_{NN}}$=62 GeV to 200 GeV (at RHIC) and 5.5 TeV (at the LHC), which changes the initial temperature from about $1.5T_c$ to about $4T_c$ and increases the lifetime by a factor of two to three.
- Vary the size of the quarkonia states by observing the three bound Υ states at LHC and RHIC, as well as the ψ' and possibly the χ_c.
- Vary the underlying heavy quark production cross sections by observing charmonium and bottomonium produced at $\sqrt{s_{NN}}$=62 and 200 GeV and 5.5 TeV. The open charm and bottom cross sections are, respectively, about 15 and 100 times higher at LHC energy than at RHIC energy of 200 GeV. When RHIC lowers the energy from 200 to 62 GeV, the charm production cross section is reduced by 1/3 and the beauty cross section by more than a factor of 10.

We note that the expected heavy quarkonia yields from RHIC and the LHC are compared in [188]. The cross sections for production of charmonium and bottomonium at the LHC

are estimated to be, respectively, about 13 and 55 times higher than at RHIC. But because of the roughly 30 times larger integrated luminosity expected at RHIC, the heavy flavor yields will be comparable to those at the LHC. This is crucial to having precision measurements across the *entire span* of the collision energy range.

Why are the different quarkonia states so important? The effects of screening will be emphasized by changing the size of the physical quarkonia bound state, and by increasing the energy density in the medium. The clearest signature will most likely be observed by comparing simultaneously the yields of the three Υ states from heavy ion collisions at RHIC and at the LHC. The relative melting temperatures (as calculated in [174]) are shown in Table 3.1 and graphically in Figure 3.26 along with the physical sizes and thus the approximate Debye screening length for disassociation. These results (along with more recent lattice QCD calculations) suggest that the $\Upsilon(1S)$ (and possibly even the $\Upsilon(2S)$) may remain bound at RHIC, but not at the LHC. The $\Upsilon(3S)$ is expected to be unbound in both cases. Therefore the effect of screening on the relative yields of the three bound states is expected to be quite different at RHIC and LHC. Also, the effect of initial state or cold nuclear matter effects should be the same for all three states, since their initial production couples to the same low-x gluons and their traversal through the initial cold nucleus is of a time scale $t < 0.1$ fm/c before the physical states with their standard sizes are formed. Lastly, the recombination effect is negligible at RHIC energies, at least in the Case 3 of initially separate $Q\overline{Q}$ pairs.

Another item to note is that the $\Upsilon(2s)$ and the J/ψ have very similar physical characteristics and thus similar expected screening effects. This comparison between the two states will be very important to check if one has separated the other interesting physics effects discussed above from the screening process. For this one needs a sufficiently large data set, and good control over systematic uncertainties.

Table 3.1: Dissociation temperatures of quarkonia states relative to the QCD critical temperature, T_{dis}/T_c.

Quarkonia state							
J/ψ	χ_c	ψ'	$\Upsilon(1s)$	$\chi_b(1p)$	$\Upsilon(2s)$	$\chi_b(2p)$	$\Upsilon(3s)$
1.10	0.74	0.20	2.31	1.13	1.10	0.83	0.75

Two additional lines of attack on the problem are currently identified as important. One relates to understanding the cold nuclear matter effects. The recent discoveries of large suppression in d+Au reactions at very forward rapidity has hinted at gluon saturation effects or possibly initial-state parton energy loss. The forward spectrometer upgrade (discussed in Section 7.2) may provide breakthrough measurements on this front. Second, the PHENIX experiment has proven its precision measurement capability for J/ψ, but

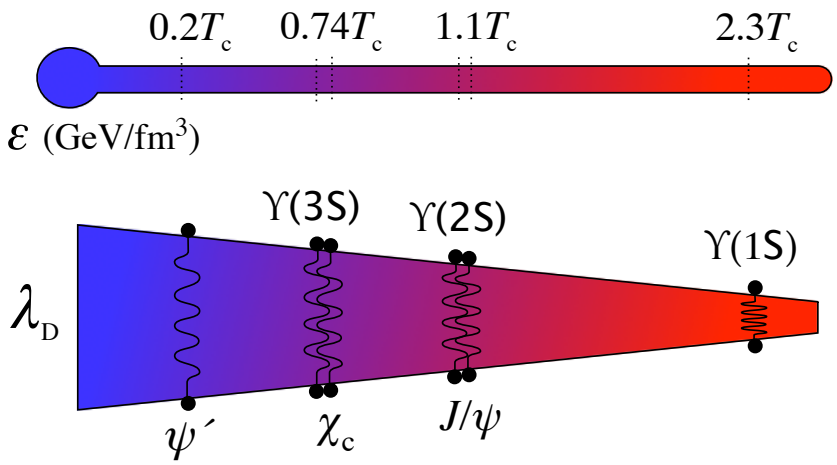

Figure 3.26: Diagram indicating one theoretical prediction for the melting point of the various quarkonia states and their relation to the physical size of the state and thus the screening length for melting.

additional discriminating measurements will be available with higher luminosities, larger acceptance, and more uniform reconstruction:

- High-p_T J/ψ over a range from p_T= 0–20 GeV/c.
- J/ψ elliptic flow (v_2) over a range of p_T= 0–10 GeV/c.
- J/ψ polarization in multiple frames, encoding information on the production mechanisms.
- Feed-down contribution to the J/ψ from the ψ' and χ_c.
- J/ψ-hadron and J/ψ-jet correlations.

To elucidate the last item, the high-p_T quarkonium must be momentum balanced, allowing one to not only look for azimuthal correlations with hadrons (as published in p+p reactions by STAR [20]), but actually look for away-side jets from the original hard scattering. In heavy ions this measurement should be feasible and may provide insight on the production mechanisms and surface/volume emission biases.

The relative acceptance with full coverage of pseudorapidity $|\eta| < 1.0$ and full azimuth $\Delta\phi = 2\pi$ compared to the current PHENIX central arm spectrometer is shown in Figure 3.27. This increased acceptance, in conjunction with much larger data samples and detector uniformity (also for triggering), will fully enable this program. Such a detector acceptance, along with high data acquisition bandwidth, could sample 50 billion Au+Au minimum bias events (see Appendix B for details). The rates and p_T reach of such measurements for the J/ψ and Υ are shown in Figure 3.28. We project being able to measure in

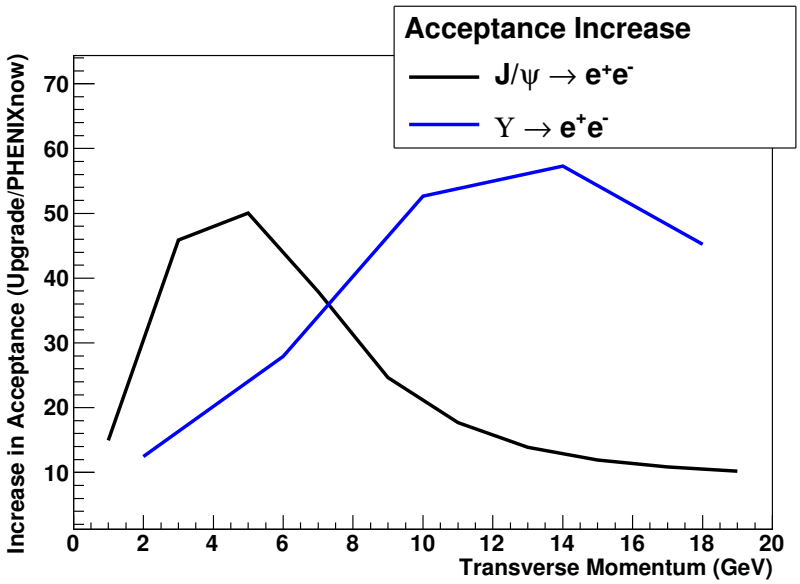

Figure 3.27: Calculation of the geometric acceptance increase with a detector with high rate and trigger-capable detectors covering $|\eta| < 1.0$ and full azimuth.

Au+Au collisions at 200 GeV of order 5000-10,000 $\Upsilon(1s)$, 1300-2600 $\Upsilon(2s)$, and 700-1400 $\Upsilon(3s)$. The relative ratios as produced in hadron-hadron collisions are $\Upsilon(2s)/\Upsilon(1s) \approx 0.3$ and $\Upsilon(3s)/\Upsilon(1s) \approx 0.15$ [21]. It is crucial to cleanly separate the three states, or else one loses key physics information.

A large advantage of the Υ states is the ability to measure all contributions directly, as opposed to current measurements of the J/ψ which has significant (of order 40%) contributions from the χ_c and ψ', and also possibly large contributions from $B \rightarrow J/\psi$ at higher p_T. The substantial increase in acceptance and rate will allow measurements of the ψ', and with displaced vertex tagging, the beauty decay contribution. The χ_c remains challenging since the decay to $J/\psi + \gamma$ results in a rather soft photon. We are studying the ability to measure this channel even in heavy ion collisions for higher p_T χ_c particles. Another potential measurement is at forward rapidity where the photon is boosted and might be measured with the FOCAL detector (detailed in Section C.2.5) or with a larger acceptance forward upgrade (detailed in Section 7.2).

In Au+Au 0-20% central collisions, where we can expect samples of 10 billion events, we expect a reach of $p_T \approx 17 - 20$ GeV/c for the J/ψ. Figure 3.29 shows the published PHENIX J/ψ R_{AA} versus p_T with four theoretical predictions for the trends at higher p_T. One sees dramatic predictions for large suppression at high p_T in the AdS/CFT calculation where the dissociation temperature changes as a function of the velocity of the quarkonia state [241, 196], in contrast with calculations without such effects but with a substantial Cronin-type p_T broadening [225, 275]. Note that the AdS/CFT calculations predict a larger suppression at higher p_T, but the exact turn on of this effect is unknown. Recent data from the STAR experiment in Cu+Cu collisions [20] offers a hint that perhaps

the opposite picture holds, where the $c\bar{c}$ pair at high p_T travels without seeing the color charges of the medium. Extending these measurements with high precision to Au+Au central collisions is of great interest. Also, the large statistical sample allows for the more differential measurements listed previously. In Figure 3.30, we show projected uncertainties for J/ψ polarization measurements in Au+Au central events. Such measurements in both p+p and Au+Au collisions will give unprecedented insight into the production and hadronization processes. In a recombination scenario, the simplest prediction would be exactly zero polarization.

We believe that this suite of measurements, in conjunction with LHC measurements, will allow us to answer the question of the color screening length scale in the QGP. We also note the possible surprises that might await in terms of a velocity dependence of the deconfinement temperature, or contrasting the large energy loss of partons via jet measurements with a possible color transparency for tightly-bound $Q\overline{Q}$ states.

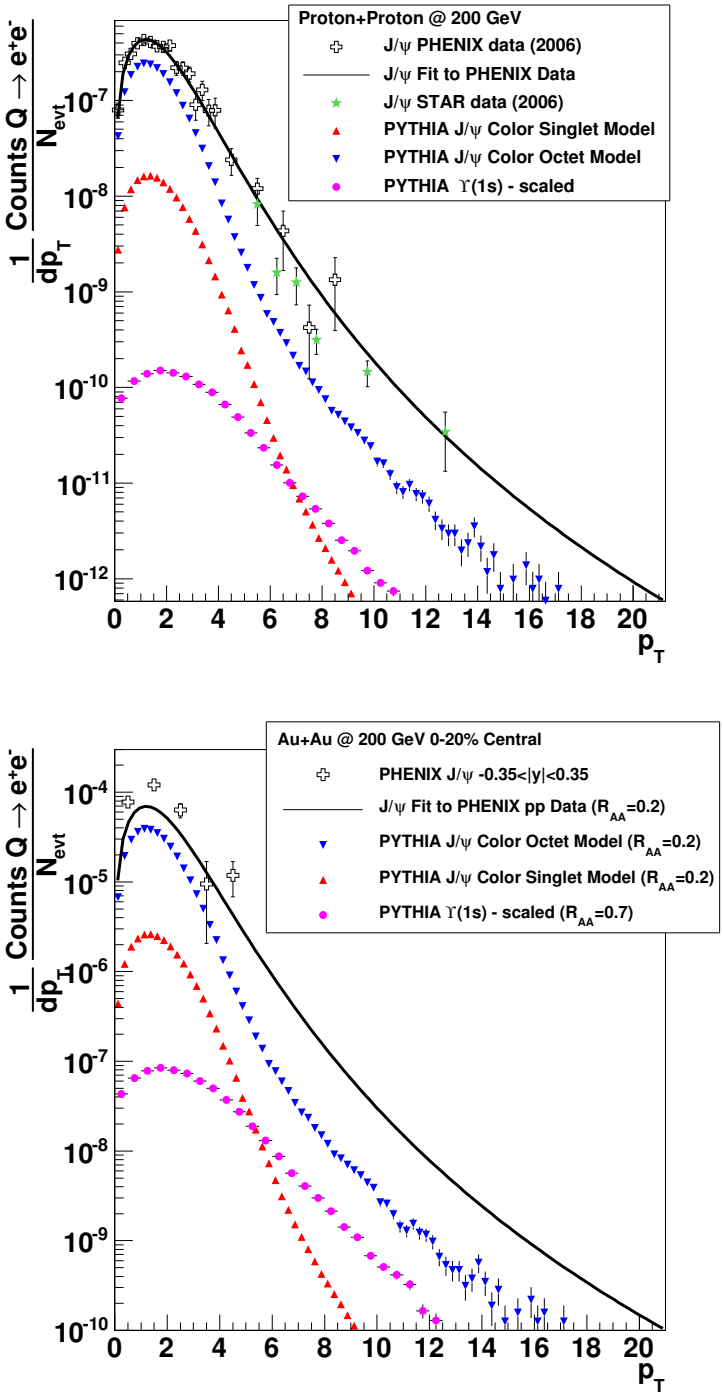

Figure 3.28: Calculated PYTHIA production rates for J/ψ and $\Upsilon(1s)$ in p+p and Au+Au collisions at $\sqrt{s_{NN}}$ = 200 GeV. Note that the Υ total cross section has been scaled to measurements at RHIC.

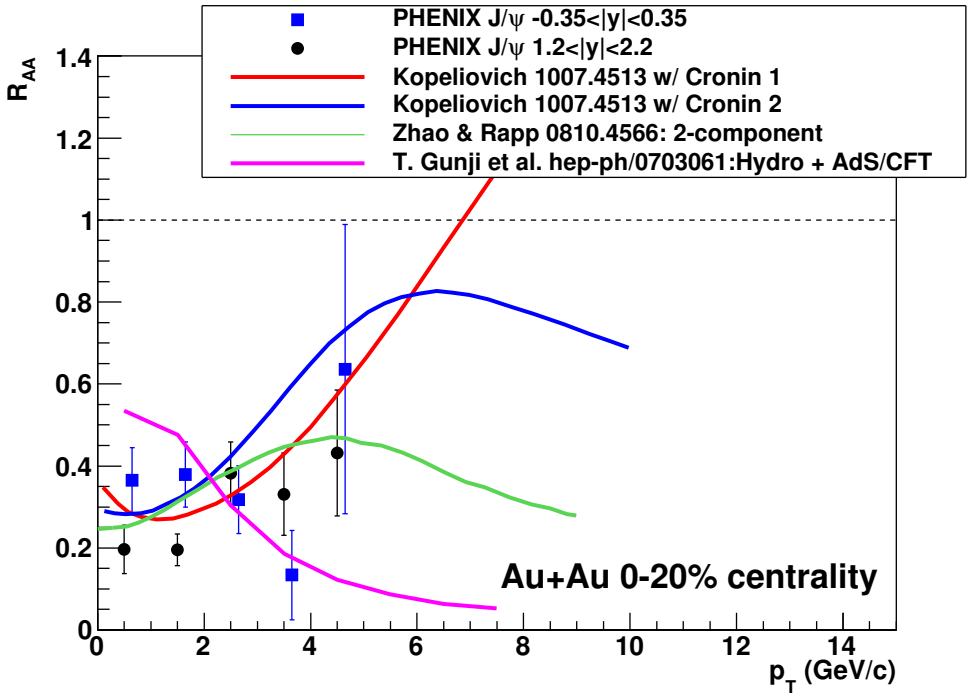

Figure 3.29: PHENIX published J/ψ R_{AA} versus p_T at mid and forward rapidity Au+Au 0-20% central collisions. Also shown are various theoretical calculations that have divergent predictions for trends at high p_T.

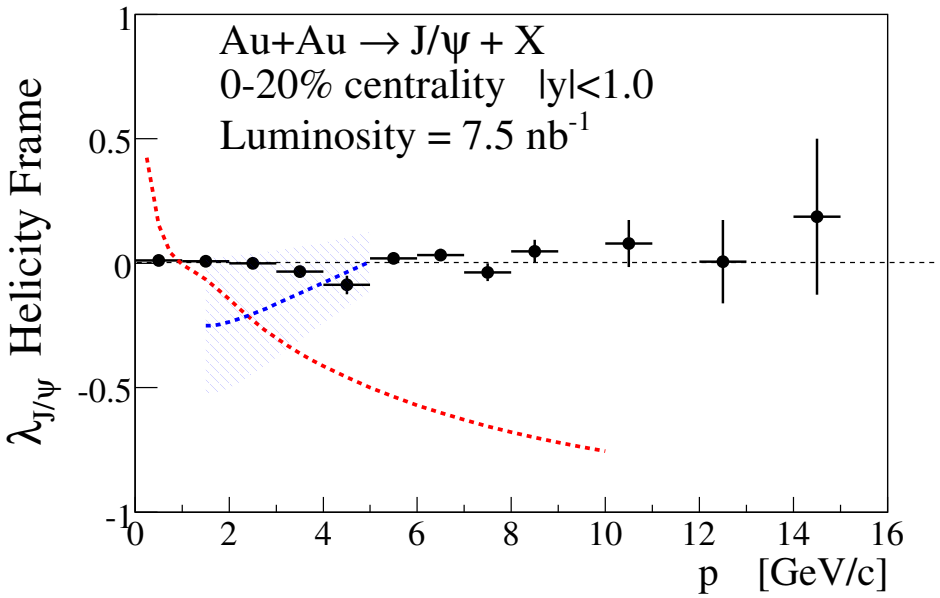

Figure 3.30: Projected J/ψ polarization uncertainties in the helicity frame for Au+Au 0-20% central collisions. The red dashed curve is a prediction for $p+p$ reactions in the S-Channel cut formalism and the blue dashed curve is a prediction in the Color Octet Model.

3.5 Early Time Dynamics

The earliest stages of a heavy ion collision involve pre-equilibrium dynamics, that cannot be described with the existing languages of perturbative, thermal, or transport QCD. A full understanding of the detailed mechanisms of equilibration and entropy production is currently lacking. The success of hydrodynamics in reproducing the observed collective flows and single hadron spectra indicates that equilibration proceeds rapidly, with the system attaining local equilibrium in less than 1 fm/c [221]. It is notable that depending on the details of pre-equilibrium evolution, longer equilibration times may be allowed – see [243] in Section IV.D for details. Although pre-equilibrium transverse motion or viscous effects may change the estimated timescale somewhat, the thermalization time required to reproduce the magnitude of hadron v_2 remains substantially shorter than can be explained by partonic rescattering with cross sections expected from perturbative QCD [252].

A number of ideas have been proposed to explain the rapid thermalization. One intriguing scenario is that instabilities in the QCD color fields, similar to the Weibel instability in QED plasmas, drive isotropization by rapid growth of color field modes due to interaction with the plasma particles in an anisotropic momentum distribution [254, 277]. Turbulent color fields should affect transport properties and govern the pre-equilibrium dynamics [107, 290]. Interaction with such locally coherent fields (or voids in the plasma density distribution) randomizes particles' momenta within a distance inversely proportional to the field strength and coupling in the plasma. Instabilities and turbulence are both predicted to increase the energy loss of jets traversing the early plasma [118].

The remarkable success of AdS/CFT in explaining the small viscosity to entropy ratio suggests that infinitely strong coupling effects on thermalization could be relevant. As the formation time of the black hole that governs the physics in the gravity dual picture is approximately 0.2 fm/c, characteristic classical oscillations of AdS-black holes and black branes may affect the approach to thermal equilibrium [117]. Such oscillations, which are nonhydrodynamic normal modes, have been predicted to produce energetic low-mass dileptons.

One of the major challenges in our field is to provide experimental observables sensitive to the details of these processes. The measurements of reconstructed light and heavy quark jets discussed above will provide detailed information on energy loss early in the collision. Furthermore, the study of thermalization of jet fragments provides experimental access to partonic thermalization mechanisms that are relevant to early times in the collision [200], as well as to energy loss in the fully developed sQGP. Electromagnetic probes are another natural observables for this physics, as they preserve information from early times. The measurement of all these probes over a broad range in rapidity is another way to test the full three-dimensional evolution and early time pre-equilibrium dynamics.

Here we discuss two approaches to gain insight into these key physics issues. First, we discuss midrapidity measurements of photons and dileptons. Second, we discuss a suite

of forward rapidity measurements to understand the three-dimensional early dynamics.

Early Time Dynamics with Photons at Midrapidity Direct photons are emitted over the entire time history of the collision. PHENIX has made a measurement of direct photons and analyzed them in the context of hydrodynamical models [43]. This was motivated by the fact that thermal radiation is dominated by the highest temperatures achieved. However, one may expect some pre-equilibrium direct photon emission, as well. A small, short-lived nonequilibrium source may yield photons with $p_T > 2$ GeV/c [120]. To determine whether the spectrum at high p_T is dominated by such radiation or from photons emitted in the later phase after equilibration and development of collective flow, we will measure v_2 for direct photons. This measurement should also provide sensitivity to any pre-equilibrium flow gradients.

The left side of Figure 3.31 shows the magnitude of v_2 expected from a three-dimensional ideal hydrodynamical calculation [239]. A substantial value is reached for photon p_T of approximately 2 GeV/c. Pre-equilibrium photons should contribute substantially also at lower p_T, where thermal photon flow is expected to be rather small. The right side of Figure 3.31 shows the difference between fragmentation and direct photon v_2 at higher p_T, illustrating the sensitivity to energy loss in measurements of direct photon v_2 [302].

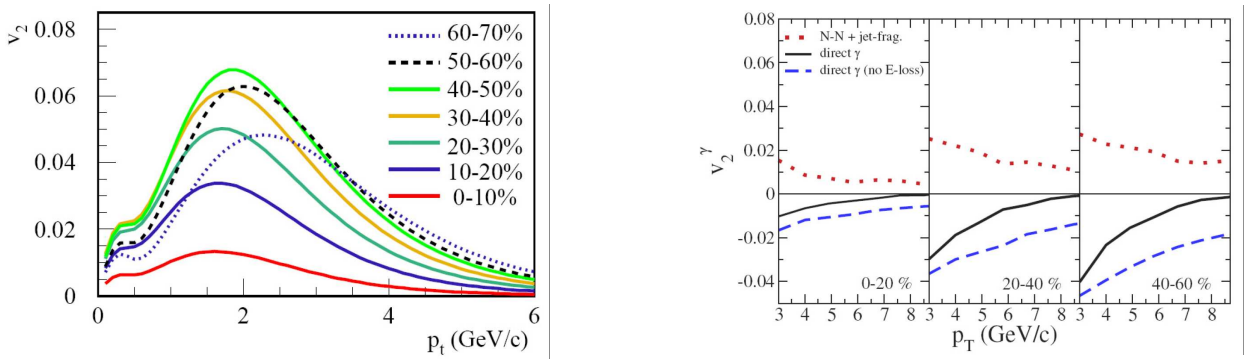

Figure 3.31: (Left) Calculation of thermal photon v_2 [239] as a function of p_T. (Right) Calculation of direct photon v_2 [302] as a function of p_T for Au+Au collisions at 200 GeV. The dotted lines show v_2 for primary hard photons and jet fragmentation, and the solid lines show all direct photons. The dashed line is all photons with without energy loss of jets.

While initial measurements of photon v_2 are currently underway, definitive answers will likely require very large data sets and enhanced acceptance for direct photons. Calorimetric measurements are most effective for $p_T \geq 2$ GeV/c, and will be greatly enhanced by the large coverage in the planned upgrade. PHENIX has already shown the ability to detect direct photons above the yield from QCD Compton scattering. Lower p_T direct photons are more difficult to measure owing to the enormous backgrounds from hadron decays. An intriguing idea to access direct photons at very low momenta is to measure two photon correlations [167] (and reviewed in [293]). The Bose-Einstein correlation allows separation of uncorrelated background photon pairs from those emitted directly

from a small source. Measurement of the HBT correlation of photons as a function of photon energy should also allow extraction of time information via the "outward" correlation function.

PHENIX has shown that moderate p_T photons are accessible by measurement of dielectrons. The data set currently in hand with the Hadron Blind Detector offers a major improvement over previous data. However, it is highly likely that measurements with additional precision and more differential study of photons will be needed to understand the pre-equilibrium dynamics. This is also true for understanding the observed dilepton excess and its possible connection to AdS oscillations. We note that electron identification at low p_T is crucial for these measurements. The electron capabilities of the planned upgrade are currently under investigation, and we envision optimizing the design of the calorimeter plus tracking system for electron measurements. A very large minimum bias sample (tens of billions of events) is crucial, to allow disentangling of backgrounds and fully utilize the large acceptance envisioned.

Exploring Early Time Dynamics at Forward Rapidity Chapter 1 describes the great advances in our understanding of hot, dense nuclear matter that have followed from measurements at RHIC. It is worth noting, however, that most of the significant evidence to date has come from measurements in the central rapidity region, which is where the most extensive collection of detectors has been fielded. Section 7.2 below describes our plans for comprehensively instrumenting the forward-angle region with tracking, calorimetry and particle ID. In this Section we outline how new and quite fundamental physics topics can be addressed if we can extend comprehensive measurement capability – full hadron tracking and PID over 2π in azimuth and a range of $\Delta\eta$ $\sim$1–2 units of pseudorapidity – to a forward rapidity range (η $\sim$1–3.5) in heavy-ion collisions.

When it was realized that a rapid pre-equilibrium transition to a locally-equilibrated state could not be achieved in a conventional parton cascade, a whole new range of mechanisms were contemplated [189]. These include the chaotic, turbulent decay of strong coherent color fields. Such mechanisms open a window onto a whole new realm of QCD which cannot be described in either perturbative or thermal language (and, interestingly, there are strong parallels to thermalization at the end of primordial inflation in the early universe [232]). Investigating this dynamical mechanism of fast, early thermalization would be a great advance for high-energy nuclear physics, beyond the goal of studying the thermalized sQGP state itself.

Staying within the hydrodynamic paradigm, we expect that the fluid which is initially created in the central rapidity range will have little or no pressure gradients in the longitudinal direction, and so all of its interesting evolution will be in the transverse directions, proceeding from its initial 2-D energy (and transverse momentum, if any) density profile. Such a 2-D profile can be expected to follow from the local 2-D projected density of participant nucleons, or gluons. This follows from very general grounds of causality: if the initial energy deposition and thermalization time is fast, i.e. $< 1\text{fm}/c$, then the separate

transverse patches of this size will be causally disconnected and can only form their initial density based on the local, 2-D projected information; see the blue and yellow regions marked in Figure 3.32. Thus we can reasonably predict the shape of the 2-D initial density profile of the central region fluid without any knowledge of the stopping or thermalization mechanisms, and this has enabled the field of 2+1D hydrodynamics to develop with such great success. By the same token, however, measuring the 2+1D evolution of the central region fluid may not help to constrain the initial stopping or thermalization mechanisms very directly.

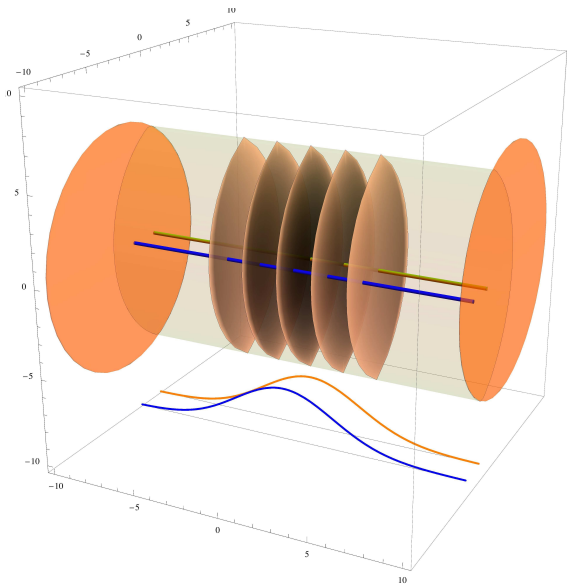

Figure 3.32: A 3-D conception of the initial condition at the start of hydrodynamics; local energy densities are shown on surfaces of constant rapidity at a given proper time, including the effects of longitudinal momentum conservation. The blue and yellow tubes indicate regions which are initially causally disconnected and so have independent patterns of initial energy deposition; the profiles indicate one pattern which conserves longitudinal momentum.

In contrast, the *longitudinal* profile of the initial deposition of energy, and other conserved quantities, within each local transverse patch should be intimately related to the stopping mechanism. And, unlike the transverse profile there is no obvious or generally accepted picture for what that mechanism should be. The fully 3D initial energy deposition forms the initial condition for fully 3+1 dimensional hydrodynamics at RHIC; this is a decidedly under-explored field to date. Initial conditions over 3D are modeled in a variety of ways, including some based on a specific picture such as the CGC description [203], while some are more schematic with a few free parameters [263], and others give detailed attention to fluctuations [199].

As shown in Figure 3.32, conservation of longitudinal momentum alone could lead to a decidedly nontrivial shape for the initial energy density in three dimensions; such a

complex shape may then evolve to produce a highly nontrivial flow pattern at forward rapidity, including the effects of longitudinal hydrodynamics. Also, the presence of fluctuations in the initial longitudinal profile at each patch is a fundamental feature of the mechanism, which would have manifestations both within a forward rapidity range and in long-range correlations across wide rapidity separations (see for example [180]).

There is an important potential distinction between the process of initial energy deposition into any particular 3-D volume, which we call *stopping*, and the process by which that local energy density becomes isotropized to the extent that pressure can be defined, which we call *local equilibration* or *local thermalization*. In principle the two could be described by different languages; for example, the initial stopping could occur through the formation of strong, coherent color fields as in the glasma scenario, which then decay [189] locally in a turbulent or chaotic manner to produce local thermalization of the energy density. However, whatever the proper language turns out to be, once it is developed it seems likely that the two stages will not be so distinct. Both stopping and thermalization are forms of fast entropy generation, in which energy is partitioned into new modes, and the two stages must fit compatibly together. So, while the theory of these early-time processes is not nearly well enough developed to say for certain, we can presume that a program of constraining the initial stopping/deposition of conserved quantities will also provide key information to constrain the thermalization mechanism.

The other main tool for diagnosis of the initial density distribution will be jet-medium interactions. In the preceding Sections we have described our program for a new era of jet-medium interaction studies, centered on detection and reconstruction of full jet objects (as opposed to just leading hadrons or hadron pairs) with new detectors in the central rapidity region. If a similar capability can be extended to measuring A+A collisions in the forward rapidity regions, however, then an even richer field of study becomes accessible. At midrapidity the scattered partons encounter a relatively simple medium, with a fairly well-defined 2-D initial distribution and complex evolution limited to the transverse directions; while partons scattered at forward rapidity may encounter a more complicated 3-D initial distribution which is also undergoing a significant evolution in three dimensions [266]. See Figure 3.33 for an illustration of how the observation of the azimuthal dependence of jet quenching as a function of rapidity can directly constrain the nontrivial 3-D initial condition which follows from the initial deposition of longitudinal momentum across transverse position in a CGC picture [51, 50]. Extending this kind of investigation with our new full jet program at forward rapidity holds great promise to learn about both early-time dynamics and jet-medium interactions in a new setting.

Initial measurements at forward rapidity in A+A collision at RHIC already exist. PHENIX has measured muons from heavy flavor decays and some single hadrons in the existing muon arms, which will be enhanced in the current upgrade program (see Appendix C.2). The PHOBOS experiment has measured patterns of charged particle production over a wide range of rapidity and full azimuth, but without momentum reconstruction or particle identification; while the BRAHMS experiment has done the complement, measuring single hadron production with particle identification over a wide range

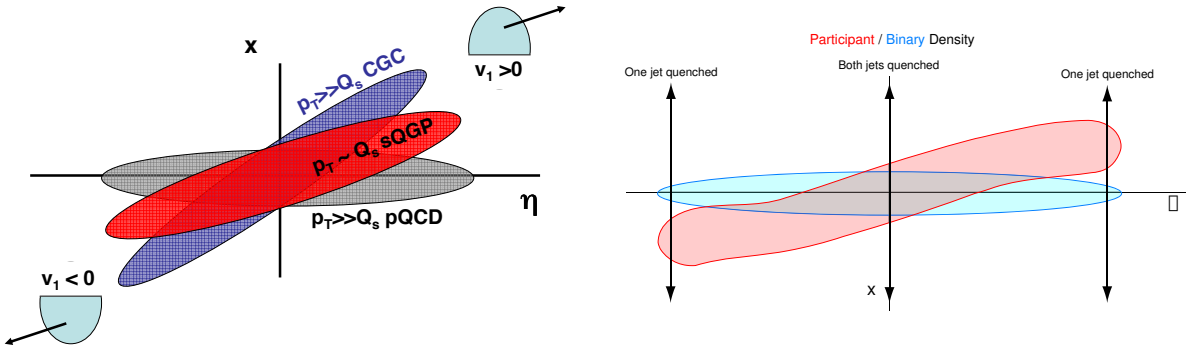

Figure 3.33: (left) Illustration from [51] of the "twisted" initial distribution of partons as drawn in the x-η plane; the shape arises from a nontrivial initial deposition of longitudinal momentum across position, following a color glass condensate description of the incoming nuclei. (right) Illustration from [50] showing how azimuthal jet quenching measurements at different rapidities could reveal/diagnose the early energy density deposition pattern.

of rapidity but only a very narrow acceptance and limited statistics.

These measurements have been intriguing in many ways that are related to the physics agenda described in this Section. However, to really carry out the proposed program of diagnosing the mechanisms of initial stopping and thermalization as described here, we will need to go beyond the previous experiments and measure tracked and identified hadrons over full azimuth and simultaneously over a substantial range in rapidity ($\Delta\eta$ ~1–2 units) at forward angles (η ~1–3.5). The reasons are that the early-time program will require 1) Identified single hadrons to map back to true rapidity and to identify/track baryon density as one conserved quantity, 2) Momentum reconstruction to diagnose the final state as consistent with an hydrodynamical picture (or not); 3) Full azimuthal coverage in order to reconstruct correlated pairs, and to distinguish them as being from flow or hard scattering sources; 4) Full azimuth at forward angles simultaneously with midrapidity in order to study correlations and fluctuations in the longitudinal energy deposition pattern; 5) A sizable range in (pseudo)rapidity in order to see the pattern of longitudinal flow and to reconstruct jet objects and their constituents, including heavy flavor production.

Making such comprehensive measurements at forward angles in A+A collisions at RHIC is very challenging. We are currently exploring occupancy studies to understand how far forward in angle, and up to what nuclear size A and centrality all or some of these measurements will be possible.

3.6 Cold Nuclear Matter and low-x Physics

During the next five years (2010-2015), we expect major advances in our understanding of cold nuclear matter effects and the dynamics of low-x and high-x partons in large nuclei. As described in Section 2.4, PHENIX measurements of open and closed heavy flavor with the FVTX and direct photons with the FOCAL will probe gluons down to $\langle x \rangle \approx 5 \times 10^{-3}$. Additional measurements from the STAR experiment at RHIC, fixed target experiment E906 at Fermilab [278], and e+A studies at Jlab (see for example [283]), along with theoretical advances will give a more coherent picture of the dominant cold nuclear matter physics. We believe that the next major advances require the utilization of multiple channel measurements that probe an order of magnitude lower in x to study the evolution of these partons as a function of x and Q^2 while deep in the saturation regime.

Proton(deuteron)-nucleus collisions at collider energies allow the study of multiple interactions of hadrons and partons passing through spatially extended QCD systems. Systematic studies with nuclei of varying size (and impact parameter) are revealing space-time properties of the strong interaction, such as the time scales and microscopic mechanisms of hadronization. The heaviest nuclei at high energies access the gluonic properties of matter, such as gluon saturation—which is a fundamental prediction of QCD [255, 194, 236, 192].

Here we discuss the physics gained by extending the PHENIX measurement capabilities down to two degrees from the beam axis (a detector upgrade discussed in Section 7.2). This upgrade would include larger coverage in existing channels (open heavy flavor, heavy quarkonia, direct photons, π^0, η) as well as opening new channels via Drell-Yan and photon-jet and jet-jet correlations (with fully reconstructed jets). With these multiple measurements, each probing the fundamental parton distributions and other cold nuclear matter effects in a different way, quantitative discriminating power can be achieved to identify the underlying dynamics for these effects. Only through a fundamental understanding of this physics, as opposed to a parameterization, can we understand the full time evolution of heavy ion collisions with high accuracy. Cold nuclear matter physics is quite rich and we are actively exploring many new ideas. Here we detail a few areas where specific new measurements will make major advances in our knowledge.

Measurements from E665 of the inclusive structure function F_2 in deep inelastic scattering off of nuclear targets reveal a substantial shadowing effect (suppression of $F_2(A)/F_2(D)$) that increases for lower x and appears to level off for $x < 5 \times 10^{-3}$ [26]. The experimental results are shown in Figure 3.34 along with two theoretical calculations with very different underlying physics. The left panel shows a calculation including dynamical high twist shadowing [307] and the right panel shows a calculation including color transparency and coherent length effects (with and without additional gluon shadowing) [223]. One simple framework for thinking about the results is that the longitudinal extent of the partons increases as their momentum decreases. Thus, for partons with $x < 0.1$ the size becomes larger than the spacing between nucleons in the nucleus and shadowing effects

may start, and then for $x < 0.003$ the size becomes larger than the entire nucleus and one might expect the maximum coherence effects. However, interpretation of the data in terms of gluon saturation is limited because for $x < 10^{-3}$ the average $Q^2 < 1$ GeV^2 and hadronic vector meson dominance and higher twist effects are important. Extending these measurements with $p(d) + A$ collisions at RHIC that are sensitive to $x \approx 10^{-3}$ but with a Q^2 scale set by heavy flavor pair production, for example, would be very elucidating.

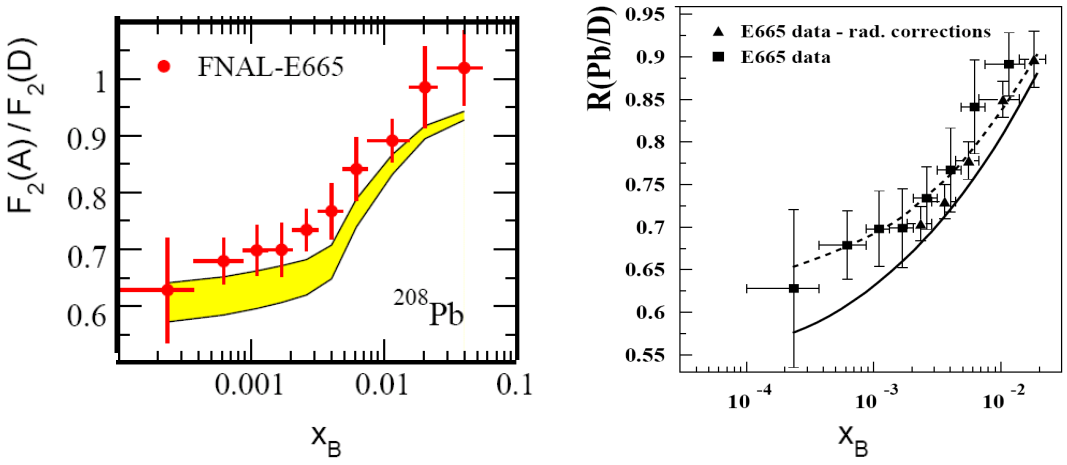

Figure 3.34: Data from E665 compared with (left) a shadowing calculation from Vitev [307] and with (right) color transparency and coherence calculations from Kopeliovich [223]. In the right panel, the solid (dashed) curve is with (without) the contribution from gluon shadowing.

Measurements of the nuclear dependence at small x for the Drell-Yan process provide crucial information on the shadowing of anti-quarks in the nucleon sea. However, other cold nuclear matter effects can also occur for the Drell-Yan process, e.g. initial-state quark energy loss, that can complicate the extraction of the shadowing effects. These two effects, shadowing and energy loss, have different dependencies on collision energy, and as has been the case for quarkonia studies (see Section 2.4 and Figure 1.14), measurements at multiple energies can be invaluable in separating the different effects. A precise measurement at RHIC energies (specifically a range of different RHIC energies), along with the existing E866/E772[75, 305] and expected E906 [278] measurements would provide this needed discriminating power. If the dominant physics is gluon saturation, one wants to know the relevant scales and relate these in a fundamental way for measurements with different colliding systems.

A very recent exciting development is that, within well-defined approximations, the saturation scale for gluons can be related to the gauge-invariant Transverse-Momentum-Dependent (TMD) gluon distribution [177] in a nucleon embedded in a nucleus [237], connecting to the saturation scale via a dipole approximation. Within the dipole picture, the saturation momentum has been shown to be equal to the transverse momen-

tum broadening for the Drell-Yan and quarkonia production processes on a nucleus [224]: $Q^2_{sat}(b,E) = \Delta p^2_T(b,E)$, where b is the impact parameter and E is the energy of the parton propagating through the medium. The physical origin of the broadening is the interaction of a propagating parton with the transverse gluonic field in the medium through gluon bremsstrahlung. The probability of gluon radiation is proportional to the gluonic parton density of the medium, and thus p_T broadening is a direct measure of the saturation phenomenon. The value of Δp^2_T has been measured in a small number of experiments where the lab-frame parton energies range from 2 GeV to 270 GeV. Interpretation of the observed hadron broadening Δp^2_T in terms of parton broadening Δk^2_T requires taking into account the nature of the propagating entity (quark, gluon, photon, dilepton), the hadron species measured in the final state, and kinematic factors. The magnitude of hadron broadening in these experiments has ranged from $\Delta k^2_T \sim 0.02$ GeV^2 for the lightest nuclei at the lowest energies to $\Delta k^2_T \sim 0.5$ GeV^2 for the heaviest nuclei at the highest energies, see Figure 3.35. The authors of [124] suggested to measure the suppression of dilepton pairs

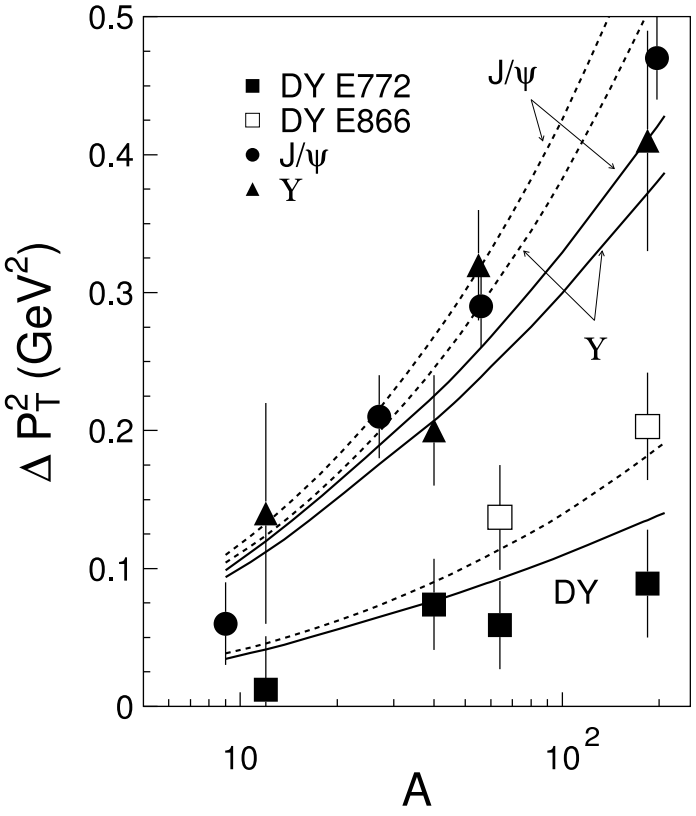

Figure 3.35: Broadening in Drell-Yan reactions on different nuclei as measured in the E772 (closed squares) [264] and E866 (open squares) [305] experiments respectively. Broadening for J/ψ [264, 76] is shown by circles and triangles respectively. The dashed and solid curves correspond to the predictions without and with the corrections for gluon shadowing.

in the forward direction in $p(d) + A$ compared to p+p at low p_T to study the gluon saturation effects. It is also worth pointing out that the authors of [193] suggest Drell-Yan at

forward rapidity at LHC in p+p collisions to study saturation effects. The study of saturation effects in e+A collisions is one of the flagship measurements proposed for EIC (see Chapter 8). It will be extremely important to to prove the universality of this phenomena to observe it in different interactions.

Drell-Yan measurements in $p(d) + A$ collisions at RHIC at very forward angles are optimal for addressing these physics questions. Initial studies for the feasibility of Drell-Yan measurements at rapidity up to $y = 4$ are discussed in the context of the measurement of transverse single spin asymmetries in Chapter 6 and Section 7.2).

Here we demonstrate what is required to achieve an order of magnitude increase in x coverage using the J/ψ and direct photons as two examples. Similar x coverage is achieved for open heavy flavor, Drell-Yan, and jet measurements within the proposed increased acceptance. In Figure 3.36, we first show the increase in x_F coverage that is obtained through an upgrade that extends the θ range of our acceptance. For projected future deuteron(proton)-nucleus luminosities, the largest x_F values can be increased from 0.3 (the current coverage of the PHENIX muon spectrometers) up to values as high as $x_F = 0.75$. These large x_F values also open the possibility to investigate the contributions to heavy quarkonia as well as to open heavy flavor from intrinsic charm [140]. Shown in Figure 3.37 are predictions for the percentage contribution to J/ψ production in p+p reactions for contributions from $g + c \rightarrow J/\psi + c$ that indicate large effects at forward rapidity (where J/ψ rapidity $y = 3.5$ corresponds to $x_F = 0.5$). The authors note that a dedicated study of J/ψ +c in $p(d) + A$ collisions provides a unique way to study shadowing effects as well as heavy-quark energy loss.

For the J/ψ the corresponding x_2 and x_1 coverage for different ranges in x_F are shown in Figure 3.38. If one compares the x_2 values in Figure 3.38 to the gluon shadowing shown for EKS09 in Figure 1.13, it is seen that this allows one to probe deep into the shadowing/saturation regime.

As a second example, a direct photon measurement at very forward rapidity also probes gluon dynamics at low-x in the nucleus. The gluon x_2 values probed for several pseudorapidity ranges with a photon detector covering the 2–37 degree range are shown in Figure 3.39. The corresponding quark x_1 values are also shown in Figure 3.39. This measurement would extend those we anticipate will be made by the FOCAL upgrade (described in Appendix C.2.5), and equally importantly, with a larger acceptance and full jet reconstruction capability, would be able to select a narrower range in x enabling one to map out the evolution of the parton dynamics in much more detail.

At the same time that the acceptance opens a new window to low-x parton dynamics in the Au nucleus, the range in high-x partons in the deuteron(proton) projectile is also significantly extended – as shown in Figure 3.39. One can access this physics via heavy quarkonia, open heavy flavor, and Drell-Yan. Another exciting way to access the physics of high-x partons in nuclei is through the production of W bosons. At previous luminosities and with the current acceptance of the PHENIX spectrometer, making $W \rightarrow e^{+/-}$ measurements in $p(d)$+Au or Au+Au collisions at $\sqrt{s_{NN}}$ = 200 GeV have not been con-

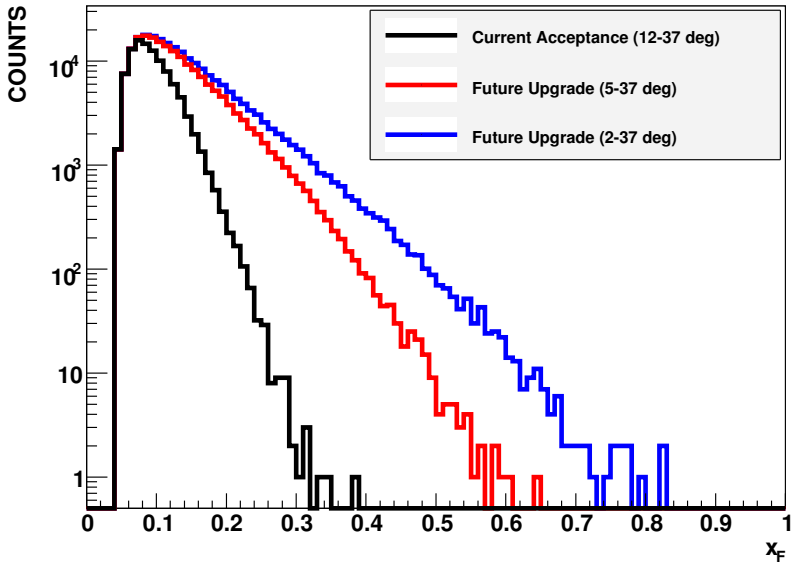

Figure 3.36: Coverage in x_F for $J/\psi \rightarrow l\,l$ given different allowed angular ranges for the leptons. The acceptance for the current muon arm, 12-37 degrees, is compared to acceptances which extend down to angles of 5 or 2 degrees.

sidered possible. Within a high rate and trigger capable acceptance of $|\eta| < 1.0$ and full azimuthal coverage, with projected luminosities we can measure hundreds of $W \rightarrow e^{+/-}$ with an electron(positron) $p_T > 20$ GeV/c. This is particularly interesting in $p(d)$+Au reactions because the W can only be produced through the interaction of very high x quarks and anti-quarks. We show a PYTHIA simulation with the above kinematics and plot the x_1 and x_2 distributions for two different pseudorapidity selections in the left panel of Figure 3.40. This x range is in the domain of the EMC effect for nuclear modified parton distribution functions (nPDFs). Measurements at this large Q^2 would be very interesting. Additionally, since at RHIC we have a well developed method for $p(d)$+Au centrality selection, one can do a first measurement of the geometric dependence of the EMC effect within large nuclei. In the right panel of Figure 3.40 we show the expected nuclear modification factor $R_{p\mathrm{Au}}$ for $W \rightarrow e^{+/-}$ using the EPS09 nPDFs (red curve) and the current theoretical range of uncertainties within the EPS09 framework (as dashed blue lines). The statistical significance of such a W measurement in $p(d)$+Au will be a challenge to discriminate between small differences in the nPDFs. However, if calculations of initial state energy loss for the high x parton in the deuteron(proton) projectile are correct, one should observe a very substantial suppression (perhaps with $R_{p\mathrm{Au}} < 0.5$) since the x distribution is falling steeply in this range. These measurements are complementary to similar measurements at midrapidity via high p_T direct photons and jets, but with different systematics and control variables.

The increased acceptance of sPHENIX at central and forward rapidity opens new avenues

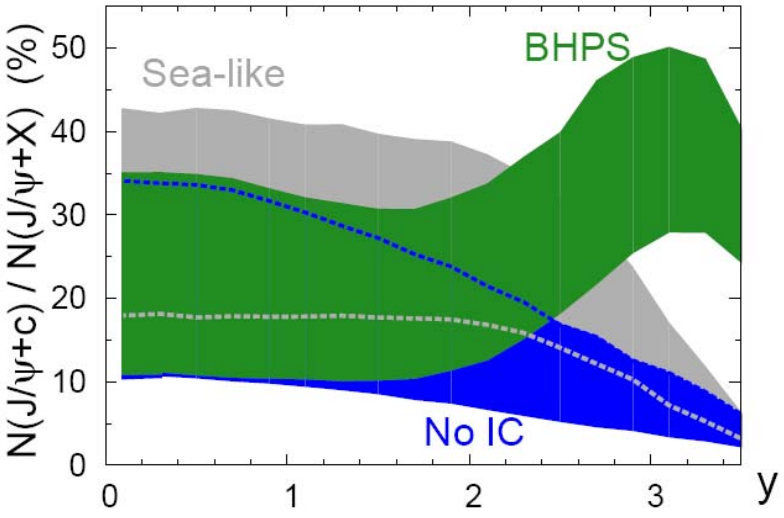

Figure 3.37: Fraction of J/ψ produced in association with a single c-quark relative to the direct yield (NLO*) as a function of rapidity for three models of $c(x)$: within Intrinsic Charm (No IC), sea-like and BHPS [140].

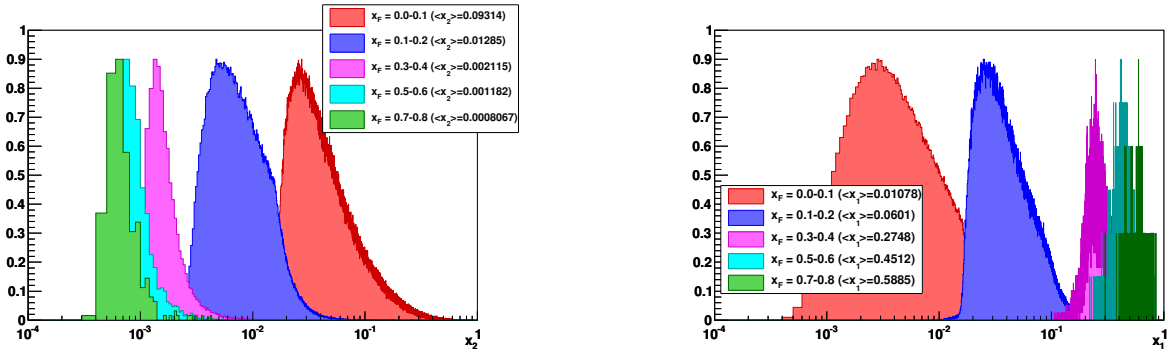

Figure 3.38: (left) Coverage in x_2 (the gluon momentum fraction in the nucleon of the nucleus) for $J/\psi \rightarrow l\ l$ for different x_F ranges. The average x_2 for each is given in parenthesis in the legend box. (right) Similarly for x_1 (the gluon momentum fraction in the nucleon of the projectile.

to study with many different probes, i.e. Drell-Yan, open and closed heavy flavor and identified hadrons, in a wide range in x and x_F, saturation and the space-time properties of the strong interaction, such as the time scales and microscopic mechanisms of hadronization. These measurements find a natural continuation in the measurements in e+A collisions at eRHIC described in Section 8.3, which will give the unique opportunity to study with one apparatus the universality of these processes.

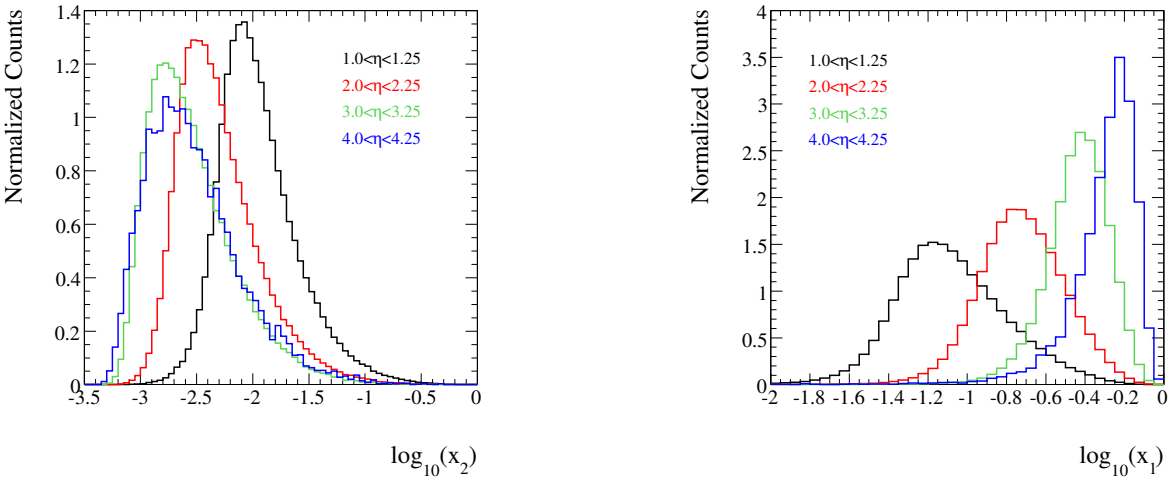

Figure 3.39: (left) Coverage in x_2 (the parton momentum fraction in the nucleon of the nucleus) and (right) x_1 (the parton momentum fraction in the proton or deuteron) for direct photons at different forward rapidities.

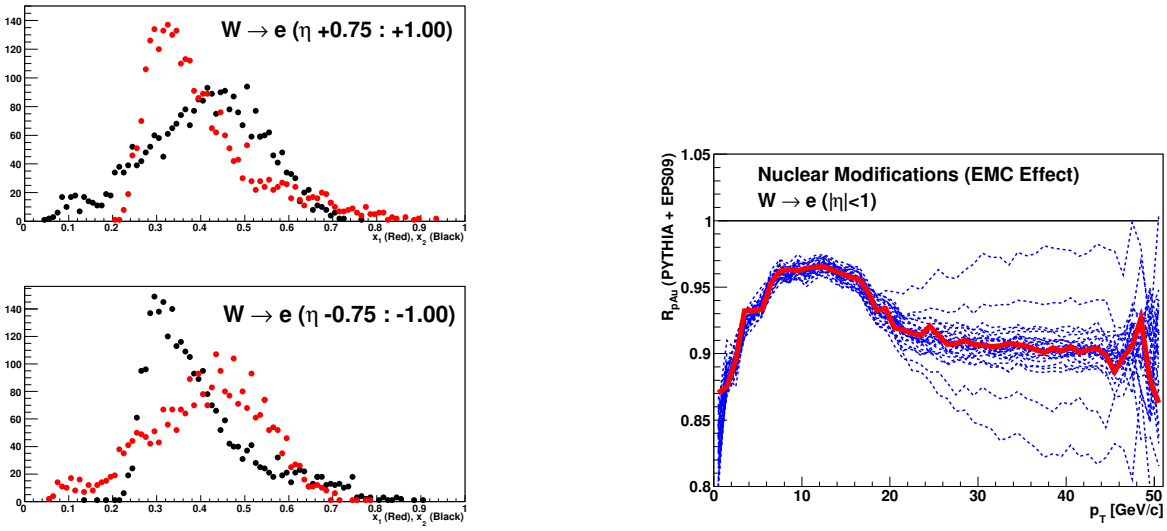

Figure 3.40: x_1 and x_2 distributions for two different pseudorapidity selections (left); and expected nuclear modification factor $R_{p\mathrm{Au}}$ for $W \rightarrow e^{\pm}$ using the EPS09 nPDFs (red curve) and the current theoretical range of uncertainties within the EPS09 framework (dashed blue lines).

Chapter 4

Nucleon Structure Physics: Current Understanding

QCD, the theory of the strong force that was proposed in the 1970s and is now well established, describes one of the fundamental forces in nature in terms of its point-like degrees of freedom: quarks and gluons. Much of the intricacy and challenge of QCD lies in its emergent properties of confinement and asymptotic freedom, and as we have sought to understand the visible matter of the universe in terms of the quarks and gluons of QCD over the past several decades, a rich picture has come to light, with several overarching questions remaining that have been and continue to be addressed by the RHIC $p+p$ program:

- What is the nature of the spin of the proton?
- How can we describe the multidimensional landscape of nucleons?
- How do quarks and gluons hadronize into final-state particles?

Much of our present knowledge of nucleon structure comes from deep-inelastic lepton-nucleon scattering (DIS) experiments, with a great wealth of data on the unpolarized structure of the proton available from the electron-proton collider, HERA, which covered a very wide range in partonic longitudinal momentum fraction (x) and four-momentum transfer squared (Q^2) [13]. From HERA we have learned that quarks carry 50% of the momentum of the proton, with the other half carried by gluons, which dominate for $x < 0.1$ [219]. In DIS, the virtual photon emitted by the lepton couples only to the quarks in the nucleon; thus, sensitivity to gluons is obtained via scaling violations, requiring measurements over a broad range of Q^2 for a given x, or via the photon-gluon fusion process.

Despite all that has been learned through DIS measurements, studying nucleon structure in a wide variety of reactions is essential in order to piece together a complete picture.

Hadron-hadron interactions offer several advantages. Direct access to gluons is possible through parton-parton scattering, making measurement of the spin contribution of the gluon to the spin of the proton a key component of the RHIC program. Clean access specifically to antiquarks is also possible in hadron-hadron collisions. Flavor separation of the light antiquark helicity distributions via W production, enabled by the very high-energy polarized proton beams at RHIC, will be a primary focus of the program in the next several years, with first results just released by both PHENIX and STAR. The Drell-Yan process is yet one more means of cleanly accessing antiquark distributions in hadron-hadron collisions, and we expect Drell-Yan to become an increasingly important part of the RHIC $p+p$ program in the future. An excellent historical example of the unique contribution that Drell-Yan measurements can make to understanding nucleon structure was the discovery of the SU(3) asymmetric sea via unpolarized Drell-Yan production with the E866 experiment [299], published in 2001 after a decade of HERA running and more than 30 years after the discovery of quarks in lepton scattering experiments.

Comparing observations from DIS and hadronic interactions also allows us to test the assumptions of *universality* across processes in describing hadron structure and hadronization within the framework of perturbative QCD (pQCD). In the high-energy limit of pQCD, calculations in which the quarks and gluons are treated as nearly free particles moving collinearly with their parent hadron, and in which hadronic interactions are assumed to factorize into a) parton distribution functions (PDFs) within the initial-state hadron, b) partonic hard-scattering cross sections, and c) fragmentation functions (FFs) describing the hadronization of the scattered parton, have had tremendous success in describing hadronic cross sections at high energies over the past several decades. The collider energies available at RHIC put high-p_T reactions comfortably within a regime described by factorized pQCD, as can be seen in Figure 4.1. It is worth noting that the relevant perturbative scale in DIS is Q^2, while in hadron-hadron interactions it is the square of the transverse momentum (p_T^2) of the produced jet or particle, and while both Q^2 and x are known in DIS, in hadron-hadron measurements the p_T of the produced particle is correlated with x, but a given p_T bin typically samples from a range of x values (as illustrated in Figure 5.5 later in this document).

At high energy, there remain two fundamental aspects of the nucleon partonic structure which are rather poorly determined by experiment. One is the nature of the nucleon spin; the other is the nature of the quark and gluon motion and spatial distributions transverse to the light-cone momentum direction.

In this Chapter we summarize the current understanding as follows. Section 4.1 reviews the longitudinal spin asymmetry measurements from PHENIX, shows the impact of data from both PHENIX and STAR upon global fits of Δg(x), and gives a first view from RHIC of the flavor separated quark helicity distribution; Section 4.2 summarizes insights regarding the polarization of quarks with nucleon spin transverse to the light cone; Section 4.3 discusses transverse momentum dependent parton distribution functions (TMDs); and Section 4.4 provides a brief summary of the program at facilities other than RHIC.

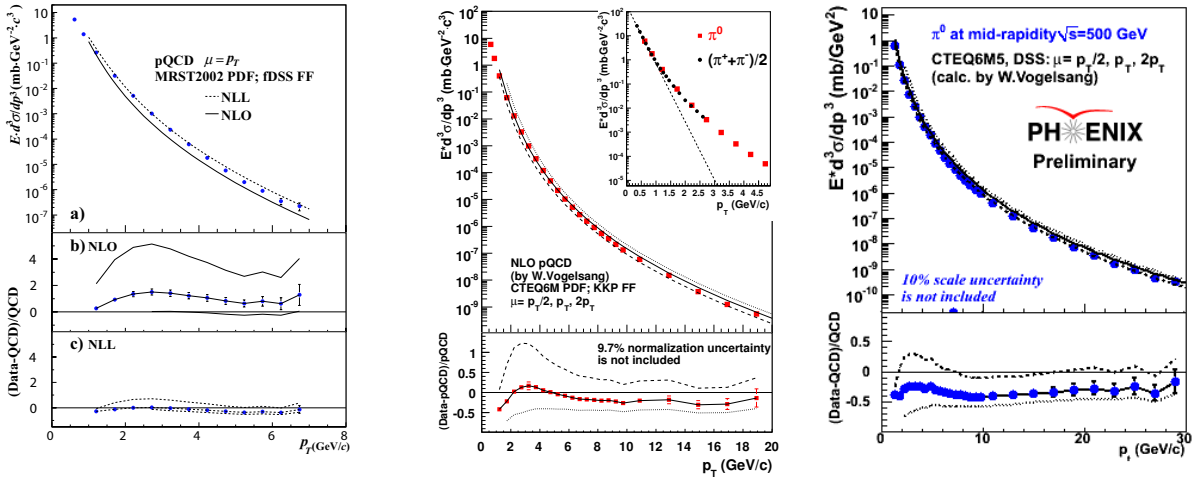

Figure 4.1: Comparisons to QCD calculations of π^0 cross sections at midrapidity measured by PHENIX at $\sqrt{s} =$ (left) 62.4 GeV, (middle) 200 GeV, and (right) 500 GeV.

4.1 Nucleon Helicity Structure

At present, we have a limited set of high-energy data which tell us the alignment of the quarks along the light-cone momentum direction as a function of the momentum fraction. These distributions are poorly known at both high and very low momentum fraction, and the range in Q^2 explored is much narrower than in the unpolarized case due to the fact that there have only been polarized fixed-target DIS experiments thus far [68, 79, 96, 16, 49, 109]. The polarized lepton scattering experiments have made it clear that the quark spins only contribute about 30% to the nucleon spin. The gluons, which make up roughly 50% of the total (unpolarized) partonic momentum distribution, may be expected to carry a significant fraction of the nucleon spin, but this distribution could previously only be determined by scaling violations in inclusive DIS over the limited range in Q^2 of available data, which give nevertheless a relatively precise determination of $g(x)$ [131]. The RHIC spin program, with high-energy polarized $p+p$ collisions, offers direct access to the gluons inside those polarized protons. Measurements using the existing PHENIX and STAR detectors [40, 37, 18] have already constrained the polarized gluon distribution to be small in the x_g range sampled, much smaller than a number of predictions made in the 1990s. Figure 4.2 shows several predictions for $\Delta g(x)$ from the period in which the RHIC spin program was being designed.

Through run-9, PHENIX has recorded a total of approximately 25 pb^{-1} (summed over run-5, run-6, and run-9) of longitudinally polarized $p+p$ collisions at 200 GeV. The double-helicity asymmetry in neutral pion production has been the flagship measurement by PHENIX sensitive to ΔG, given the abundance of pions and the excellent PHENIX capability to trigger on the π^0 decay to two photons. Figure 4.3 shows the current status of A_{LL} for neutral pion production at $\sqrt{s} = 200$ GeV through run-9.

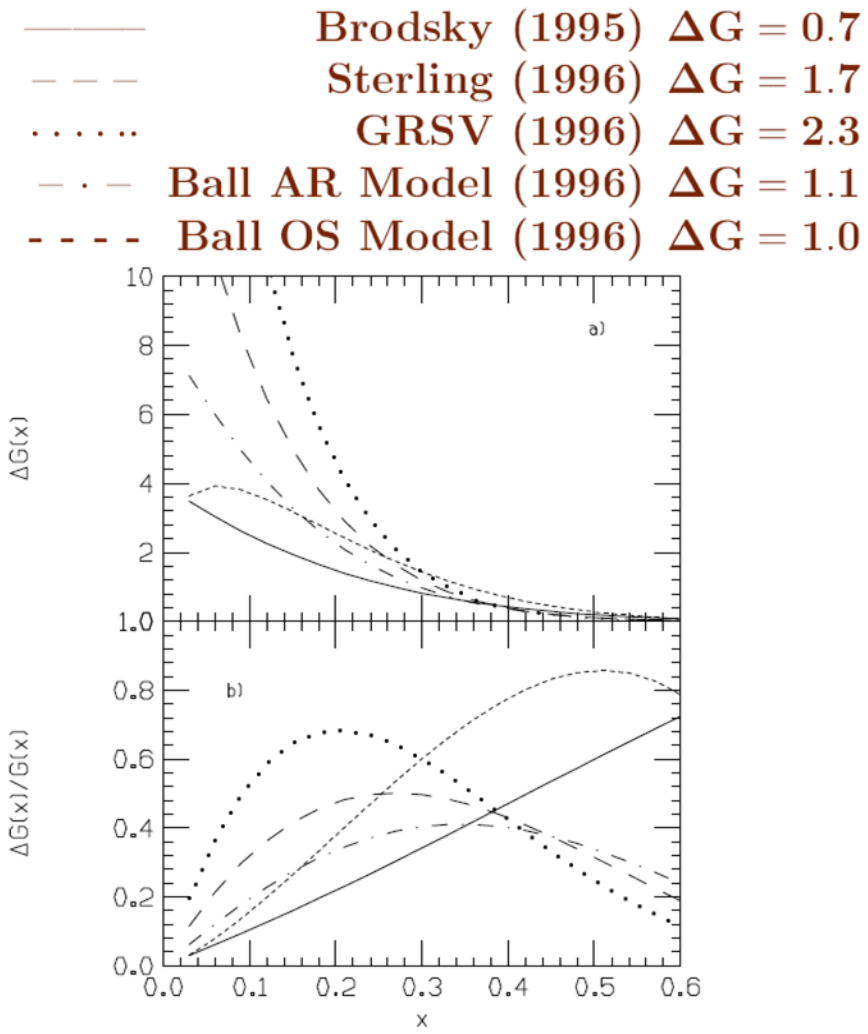

Figure 4.2: Historical expectations and predictions for $\Delta g(x)$.

As the available luminosity has increased, in particular with the 2009 data set, other probes have become increasingly interesting. Preliminary results for A_{LL} in η meson production at $\sqrt{s} = 200\,\text{GeV}$ are shown in Figure 4.4. The theory curves assuming different gluon polarizations were made possible by the recent parametrization of the η fragmentation functions for the first time, including PHENIX η cross section data from 2003 and 2006 in addition to world e^+e^- data. We note that PHENIX neutral pion cross section data had been used earlier to improve constraints on fragmentation functions for pions [168], in turn reducing uncertainties on ΔG extracted from pion A_{LL} measurements. In addition to the neutral pion results, A_{LL} for charged pions has been measured by PHENIX and is shown for run-5, run-6, and run-9 combined in Figure 4.5. While produced as copiously as neutral pions, charged pion measurements at PHENIX have more limited statistics due to triggering capabilities. However, the charged pion asymmetries are of particular interest because the ordering of the three pion species asymmetries provides sensitivity to the

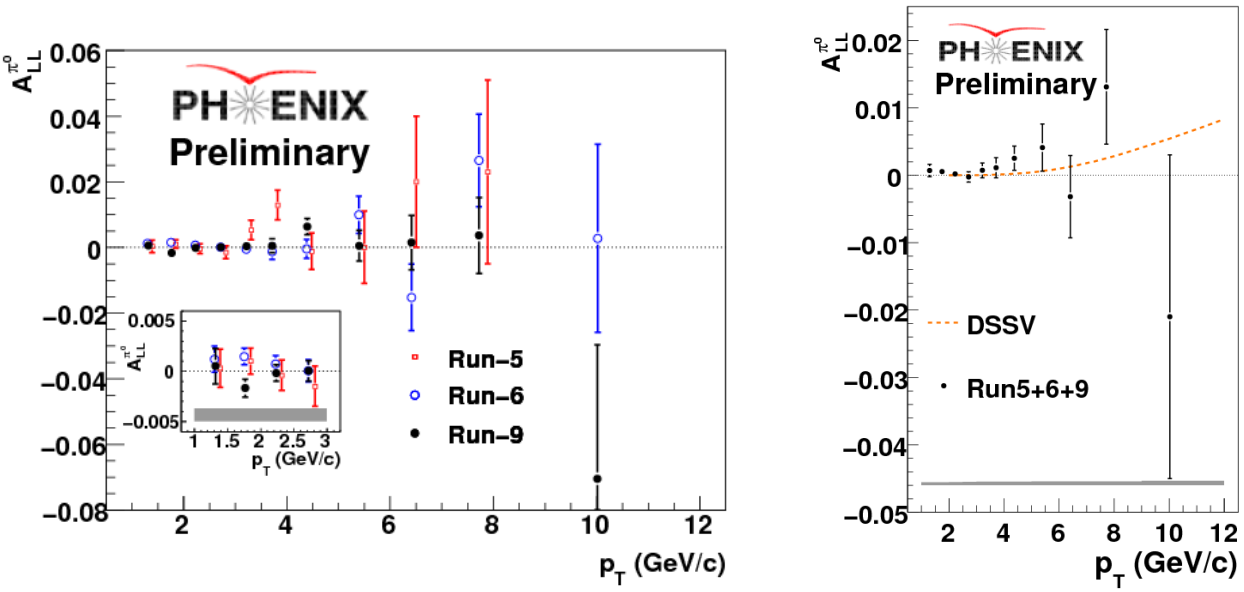

Figure 4.3: The double spin asymmetry vs p_t for inclusive π^0 production at $\sqrt{s} = 200\,\text{GeV}$ compared to the asymmetry using the polarized PDFs from DSSV for (left) each of the years 2005, 2006, and 2009 and (right) the combined 2005–2009 results.

sign of ΔG.

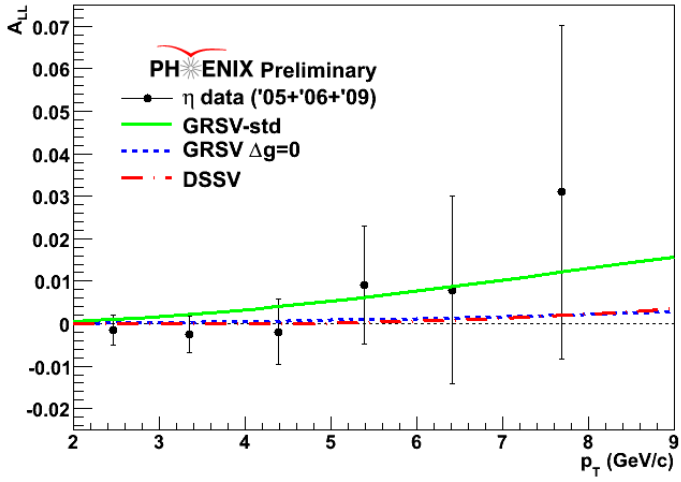

Figure 4.4: The double spin asymmetry for inclusive η production at $\sqrt{s} = 200\,\text{GeV}$, for the combined 2005–2009 results.

The results of a recent analysis [169] of the available polarized DIS data from SLAC, CERN, and DESY and RHIC data from both PHENIX and STAR (as of 2008) are displayed in Figure 4.6, clearly illustrating how much knowledge of the gluon spin contribution to the spin of the proton has improved in the recent years. It is important to note that while

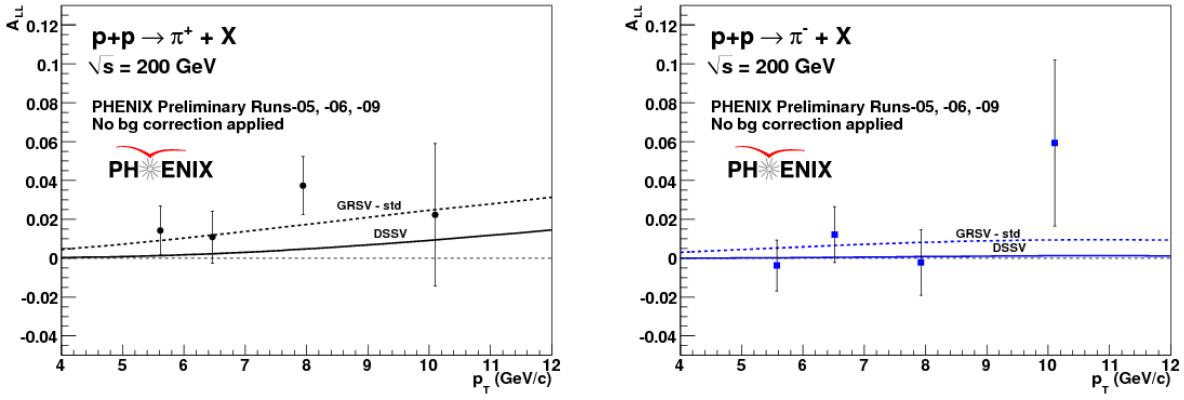

Figure 4.5: The double spin asymmetry for inclusive (left) π^+ and (right) π^- production at $\sqrt{s} = 200\,\text{GeV}$, for the combined 2005–2009 results.

the RHIC data have placed constraints on the polarized gluon distribution in the region $0.02 < x_g < 0.3$, the uncertainties in the $g(x)$ parametrization in the DSSV analysis for $x_g < 0.02$ are still large. Thus, if we assume that ΔG(x) changes sign as a function of x, it is still possible that the overall integral for ΔG is large. We expect publication of the helicity asymmetry results from the 200 and 500 GeV data sets taken in 2009 and the anticipated 2011 data set at 500 GeV and their subsequent incorporation into global analyses to fulfill DOE milestone HP12.

The helicity distributions for charged partons, the quarks in the nucleon, can be extracted directly from inclusive deep inelastic lepton scattering (DIS) experiments (in which only the scattered lepton is detected) if the Q^2 of the virtual photon is sufficiently high. While the total quark and antiquark spin contribution to the spin of the proton can be measured in DIS using electrons or muons, deep inelastic neutrino scattering allows one to separate quark and antiquark distributions, which the charged lepton scattering cannot distinguish. One can attempt to isolate the charged partons by flavor using so-called flavor tagging, where the known valence quark content of hadrons is correlated with the flavor of the quark which absorbed the virtual photon [65, 80]. Extracting information on flavor from the detection of a DIS lepton and a produced hadron, known as semi-inclusive DIS (SIDIS), necessarily depends on modeling of the fragmentation process.

At the highest present center-of-mass energy for protons at RHIC, $\sqrt{s} = 500\,\text{GeV}$, W bosons are produced abundantly enough to offer a complementary means of probing the flavor-separated quark helicity distributions. As charged mediators of the weak force, W bosons couple directly to flavor, and due to the V-A nature of the interaction, a W boson of a particular charge corresponds to a particular helicity state. Probing the flavor-separated quark helicity distributions in single-longitudinal spin asymmetry measurements of W production at RHIC is complementary to semi-inclusive DIS measurements in that the distributions are probed at a much higher scale (m_W^2) and no reliance on fragmentation functions is necessary.

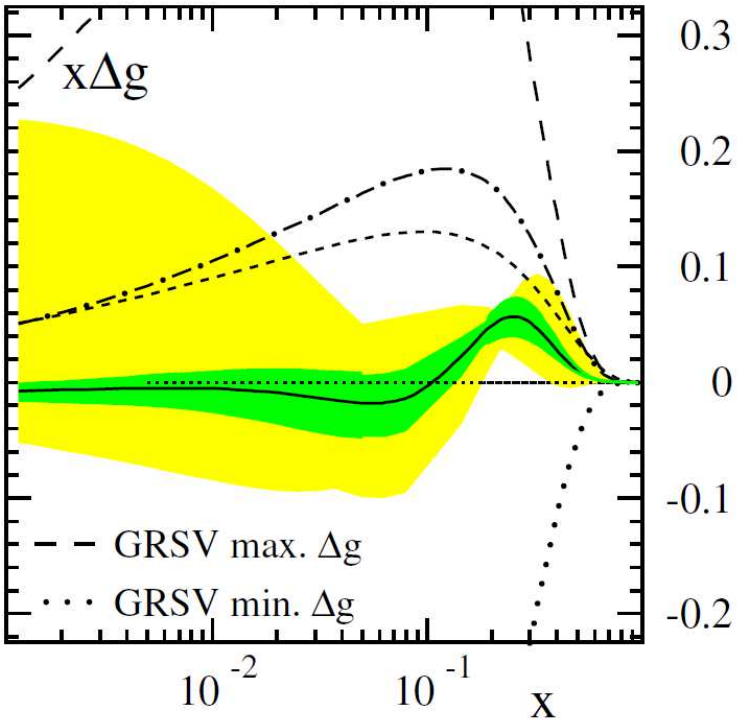

Figure 4.6: The polarized gluon distributions distribution derived from the DSSV NLO-pQCD analysis [169] of existing DIS and RHIC data.

RHIC had a first exploratory run at $\sqrt{s} = 500\,\text{GeV}$ in 2009, and PHENIX has already submitted results for both the $W^{\pm} \to e^{\pm}$ cross sections at this energy, shown in Figure 4.7, as well as A_L at midrapidity, with a clear parity-violating asymmetry observed, as can be seen in Figure 4.8, submitted for publication [27].

The spin of the proton not carried by parton spin must be due to orbital angular momentum of the partons, yet there is no unique way to describe the decomposition of the angular momentum among the interacting partons within a nucleon (see e.g. [145]). There are two helicity sum rules that have been established for a number of years, one by Jaffe and Manohar [208] in the infinite momentum frame and the other by Ji [211] in the proton rest frame. More recently, another decomposition of nucleon spin has been proposed by Chen *et al.* [155, 156]. While the relationship among these decompositions has been unclear, very recent work by Wakamatsu [313, 314] has broken ground in reconciling these different approaches and clarifying their relationship to experimental observables. These would allow for the first time ever the unraveling of the different contributions from quarks and gluons to the spin of the proton with measurements at an electron-ion collider (EIC).

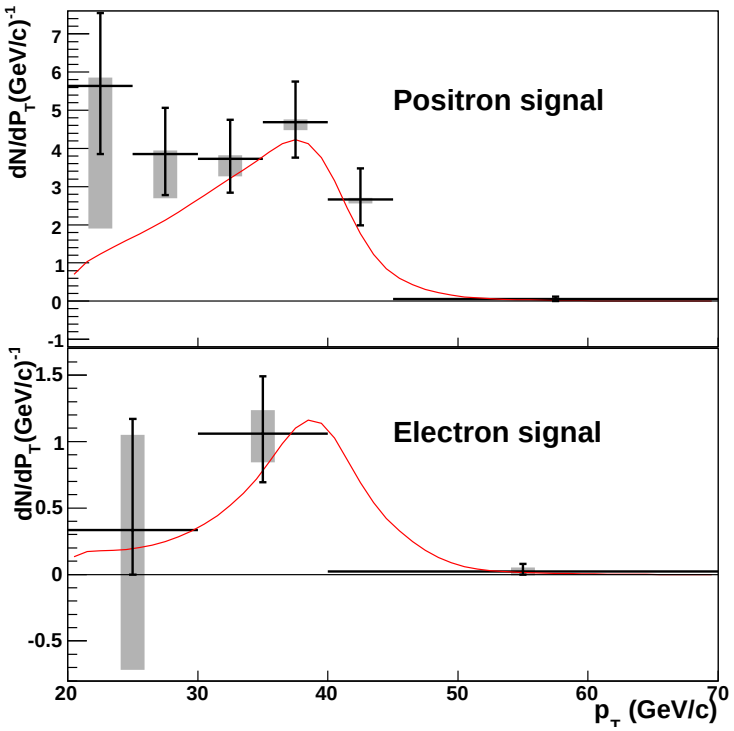

Figure 4.7: Background-subtracted spectra of (upper) positron and (lower) electron candidates measured in run-9 [27] compared to the spectrum of W and Z decays from an NLO calculation [171, 259]. The gray bands reflect the range of background estimates used in the analysis.

4.2 Nucleon Spin Structure: Transversity

When one explores the polarization of quarks with the nucleon spin perpendicular to the light cone, our understanding of both transverse momentum and spin is strongly tested. Ever since the observation of a large asymmetry in high-energy proton scattering [220], it has been clear that transverse effects play an important role. These effects have been confirmed in numerous other polarized hadron scattering experiments [97, 23, 22, 84] and found to persist even at RHIC energies, almost undiminished in size [106, 24, 19]. Recent progress has been spurred by measurements of transverse asymmetries in lepton scattering from transversely polarized protons and deuterons at HERMES and COMPASS [66, 82, 59, 69, 77, 70, 78].

The strikingly similar behavior of the pion asymmetries across a wide range of energies, from $\sqrt{s} = 19.4\,\text{GeV}$ to 200 GeV, can be seen in the lower plot of Figure 4.9; a comparison of neutral and charged pion asymmetries at $\sqrt{s} = 62.4\,\text{GeV}$ from PHENIX and BRAHMS can be seen in the upper plot of the same figure. Thanks to significant transversely polarized data sets at $\sqrt{s} = 200\,\text{GeV}$ taken in 2006 and 2008, PHENIX now has A_N measurements in forward hadron production that are differential in p_T as well as x_F, as shown in

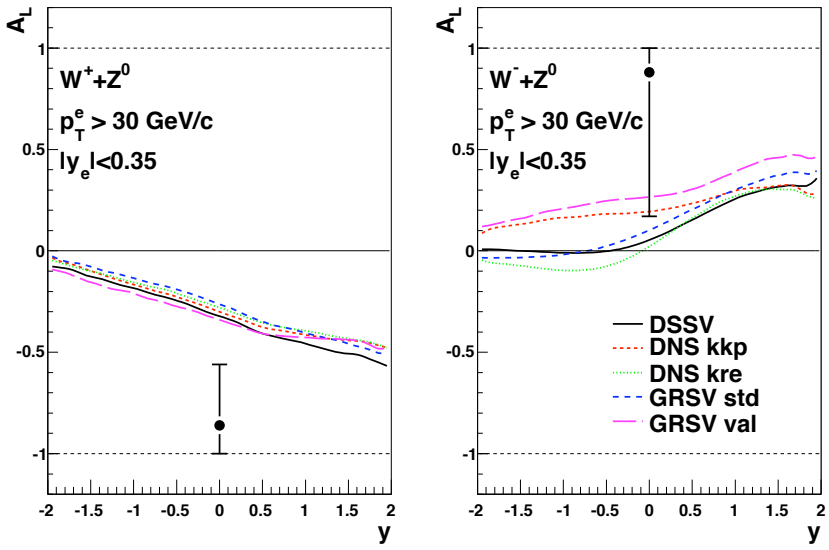

Figure 4.8: Parity-violating asymmetry of positrons from (left) W^+ and Z (right) and W^- and Z decay, measured by PHENIX in run-9 [27].

Figure 4.10. All of these forward asymmetries are quite large, contrary to early expectations based on perturbative QCD [214], and in stark contrast to measurements at midrapidity, as can also be seen in Figure 4.10 for comparison. One might question whether the forward reactions are too soft to apply pQCD, but as shown in Figure 4.11 the cross sections are well described by NLO pQCD [127] as well as by PYTHIA [288]. The existence of large single spin asymmetries at RHIC, along with the good theoretical understanding of the unpolarized cross sections gives hope that transverse spin effects can be used as a tool to probe parton dynamics within the proton.

One possible origin of these large asymmetries is due the transversity distribution [272], which describes the correlation of transversely polarized quarks within a transversely polarized proton, analogous to the quark helicity distributions within a longitudinally polarized proton. As is the case with the standard unpolarized PDFs and helicity PDFs, transversity is a leading-twist, collinear distribution function, and it completes the description of the nucleon wave-function within this framework. While on the same footing as the unpolarized and helicity parton distributions, transversity has two distinct properties. One is that there is no transversity distribution for gluons. The other is that it is a chiral-odd distribution, and thus can only be probed in conjunction with another chiral-odd object, as QCD processes are chiral-even.

Due to the fact that gluons cannot be transversely polarized, the quark transversity distribution evolves in Q^2 as a color nonsinglet, with only the quark-quark splitting function contributing. The simpler evolution of the transversity PDF compared to the unpolarized and helicity PDFs offers an opportunity to test the Q^2 evolution of polarized distribution functions that is more straightforward than studying the Q^2 dependence of the polarized structure function g_1 or the helicity PDFs.

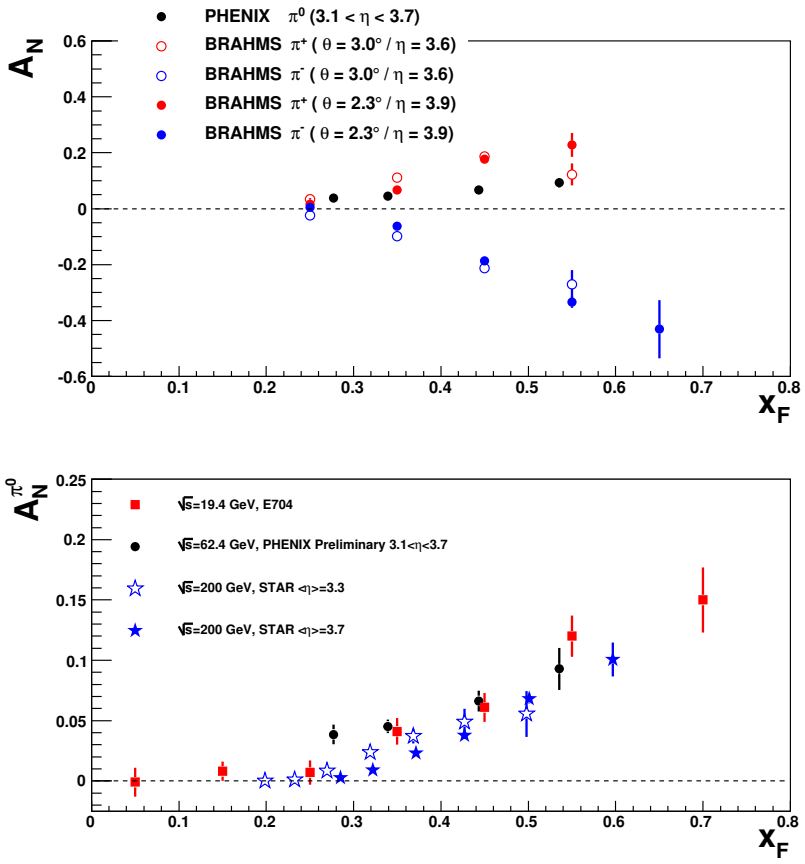

Figure 4.9: (upper) Single-spin asymmetry for neutral and charged pions produced in transversely polarized p+p collisions at $\sqrt{s} = 62.4\,\text{GeV}$, measured by PHENIX [158] and BRAHMS [106]. (lower) Single-spin asymmetry for π^0 mesons produced in transversely polarized p+p collisions as a function of Feynman x, measured at three center-of-mass energies: $\sqrt{s} = 19.4\,\text{GeV}$ [23], $\sqrt{s} = 62.4\,\text{GeV}$ [158], and $\sqrt{s} = 200\,\text{GeV}$ [24].

Two chiral-odd fragmentation functions that can offer sensitivity to transversity are the interference fragmentation function [162], which is a leading-twist, collinear FF of two hadrons from the same scattered parton, and the Collins FF [160], which describes the correlation between the transverse spin of a fragmenting quark and its transverse momentum. The Collins FF is thus a transverse-momentum-dependent (TMD) rather than collinear FF. As a fragmentation function, the Collins FF can be measured in e^+e^- annihilation, free of the complexities of any initial-state hadrons, and was measured several years ago to be nonzero by the BELLE Collaboration [17]. An extraction of the Collins FF from global fits to semi-inclusive DIS and BELLE e^+e^- data is shown in Figure 4.12.

The existence of sizable Collins fragmentation functions has in turn allowed initial extractions of the transversity distributions for up and down quarks within the nucleon from SIDIS-data on the proton and deuteron, with one such extraction [93] shown in Figure 4.13. The distributions for both up and down quarks are relatively large, and carry

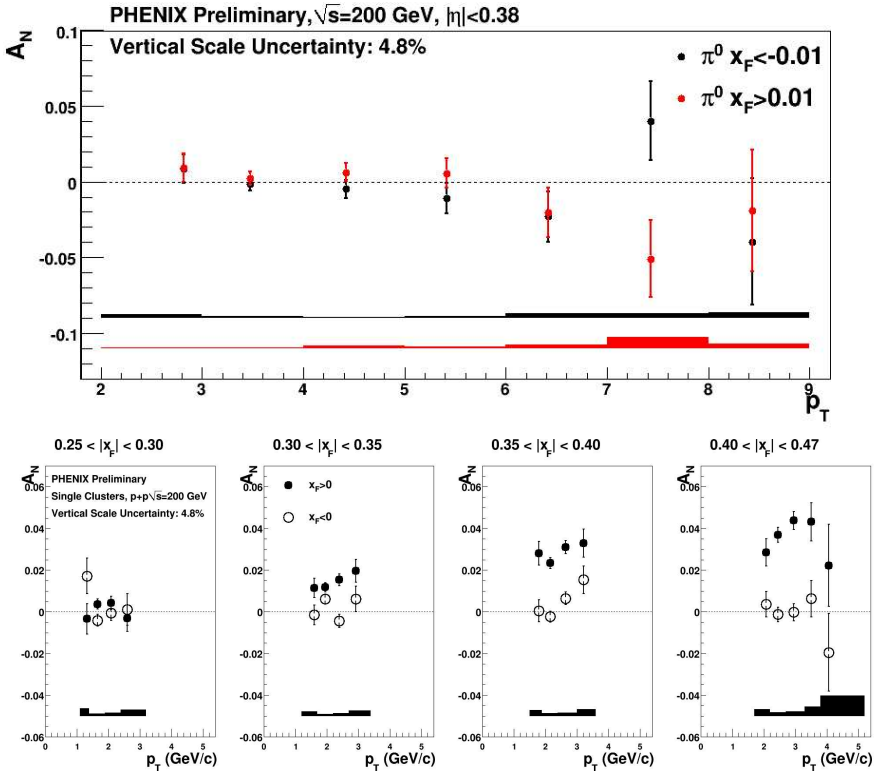

Figure 4.10: (upper) Transverse single-spin asymmetry $A_N^{\pi^0}$ for π^0 in the central arm. (lower) Single spin asymmetries for clusters in the MPC, which are dominated by merged photons from π^0 decays.

opposite signs, analogous to the helicity case.

4.3 Beyond a One-Dimensional Landscape of the Nucleon

Transverse-momentum-dependent distributions (TMDs) The large transverse spin effects observed in both hadronic collisions and semi-inclusive DIS have prompted intense theoretical activity, with a number of possible origins identified. Not only can large asymmetries be generated by correlations between partonic spin and transverse momentum in the hadronization process, as in the Collins FF, but also in the partonic distribution functions within the initial-state nucleon. The subfield of transverse-momentum-dependent distribution functions (TMDs) has made tremendous progress in the last decade, opening up a new realm in which to explore the partonic momentum structure of the nucleon, one which is sensitive to parton dynamics. TMDs depend not only on momentum fraction x and Q^2, but as well on transverse parton momentum (k_T).

The Sivers function [286] is a TMD distribution function that can generate large transverse single-spin asymmetries. It describes a correlation between the intrinsic transverse

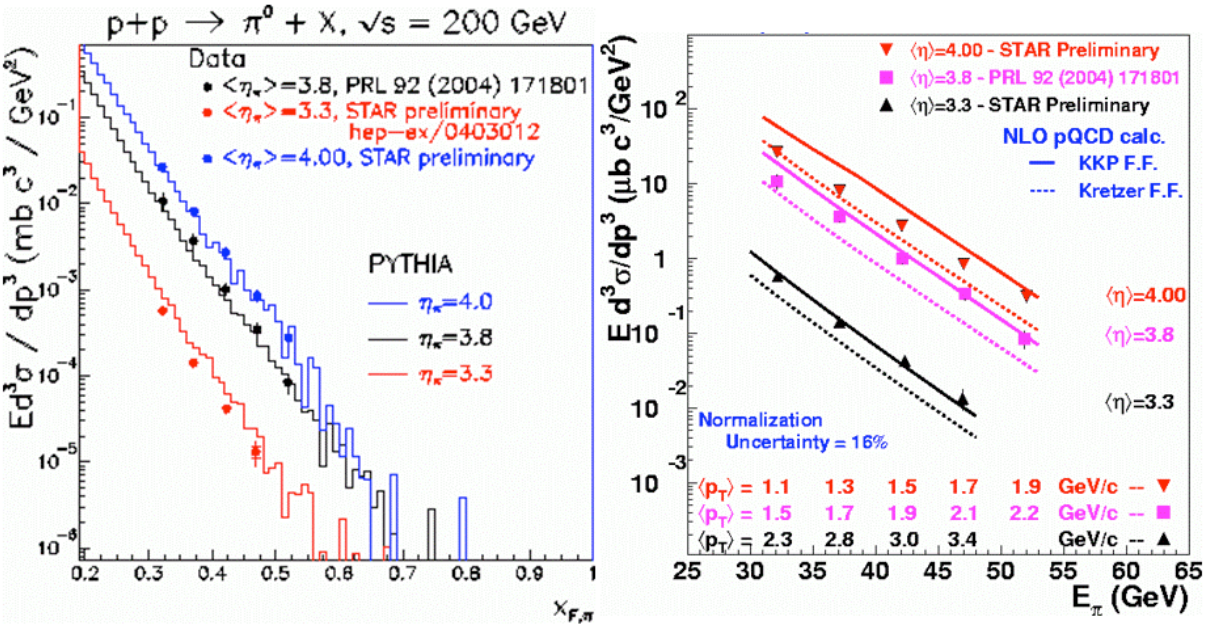

Figure 4.11: Forward inclusive π^0 cross sections measured by the STAR experiment from transversely polarized $p+p$ collisions at $\sqrt{s} = 200\,\text{GeV}$ [24]; the average pseudorapidity is $\langle\eta\rangle = 3.8$. Results are compared (left) to predictions using PYTHIA [288] as a function of x_F and (right) to NLO pQCD [127] as a function of the pion energy.

momentum of the partons within a transversely polarized nucleon and the direction of nucleon spin. Orbital angular momentum of the partons about the spin axis would naturally provide just such a correlation; however, this connection is still not understood theoretically at the partonic level, and it is unclear whether it would be possible to eventually extract model independent orbital angular momentum based on measurements of the Sivers distribution [143].

In semi-inclusive DIS it is possible to select out separately transverse single-spin asymmetries generated by Sivers functions or the transversity distribution convoluted with the Collins FF. Using results from SIDIS, a first extraction of the quark Sivers distributions has been performed [94], as shown in Figure 4.14, which indicates finite Sivers functions for up and down quarks that are of opposite signs.

Very importantly, the study of processes involving TMDs has led to new insight into the role of gauge links in calculating partonic field operators. The Sivers function, along with other time-reversal-odd TMDs, is notable for its "modified" universality property, such that the sign of the Sivers distribution as measured in a Drell-Yan process will be opposite the sign of the distribution as measured in SIDIS [161]. The modified universality is an important test of the QCD gauge-link formalism used to calculate these initial/final state interactions of the incoming/outgoing parton lines, and experimental verification of this property has been designated an NSAC milestone. Further theoretical investigation of the role of gauge links in processes involving TMDs has led to deeper questions regarding

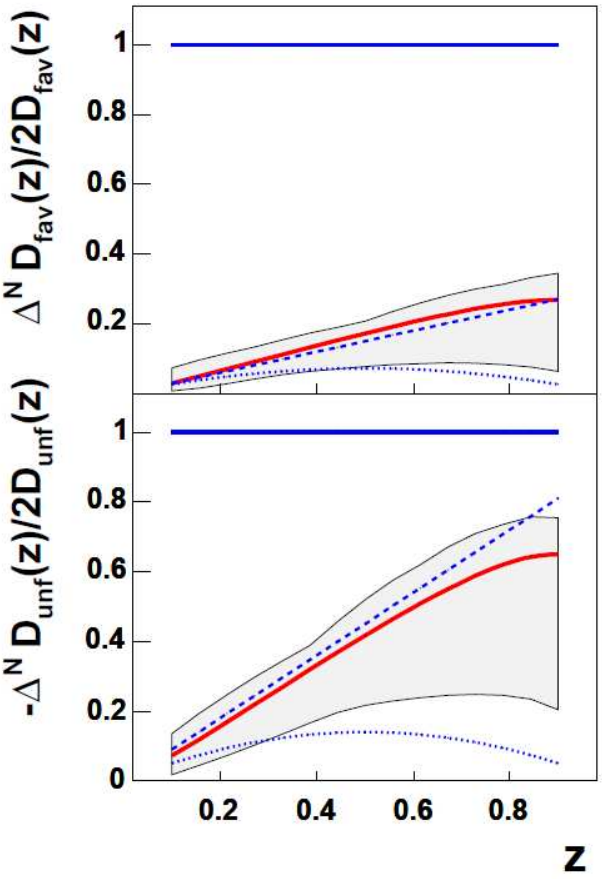

Figure 4.12: Dependence of the favored and unfavored Collins fragmentation functions on the hadron momentum fraction z, as extracted from a global fit to SIDIS data and BELLE e^+e^- data [93]. Shown are (solid curves) best fit, (gray bands) the corresponding uncertainty, (dashed and dotted lines) comparison to earlier results, and (solid lines at 1) the positivity bound.

universality and factorization, and a recent paper [280] states that a factorized description using TMD PDFs and FFs is not possible in high-p_T processes involving more than two hadrons total.

It is important to note that the large effects that can be described by TMDs can also be described within a collinear but higher-twist framework involving multiparton correlation functions. The TMD and collinear higher-twist approaches have different but overlapping kinematic regions of applicability and have been shown to correspond exactly in their region of overlap [213]. The process dependence between hadronic and SIDIS interactions embodied in the modified universality of the Sivers function within the TMD approach remains in the collinear, higher-twist picture. As factorization is believed to hold in the collinear framework, this should allow us to explore issues of universality independently of factorization.

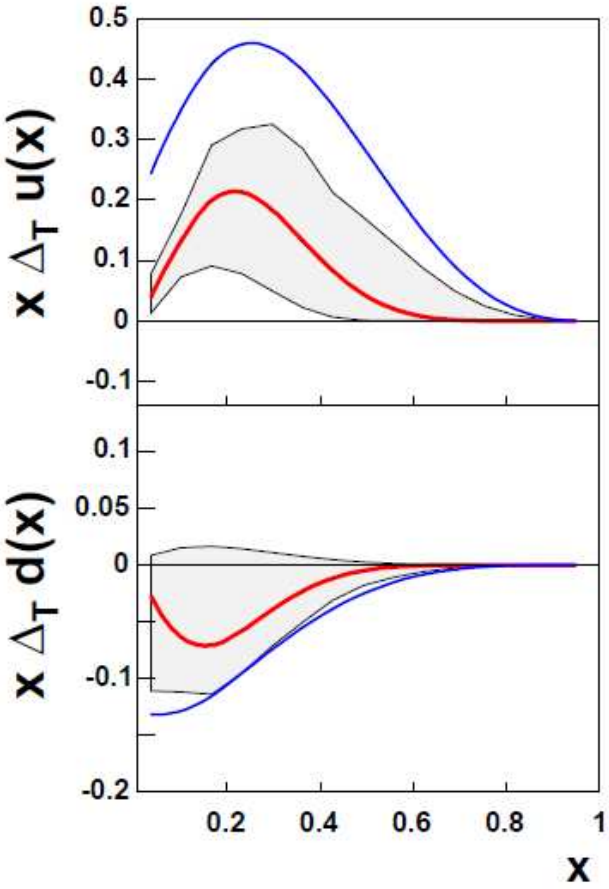

Figure 4.13: The transversity distributions for up and down valence quarks, as extracted from SIDIS and e^+e^- data [93]. Shown are (solid red curve) the distributions as determined by the global best fit to the data, (gray bands) the uncertainty in the extraction, and (solid blue curves) the Soffer bound [289].

Very little is presently known about gluon TMDs or the corresponding collinear, higher-twist trigluon correlation functions. An earlier PHENIX measurement of the transverse single-spin asymmetry in neutral pion production at midrapidity from 2002 data [53] was used to place initial constraints on the gluon Sivers function [91]. The experimental uncertainties have been greatly reduced by subsequent data sets, with preliminary results shown above in Figure 4.10, which should lead to improved constraints. Figure 4.15 shows the very recent PHENIX measurement [28] of the transverse single-spin asymmetry in J/ψ production. At modestly forward rapidity, a negative asymmetry is measured, with a significance of 3.3σ from zero. This suggests nonzero trigluon correlation functions in transversely polarized protons, and, if well defined in the reaction, a nonzero gluon Sivers function. While the J/ψ measurement may seem to contradict the very small asymmetries observed in π^0 production at midrapidity, the color interactions for pion and charmonium production differ, and further theoretical work will be needed to understand the relationship between the measured asymmetries. Single-spin asymmetries in charmo-

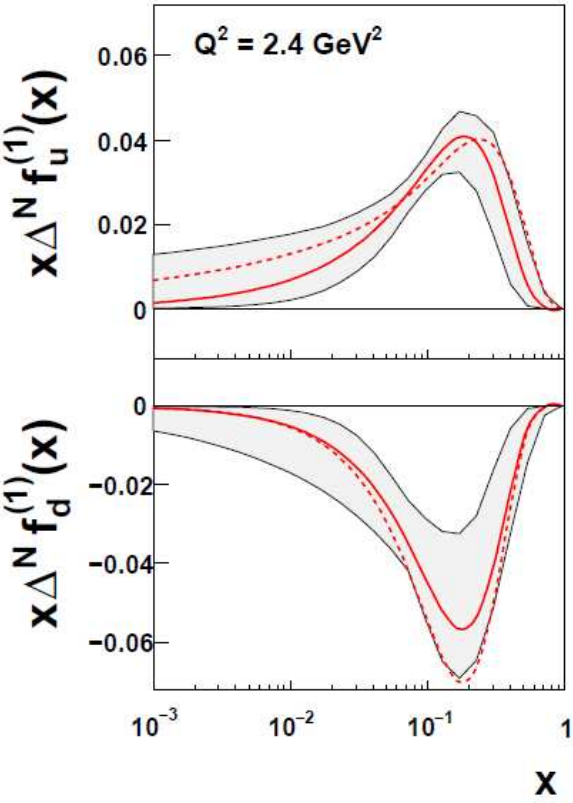

Figure 4.14: The Sivers distributions, as extracted from SIDIS data [94]. The solid red curve indicates the distributions as determined by the global best fit to the data; the dashed curve is the result of an earlier extraction by the same group [92]. The gray bands are an indication of the uncertainty in the present extraction.

nium and open heavy flavor production at PHENIX will play an important role over the next several years in understanding gluon dynamics in the nucleon.

Effects in forward hadron production from transversely polarized $p+p$ collisions are indeed somewhat more complicated than in polarized SIDIS, but the effects are typically larger and easier to study. The main goal of further measurements in $p+p$ must be to isolate the individual effects in order to gain a deeper understanding of the fundamental physics; just measuring a new set of single-spin asymmetries is not sufficient. Measurements that shed light on the nature of the universality and factorization breaking within the TMD framework will be essential; as we push forward our understanding of QCD in hadrons, this physics must be confronted and understood. For example, comparing extractions of the (collinear) transversity distribution via the k_T-dependent Collins FF vs. the collinear interference FF would be a valuable way to investigate this factorization breaking.

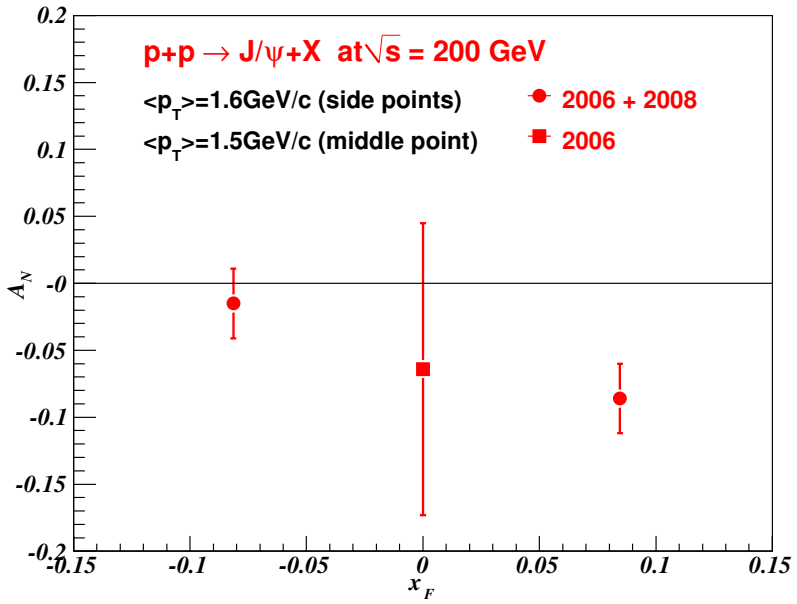

Figure 4.15: Transverse single-spin asymmetry $A_N^{J/\psi}$ for J/ψ in the central and muon arms [28].

Generalized parton distributions (GPDs) The distributions of partons in the nucleon are usually parametrized in terms of parton distribution functions. These functions depend on a resolution scale Q^2 and on x, which can be interpreted as the fraction of the nucleon momentum carried by a parton in the nucleon. In particular, the scattering experiments carried out at DESY led to a very precise determination of the unpolarized proton PDFs, as discussed above. The lepton (electron or positron) beams of HERA were scattered off protons, with energies high enough to penetrate the proton and thus probe its quark-gluon substructure in the direction of motion of the beam. No information about the transverse distribution of quarks and gluons is encoded in these PDFs. This is in contrast to so-called generalized parton distributions (GPDs) [256, 211, 213, 271, 270], in which the usual PDFs have been subsumed. The ability to describe longitudinal momentum distributions as a function of transverse localization is a prerequisite for the so-called Ji relation [211, 213], which gives the relation between a kinematic limit of a certain combination of GPDs and the total angular momentum of a given quark species in the nucleon. This is in fact the only quantitative way known today to access total quark angular momentum.

While $p+p$ collisions at RHIC are not anticipated to make significant contributions to knowledge of GPDs, an EIC at RHIC would be an excellent facility to explore GPDs in detail, and they are discussed further in Chapter 8.

In addition to initial experimental steps forward in investigating orbital angular momentum of quarks, lattice calculations from the LHPC Collaboration have made enormous progress [136] in providing information on the quark contributions to the spin of the nucleon. The newest results indicate that the orbital angular momenta of both u and d

quarks are sizable, but of opposite sign, such that their contribution to the total spin of the nucleon is small. These lattice results, despite the fact that not yet all contributions—e.g. disconnected diagrams—are included in the calculations, show how highly advanced these calculations have become.

4.4 Activities Outside of RHIC

There are several facilities around the world, predominantly using deep-inelastic scattering, which have active complementary nucleon structure physics programs. There is COMPASS at CERN, which will in the next two years run with longitudinally polarized muon beams and longitudinally and transversely polarized proton targets, to improve on their measurements of the quark and gluon polarizations in the proton as well as on their single spin asymmetries sensitive to the Sivers function and transversity. To continue their program farther in the future COMPASS has submitted a new proposal which focuses on measurements of exclusive reactions to constrain GPDs and Drell-Yan to measure the sign change between SIDIS and Drell-Yan for the Sivers function [10]. The kinematic coverage of the Drell-Yan measurements is completely complementary to the measurements planned at PHENIX. With the 12 GeV program coming online at Jlab in the next 4 years, the focus of Halls A, B, and C will be on the longitudinal and transverse quark structure of protons and neutrons at high virtuality Q^2 and momentum fraction x. Another focus will be on exclusive measurements, i.e. Deeply Virtual Compton Scattering (DVCS), to constrain GPDs. E906 at Fermilab will exploit the Drell-Yan process to probe selectively the antiquark distributions of target protons, deuterons, and nuclei. As with its precursor experiment, E866, this technique will be used to determine the ratio of $\overline{d}$ to $\overline{u}$ quarks in the nucleon. E906 will extend the earlier measurement with significantly better statistical precision to larger values of x. Furthermore it will be possible to extract the Boer-Mulders function, a TMD which describes the correlation of the transverse momentum distribution of quarks with the transverse spin of the quarks in a unpolarized nucleon. HERMES at DESY finished data taking in summer 2007 and will in the next few years finalize their analysis on observables sensitive to TMDs and GPDs.

Chapter 5

Nucleon Structure Physics: Midterm Plan

The next five years of the spin program focuses on:

- Constraining the flavor-separated sea quark helicity distributions via W measurements in longitudinally polarized $p+p$ collisions at $\sqrt{s} = 500$ GeV.
- Probing $\Delta g(x)$ down to lower momentum fractions in longitudinally polarized $p+p$ collisions at $\sqrt{s} = 500$ GeV.
- Explore several transverse spin measurements in transversely polarized $p+p$ collisions at $\sqrt{s} = 200$ GeV and at lower energies.

We discuss each of these in detail in the following sections. The five-year run plan is detailed in Appendix B, and most of the $p+p$ running is at $\sqrt{s} = 500$ GeV and longitudinally polarized. The transverse or longitudinal $p+p$ running at $\sqrt{s} = 200$ GeV also provides critical heavy ion baseline measurements.

5.1 Flavor separated helicity distributions via W boson measurements

As W bosons are produced through a pure $V - A$ interaction, a beam of polarized protons of negative helicity essentially provides a beam of left-handed up quarks. As a manifestation of the maximal parity violation of the W bosons, they precisely couple only to left-handed particles and right-handed antiparticles. This makes W production in polarized $p+p$ an ideal process to study the spin-flavor structure of the proton.

In PHENIX, this is done via the detection of high p_T electrons/positrons in the central arms from the decay $W^{\pm} \rightarrow e^{\pm}\nu$, and of high p_T muons in the muon arms from $W^{\pm} \rightarrow \mu^{\pm}\nu$. Our simultaneous coverage in forward, backward, and central rapidity provides a powerful means of determining the quantities $\Delta\overline{u}/\overline{u}$, and $\Delta\overline{d}/\overline{d}$ in the parton momentum range $0.05 < x < 0.6$. Nearly direct quark/anti-quark separation is possible with forward/backward leptons from W^- production in the PHENIX muon arms due to much larger quark density vs. anti-quark density at large momentum transfer. In this case, $A_L(\text{forward } W^- \rightarrow \mu^-) \approx \Delta d/d$. Similarly, $A_L(\text{backward } W^- \rightarrow \mu^-) \approx \Delta\overline{u}/\overline{u}$. Additionally, measurement of W^+ production gives access to $\Delta u/u$ and $\Delta\overline{d}/\overline{d}$. However, due to the fixed neutrino helicity, the flavor contributions at forward and backward rapidity are mixed. Similarly, the parity-violating asymmetry of W^+ production in central rapidity combines contributions from both u and $\overline{d}$ polarizations, and from d and $\overline{u}$ polarizations in W^- production. In general, the asymmetry is the superposition of the two cases shown in Figure 5.1:

$$A_L^{W^+} = -\frac{\Delta u(x_1)\overline{d}(x_2) - \Delta\overline{d}(x_1)u(x_2)}{u(x_1)\overline{d}(x_2) + \overline{d}(x_1)u(x_2)}, \tag{5.1}$$

with the asymmetry for W^- production given by exchanging u and d.

Present knowledge of flavor-separated quark helicity distributions comes from combined information from DIS measurements on polarized proton and neutron targets as well as polarized semi-inclusive DIS measurements, in which a variety of final-state hadron species are used to tag different quark flavors [169, 170]. Probing the flavor separation of the quark helicity distributions at RHIC via W boson production is complementary to these semi-inclusive DIS measurements in that the distributions are probed at a significantly higher energy scale (m_W^2), and no reliance on form factors is necessary.

PHENIX has already submitted results for the $W^{\pm} \rightarrow e^{\pm}$ cross sections and A_L from the first RHIC p+p run at $\sqrt{s} = 500$ GeV in 2009 for publication [27], shown in Figure 4.7 and Figure 4.8 in Chapter 4. While in the 2009 run all experimental subsystems were in place to measure the W decay to electrons, an upgraded trigger is needed in order to measure $W^{\pm} \rightarrow \mu^{\pm}$, described below.

Muon trigger Measurements of parity violating spin asymmetries in W-production with the PHENIX muon arms require a first-level muon trigger that selects high momentum muons ($p > 10$ GeV/c) and rejects the abundant muons from hadron decays, cosmic rays, and beam backgrounds. The existing muon trigger identifies muon candidates based on their ability to penetrate a sandwich of steel absorber and muon detector planes. Muons with momenta $p > 2$ GeV/c are selected. The resulting trigger rejection factors R range from 200 to 500 at $\sqrt{s} = 200$ GeV operation, depending on the (varying) beam background levels. The rejection factor gets worse, e.g. $R \sim 100$ or even less under the higher background rate conditions for collisions at $\sqrt{s} = 500$ GeV. The muon trigger upgrade

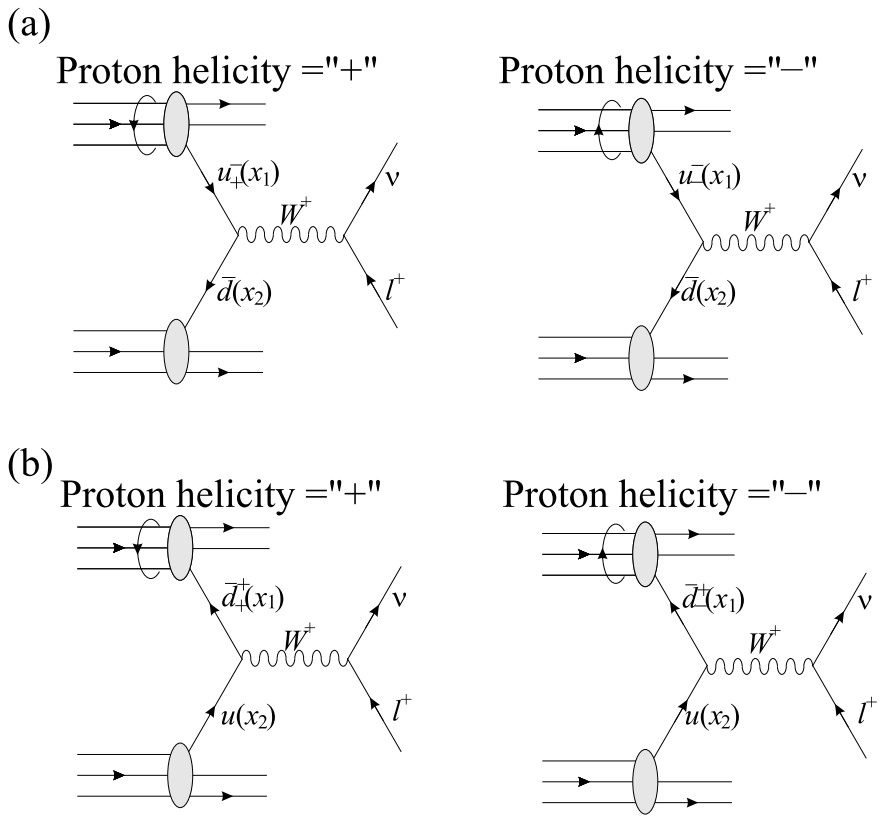

Figure 5.1: Leading-order production of a W^+ in a single-longitudinally polarized $p+p$ collision: (a) Δu is probed. (b) $\Delta\bar{d}$ is probed. '+' and '-' subscripts on the quarks indicate the helicity of the parent proton, while superscripts indicate the handedness of the quark.

provides tracking and timing information to a new set of muon trigger processors to complement the current trigger and to improve the overall rejection power. The observed rejection factors are summarized in Table 5.1 for various options of the new momentum-sensitive trigger. The rejection factors evaluated so far do not yet include additional timing and spatial constraints available from the RPCs.

The PHENIX muon trigger upgrade has two components: (I) new front-end electronics for the muon tracking chambers to send tracking information to new dedicated muon trigger processors, and (II) two resistive plate chamber trigger detector stations in each muon arm: RPC-1 at the entrance and RPC-3 at the exit of the muon tracker volume. The RPC stations provide both tracking and timing and are based on technology developed for the CMS muon trigger. The timing information adds background rejection power in the offline analysis, particularly in removing tracks due to cosmic rays, while making the online trigger much less sensitive to beam-related backgrounds.

The baseline muon trigger upgrade for run-11 includes the new muon tracker trigger electronics for stations 1-3, and RPC-3 installed both in the south and north muon spectrometers. Also required are the first level trigger processors (LL1) that combine muon

Table 5.1: Rejection factors of the new momentum sensitive muon trigger observed during $\sqrt{s} = 500$ GeV operation of run-9. $\Delta strip = 1$ corresponds to about 1 cm sagged of the trajectory in the MuTr volume. Larger $\Delta strip$ accommodates larger curvature of the trajectory, thus the momentum threshold becomes lower and the rejection factor becomes smaller. The clustering algorithm of hit patterns was introduced to Obediah higher rejection power. However it may come at the cost of lower trigger efficiency for true high momentum tracks, and therefore further study is required before this method is implemented.

$\Delta strip$	0	1	2
w/o clustering	20	13	9
w/ clustering	86	24	15

tracker hit and RPC hit information and execute the actual muon trigger algorithm.

The muon tracker trigger electronics for all stations have already been installed and successfully tested, including complete trigger chain tests with the muon tracker trigger electronics and the LL1 trigger processors.

The RPC-3 north front end electronics was installed during run-10 using accelerator access days, and initial testing has been carried out. Installation of RPC-3 south will be completed before the beginning of run-11. RPC-1 chamber construction and installation in both arms will be completed before the start of run-12.

Full suppression of offline backgrounds in the W-physics analysis also requires two new 35 cm thick steel absorbers upstream of the PHENIX muon spectrometer arms. 1-2% of hadrons with low momentum punch through the central magnet yoke upstream of the PHENIX muon spectrometers. A small fraction of these hadrons decay into muons in the spectrometer magnet volume such that the upstream hadron track combined with the downstream decay muon track mimic a high momentum muon track. We have carried out detailed Monte Carlo simulations that identify false high p_T tracks as the dominant source of the off-line background. We have shown in simulations and through data taken with a prototype absorber in run-9 that an absorber with a thickness of two nuclear interaction lengths reduces the background to acceptable levels. The new absorbers will be in place for run-11.

Projections for the next five years We expect the next 500 GeV polarized $p+p$ run to be in run-11, and have set a goal of recording 50 pb^{-1}, followed by 100 pb^{-1} in run-12. It is imperative to collect sufficient data before 2013 to achieve NSAC milestone HP8, which requires measurement of flavor-identified q and $\bar{q}$ contributions to the spin of the proton via the longitudinal-spin asymmetry of W production in calendar year 2013. We anticipate that this milestone can probably be at least partially satisfied with with the requested luminosity; the ultimate result will require a total integrated luminosity of 300 pb^{-1}. In runs 11-14, the beam polarizations should be at least 50%, and it should be increased to

60% as soon as possible.

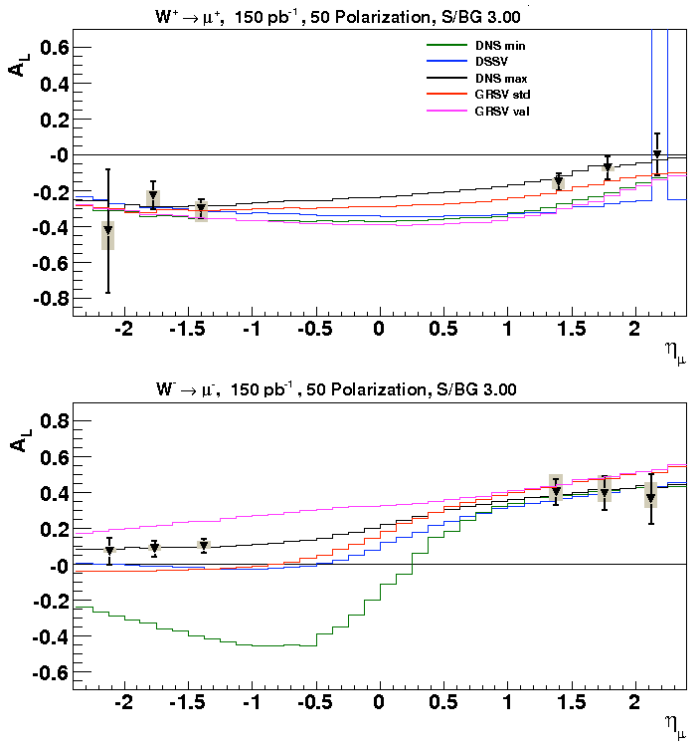

Figure 5.2: Expectation for uncertainties in W asymmetry measurements with 150 pb^{-1} recorded with 50% polarization and S/B=3.0.

Combining the data from the run-11 and run-12 500 GeV p+p runs is expected to provide 150 pb^{-1} integrated luminosity. We expect the error bars shown in Figure 5.2 from the combined run-11 and run-12 data sets. A signal-to-background ratio of 3.0 has been assumed, which we hope to be able to achieve. The curves show the results of various pQCD fits including different inclusive and semi-inclusive DIS data, along with RHIC polarized p+p data from previous runs. It is clear that the 500 GeV data from PHENIX will have a substantial impact.

The plots in Figure 5.3 show the current uncertainties obtained by a pQCD fit [169, 170] to the world data from inclusive and semi-inclusive deep inelastic scattering. Figure 5.3 shows the impact of the $W^{\pm}A_L$ for a total integrated luminosity of 300 pb^{-1} with a mean polarization of 60%. The W data reduce the uncertainties on the sea-quark polarizations for $0.05 < x < 0.6$ significantly, furthermore serving as a set of complementary measurements to the ones in semi-inclusive DIS, as discussed above. It should be mentioned that measuring the A_L for W^- production for forward rapidity might provide a test of the different assumptions of the behavior of $\Delta d/d$ at high x. The constituent quark model predicts a value of $\Delta d/d$ of -1/3 at x=1, whereas the pQCD based on counting rules predicts $\Delta d/d = 1$. The current data don't support any change of sign for $\Delta d/d$ for $x = 0.6$ [113].

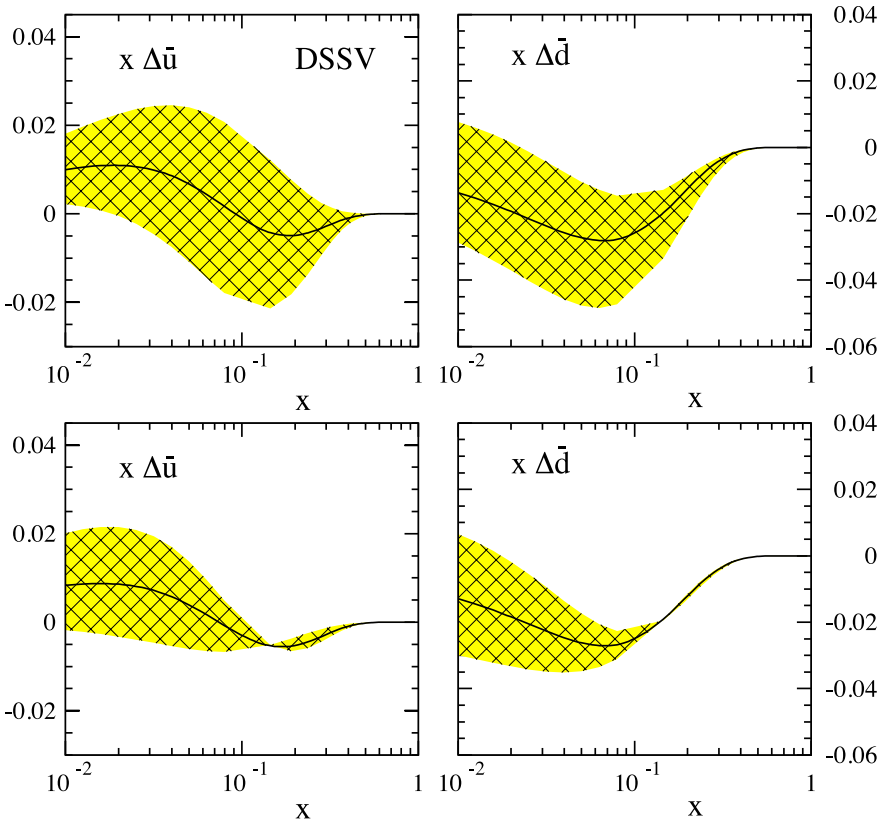

Figure 5.3: Upper plot: Uncertainty band on $x\Delta\overline{u}$ and $x\Delta\overline{d}$ resulting from the current fit to the world data from inclusive and semi-inclusive DIS by DSSV[169, 170]. Lower plot: Improvement in the uncertainties adding constraint from $W^{\pm}$ A_L measured with a total integrated luminosity of 300 pb^{-1} at 500 GeV p+p collisions with 60% polarization.

5.1.1 Constraints on the flavor-separated unpolarized sea quark distributions

The ratio $R = \sigma^{W^+}/\sigma^{W^-}$ of cross sections for W^- and W^+ production in p+p collisions at RHIC provides a new way to measure the asymmetry $\overline{d}/\overline{u}$ of the quark sea in the nucleon. Previous measurements through the Gottfried sum rule in DIS and Drell-Yan production in p+p scattering have relied on combining data from proton and deuteron targets assuming charge symmetry, $u_p(x) = d_n(x)$, $d_p(x) = u_n(x)$, $\overline{u}_p(x) = \overline{d}_n(x)$ and $\overline{d}_p(x) = \overline{u}_n(x)$, and assuming that nuclear effects are negligible. In W production $\overline{d}/\overline{u}$ can be obtained from the proton data alone, independent of assumptions about charge symmetry. Figure 5.4 compares calculations for the W cross section ratio R for four different sets of parton distribution functions with errors projected for an integrated luminosity of 300 pb^{-1}. The PDF set 'MRS S0' assumes a symmetric quark sea, $\overline{d}(x) = \overline{u}(x)$, and can be well separated within the projected experimental uncertainties from PDF sets that include the breaking of the quark sea. A detailed discussion of this measurement can be found in [320].

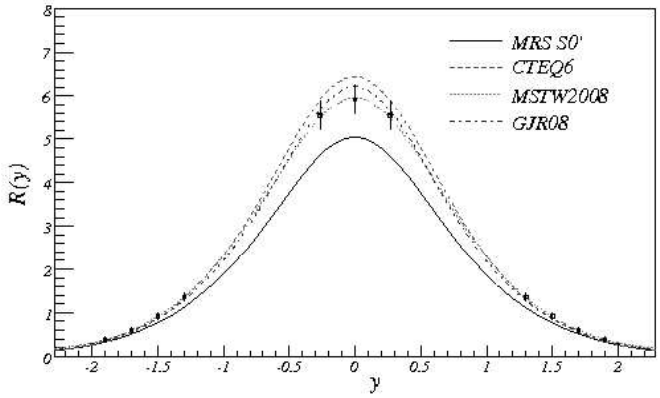

Figure 5.4: The ratio, R, of cross sections for W^+ and W^- production at $\sqrt{s} = 500$ GeV plotted versus the rapidity of the decay lepton. The projected errors represent an integrated luminosity of 300 pb^{-1} into the PHENIX central and muon arms. The curves represent calculations of R for different PDF sets. The PDF set 'MRS S0' assumes a symmetric quark sea whereas the other PDF sets are based on asymmetric quark seas.

5.2 Improving constraints on $\Delta g(x)$

In recent years the preferred channel at PHENIX to constrain the gluon polarization has been through the abundant inclusive π^0 production. Through run-9, PHENIX has recorded a total of approximately 25 pb^{-1} (summed over run-5, run-6, and run-9) of polarized p+p collisions at 200 GeV. Figure 4.3 in Chapter 4 shows the current status of A_{LL} for π^0 production.

Our goal at 200 GeV had been to record approximately 65 pb^{-1}; however, it is clear that with the currently achievable luminosity (recorded luminosity in 10 weeks: 12 pb^{-1} with collisions inside $\pm$10 cm) meeting this goal would require 3 to 4 10-week runs. Starting in run-11 the vertex distribution in the central detector is limited to $\pm$10 cm compared to the current $\pm$30 cm, because with the installation of the new vertex detector in summer 2010, there will be considerable material thickness due to the vertex detector support structure beyond the $\pm$10 cm vertex region. The measured double-spin asymmetry in inclusive π^0 production, $A_{LL}^{\pi^0}$, is consistent with zero in the transverse momentum range $1 < p_T < 10$ GeV/c, limiting the gluon spin contribution to the proton spin in the parton momentum range $0.02 < x_g < 0.3$ to $-0.7 < \Delta G^{[0.02,0.3]} < 0.5$ at 3σ [40]. Even though the measurements have become very precise and have started to constrain the gluon polarization [170], there remain several open questions, such as what is the gluon polarization at low x where the gluon density in the proton is largest, and can higher-twist contributions become important while the leading twist contribution is small? PHENIX plans to move forward with the accumulation of data at 500 GeV over the next several years to extend the study of gluon polarization to smaller x_g, while beginning exploration of the spin polarization of $\overline{u}$, and $\overline{d}$ quarks via the parity-violating asymmetry in W boson production.

Figure 5.5 shows that the lowest value of x reached via midrapidity π^0 production at 500 GeV falls below the lowest x in the 200 GeV data, extending our sensitivity down to $x < 0.02$. The expected magnitude of the asymmetries at $\sqrt{s}$ of 200 GeV and 500 GeV can be related to good approximation by using x_T-scaling ($x_T = 2p_T/\sqrt{s}$).

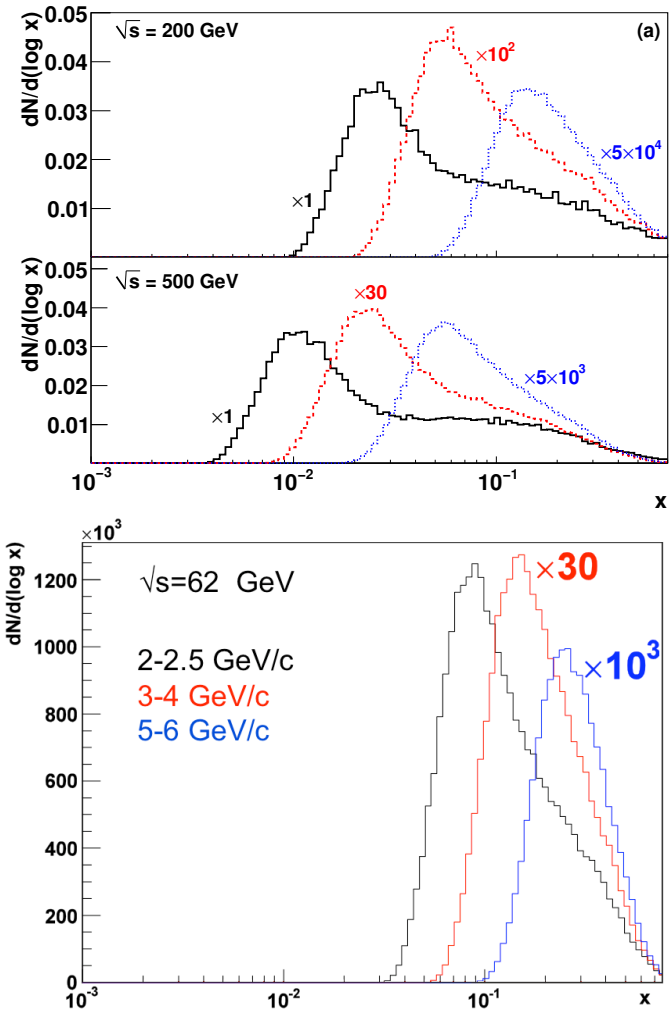

Figure 5.5: x range covered by π^0 at different p_T in 200, 500, and 62 GeV collisions. Black, red, and blue curves correspond to 2–2.5, 4–5, and 9–12 GeV/c p_T, respectively. The different x-ranges are multiplied by the factors indicated to allow comparison.

Figure 5.6 shows the expected uncertainties in $A_{LL}^{\pi^0}$ as a function of p_T at 500 GeV assuming we accumulate 350 pb^{-1} (130 pb^{-1}) in the years 2011–2015 within the current (future) $\pm$30 cm ($\pm$10 cm) vertex and with 50% polarization. Since $A_{LL}^{\pi^0}$ is a double spin asymmetry, it is important to have the highest polarization achievable: the difference between 50% (40%) and 60% polarization is the equivalent to recording more than a factor of two (five) times higher luminosity. This is especially important for the measurement at $\sqrt{s}$=500 GeV compared to that at 200 GeV, as the unpolarized cross section in the denominator of $A_{LL}^{\pi^0}$

is growing due to the strongly rising gluon and sea quark densities, making the expected asymmetries at low p_T very small.

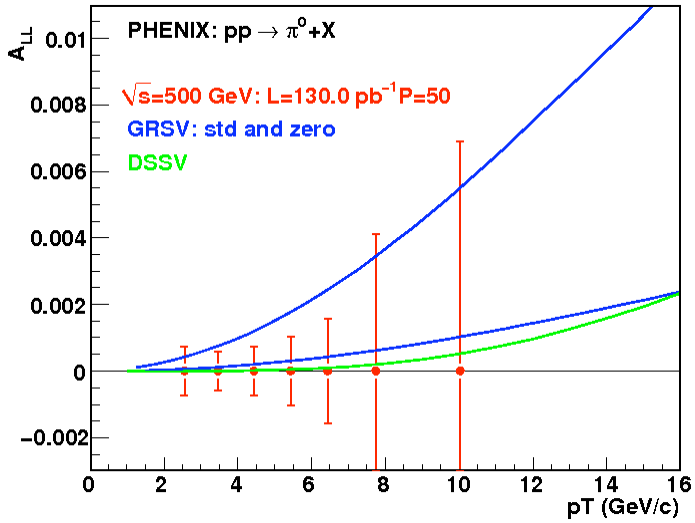

Figure 5.6: Expected uncertainties in $A_{LL}^{\pi^0}$ as a function of p_T for a recorded luminosity of 130 pb^{-1} and a polarization of 0.5. Only collisions with vertex inside $\pm$10 cm are included.

It is possible to increase the x-range to even lower values at the same $\sqrt{s}$ by going to more forward rapidity ($x = Q/\sqrt{s} \times e^{y}$). In principle, a forward upgrade to the PHENIX experiment as discussed in Chapter 6 will allow us to greatly extend the x-range of the PHENIX measurements and provide information on the x dependence of ΔG. Even if the gluon polarization falls off with decreasing x, the integral, ΔG, is dominated by contributions from $x < 0.1$ since this is the region where the gluons are most abundant. It is thus important to measure ΔG to values of x as far below 0.1 as feasible. Historically it is interesting to note that the quark spin crisis only arose with the EMC measurement [108] of quark spin contributions and the extrapolation of PDFs to low x. Extrapolations of the SLAC [121] data alone led to results for the quark spin contribution consistent with expectations from naive quark models.

PHENIX already has the capability to constrain ΔG at forward rapidity by utilizing the Muon Piston Calorimeter (MPC) ($3.3 < \eta < 3.7$) to measure the inclusive cluster A_{LL}. Figure 5.7 shows the projected uncertainties for $A_{LL}^{Cluster}$ requiring $p_T > 3$ GeV and for a sampled integrated luminosity of 100 pb^{-1}. Also shown are the expected uncertainties for a gluon polarization measurement based on DSSV and GS-C. We are aware of the fact that GS-polarized parton distributions are inconsistent with the world data, but as the low-x behavior for $\Delta g(x)$ is unknown, GS-C is an example of a polarized gluon PDF which has a slow behavior for $\Delta g(x) \rightarrow 0$ as x goes to zero. But even for this extreme behavior of GS-C the asymmetries are only on the 10^{-4} level. The measurement of such small asymmetries with good precision requires excellent control of all the systematic uncertainties; especially the relative luminosity uncertainty needs to be controlled to values

smaller than the magnitude of the asymmetries. Currently the uncertainties on the relative luminosity are on the level of 7×10^{-4} in run-6 and 1.4×10^{-3} in run-9. Reducing this to a level $\leq 10^{-4}$ might require an upgrade of the PHENIX luminosity monitor. Ideas to use position-sensitive single-arm telescopes as relative luminosity counters were tested in run-4. To reach the needed statistical precision, an efficient trigger and sufficient DAQ bandwidth are required to record enough data in the relevant kinematic region. The histogram in the right plot of Figure 5.7 shows how the extended x-range reaches down to $x \sim 10^{-3}$. The yellow band indicates the current x-range at $\sqrt{s} = 200GeV$.

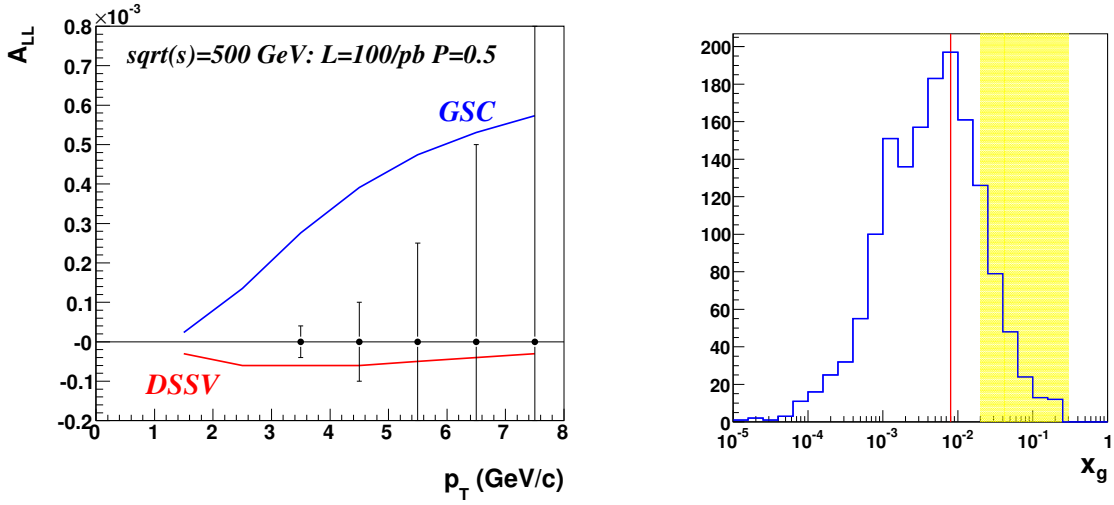

Figure 5.7: Expected uncertainties in $A_{LL}^{Cluster}$ as a function of p_T measured with the MPC for an integrated sampled luminosity of 100 pb^{-1}. Also shown is the x-range covered by this measurement. The yellow band indicates the x-range covered by measurements in the present central arm at 200 GeV and the red line indicates the lowest x reachable in the central arm with 500 GeV collisions.

Another possibility to reach lower x, and also to constrain the correlation between x and p_T, is to measure A_{LL} in two particle correlations at forward rapidity. Figure 5.8 (left) shows the fractions for the different subprocesses contributing to $A_{LL}^{Cluster}$ requiring 2 back-to-back clusters ($\Delta\phi \sim \pi$) in the MPC with the trigger particle having $p_T > 3$ GeV and the p_T of the associated particle to be bigger than 1.5 GeV. The qg-scattering process dominates. The corresponding x distribution is shown in Figure 5.8 (right). The asymmetries to be expected are on the level $\sim 10^{-3}$.

Decreasing $\sqrt{s}$ to 62 GeV allows access the high-x region of $\Delta g(x)$ (see Figure 5.5). The high-x region is currently constrained by inclusive DIS data. Figure 5.9 shows the impact on the uncertainties of the polarized gluon distribution adding pseudo-data of $A_{LL}^{\pi^0}$ at $\sqrt{s}$ = 62 GeV to the datasets used in DSSV. The plot assumes a luminosity of 0.4 pb^{-1} and a polarization of 60%, which is twice the recorded luminosity foreseen in run-14. The impact to constrain the gluon polarization (the reduction from the uncertainty band indicated by the red curves to the uncertainty band indicated by the black lines) is small.

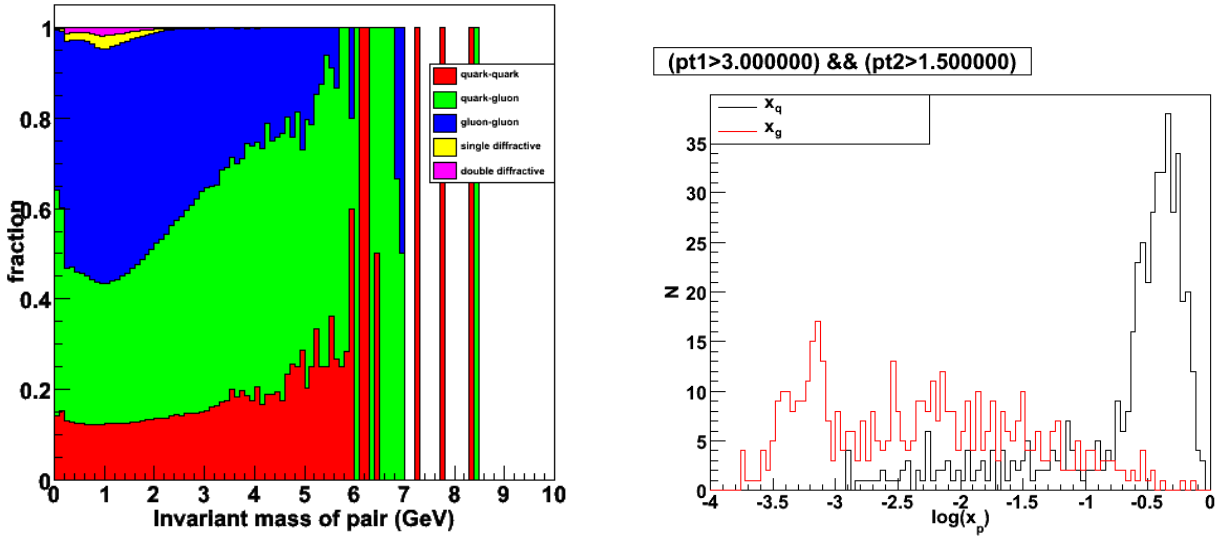

Figure 5.8: (left) Subprocess fractions contributing to two particle clusters in the MPC. (right) For the quark-gluon subprocess, we show the x distribution for $A_{LL}^{Cluster}$ requiring two back-to-back clusters in the MPC.

Extending the x-range is extremely important, but it is equally important to study the gluon polarization by measuring different final states, i.e neutral hadrons (η, π^0), charged hadrons, heavy flavor mesons and jets. Despite the fact that for some of these final states the statistical uncertainties might be larger, this will nonetheless allow us to determine systematic uncertainties due to restrictions in the current theoretical models. For example, currently all extractions of the gluon polarization are made at leading twist, but the leading-twist cross section is very small, and higher-twist contributions could become important. An example for such an effect is the sizable A_N, which is predicted to be small in pQCD at leading-twist level. Since it is very difficult to calculate such higher-twist contributions, the comparison of different final states allows one to test this experimentally as higher-twist contributions are process dependent. The higher luminosity at 500 GeV compared to 200 GeV will finally provide the possibility to measure some of the processes that depend on such high luminosities. The measurement of the direct photon asymmetry is thus within reach, offering an independent determination of ΔG. At RHIC, direct photon production is dominated by quark-gluon Compton scattering ($qg \rightarrow q\gamma$), which ensures that the double spin asymmetries from direct photon production provide clean theoretical access to the gluon polarization $\Delta g/g$. An advantage is also that the double helicity asymmetry will be linear in the gluon polarization; consequently, PHENIX will be able to constrain both the sign and magnitude of ΔG through this channel.

Figure 5.10 shows the preliminary PHENIX results for A_{LL}^{γ} from 2005 and 2006 (left plot) compared to the expected statistical uncertainties in 2015 (right plot). The plot clearly shows that a wider acceptance together with a higher integrated luminosity could im-

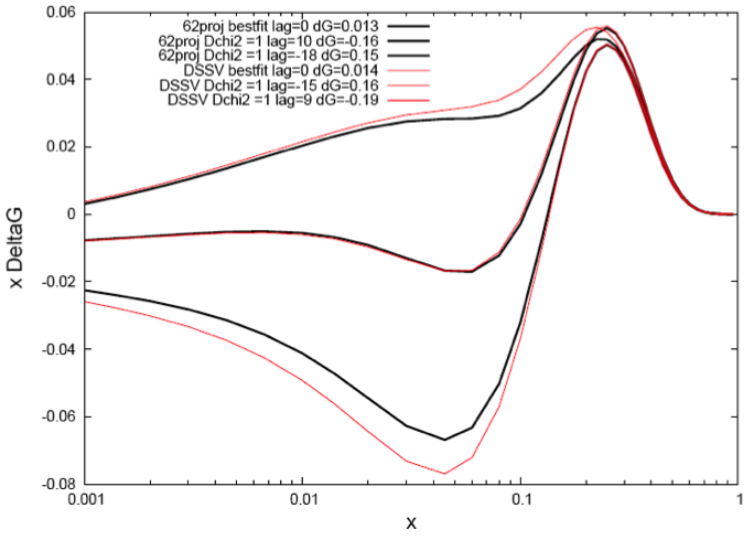

Figure 5.9: Impact on the uncertainties of the polarized gluon distribution by adding pseudo-data of $A_{LL}^{\pi^0}$ at $\sqrt{s}$ = 62 GeV to the datasets used in DSSV, assuming an integrated luminosity of 0.4 pb^{-1}. The reduction on the gluon polarization uncertainty is indicated by the reduction of the red band to the black one.

prove the statistical significance.

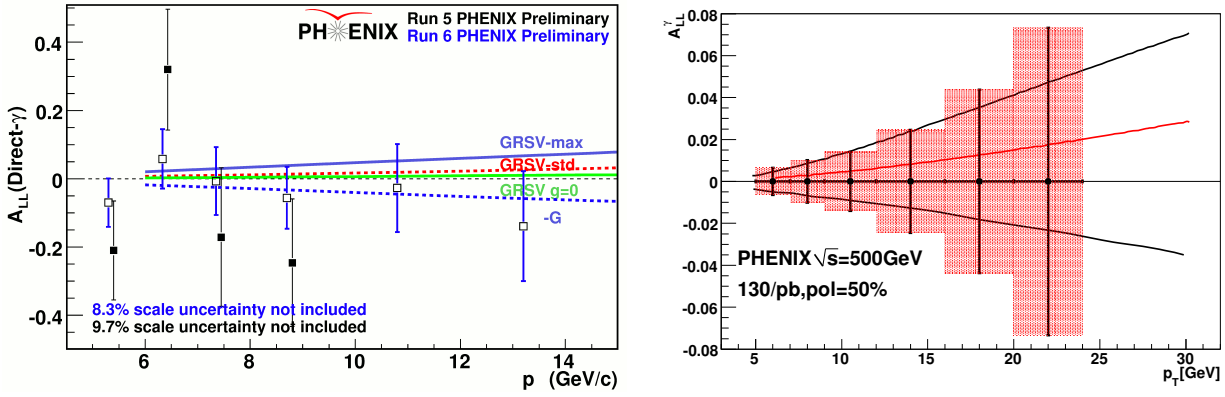

Figure 5.10: (left) Preliminary A_{LL}^{γ} for run-5 and run-6. (right) Expected uncertainties in A_{LL}^{γ} as a function of p_T for a recorded luminosity of 130 pb^{-1} and a polarization of 0.5. Only collisions with vertex inside $\pm$10 cm are included. The red curve corresponds to GRSV-std and the two black curves corresponded to GRSV-max and GRSV-min.

The measurement of a double spin asymmetry by detecting only the direct photon, typically as a function of p_T, necessarily involves a convolution over the momentum fractions of the colliding partons. In principle, if one could also detect the opposing quark jet, one may extract the shape of the gluon distribution more directly, as the initial momentum fractions x_A and x_B are now known in LO (though the flavors and gluon combinations

remain unknown and are summed over). This essentially allows a much more direct determination of the shape of the polarized gluon distribution. Unfortunately, the limited acceptance, $|\eta| \leq 0.35$, of the current PHENIX detector and the absence of hadronic calorimetry presently make it challenging for us to reconstruct jets. The availability of the VTX detector after 2010 may allow reconstruction of a jet axis (via charged particles alone) in a wider acceptance $|\eta| \leq 1.0$. Detailed studies of this technique are still underway. With the PHENIX central detector upgrade the direct photon channel becomes much easier to access (see Chapter 6).

With the installation of the vertex and forward vertex silicon detectors in PHENIX another channel sensitive to the gluon polarization becomes accessible. Open charm production in $p+p$ collisions at high energies as at RHIC is predominantly produced by gluon-gluon fusion. Measuring the double spin asymmetry for inclusive single electrons at midrapidity and for muons at forward rapidity, or for the correlation between an electron and a muon, as well as two muons in the muon arms, allows one to produce another constraint on the gluon polarization. As the open charm mesons are produced in gluon-gluon fusion, the process scales as the square of the polarized gluon distribution; thus, no access to the sign of the gluon polarization is possible. The vertex detectors are critical for this measurement, since only the requirement of a displaced vertex for the electron and muons can ensure that they are decay products from charmed mesons. Figure 5.11 shows the expected magnitude of $A_{LL}^{c\bar{c}}$ for single leptons and for correlations between leptons coming from charmed mesons based on the current knowledge of the gluon polarization from the fits to the world data [279].

For all configurations the asymmetries based on the polarized gluon distribution from DSSV [169], which is constrained by the PHENIX $A_{LL}^{\pi 0}$ and the STAR A_{LL}^{jet} data, are at the 0.001 level. Therefore a measurement of $A_{LL}^{c\bar{c}}$, which gives a constraint for Δg in global pQCD fits like DSSV, is only feasible with very high sampled luminosity or high polarization.

5.3 Transverse spin and spin-momentum correlations

In addition to the dedicated $p+p$ running at 500 GeV for the nucleon spin program, a significant amount of $p+p$ data at 200 GeV (40 pb^{-1} within $\pm$30 cm through 2015) and lower center-of-mass energies is anticipated over the next several years, driven primarily by the heavy ion program's requirements for $p+p$ reference data. This provides a good overlap with the luminosity needs for the transverse physics program at PHENIX. Currently the total recorded luminosity with transverse polarization is 8 pb^{-1} at 200 GeV with a beam polarization of 0.51 (2006) and 0.45 (2008). If a significantly larger transverse data set with PHENIX were collected it would give the opportunity to pursue currently marginal measurements with good statistical significance. For the MPC cluster transverse single-spin asymmetry, dominated by merged photons from π^0 decay, it would be extremely interest-

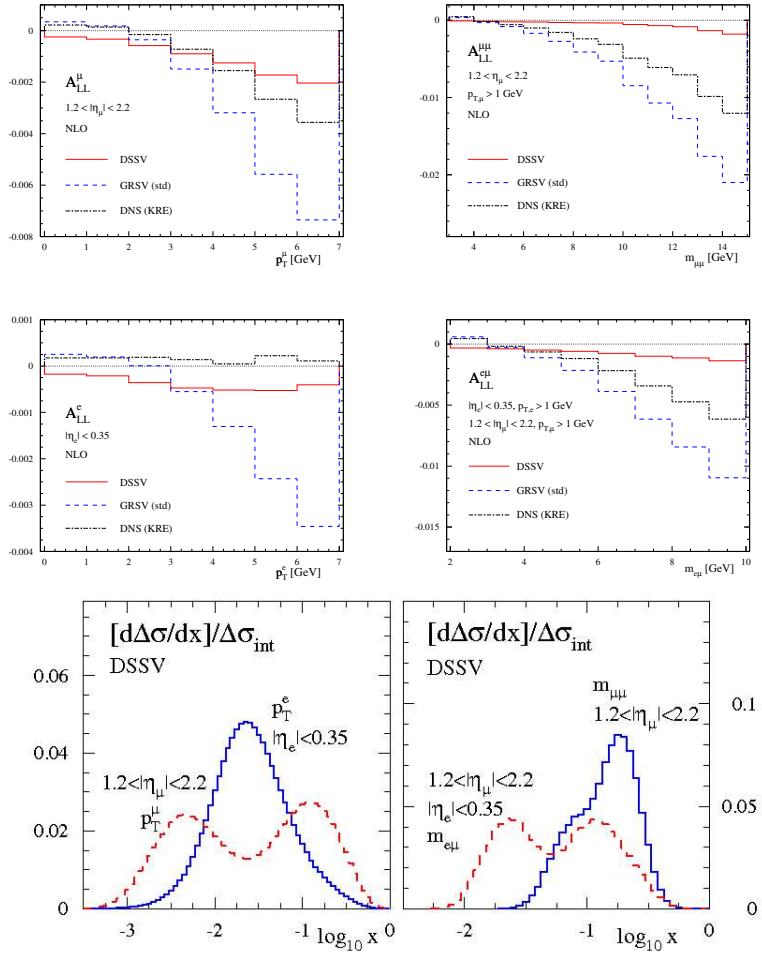

Figure 5.11: $A_{LL}^{c\bar{c}}$ for single electrons/muons (left column) and for correlations between leptons (right column) coming from charmed mesons for $\sqrt{s}$=200 GeV. In the last row the x coverage for these different asymmetries is shown.

ing to see the behavior at higher p_T more clearly as theoretical models based on collinear pQCD predict a drop of A_N at high p_T. As can be seen in Figure 5.12, we expect the data taken over the next several years to be able to clearly differentiate between models for the behavior of the asymmetry with transverse momentum.

Current results for $A_N^{J/\psi}$, plotted versus x_F in Figure 4.15 in Chapter 4, suggest a nonzero gluon Sivers function at moderately forward rapidity at the level of 3.3σ. Figure 5.13 gives the current results as a function of p_T and shows projections for future running. It is very important to confirm the observed asymmetry with higher significance and learn more about its behavior as a function of p_T.

Open heavy flavor SSA measurements offer another means of probing gluon dynamics in the proton. Similar to the longitudinal case, the availability of the vertex and forward ver-

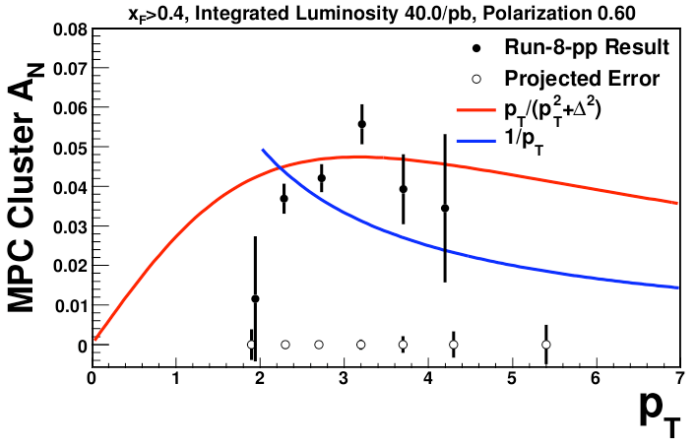

Figure 5.12: Current results for the cluster transverse SSA in the MPC as a function of p_T and projected uncertainties for 40 pb^{-1} and 60% polarization. The two curves shown are for two different models of the behavior of the asymmetry.

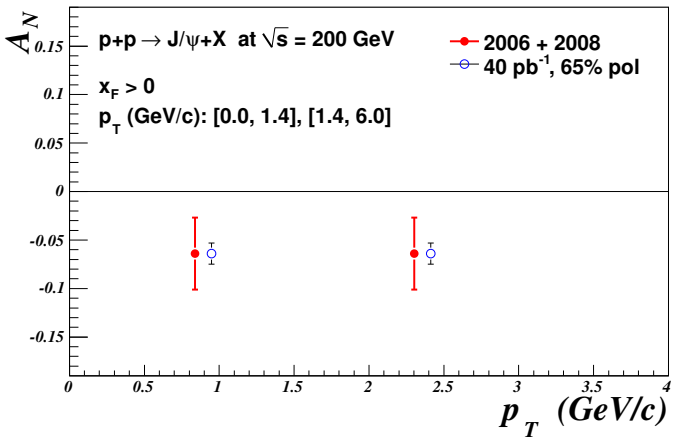

Figure 5.13: Current results for J/ψ A_N as a function of p_T measured at forward rapidity in the muon arms, and projected uncertainties for 40 pb^{-1} and 65% polarization.

tex silicon detectors make it possible to measure the single spin asymmetries for leptons coming from charmed mesons, greatly improving upon the current preliminary measurement shown in Figure 5.14. This gives a unique opportunity to measure the currently unknown Sivers function for gluons as a function of rapidity (-2.4 $< \eta <$ 2.4) and x_F. The comparison of $A_N^{c\bar{c}}$ with $A_N^{\pi^0}$ from the central arm, which is dominated by gluon-gluon interactions at low to moderate p_T, and with $A_N^{J/\psi}$ from the central and muon arms offers the opportunity to study, for the same observable with the same detector, the magnitude of the factorization breaking [280] due to the different color interactions for different final states. For illustration Figure 5.15 shows the expected size of the $A_N^{c\bar{c}}$ based on calculations from [90].

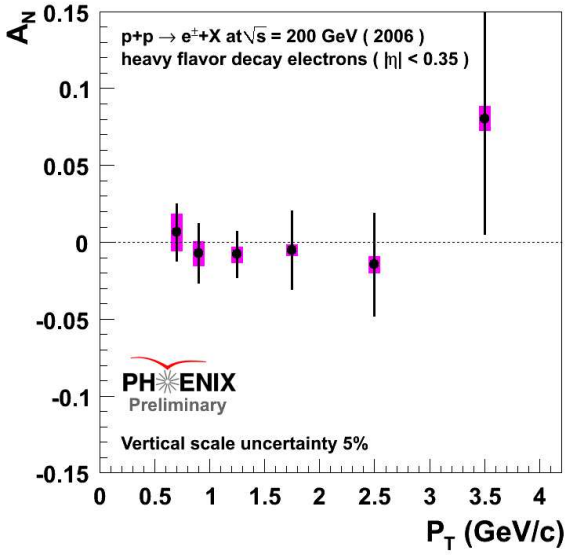

Figure 5.14: Single spin asymmetry $A_N^{c\bar{c}}$ for heavy flavor decay electrons measured in the PHENIX central arm spectrometer.

All the measurements described above suffer unfortunately from the problem of factorization/universality breaking as described in [280]. This is different for the dihadron interference fragmentation function (IFF), suggested first in [162], which describes the production of unpolarized hadron pairs in a jet from a transversely polarized quark. The transverse polarization is translated into an azimuthal modulation of the yields of hadron pairs around the jet axis. In addition the IFF is chiral odd and can therefore act as a partner for the likewise chiral odd quark-transversity function. The resulting amplitude is chiral even and therefore leads to observable effects in semi-inclusive deep inelastic scattering off a transversely polarized target [69], or in $p+p$ collisions in which one beam is transversely polarized. The first measurement of the IFF was done by BELLE [311], which enables the determination of transversity.

There are a number of advantages related to this method, which are connected to the additional degree of freedom provided by the second hadron. It allows one to define the azimuthal angle between the two hadrons as a leading-twist observable in the transverse plane and at the same time integrate over transverse momenta of the quarks and hadrons involved. Because transverse momenta are integrated over, known collinear schemes in factorization and evolution can be used which do not need assumptions of the intrinsic transverse momenta [152]. Since the IFF is not a transverse momentum dependent function (TMD) it is universal and therefore directly applicable to SIDIS and $p+p$ data. In fact, the IFF measurements could be compared with charged hadron A_N (as measured through decay muons in the same acceptance). An interpretation of these data in the TMD-based approach and a comparison with the IFF measurements would help establish the size of TMD factorization breaking effects in polarized $p+p$ collisions at RHIC. The

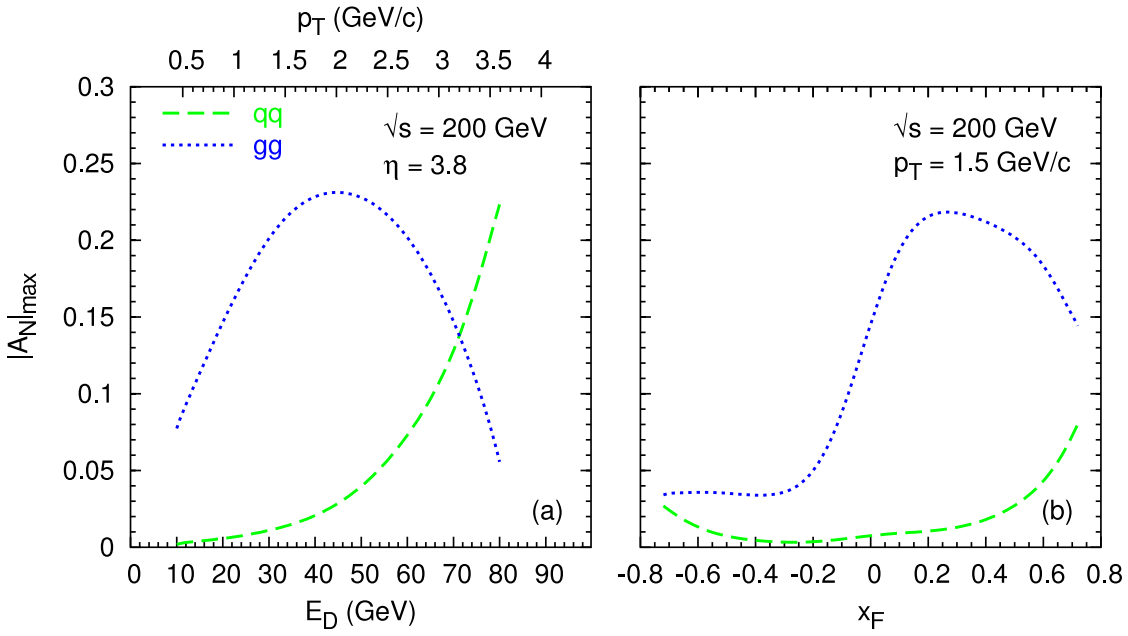

Figure 5.15: Maximized values of $|A_N|$ for inclusive charm meson production as a function of E_D and p_T at fixed pseudorapidity (a), and as a function of x_F at fixed transverse momentum, calculated using saturated Sivers functions. The dashed line corresponds to a maximized quark Sivers function (with the gluon Sivers function set to zero), while the dotted line corresponds to a maximized gluon Sivers function (with the quark Sivers function set to zero).

currently available PHENIX data and the expected statistical uncertainties after collecting 40 pb^{-1} with transversely polarized p+p collisions, see Figure 5.16 could be significantly expanded by having a larger data set and going to much larger x_F by exploring correlations between hadrons in the central detector and the MPC and correlations when both hadrons are in the MPC.

The possibilities for measuring A_N for Drell-Yan during a $\sqrt{s}$=200 GeV transverse polarized p+p run are discussed in section 6.1.1.

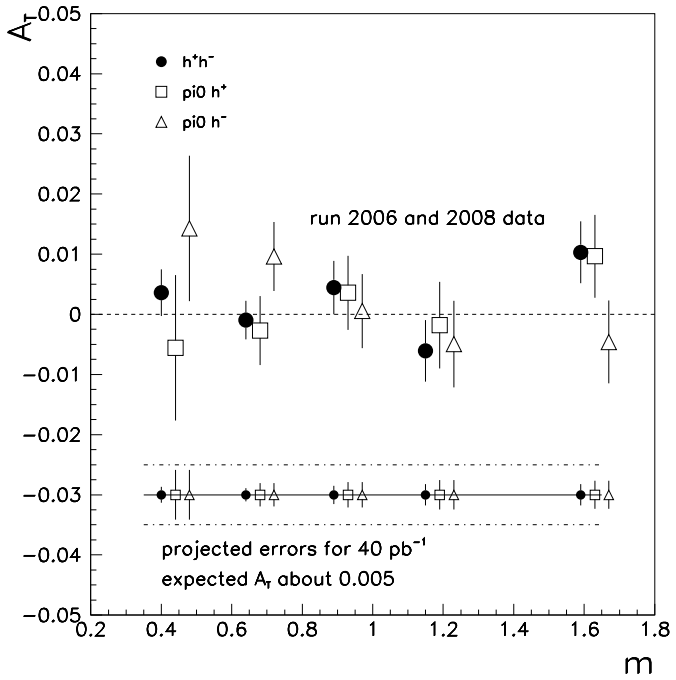

Figure 5.16: Single spin asymmetry for different combinations of hadron pairs in the central arm plotted vs. the mass of the hadron pair for run-6 and 8 combined. Also shown are the expected statistical uncertainties after collecting 40 pb^{-1} over the next 5 years. This observable is sensitive to transversity times the IFF.

Chapter 6

Nucleon Structure Physics: sPHENIX Plan

The state of the our knowledge of nucleon structure physics will see major advances over the five years 2010–2015, as described in the previous Chapter. These measurements will open the door to a new frontier of spin structure physics that requires increased luminosities and new detector capabilities, in particular with larger coverage at very forward angles. We see the quest to understand parton *dynamics* within hadrons as the new frontier in RHIC spin studies. We also anticipate opportunities to improve our knowledge of the momentum fraction dependence of $\Delta g(x)$, as well as completely new avenues for the study of both longitudinal and transverse spin effects when polarized ^{3}He beams become available at RHIC and the possible increase in beam energies. We detail these areas in the following three sections:

- Dynamical Origins of Spin-Dependent Interactions
- New Probes of Longitudinal Spin Effects
- Measurements with Polarized He^3 and Increased Energies

We note that the physics plan presented in this Chapter assumes that the primary goals in terms of flavor-separated sea quark helicity distributions and $\Delta g(x)$ from the Midterm Plan (as detailed in Chapter 5) are achieved.

6.1 Dynamical Origins of Spin-Dependent Interactions

In order to obtain a deeper understanding of the dynamical origins of partonic interactions in both spin-dependent and spin-independent hadronic and lepton-hadron interactions, one must move beyond the simple collinear perturbative QCD picture. There are

currently two areas to pursue this dynamical understanding. The first is via the study of transverse momentum dependent (TMD) parton distribution functions (PDFs) and fragmentation functions (FFs), which we specifically address here with measurements with an upgraded PHENIX detector. The second is via the study of generalized parton distributions (GPDs), which are addressed via exclusive reactions at Jlab and a future Electron-Ion Collider. The theoretical challenges involving factorization and universality for TMD PDFs and FFs have been discussed previously in Chapter 4 and Chapter 5. Polarized $p+p$ collisions in RHIC give the unique opportunity to test the theoretical assumptions in the underlying formalism for k_t-dependent parton distribution functions by testing the prediction for the sign change for the analyzing power of the Sivers function in Drell-Yan (DY) and semi-inclusive deep inelastic scattering (SIDIS). Further measurements of observables sensitive to the factorization and universality breaking in TMDs (i.e. Sivers function via γ-jet) will allow us to gain a deeper understanding of the partonic dynamics that leads to the breaking of factorization and universality for these processes.

In this Chapter we identify the key measurements needed to access this exciting physics, and detail the basic detector and luminosity requirements to make those measurements. A proposed suite of upgrades to the PHENIX detector to realize this physics is then presented in Chapter 7.

6.1.1 Drell-Yan in transversely polarized $p+p$ scattering

Current Theoretical Understanding Large transverse single-spin asymmetries (SSAs) have presented a challenge to theory since 1976, when the first A_N was measured at ZGS at ANL [220], because in collinear pQCD at leading twist a sizable A_N is not expected, due to the chiral properties of the theory [214]. Transverse single-spin asymmetries (SSAs) for particle production have been measured at RHIC and surprisingly found to also be large, particularly for meson production in the forward direction [24, 19, 106]. The measured quantity is the analyzing power, A_N, corresponding to a left-right asymmetry of the produced particles when vertical polarization is used. The observation of a large A_N for inclusive pion production in $p^{\uparrow}+p$ collisions over a broad range of collision energies [133, 137, 23, 22, 229, 84, 282, 134, 220, 178] together with the observation of single spin asymmetries in semi-inclusive deep inelastic scattering [70, 67, 66, 63, 62, 61, 82, 59, 77] have prompted extensions to pQCD that introduce partonic transverse momentum that is correlated with the spin degree of freedom. For example, A_N could be generated by spin-correlated TMD fragmentation if there is transverse quark polarization in a transversely polarized proton – the so-called Collins effect [160]. Spin-correlated TMD parton distribution functions (referred to as Sivers functions) can also explain a large A_N [286, 287]. These distribution functions describe partonic orbital motion within the proton, and so are important for understanding the dynamical workings of the proton.

In SIDIS, the mesonic fragments from the bare constituent quark are observed to vary with azimuthal angle for measurements with a transversely polarized proton target. The

Collins effect can be separated from the Sivers effect in these measurements, and each separately has been measured experimentally to be nonzero. The Sivers effect requires a correlation of the form $\vec{S}_p \bullet (\vec{p}_\pi \times \vec{q})$, where $\vec{S}_p$ refers to the proton spin, $\vec{p}_\pi$ refers to the final-state pion momentum, and $\vec{q}$ refers to the quark momentum. A color-charge interaction between the current quark and the spectators is required by gauge invariance, and results in the Sivers effect being an allowed leading-twist effect [139]. This color-charge interaction occurs in the final state in SIDIS, and is necessarily attractive [144], as expected since the proton is initially color neutral, meaning that the current quark and the spectators must have equal magnitude, but opposite sign color charges.

Phenomenological fits to extract the Sivers function from SIDIS as well as the Collins FF from SIDIS and e^+e^- data have been made [94, 93]. Model calculations [132] that presume that TMD distribution functions can be included in a factorized calculation were first found to be consistent with transverse SSAs measured for pion production at RHIC energies, using the phenomenological fits to SIDIS results. More refined calculations [89] show that the Sivers effect alone cannot describe the A_N measurements.

An alternative approach to describe the underlying subprocesses contributing to A_N is based on collinear pQCD using higher-twist quark-gluon correlators. This method has a proven factorized form for inclusive meson production [267]. Phenomenological fits to the quark-gluon correlators give a good description of the x_F dependence of inclusive meson production. However, these fits do not currently account for any Collins effect contribution. It has been found that moments of the Sivers functions extracted in the TMD formalism from SIDIS data are related to the quark-gluon correlators in the collinear twist-3 pQCD approach [213].

The intense interest in the understanding of transverse SSAs has resulted in numerous theoretical predictions of quantities sensitive to color-charge interactions. However, after significant theoretical work, it has been recognized [280] that there is no factorization of TMD distributions nor fragmentation functions in $p+p$ interactions that produce hadronic final states. This is in contrast to the case for SIDIS and Drell-Yan production, where robust factorization theorems exist [85, 163, 212], since the color structure of these processes is particularly simple.

Furthermore the attractive final-state interaction in SIDIS becomes a repulsive initial-state interaction in the DY production of a virtual photon. Present theoretical understanding of transverse SSAs then predicts that the sign of the analyzing power for DY will be opposite to that observed in SIDIS (see Figure 6.1). This fact is independent of whether the DY analyzing power is calculated in a TMD or collinear twist-3 pQCD approach. The test of this theoretical prediction is the primary objective of the most recent update (2008) to Performance Measures by the Nuclear Science Advisory Committee [9] HP13. This test is also a major focus of the PHENIX upgraded spin program.

Figure 6.2 shows the calculation for A_N of DY based on a TMD approach utilizing the gauge link formalism from [216] for transversely polarized $p+p$ collisions at RHIC energies ($\sqrt{s} = 200\,\text{GeV}$ and 500 GeV) as a function of rapidity and Feynman x_F ($x_F =$

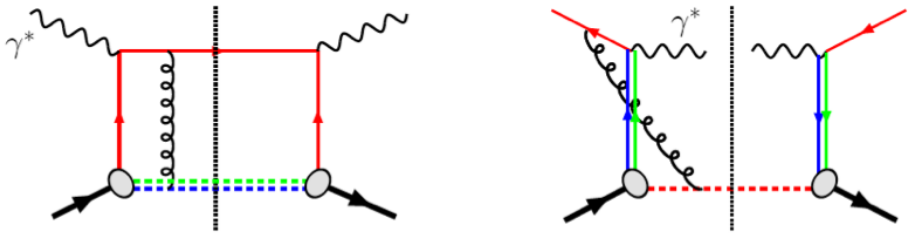

Figure 6.1: Feynman diagram for SIDIS (left) and Drell-Yan (right) showing the color structure and the final- and initial-state interaction via gluon exchange.

$Q/\sqrt{s} \cdot (e^y - e^{-y})$). Similar results have also been obtained by the Torino group [95].

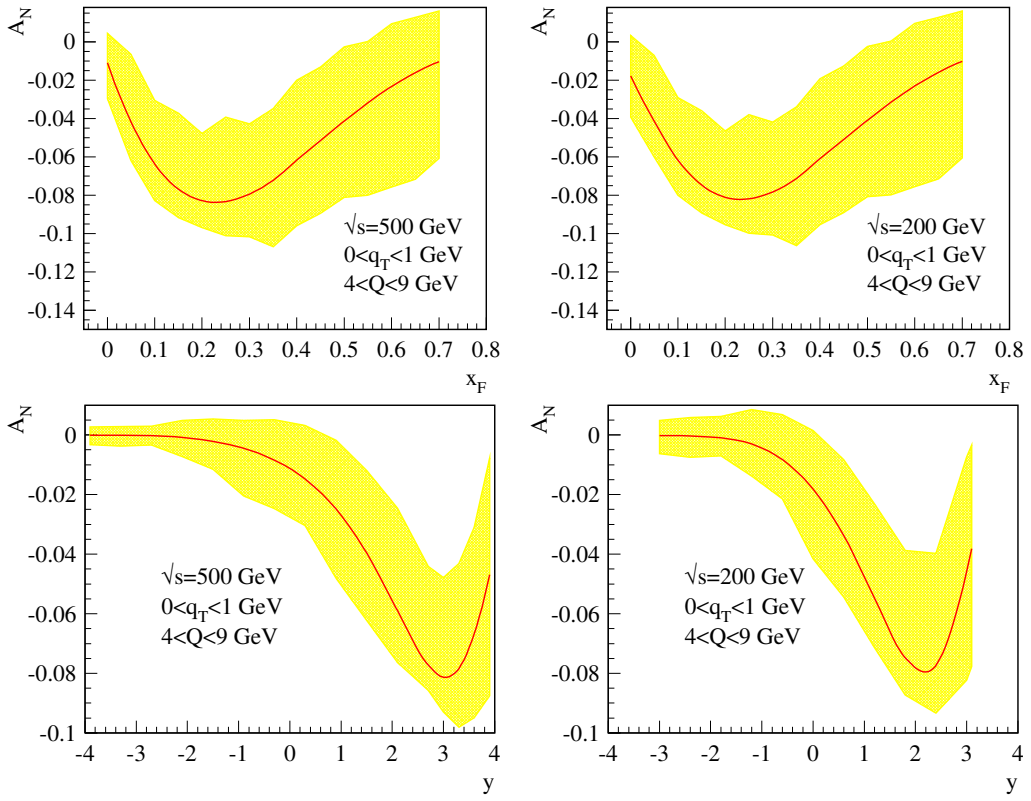

Figure 6.2: A_N as function of Feynman x_F (top) and rapidity (bottom) for Drell-Yan for $\sqrt{s} = 500$ GeV (left) and 200 GeV (right). Note that only forward x_F corresponding to positive rapidities is shown in the upper panels. The uncertainties shown as yellow bands are a result of the uncertainties from the Sivers function extraction from the SIDIS data.

A precision measurement of A_N for Drell-Yan will lead to an immediate advance in our understanding. A nonzero A_N for DY production would be consistent with the presence of a correlation between the spin of the proton and the intrinsic transverse momentum of

the quarks inside the proton. A nonzero and negative A_N for DY production, as predicted by theories that include gauge links in their formalism, would suggest that the k_T factorization for DY production is indeed robust. A way to view the gauge link impacts on DY and on semi-inclusive deep inelastic scattering is that unlike colored charges have an attractive interaction and like colored charges have a repulsive interaction. A nonzero and positive A_N for DY production, opposite to theories that include the gauge link, would challenge k_T factorization theorems for the DY process. However, if one finds A_N for DY production to be zero, this would mean that our present description of transverse SSAs measured in semi-inclusive deep inelastic scattering and for pion production analyzing powers is incorrect (or at least substantially incomplete).

There are plans by several other laboratories (JPARC, FAIR, Fermilab) to measure the transverse SSA in DY production. Only one other plan has a time scale comparable to or shorter than the plan presented here for a PHENIX measurement. The COMPASS collaboration plans to measure the analyzing power for DY production using high-energy pion beams incident on a transversely polarized proton target [10] The kinematics covered by the COMPASS experiment are very complementary to what is proposed here, leading to a well integrated world program if both measurements are made.

Experimental Measurement of Drell-Yan A_N The original RHIC Drell-Yan planning document [128] submitted for consideration to the 2007 Long Range Plan by the Nuclear Science Advisory Committee concluded that a transverse spin DY measurement at RHIC is optimized by running at $\sqrt{s} = 200$ GeV. New studies indicate that the sensitivity is increased by running at the higher energy $\sqrt{s} = 500$ GeV. Thus, we first update the discussion on the optimum energy as originally detailed in [128]. The hard-scattering, partonic-level cross section ($\hat{\sigma}$) for $q\bar{q} \to \gamma^*$ is proportional to $1/\hat{s}$, where $\hat{s}$ is the squared collision energy in the partonic center of mass. The DY cross section for $p + p \to \gamma^* + X$ is a convolution of $\hat{\sigma}$ with quark and antiquark distribution functions. The parton densities, especially the sea quark densities, have a strong increase with the center of mass energy and lower x. This increased partonic-level luminosity is the reason for the larger dilepton yields as the collision energy increases, as shown in Figure 6.3.

Another reason to prefer $\sqrt{s} = 500$ GeV over $\sqrt{s} = 200$ GeV polarized proton collisions is the growth of the collision luminosity with $\sqrt{s}$, caused by the smaller transverse size of the beams at higher energy. The current projections from CAD indicated a factor of 3–5 luminosity increase going from 200 GeV to 500 GeV [5].

The existing PHENIX forward muon spectrometers are ready to make a measurement of the transverse SSA for DY production via dimuons. The muon spectrometers have acceptance for DY rapidity $1.2 < y_{DY} < 2.2$ in the south arm and $1.2 < y_{DY} < 2.4$ in the north arm. Thus, the x_F coverage is primarily below $x_F < 0.1$ where the predicted asymmetry is decreasing, though nonzero, as shown in Figure 6.2. With a $p+p$ at $\sqrt{s} = 500$ GeV sampled luminosity of $110\,\text{pb}^{-1}$ within the z-vertex acceptance range of $|z| < 30$ cm, with a predicted $A_N \approx 4 - 5\%$ in the muon arm rapidity interval, we project a 3σ statistical

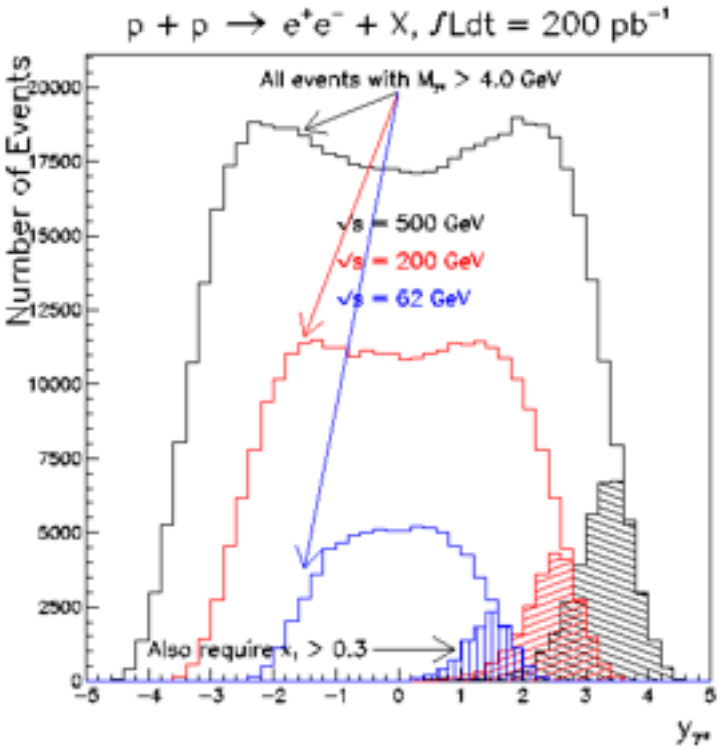

Figure 6.3: The number of dielectron events from virtual photon production with a mass greater than 4 GeV/c^2 as simulated by PYTHIA 6.222, distributed according to the rapidity of the virtual photon. The integrated luminosity is 200 pb^{-1} for all collision energies. As the collision energy increases, the rapidity distribution broadens, given the increased phase space, and the dielectron cross section increases, even though the hard scattering DY cross section decreases. The increase in the dielectron cross section is a consequence of an increase in the partonic luminosity as the collision energy increases.

significance for a nonzero A_N. This projection assumes that backgrounds are suppressed using additional cuts from the FVTX for DY invariant masses greater than 4 GeV/c^2. This assumption is nontrivial given the larger contribution of correlated dimuons from charm and beauty in this rapidity and invariant mass range. Such a measurement requires substantial running time of p+p at $\sqrt{s}$ = 500 GeV with transverse polarization—which is not envisioned during the 2010-2015 time frame as detailed in Section B.2. It is notable that the PHENIX muon arms will allow for the measurement of the DY cross section in the rapidity range $1.2 < y_{DY} < 2.4$ already during the longitudinal polarized p+p running at $\sqrt{s} = 500$ GeV. In the current Midterm Plan running, there is 34 pb^{-1} of p+p at $\sqrt{s}$ = 200 GeV with transverse polarization (that also serves as heavy ion comparison running). These results could result in a 2σ measurement of A_N away from zero – though this does not account for the lower Drell-Yan signal to background ratio at the lower colliding energy. Therefore, the Drell-Yan measurements in the 2010–2015 timeframe should be regarded as exploratory. While these measurements will be vital to initiating the PHENIX Drell-Yan physics program, additional running time beyond 2015 will be required.

We believe that ultimately it will be crucial to answer these physics questions definitively, which necessitates a larger acceptance extending to the most forward rapidities $2 < y_{DY} < 4$. Note that a measurement with a new forward spectrometer of A_N^{DY} for y_{DY} = 3–4 at $\sqrt{s}$ = 500 GeV with an uncertainty corresponding to 6σ from zero requires a sampled luminosity of 110 pb^{-1} within the z-vertex range $|z| < 30$ cm. This indicates that a definitive measurement is achievable with the right detector. Thus, PHENIX is considering a proposal to remove one of the muon spectrometers and replace it with a forward angle spectrometer shown schematically in Figure 6.4. The specific details of the proposal and the R&D and simulations necessary to formulate a concrete design are given in Section 7.2. The proposed spectrometer has an open geometry and covers a single particle pseudorapidity range from $2.0 < \eta < 4.0$ with excellent electron identification. The decision to pursue the DY measurement via dielectrons (as opposed to dimuons) is in part driven by our interest to have this forward spectrometer also serve as a detector for measuring the scattering lepton in e+p and e+A collisions at a future Electron-Ion Collider (EIC) – as detailed in Chapter 8. There are also important measurements related to transverse physics that require photon and full reconstructed jets that are enabled by this design – as discussed later in Section 6.1.2. There has been discussion of extending the rapidity range of the current muon spectrometers with a new detector behind the muon magnet piston. However, since that would not address the EIC physics and nonmuon physics channels, we have focused on the electron spectrometer design.

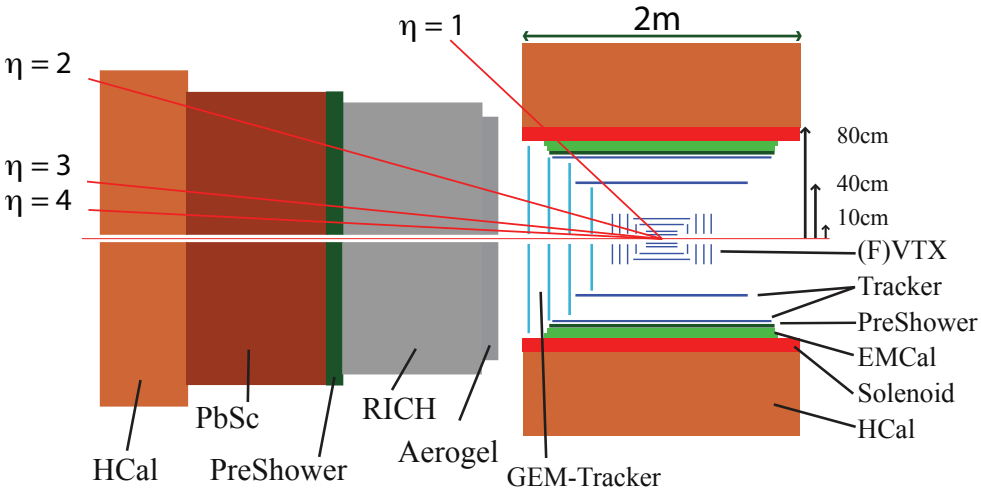

Figure 6.4: Schematic layout of the new forward spectrometer integrated into the upgraded sPHENIX detector, as detailed in Chapter 7.

In this early stage of simulations, we have utilized the PYTHIA simulation to understand the major sources of background to the DY measurement as a function of rapidity. The major sources of correlation opposite sign dielectrons are:

- Open charm ($c\bar{c} \rightarrow e^+e^- + X$)

- Open beauty ($b\bar{b} \rightarrow e^+e^- + X$)
- Hadronic background from QCD $2 \rightarrow 2$
- Photon conversion in the beampipe and other materials

The contribution from open heavy flavor due to the semileptonic decay of both D and $\overline{D}$ or B and $\overline{B}$ for example, is a significant source of background for the Drell-Yan measurement near midrapidity and for invariant masses below the Upsilon states. However, for rapidities $y > 3$ studies indicate that the open heavy flavor contributions are below that of Drell-Yan for invariant masses $M > 4\,\mathrm{GeV}/c^2$. This result is understood because $c\bar{c}$ and $b\bar{b}$ pairs are predominantly produced in $p+p$ reactions via gluon-gluon fusion. At very forward rapidities, this necessarily involves a very low-x and a very high-x gluon. The low abundance of such high-x gluons suppresses the heavy flavor production. Additionally, the open heavy flavor contribution can be even further suppressed by selecting against leptons with a displaced vertex relative to the interaction point. This anti-displaced vertex selection will already be possible with the FVTX.

Figure 6.5 shows a PYTHIA simulation result for the invariant mass dependence of the DY cross section (open symbols) for $p+p$ collisions at $\sqrt{s} = 500\,\mathrm{GeV}$. The different colors correspond to different pseudorapidity selections on the two decay electrons. It is notable that for DY with $p_T << M$, the DY rapidity $y_{DY} \approx 0.5 \times (\eta_{e^+} + \eta_{e^-})$. Thus, the selection for electrons with $\eta > 3$ yields a subset of DY with $y_{DY} > 3$. Also, the simulation was run with PYTHIA settings CKIN(1) = 3 GeV ($\hat{m} = \sqrt{\hat{s}}_{\mathrm{min}}$) and CKIN(3) = 1.5 GeV ($\hat{p_T}_{\mathrm{min}}$) and thus the results are only meaningful for invariant masses $M > 3\,\mathrm{GeV}/c^2$. Also shown are all charged track pairs, electrons and hadrons, from minimum bias PYTHIA events (closed symbols). For the most forward rapidity selection a suppression of 10^{-6} is needed to have a Drell-Yan signal-to-background of 1:1.

For the most forward rapidity, which is also the most sensitive to the predicted large DY A_N, the background has a large contribution from QCD $2 \rightarrow 2$ processes. Thus, any detector designed for this measurement requires excellent electron identification to reject hadron and photon backgrounds. In order to study various scenarios for achieving the required rejection, we have implemented a fast detector simulation consistent with our proposed forward spectrometer upgrade. The spectrometer consists of a tracking detector (TRACK) in a magnetic field, a ring imaging Čerenkov counter (RICH), an electromagnetic calorimeter (EMCal), and an hadronic calorimeter (HCAL). The following conservative assumptions in terms of parameterized performance have been made.

- TRACK has a momentum resolution of $\Delta p/p \approx 2\%$.
- RICH has an electron efficiency of 94% for $p > 10\,\mathrm{GeV}/c$.
- EMCal has the resolution of the current PHENIX PbGl: $5.95\%/\sqrt{E} + 0.76\%$
- HCAL has the resolution: $50\%/\sqrt{E} + 5\%$ (similar to CMS or LHCb)

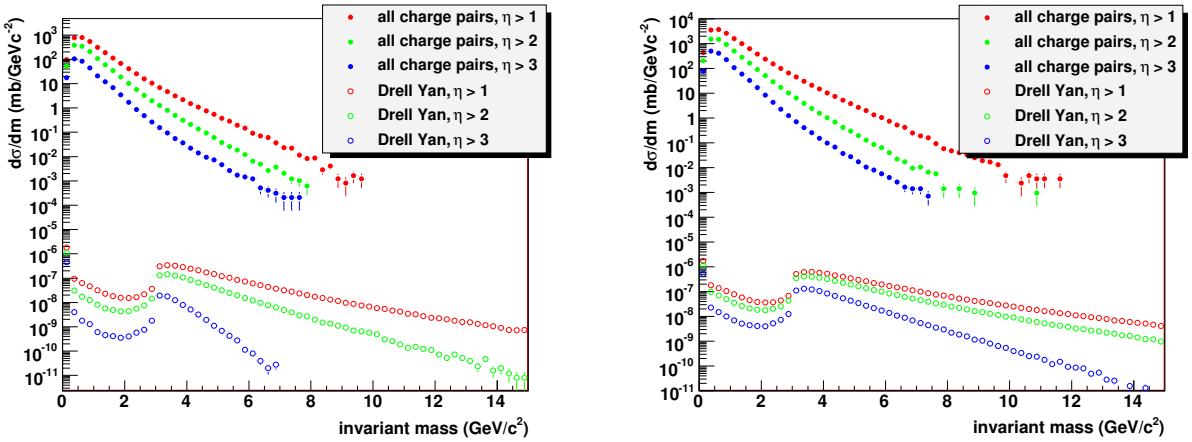

Figure 6.5: Invariant mass dependence for the Drell-Yan signal (open symbols) and for the background from minimum bias QCD processes resulting in dielectron and dihadron pairs (closed symbols). There are three different forward angle selections for the resulting electrons/hadrons. The left (right) panel corresponds to collisions at $\sqrt{s} = 200\,\text{GeV}$ ($\sqrt{s} = 500\,\text{GeV}$).

We then run our signal and background PYTHIA events through the fast simulation with the following selections: minimum EMCal energy > 1 GeV, $0.8 < E_{\text{EMCal}}/p < 1.25$, RICH detector hit correlated with TRACK, and a minimum HCAL energy cut.

The resulting invariant mass distributions after cuts are applied are shown in Figure 6.6. One can see that for the most forward rapidity selection, the background contribution is dropping very steeply as a function of invariant mass. Though additional statistics in the simulation are necessary for any final conclusion, it appears that for $\eta_{lepton} > 3$ selection and $M_{e-e+} > 4$ GeV$/c^2$ the Drell-Yan is becoming the dominant process. One wants to extend the kinematic range of the measurement over lower rapidities as well, and thus we describe below additional background rejection methods that we are exploring. Also, we have currently placed separate cuts on a number of individual detector response quantities, while in the future an optimized electron probability selection will improve the background rejection while maintaining high electron efficiency. It is clear that full GEANT based simulations are required for a final design, but the initial fast simulation results are quite encouraging.

The above background rejections require robust discrimination between neutral and charged showering particles. This discrimination is achieved with a highly efficient track pointing to the EMCal or with a coarse position sensitive scintillator array at the front of the EMCal. Additionally, the EMCal energy and TRACK momentum match selection reduces the hadron background by more than a factor of 100.

Further hadron-lepton separation is achieved by identifying lepton pair candidates for which there is no energy deposition in the hadronic calorimeter for at least one of the

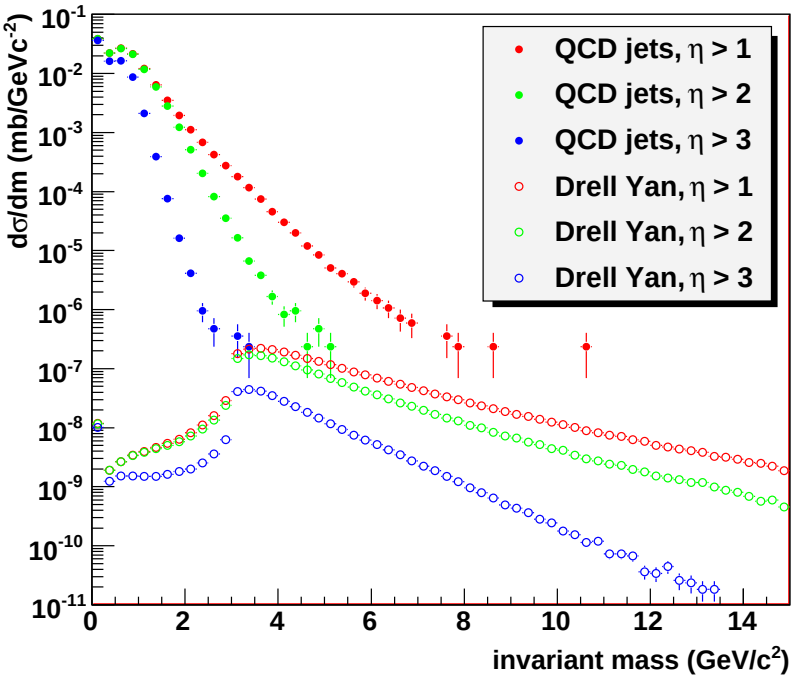

Figure 6.6: Invariant mass dependence for the DY and the minimum bias cross section for electron pairs for different lepton pseudorapidity selections after applying cuts on detector responses in the RICH, the EMCal and the HCAL ($\sqrt{s} = 500\,\text{GeV}$).

particles in the pair. We expect to have charge sign identification via TRACK, and this reduces the background by an additional $\sim 20\%$.

A preshower detector in front of the EMCal can be also used to isolate photon conversions prior to the EMCal. Some photons will be converted to electron-positron pairs in upstream materials. For high-energy photons, the opening angle of conversion e^+e^- pairs is small. Separating the 2-MIP responses from 1-MIP responses in the preshower detector can identify these pairs. There is a small probability that photons convert in the preshower detector itself; the impact of these needs to estimated in a detailed MC detector simulation. A large fraction of the photons come from the decay of π^0's, which can be suppressed by reconstructing their invariant mass with the EMCal. The preshower detector provides important discrimination between leptons and hadrons, which is accomplished with the passive radiator that initiates electromagnetic showers that deposit typically much more energy in the scintillator than minimum ionizing particles. No cut was yet applied on the preshower detector, which should reduce hadron contamination even further.

There are also important kinematic cuts that can increase the signal to background ratio. Figure 6.7 shows the energy correlation between the two DY leptons and their opening angle depending on the pseudorapidity of both leptons, and the invariant mass for minimum bias lepton and hadron pairs, both for a series of minimum energy cuts on each lepton/hadron. The opening angle for different pseudorapidities is also shown. For both QCD minimum bias unlike-sign pairs and DY lepton pairs the opening angle is reduced going to more forward pseudorapidity. The energy of each of the DY leptons is above 15 GeV for $\eta > 3$ and $M_{ee} > 3$ GeV; this allows one to apply a minimum energy cut on the each of the partners in the pairs from minimum bias events, limiting their invariant mass to below 3 GeV for pairs with $\eta > 3$. We are continuing to explore the utilization of various cuts.

6.1.2 Jet, photonic, and hadronic observables with transversely polarized $p+p$ collisions

There are other measurement channels for disentangling the underlying subprocesses in single spin asymmetries, though with different caveats compared with the theoretically clean Drell-Yan channel previously discussed. These other important channels are measurable with the same forward spectrometer upgrade depicted in Figure 6.4. There are specific measurements sensitive to the Sivers function and others directly sensitive to the Collins function.

Measuring the analyzing power for forward inclusive jet production probes the Sivers effect [322, 226], because a nonzero analyzing power for the produced jets can result only from initial-state effects. This is because all effects from spin-dependent fragmentation functions (i.e. the Collins fragmentation function) are unresolved by full jet reconstruction. The same argument holds for the measurement of direct photon-jet production.

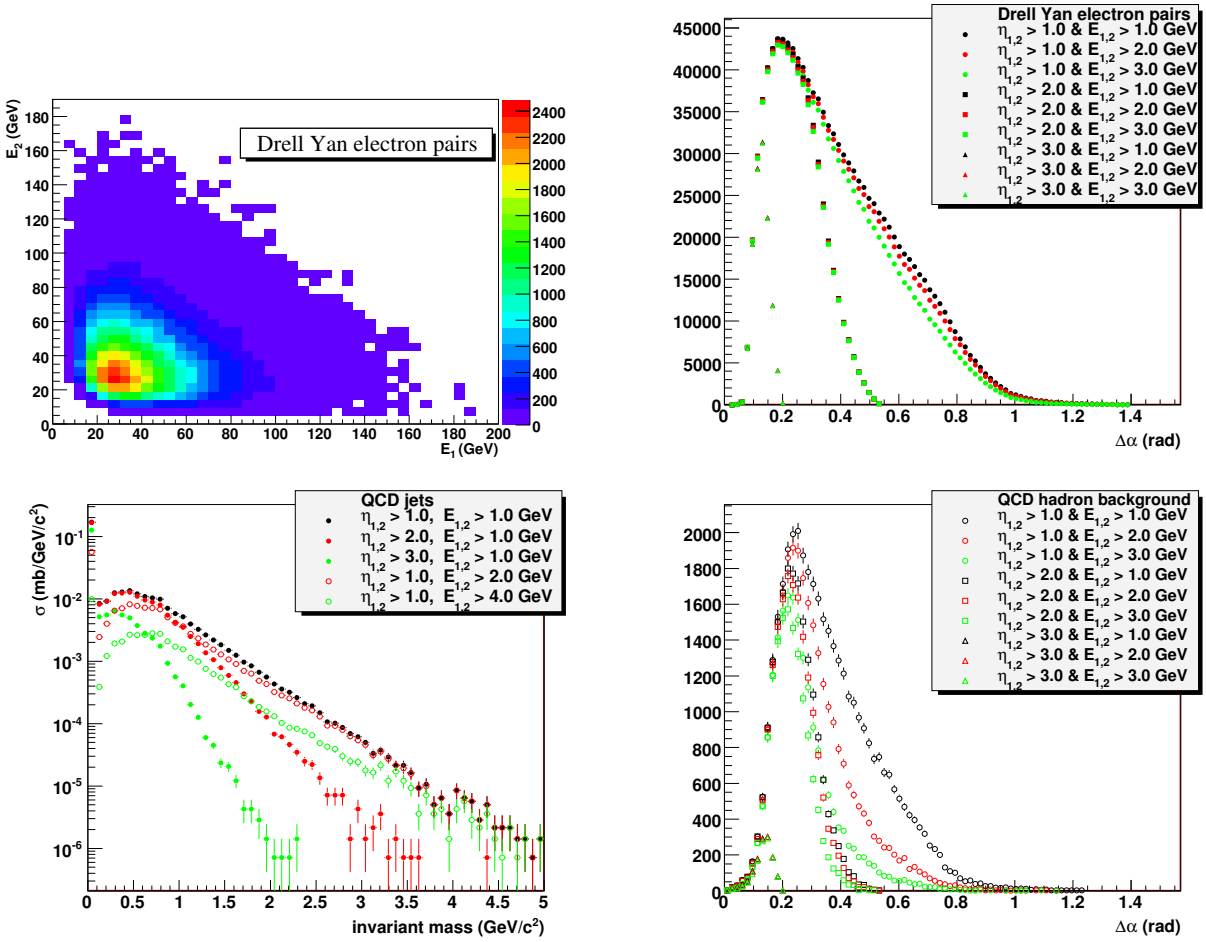

Figure 6.7: (Upper Left) Energy correlation between the two Drell-Yan decay leptons. (Upper Right) Opening angle ($\Delta\alpha$) between the two decay leptons for different selections on the lepton pseudorapidity (η) and Energy ($E_{1,2}$). (Lower Left) Invariant mass for minimum bias lepton and hadron pairs for different minimum energy selections on each lepton/hadron. (Lower Right) Opening angle ($\Delta\alpha$) for all hadron pair backgrounds for different selections on on the lepton pseudorapidity (η) and Energy ($E_{1,2}$). All plots are for DY produced in p+p collisions at $\sqrt{s} = 500$ GeV.

Again a nonzero analyzing power only results from the Sivers effect as all spin-dependent fragmentation effects cancel out. This measurement has the additional advantage that in leading-order (LO) pQCD, the momentum fractions of the partons involved in the hard interaction are directly correlated to the rapidity of the observed jet and direct photon, as shown in Figure 6.8. The proposed forward upgrade with full EMCal and HCAL coverage has excellent capabilities in both the inclusive jet and photon-jet channels.

The anticipated asymmetry in the photon-jet channel is shown in Figure 6.9. As noted previously, this prediction assumes TMD factorization. Therefore, a comparison between the

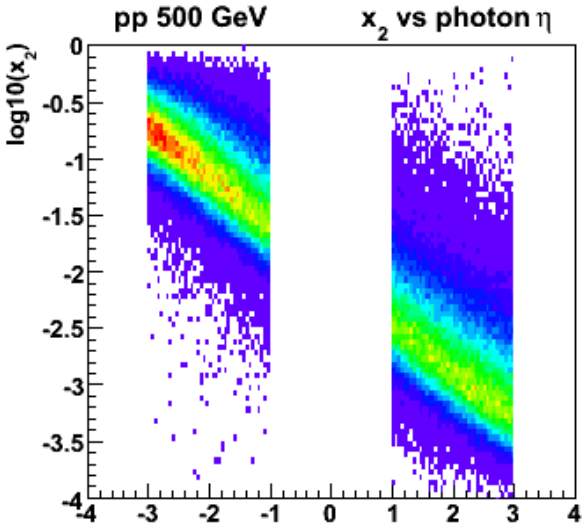

Figure 6.8: Rapidity-x correlation for direct photon-jet events. The jet is selected at midrapidity ($-1.0 < y < 1.0$) and the photon at forward rapidity. The calculation is for $p_T^\gamma > 3\,\text{GeV}$.

asymmetries measured in Drell-Yan and those measured in photon-jet production would give a direct measure of the size of TMD factorization breaking effects. This information would prove extremely valuable in theoretical efforts to develop new approaches to factorization and universality.

The other key set of measurements address the Collins effect, the combination of transversity distributions folded with the Collins fragmentation function. Transverse polarized scattering presents the possibility to measure the relation of the transverse spin of a quark with the azimuthal distribution of a final state hadron around the quark's axis, and thus investigates spin-dependent fragmentation functions [257, 209]. This process is also useful in the study of the quark transversity distribution [273]. The transversity function is chiral-odd, and therefore not accessible through measurements of inclusive lepton-hadron scattering. Semi-inclusive DIS or hadron production in $p+p$ scattering, in which another chiral-odd observable may be involved, provides a valuable tool to probe transversity. The Collins fragmentation function [160] relates the transverse polarization of the quark to that of the final hadron. It is chiral-odd and naive T-odd, leading to a characteristic single spin asymmetry in the azimuthal angular distribution of the produced hadron in the hadron scattering plane. Therefore measuring the azimuthal distribution of hadrons in a jet will allow access to the Collins effect. With the new forward upgrade such a measurement in a region of high x_F (where the effects are largest) is made possible.

All the measurements described above involve processes for which factorization and universality are broken [280], as described already in earlier sections. In contrast, the dihadron interference fragmentation function (IFF) does not suffer from this problem, and is therefore an important measurement to extract transversity. The dihadron IFF also al-

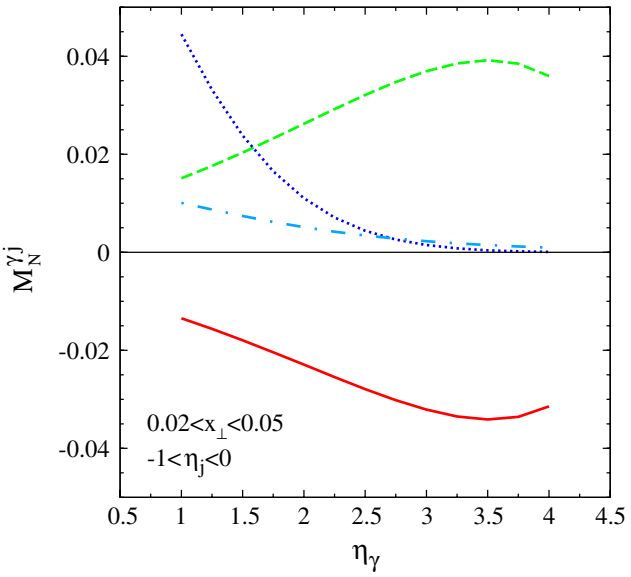

Figure 6.9: The anticipated azimuthal moment, $M_N^{\gamma j}$, determined via photon-jet measurements in polarized p+p collisions at $\sqrt{s} = 200\,\text{GeV}$ [115]. The red line is for gluonic-pole cross sections, the green line for standard partonic cross sections, the blue line for maximum gluon Sivers function contribution, and the dot-dashed line for maximum gluon Boer-Mulders function contribution.

lows one to study, for the same observable with the same detector, the magnitude of the factorization breaking between transversity extracted in the TMD formalism and in the collinear leading twist formalism. The IFF is not a TMD function and therefore the extraction of transversity convoluted with the IFF is not dependent on a model of the transverse momentum dependence, which is the case in the measurement of the Collins effect. The first extraction of the IFF was done by BELLE [311]; combining this measurement with measurements in polarized p+p scattering with both hadrons identified will allow a flavor separation of transversity. With the new forward upgrade, such a measurement will be possible for the first time in polarized p+p collisions.

6.2 New Probes of Longitudinal Spin Effects

The question of the individual parton (quark and gluon) contributions to the spin of the nucleon will remain important until a full decomposition is possible. All measurements to date in longitudinal polarized p+p collisions have been made in a relatively small x-range. This results in large uncertainties in the low-x extrapolation of the polarized parton distributions and their integrals. Additionally, the number of channels with statistical power for constraining ΔG has been limited thus far at RHIC. Significant increases in luminosity for $\sqrt{s} = 500\,\text{GeV}$ combined with increased detector acceptance at midrapidity as described in Chapter 7, will provide sufficiently large data samples to measure A_{LL}

for direct photons as shown in Figure 6.10. The dominance of a single leading order process at midrapidity (quark-gluon Compton scattering) [45] reduces theoretical questions about interferences of diagrams and canceling spin contributions, and thus remains a key check for global constraint fits.

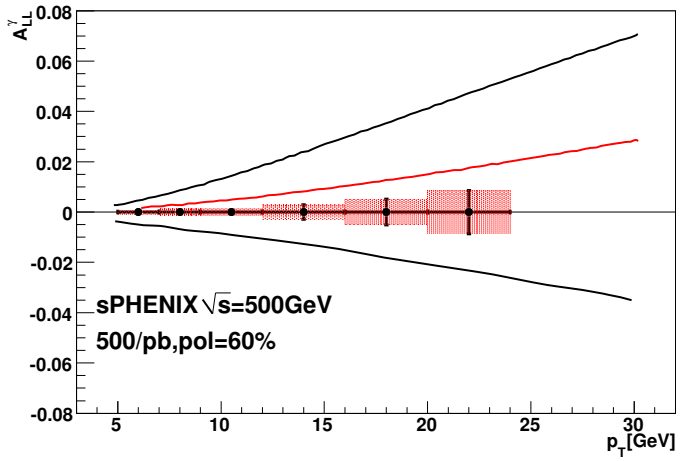

Figure 6.10: Expected uncertainties in A_{LL}^{γ} as a function of p_T for $|\eta| < 1$ and 2π acceptance for $\sqrt{s} = 500\,\text{GeV}$ $500\,\text{pb}^{-1}$ and a polarization of 0.6. The red curve corresponds to GRSV-std and the black curves corresponds to GRSV-max and GRSV-min.

Other future measurements should focus on extending the x-range to lower parton momentum fractions, as discussed already earlier in this document (see Section 5.2). Additionally, correlation measurements via dijets or photon-jet allow one to more directly constrain the shape of the polarized parton distributions in x. Both of these can be achieved with the new PHENIX detector, especially with the combination of the much larger acceptance of the central detector and the forward upgrade. Forward rapidity measurements probe a different combination of underlying hard subprocesses as shown in Figure 6.11, in addition to probing partons at lower x.

For correlation measurements, at leading order in pQCD, the momentum fractions of the partons involved in the hard interaction are directly correlated to the rapidity of the observed jets/hadrons (as was discussed in the previous section). Such measurements provide a much better handle on the parton kinematics and are therefore a very useful tool for constraining the shape of the polarized parton distributions. It is notable that these measurements are quite challenging. A_{LL} is given by the ratio of polarized to unpolarized cross sections

$$A_{LL} = \frac{\Delta\sigma(gg \to gg) + \Delta\sigma(qg \to qg) + \Delta\sigma(qq \to qq)}{\sigma(gg \to gg) + \sigma(qg \to qg) + \sigma(qq \to qq)}$$

As x decreases the unpolarized cross section increases because of the fast-rising gluon and sea quark densities. Even if the polarized quark densities rose as fast as the unpolarized

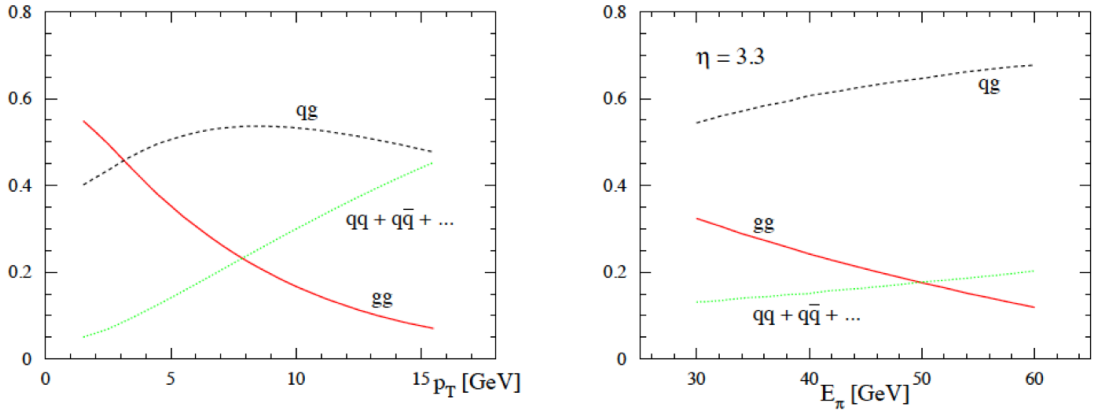

Figure 6.11: Decomposition of the NLO cross sections for $p + p \rightarrow \pi^0 + X$ collisions at $\sqrt{s} = 200\,\text{GeV}$ into the contributions from initial gg, qg, and qq states. The left plot is for $|\eta| < 0.35$ and the right plot for $\eta = 3.3$.

ones as a function of x, which they do not, the asymmetries would become increasingly small. This presents a challenge with respect to controlling systematic effects and puts high demands on luminosity to measure asymmetries on the order of 10^{-4}. If we obtain

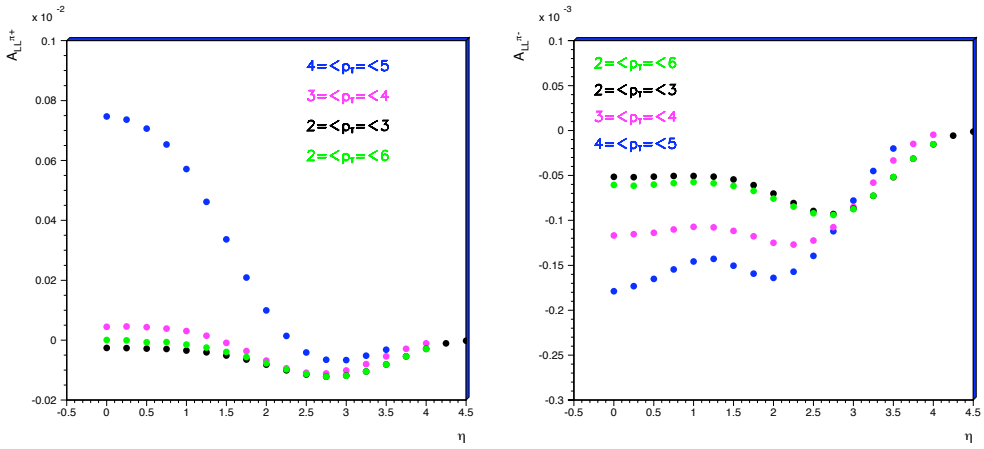

Figure 6.12: A_{LL} as a function of rapidity for π^+ and π^- for $\sqrt{s} = 200\,\text{GeV}$ for different p_T selections.

the required luminosity and control the systematic uncertainties for asymmetries of identified inclusive hadrons, and for hadron-hadron and hadron-jet correlations, measured as a function of rapidity down to rapidity $y = 4$, as shown in Figure 6.12, it would provide extremely valuable data to the NLO pQCD fits like the one from DSSV [170]. These measurements would constrain not only the polarized gluon distribution but also the polarized quark and antiquark distributions.

6.3 ^{3}He beams and Higher $\sqrt{s}$

In the years beyond 2015 there is the possibility of increasing the beam energies for RHIC by 30%, by either changing or removing the current DX magnets—which in any case is a likely requirement for running a simultaneous Electron-Ion Collider and RHIC. For protons this change results in $\sqrt{s} = 650$ GeV, leading to an increase in the cross section for $W^{\pm}$ production by approximately a factor of two. Together with having polarized ^{3}He beams this will give the possibility to do a full flavor separation for the polarized light quark distributions [295]. Figure 6.13 shows the longitudinal single spin asymmetries for $W^{\pm}$ production in polarized p+p and p+^{3}He collisions. The left panels are for polarized p+p collisions and the right panels are for p+^{3}He collisions. There is a striking difference in the A_L for W^- in the two cases at forward rapidity due to the different valence quark content of p+p and p+^{3}He.

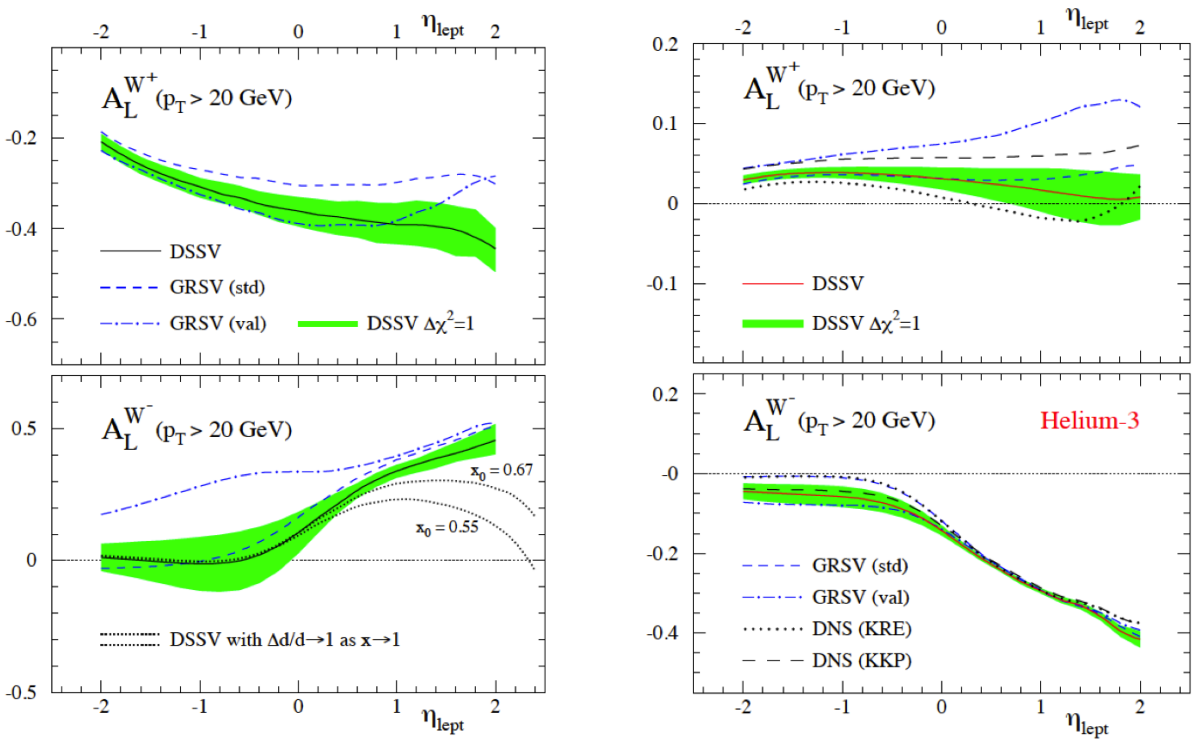

Figure 6.13: A_L for $W^{\pm}$ in polarized p+p (left) and p+^{3}He (right) collisions at $\sqrt{s} = 500$ GeV and 432 GeV.

In the years beyond 2015 there is the possibility to increase the beam energies for RHIC by 30%, by either changing or removing the current DX magnets – which in any case us a likely requirement for running a simultaneous Electron-Ion Collider and RHIC. For protons this change results in $\sqrt{s} = 650$ GeV, leading to an increase in the cross section for $W^{\pm}$ production by approximately a factor of two. Together with having polarized ^{3}He beams this will give the possibility to do a full flavor separation for the polarized light

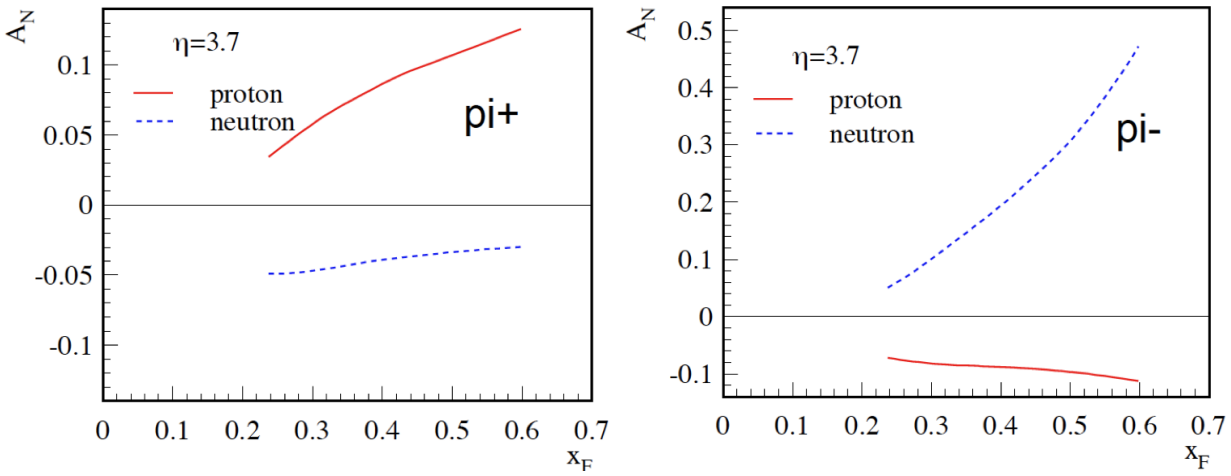

Figure 6.14: A_N for π^+ and π^- vs x_F.

quark distributions [295]. Figure 6.13 shows the longitudinal single spin asymmetries for $W^{\pm}$ production in polarized p+p and p+^{3}He collisions.

Figure 6.14 illustrates how having p+^{3}He collisions would allow a flavor separation for the transverse spin observables. A_N is shown for π^+ and π^- vs x_F for a fixed rapidity of $\eta = 3.7$, for scattering of a proton or a neutron calculated in the twist-3 approach [215]. Performing this measurement offers the possibility to test the predictions in the collinear higher-twist approach.

There are other channels of interest with ^{3}He beams and also other areas of physics that would benefits from the higher collision energies. We are just starting to explore the possible physics with these potential new tools.

Chapter 7

sPHENIX Detector Upgrades

In Chapters 3 and 6, we have outlined an exciting program in heavy ion and spin physics focused on an investigation of the interplay between perturbative and nonperturbative physics in QCD and on the relative importance of strong and weak coupling. In those Chapters, the physics aims were translated into an extensive set of required physics observables to answer these key scientific questions. In this Chapter, we detail the R&D and simulation work required to converge on a full detector upgrade proposal (referred to as sPHENIX).

As reviewed in the Executive Summary, the sPHENIX upgrade plan involves replacing the PHENIX central magnet with a new compact solenoid. The limited aperture provided by the outer central arm detectors would be replaced with a compact EMCal and a Hadronic Calorimeter covering two units in pseudorapidity and full azimuth, complemented by the existing VTX and FVTX inner silicon tracking. Two additional tracking layers would be added. We highlight that the large acceptance and excellent detector capability is combined with high rate and bandwidth, allowing the accumulation of 25 billion Au+Au collisions recorded and 50 billion Au+Au collisions sampled with spectrometer triggers in a single 20-week run period—an increase by an order of magnitude over current data samples. The limited forward coverage of the current PHENIX detector does not allow us to adequately address the questions driving the nucleon structure and cold nuclear matter community, nor does it provide any capabilities for e+p or e+A collisions. Hence, we are considering an upgrade where one muon arm would be replaced by a new large-acceptance forward spectrometer with excellent PID for hadrons, electrons, and photons and full jet reconstruction capability. The modified detector layout is shown schematically in Figure 7.1. The increase in overall acceptance is shown in Figure 7.2. The new compact barrel component at midrapidity is designed for excellent jet reconstruction and PID for photons, electrons, and π^0 in p+p, proton-nucleus, through central nucleus-nucleus collisions. The forward upgrade design is driven by nucleon structure physics, cold nuclear matter physics, and the capability to study first collisions at the EIC (as detailed in Chapter 8).

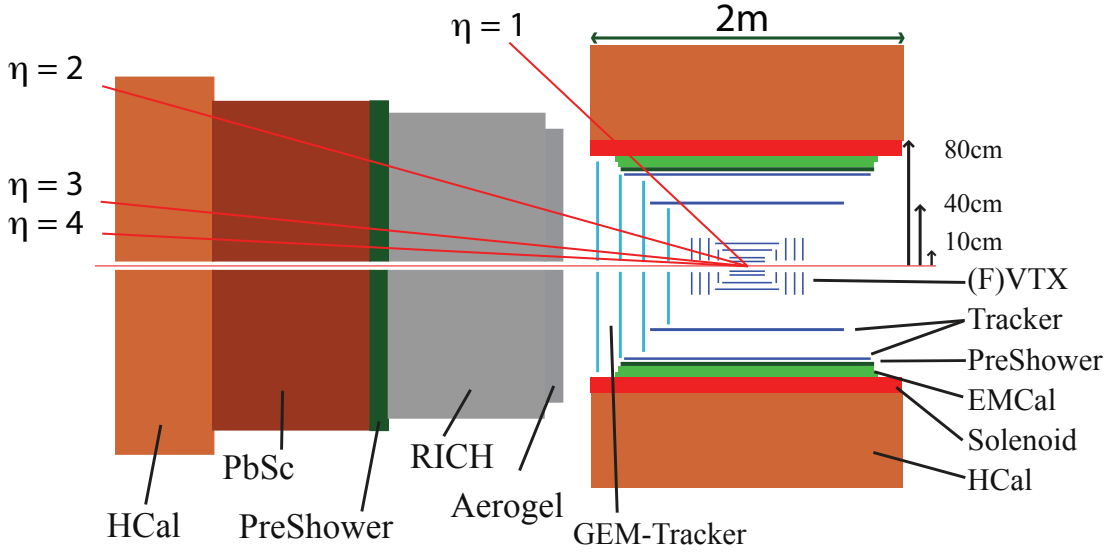

Figure 7.1: Schematic diagram of strawman PHENIX upgrade—referred to as sPHENIX.

The collaboration is in the early stages of a full detector design, so we will emphasize the detector requirements for the physics measurements of interest and present the current state of the design. As a second-generation RHIC detector with a more focused physics program, building upon and extending the results obtained by the current detectors, we emphasize new capabilities in this concept. We believe that this design has many advantages, notably large acceptance and high-rate capability, and through its compact design and the open geometry of its solenoidal magnet, there is room for hadronic calorimetry and the potential for an extended forward physics program.

Most of the discussion of the midrapidity upgrade in this Chapter focuses on heavy-ion physics topics; likewise most of the discussion for the forward upgrade focuses on spin physics topics. However, this factorization is only a convenience for the discussion and there are compelling topics, such as the study of cold nuclear matter, particle production in heavy-ion collisions at forward rapidity, and the use of particle correlation measurements for A_{LL} to constrain the x-shape of $\Delta g(\mathrm{x})$ that cross those lines and tie the central barrel and the forward detector concepts together.

Upgrades in the forward and central regions are also coupled for the simple reason that for PHENIX to have the capability to measure electrons in the forward direction will require opening the geometry of the existing PHENIX main magnet. So, although this chapter is divided into sections describing a midrapidity upgrade and a forward upgrade, one should keep in mind that there are good reasons for considering them together.

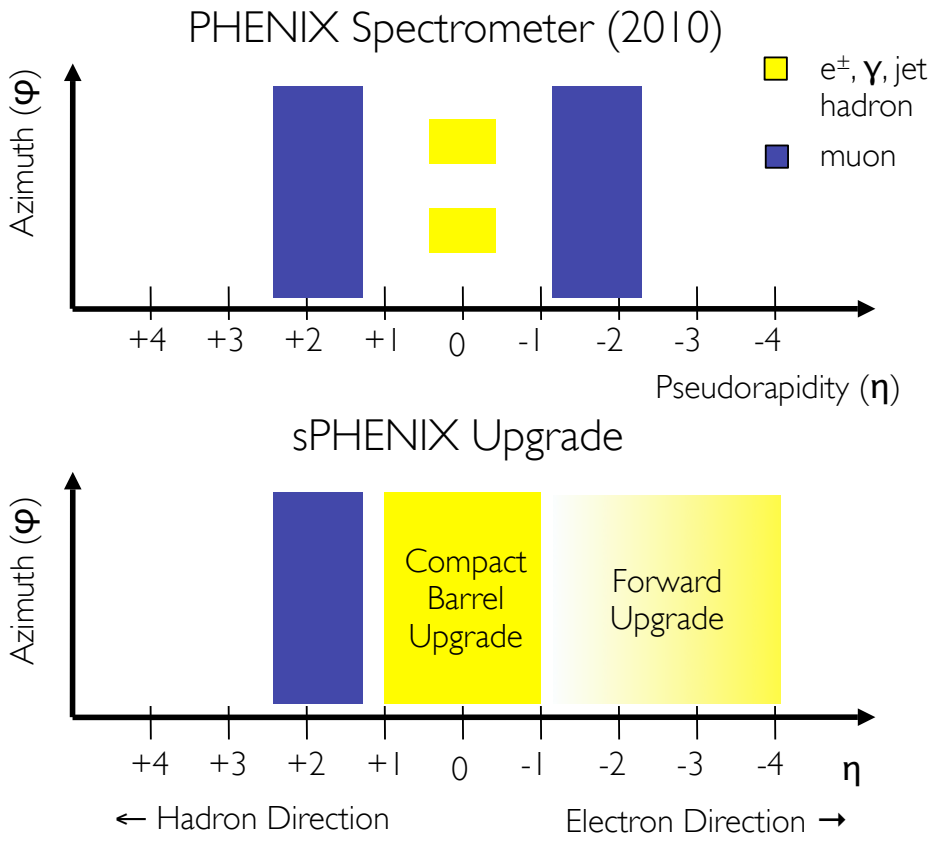

Figure 7.2: Acceptance of strawman sPHENIX design (below) compared to current PHENIX acceptance (above). The central barrel detector covers $|\eta| < 1.0$; the forward detector has tracking coverage for $1 < \eta < 4$, with full EMCal and HCAL coverage for 1.5–2.0 $< \eta <$ 4.0, with the exact range dependent on the final design configuration

7.1 Midrapidity Upgrades

The current PHENIX central arm spectrometers were designed in the mid-1990's to have excellent electron, photon, and hadron identification, but in order to balance cost and construction considerations they were designed with a limited acceptance. The spectrometers cover pseudorapidity $|\eta| < 0.35$ and two sections in azimuth $\Delta\phi = 90$ degrees. A significant increase in this acceptance is needed to make major advances in answering the key physics questions outlined earlier, but this increase must come without sacrificing electron and photon identification and the high rate and trigger capabilities that are the strengths of the current PHENIX detector. This is now achievable at a much lower cost scale than when the original RHIC experiments were designed due to technology advances over the last 15 years.

We believe the following are critical detector requirements for carrying out the physics program of the next decade.

- Uniform acceptance over two units of pseudorapidity and full azimuth
- High rate capabilities, fast readout, deadtimeless data acquisition
- Precision inner and outer tracking with excellent momentum resolution
- Full coverage hadronic calorimetry
- Highly segmented electromagnetic calorimetry
- Excellent γ/π^0 separation out to $p_T > 40\,\mathrm{GeV}$
- Electron identification over a broad momentum range
- Displaced vertex tagging of heavy flavor decays

We have calculated the simple geometric acceptance ratio for a detector with coverage of $|\eta| < 1.0$ and full azimuth compared with the current PHENIX configuration. Figure 7.3 shows the results for heavy quarkonia J/ψ and Υ states, open charm mesons ($D \to \pi K$), single jets, dijets, and direct photon-jet events. This large acceptance does not just increase our statistics and kinematic reach in an arbitrary way, but instead allows fundamental advances in our measurement capabilities.

It is important to increase the acceptance of the detector, but it is just as crucial to retain the current high rate capability of the PHENIX detector. "High rate capability" means being able to sample the probes of interest efficiently and with minimal trigger bias, record large unbiased data samples, and avoid significant pile-up effects in the detector readout. All of these are important capabilities, as the projected increase in RHIC luminosities (see Appendix B) will enable more precise measurements while challenging the detector performances and analysis methods. The acceptance described above is similar to the current

acceptance of the STAR central barrel detector, but the combination of fast detectors coupled with an extremely high rate data acquisition system will provide the ability to sample the full projected RHIC luminosity and to acquire large data samples with minimal trigger bias—capabilities which are needed to carry out the physics program described earlier in this document.

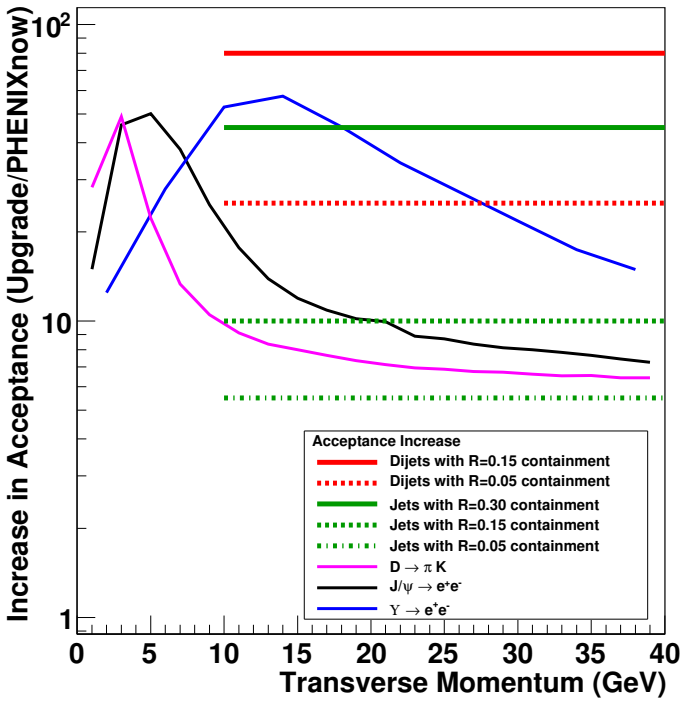

Figure 7.3: Acceptance factor increase with $|\eta| < 1.0$ and $\Delta\phi = 2\pi$ compared with the current PHENIX configuration. Shown are the results for $D \rightarrow \pi K$, J/ψ, and $\Upsilon(1s, 2s, 3s)$ decays and for jets and dijets for different requirements on the jet energy containment in terms of $R = \sqrt{\Delta\eta^2 + \Delta\phi^2}$ being less than the values shown.

The measurement of fully reconstructed jets in heavy ion reactions and the structure and correlations within and between these jets is key to answering many of our physics questions. These are extremely challenging measurements that will require multiple, well-developed tools to allow us to cross-check results. Having uniform and nearly hermetic electromagnetic and hadronic calorimetry is a crucial prerequisite for being able to pursue such jet measurements. This methodology has been well tested over two decades in particle physics—in particular by CDF and D0 [183]. STAR has had recent success reconstructing jets in p+p collisions using a combination of charged particle tracking and coarse granularity electromagnetic calorimetry [18]. The ALICE, ATLAS, and CMS experiments have been developing "hybrid" jet reconstruction (utilizing full EMCal, HCAL, and charged tracking). We believe that all of these tools will be required in order to have robust results for jet reconstruction yields, fragmentation functions and measurements of

modified radiation angular distributions. We demonstrate some of these advantages and disadvantages that make the cross comparison of these methods so important.

In addition to the larger coverage for the EMCal, one needs fine enough transverse segmentation that it is possible to match individual charged tracks within a jet to individual showers in the EMCal. For the measurement of charm and beauty jets tagged with a displaced vertex electron, it is important in the hybrid method to avoid any double counting of the electron energies obtained by charged particle tracking and the EMCal. The same is true for the charged hadrons, where one needs to avoid double counting of energy in the EMCal (not just for the average minimum ionizing dE/dx assumption). Having fine transverse segmentation is in keeping with our interest in cleanly separating single direct photons over the full kinematic p_T range at RHIC from the two nearby decay photons from high p_T π^0s. The full understanding of jet physics will require both the measurement of dijets as well as direct photon-jet measurements. Figure 3.4 in Chapter 3 shows that with data samples of 50 billion Au+Au events into the large acceptance of the strawman design, one will have a significant sample of direct photons to $p_T > 50\,\text{GeV}$ and π^0s to $p_T > 40\,\text{GeV}$.

The matching of electron and charged tracks requires an EMCal segmentation of roughly $\Delta\eta = 0.0125$ and $\Delta\phi = 0.0125$ and a detector with a small Molière radius to keep the showers tightly contained. Even a detector with these characteristics only has clean two cluster separation for π^0s to up $p_T \approx 10$–$15\,\text{GeV}$. A preshower or shower maximum detector is required to select π^0 candidates at even higher p_T. This is also important for the ability to measure the jet fragmentation function for π^0.

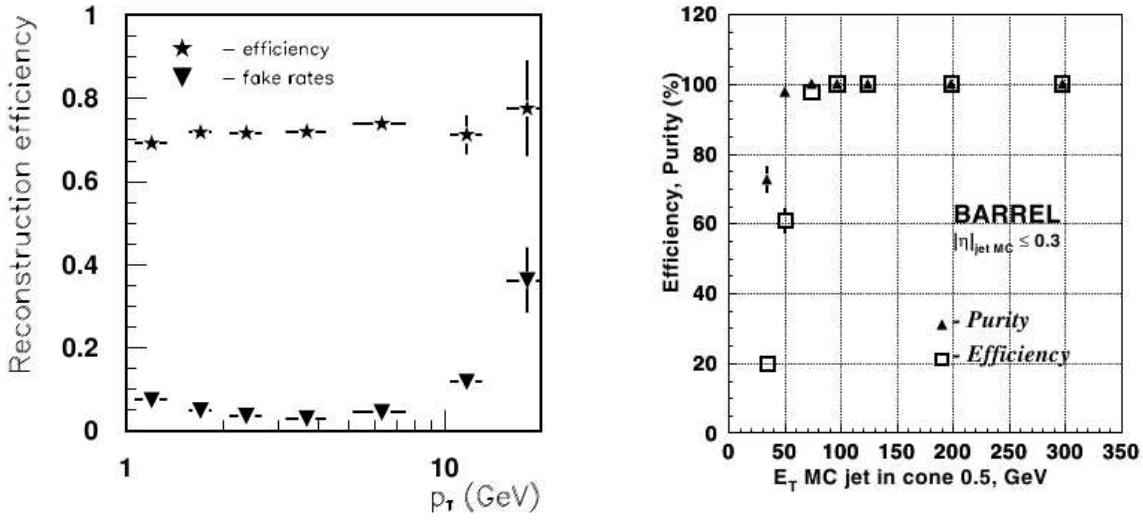

Figure 7.4: Track reconstruction efficiency and percentage of fake tracks, as a function of the reconstructed p_T from the ATLAS HI LoI (left). Purity and efficiency of jet reconstruction versus generated jet energy at CMS (right).

In order to measure fragmentation functions with charged hadrons, one needs excellent fake high p_T track rejection. Here "fake" is defined as a low p_T track or a track originating from a noncollision vertex decay that is incorrectly reconstructed as a track with much higher p_T. Because the fragmentation function is steeply falling as a function of the momentum fraction of the hadron relative to the jet ($z = p_h/p_{\text{jet}}$), any fake track which is also added to the reconstructed jet energy (in a Track+EMCal approach) immediately contaminates the high z measurement. To be explicit, imagine reconstructing a 19 GeV fake track that coincides with 1 GeV of EMCal and other track energy. In this case, one would get a not only a fake track at 19 GeV, but a fake jet at 20 GeV with a fragmentation fraction $z = 19/20 = 0.95$. One needs to ensure that such track contributions are not just sub-dominant, but that they are only a very small fraction of the total tracks. For example, in the current ATLAS tracking configuration at the LHC, they have studied the inclusive charge tracking capability in Pb+Pb and find that even with 13 layers of silicon tracking, the fake track contribution becomes appreciable for $p_T > 10\,\text{GeV}/c$ [110], see the left panel of Figure 7.4. Shown in the right panel of Figure 7.4 is the efficiency and purity for jet reconstruction in CMS [242]. In this case the purity for jets with E_T is quite good, and the CMS study was done on a jet-triggered sample, where the jet trigger requires a large EMCal and hadronic calorimeter summed energy. This indirectly demonstrates the power of the hadronic calorimeter to reject fake tracks. There are preliminary studies from STAR, with the large number of three-dimensional space points from the Time Projection Chamber, that include charged tracks up to $p_T < 15\,\text{GeV}$ [265]. It is possible this can be pushed to higher p_T, though they do not currently have an evaluation of the fake fraction and its impact on the future fragmentation function measurements. Again, this highlights the utility of being able to compare different jet methodologies with different systematics.

Full coverage hadronic calorimetry removes this source of background by separating the jet energy measurement from the charged track measurement. For example, if one is interested in charged tracks with momentum $20\,\text{GeV}/c$ in reconstructed jets of energy 20–40 GeV, in the charged track plus EMCal scenario, one has to reject fake 20 GeV/c tracks at the level of a single fake track in hundreds of millions of Au+Au central events. However, in the case of a jet measurement done with an EMCal together with an HCAL, one only has to account for fake tracks in the small subset of those events where there is a reconstructed 20–40 GeV jet, and then only within the η and ϕ region around the jet axis. Our studies to date indicate that the hadronic calorimeter only needs a modest segmentation of $\Delta\eta \times \Delta\phi = 0.1 \times 0.1$ since one does not require a direct individual track to HCAL shower match within the jet.

Figure 7.5 shows the results of a fast simulation, with parameterized but realistic detector response, for the jet response matrix (with full anti-k_T jet reconstruction) for PYTHIA simulated events with and without hadronic calorimetry. In the simulation without hadronic calorimetry, there are fake contributions for tracks with $p_T > 10\,\text{GeV}$, and these jet events are eliminated from the sample, resulting in a substantial inefficiency for jet reconstruction. One can also see a much broader low energy reconstruction band due to lost con-

tributions from neutral particles including neutrons, Λ's, and K_L in the case without hadronic calorimetry.

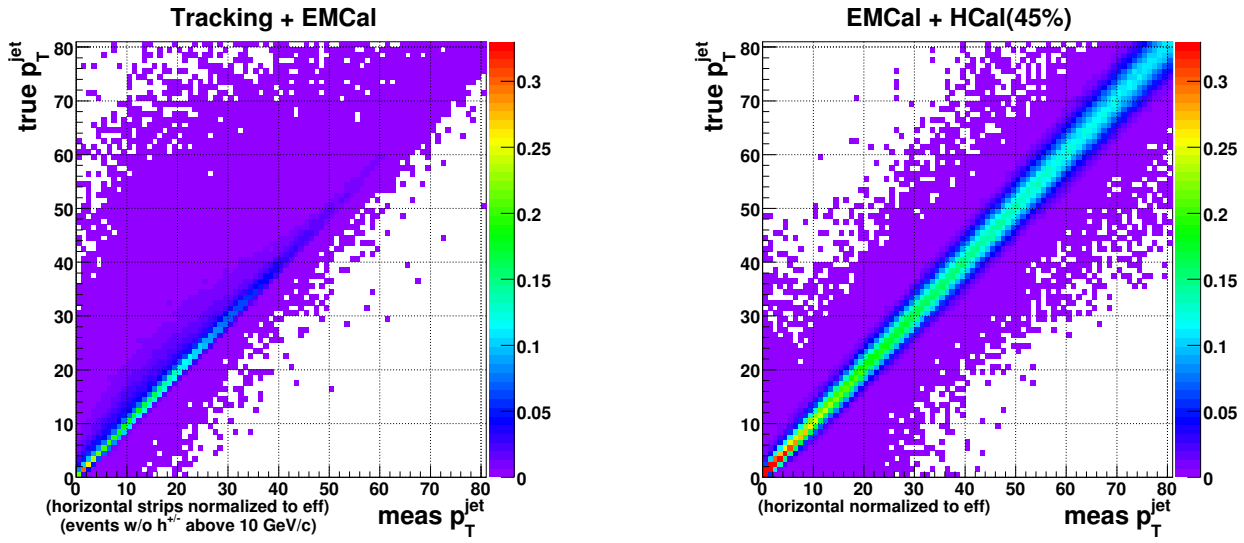

Figure 7.5: Fast simulation response matrices demonstrating the improved correlation between measured and true p_T of jets when tracking (left) is replaced by hadronic calorimetry with $\sigma_E/E = 45\%$ (right).

Without hadronic calorimetry, the situation is even more challenging for the case of measuring the fragmentation function. Figure 7.6 shows QPYTHIA simulations with quenching parameter $\hat{q} = 0$ and $10\,\mathrm{GeV}^2/\mathrm{fm}$ for the fragmentation function of light quark and gluon jets as a function of z (the fraction of the momentum of the reconstructed jet carried by the leading hadron) in the upper plot and as a function of $\xi = \log(1/z)$ in the lower plot. Without hadronic calorimetry if one removes jets containing tracks with $p_T > 10\,\mathrm{GeV}/c$, one only measures the range for $z < 0.25$ for these 40 GeV jets, and thus one loses most of the important physics information.

We have also begun simulations in full HIJING Au+Au central events to understand the impact of the underlying event on the jet reconstruction, resolution, and fake jet rates. Figure 7.7 shows the jet response matrix with hadronic calorimetry with and without the Au+Au underlying event overlaid. These results are encouraging, and more detailed simulations are a high priority.

The current PHENIX detector has excellent electromagnetic calorimetry (75% Lead Scintillator and 25% Lead-Glass), located at a radius of approximately 5 m. PHENIX has been well served by these detectors, and the single photon to π^0 separation in our current published analyses extends up to just $p_T = 18\,\mathrm{GeV}$. It is also not practical to imagine extending these types of calorimeter modules to cover $|\eta| < 1.0$ and full azimuth, nor is there space available in any of the RHIC interaction regions (including the current PHENIX 1008 hall) for hadronic calorimetry outside that envelope. Over the last six months, we have studied a new concept for addressing all of the issues presented above.

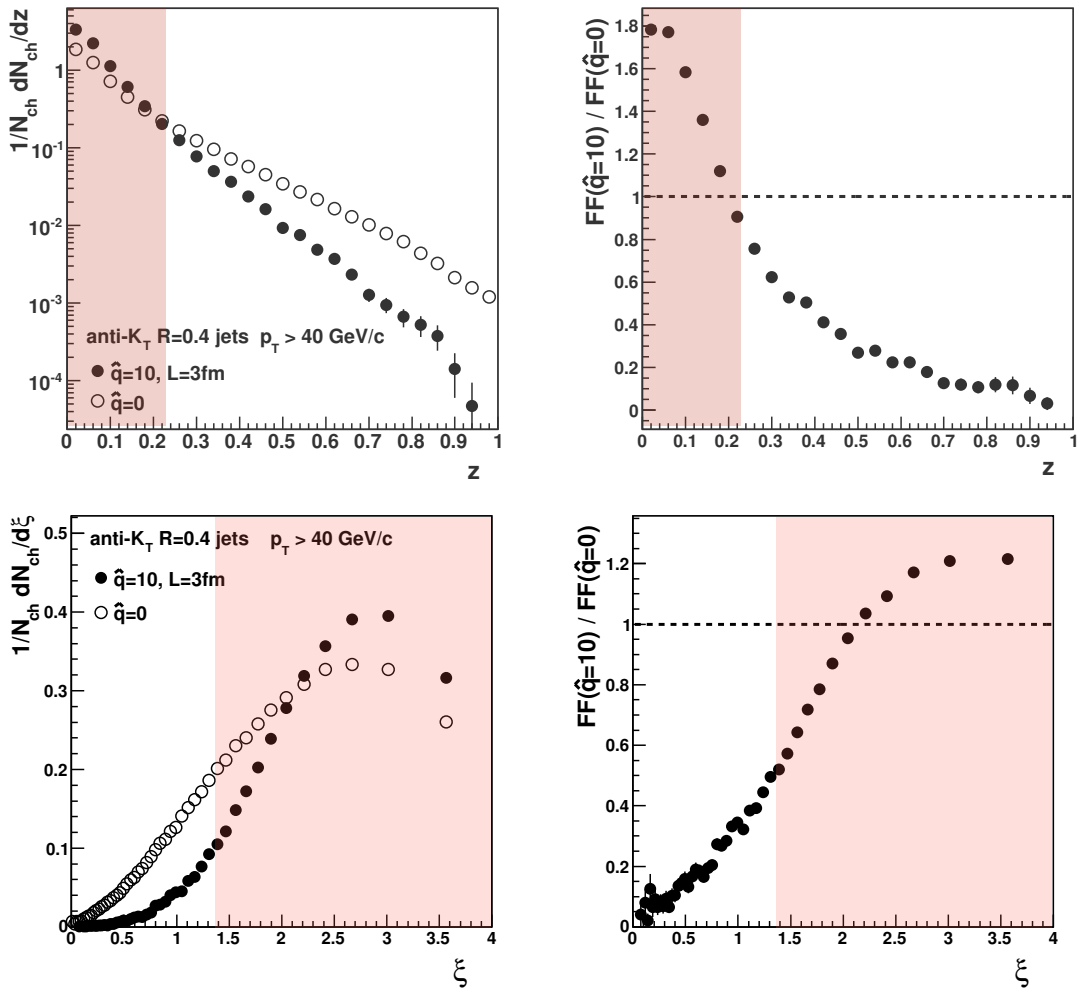

Figure 7.6: QPYTHIA simulation with quenching parameter $\hat{q} = 0$ and $10\,\mathrm{GeV}^2/fm$ for the fragmentation function of light quark and gluon jets as a function of z in the upper plot and as a function of $\xi = \log(1/z)$ in the lower plot. Without hadronic calorimetry if one removes jets containing tracks with $p_T > 10\,\mathrm{GeV}/c$, one only measures the range for $z < 0.25$ for these 40 GeV jets. The white regions in the figures are enabled by hadronic calorimetry.

The concept is to have a very compact electromagnetic calorimetry (CEMCal), for example starting at a radius of 60 cm from the beam line and utilizing a silicon-tungsten (Si-W) electromagnetic calorimeter. A key feature is to have at least one preshower layer with 1–2 radiation lengths of tungsten and silicon strip layers (possibly with two spatial projections) to allow for single photon - π^0 separation to up $p_T \approx 50\,\mathrm{GeV}$, as well as enhanced electron-identification. The strawman design has silicon strips with $\Delta\eta = 0.0005$ and $\Delta\phi = 0.1$. The back sections for full electromagnetic energy capture could also be Si-W design, although it may be more cost effective and allow for better uniformity to have an accordion Lead-Scintillator Design (or other options see Section 7.1.3). One major advantage to the silicon technology would be the gain in uniformity and the ability to calibrate

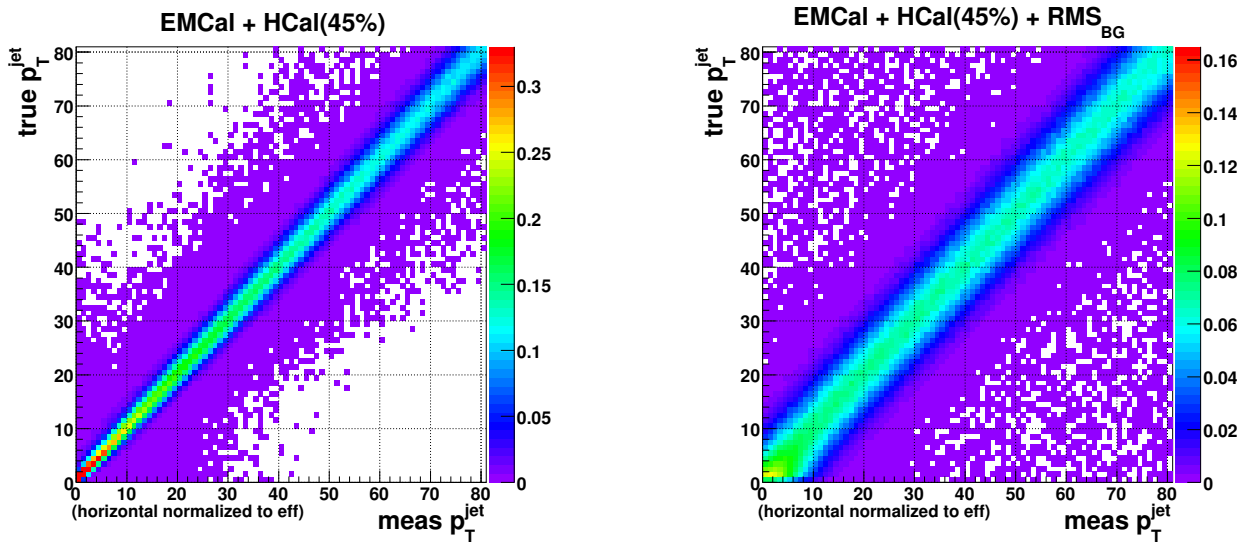

Figure 7.7: Plots which show the effect of the underlying event on jet reconstruction in the strawman detector. The plot on the left corresponds to a pure p+p event (i.e., no underlying event), while the plot on the right shows the effect of adding in a underlying HIJING Au+Au central event multiplicity.

the device. In Section 7.1.3, we show some initial GEANT4 performance studies for single particles with a fully Si-W design. If the entire CEMCal were a tungsten radiator, the entire detector could be 7.8 cm thick for a total radiation length of $X_0 = 22.3$.

The compact design has many advantages, but it also presents challenges. For example, the EMCal, situated 60 cm radially from the beampipe, has to be able to handle shower overlaps in central Au+Au collisions. The CMS EMCal also has a compact design, and we are in the fortunate position of being able to benefit from the experience that will be gained by CMS over the next year as they use their EMCal to study heavy-ion collisions. The midrapidity particle density in full-energy central Pb+Pb collisions at the LHC is expected to be roughly three times that seen in central Au+Au collisions at RHIC [98], and the front face of the CMS EMCal sits at a radius of 1.29 m—about a factor of four more detector area per unit rapidity than the sPHENIX design. The net result is a particle density at the face of the sPHENIX EMCal similar to the density CMS expects to be able to handle. We note that the strawman design has the EMCal at 60 cm, though we believe the benefits of a compact design for sPHENIX are still realized for EMCal radii up to about 1.5 m. Thus, further simulations, R&D, and the experience gained by CMS with triggering, the impact of the underlying event, and the effect on energy resolution of such an environment will certainly inform the design of our EMCal. The final values of the key parameters of the sPHENIX EMCal will be a trade-off between physics needs, technology and cost—all of which is a focus of current work.

The existing PHENIX axial field magnet is not an ideal match for a compact detector with an emphasis on jet measurements. The existing magnet also presents a severe conflict for

our proposed forward physics upgrade (see Chapter 7.2). We imagine replacing the current magnet with a small magnetic solenoid similar to—though possibly smaller in radius than—the current D0 solenoid [14]. Our momentum resolution requirements are driven by the need to separate the various Υ states (Section 7.1.2) and to have adequate momentum resolution for charged hadrons at high p_T in measuring fragmentation functions. From these we determine that a field strength of 2 Tesla is required. We are currently having detailed discussion with the Brookhaven Magnet Division about the design and cost for such a magnet. The current specifications are for an inner radius = 60 cm magnet with the B-field z-extent of $\pm$80 cm, a 2 Tesla field strength, and a radiation length for particles traversing the magnet of roughly 1.0–1.5 radiation lengths. The last requirement would allow having only the inner preshower layers of the CEMCal inside the magnet, and the remainder outside (which simplifies the design requirements and allows more possible technology and readout options). There are potentially additional requirements on the field configuration at the ends for the forward physics upgrade discussed in Section 7.1.3.

The hadronic calorimeter design has not yet been investigated in great detail. The default in our GEANT4 simulations is a simple iron-scintillator design starting at a radius of 80 cm and extending to 142 cm (i.e., 60 cm, or 3.5 interaction lengths, deep). Of course, we are investigating various calorimeter technologies—e.g., the dual-readout Čerenkov/scintillator "DREAM" calorimeter [317]. However, the resolution requirements we envision are not particularly demanding, given that one is also competing with the jet event-by-event resolution from the underlying event subtraction (or order RMS $\approx$ 5 GeV for a anti-k_T jet size = 0.3), and we anticipate that a fairly conventional iron-scintillator calorimeter will be able to meet these requirements.

7.1.1 GEANT4 Implementation

We present results of a GEANT4 simulation put together to start answering some of the performance and acceptance questions with a strawman design. This section details those results. Next we explore the different technology options and what research and development work (and what performance trade-offs) need to be investigated to converge on a full design proposal.

Through a series of two week-long workshops, a team from PHENIX put together a complete GEANT4 detector package all within the framework of the PHENIX offline analysis software. This allows for a flexible and modular detector implementation and is an investment in the long term future of PHENIX. We now have a team familiar with GEANT4 as we consider moving our entire PHENIX simulations to this new package. Additionally, this makes relatively fast simulation changes for testing different configurations and technologies much easier than in the previous PHENIX GEANT3 implementation.

A schematic drawing of the GEANT4 implementation is shown in Figure 7.8 and a QPYTHIA dijet event-display visualization is shown in Figure 7.9. The detector configuration details as implemented in GEANT4 are given in Table 7.1.

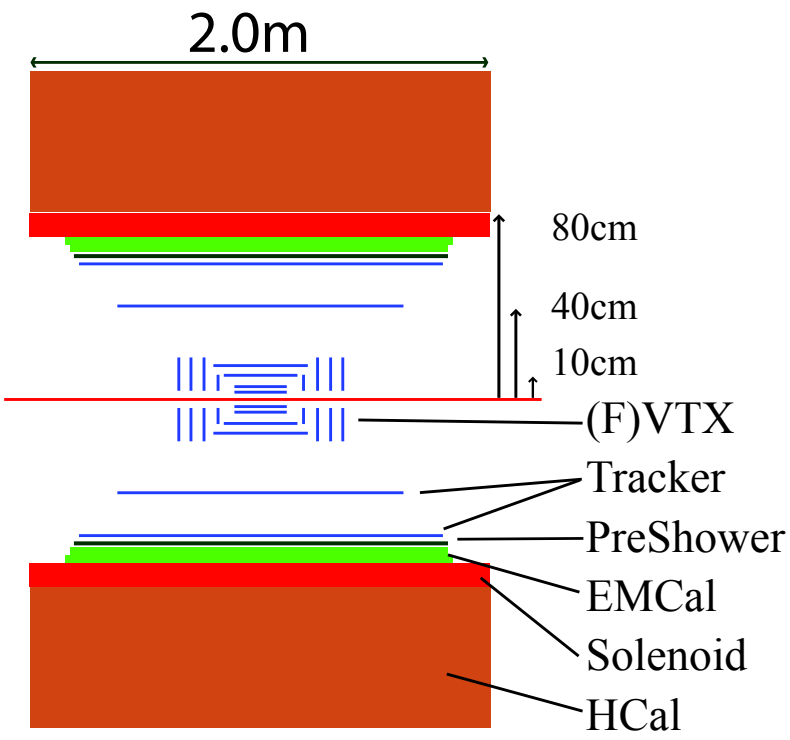

Figure 7.8: An elevation view of the strawman detector as implemented in GEANT4. Nearest the beampipe are the several layers of silicon of the current PHENIX VTX upgrade. Proceeding outward in radius one encounters two additional layers of tracking, the compact EMCal, the coils of the superconducting solenoid, and the HCAL.

The silicon vertex tracker (VTX) upgrade currently being installed in PHENIX (2010) is the centerpiece for the future charged particle tracking and heavy flavor displaced vertex tagging. The two inner layers (pixels) are at a radius of 2.5 and 5.0 cm from the beam line, and the outer two layers (strips) are at a radius of 10 and 14 cm. In the default upgrade, we have two additional silicon tracking planes at a radius of 40 and 60 cm. We require the material thickness of the intermediate layer at 40 cm to be thin (0.03 radiation lengths) to reduce multiple scattering and have good momentum resolution.

For the default compact electromagnetic calorimeter (CEMCal), we have used a design based entirely on silicon-tungsten. We have chosen this default for two reasons. First, there is significant simulation experience within the collaboration for this technology and configuration in the forward calorimeter (FOCAL) proposal and related R&D. Also, the uniformity of the detector layout results in a straightforward GEANT4 implementation. The GEANT4 layout includes an initial preshower tungsten layer 2.3 radiation lengths thick at a radius of 60 cm, backed by a silicon layer with strips 300 μm $\times$ 6 cm as a presampler. This segmentation corresponds to $\Delta\eta = 0.0005$ by $\Delta\phi = 0.1$. We are still investigating whether two views are necessary for the physics performance in all channels (particularly the efficiency for tagging two photons from a very high p_T π^0 decay). The back compartments of the detector then consist of alternating layers of tungsten 0.4 cm

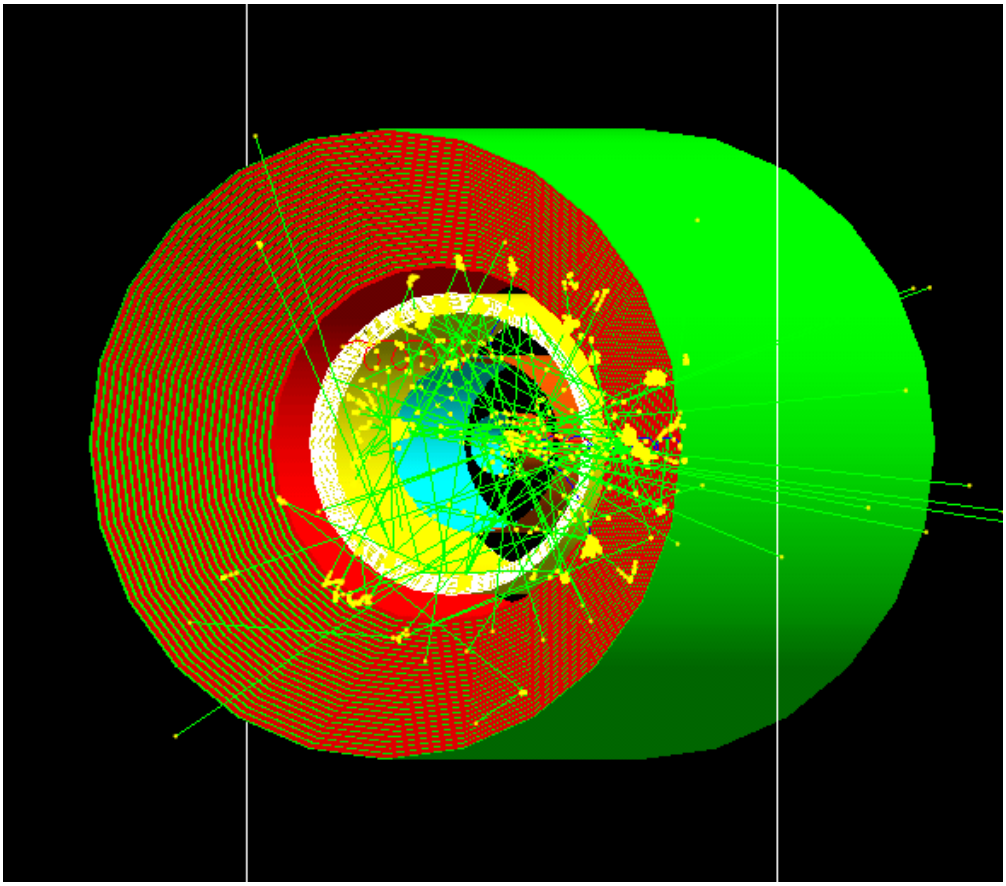

Figure 7.9: A GEANT4 visualization of a single dijet event in the strawman detector.

thick (0.065 radiation lengths) and active silicon readout layers. The first seven active layers have the silicon segmented into 0.75 cm $\times$ 0.75 cm pads with the readout between the seven pads grouped together. The next eight active layers have the silicon segmented into 1.50 cm $\times$ 1.50 cm pads with the readout between the seven pads grouped together. This segmentation is based on the transverse size development of the electromagnetic shower. The entire thickness of the CEMCal stack is 6.8 cm. In the current GEANT4 geometry, the magnet structure is outside the CEMCal just for convenience of implementation. As we discuss in Section 7.1.3, for a magnet (i.e. cryostat plus coils) 1.0–1.5 radiation lengths thick, the magnet would most likely be placed just after the preshower and presampler layers, with the remainder of the CEMCal outside of the magnetic field.

Maintaining a modest outer radius for the CEMCal, allows for the space and budget constraints to be met with a modestly sized hadronic calorimeter. We have only begun to explore design options, but the default GEANT4 implementation is an Iron-Scintillator calorimeter with segmentation of $\Delta\eta = 0.1$ by $\Delta\phi = 0.1$. The entire thickness in Iron of the stack is 50 cm, with 25 evenly spaced interleaved scintillator.

Table 7.1: Technology options and possible parameters of a strawman central barrel charged tracking system.

Detector	Technology	Segmentation	R (cm)	N_{chan} ($\times 10^6$)
Inner Tracking	VTX Pixels	50 μm $\times$ 425 μm	2.5	1.5
			5	3
Inner Tracking II	VTX Strip Pixels	80 μm$\times$0.1 cm	10	1.6
			14	2.2
Outer Tracking	New Strips	80 μm$\times$3 cm	40	1
			60	2.2
Compact EMCal PS	Si-W	300 μm$\times$6 cm	61	0.3
Compact EMCal	Si-W E1	0.75 cm$\times$0.75 cm	61–64	0.110
	Si-W E2	1.50 cm$\times$1.50 cm	64–68	0.03
Hadronic Cal	Fe-Sc	$0.1\eta \times 0.1\phi$	80–142	0.0012

7.1.2 Performance Plots

Here, we assess the tracking performance of the strawman detector design. We have implemented an initial pattern recognition and track reconstruction model based largely on software development for the VTX upgrade, and have used that software to track single muons generated and thrown over a broad range of momenta. The momentum resolution performance has an RMS $\Delta p/p = 0.007 + 0.0015 \times p$ for momentum $|p_T| >$ 1 GeV, as shown in Figure 7.10. Also shown is the momentum averaged resolution as a function of the polar angle θ. In order to have good separation of the three Υ states ($\Upsilon(1s), \Upsilon(2s), \Upsilon(3s)$)—crucial to the physics of the screening length—we need the term linear in the momentum be less than 0.002.

We do not have muon identifier detectors outside the hadronic calorimeter in the strawman detector design. This is largely due to our focus on the performance in the electron channel, but this may reconsidered in the future giving a factor of two increase in accep-

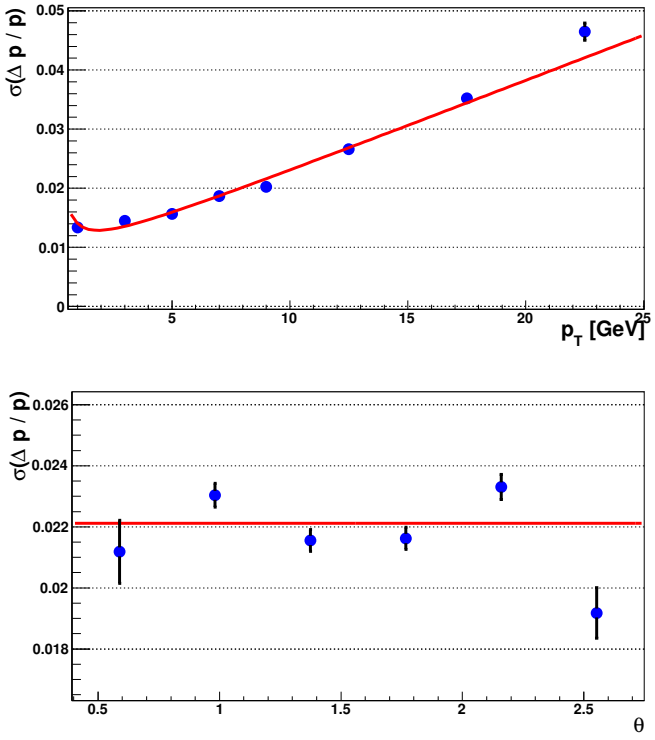

Figure 7.10: GEANT4 and track model evaluation for single particle momentum resolution. From a fit to the data in the upper panel, shown as the red line, we determine the momentum resolution to be $\Delta p/p = 0.007 + 0.0015 \times p$. The lower panel shows the momentum resolution as a function of the polar angle of the track.

tance in some channels. However, we show first in Figure 7.11 (left) the invariant mass resolution for the three Υ states as reconstructed via the dimuon decay channel. Note that we have not included any background contributions at this simulation stage. One observes a clean separation of the states, where the relative ratio between the states is determined by previous $p+p$ and anti$p+p$ measurements [21]. The width of the peaks is determined by the momentum resolution of the proposed compact spectrometer. For the electron channel, also shown in Figure 7.11 (right), there is a significant bremsstrahlung low mass tail due to the material budget of the tracking detectors. Although the tail is important to account for in the final signal extraction, the separation between the states remains good.

First studies of γ to π^0 separation and electron identification with the GEANT4 simulation are underway. Shown in Figure 7.12 is an event display of the energy deposition from a 42.8 GeV π^0 in the preshower and back two compartments of the EMCal. A clear separation of the two photons is seen in the preshower layer. Shown in Figure 7.13 (left) is the response of the EMCal total energy versus the preshower energy for electrons and charged pions. The combination of information provides a powerful discriminator for

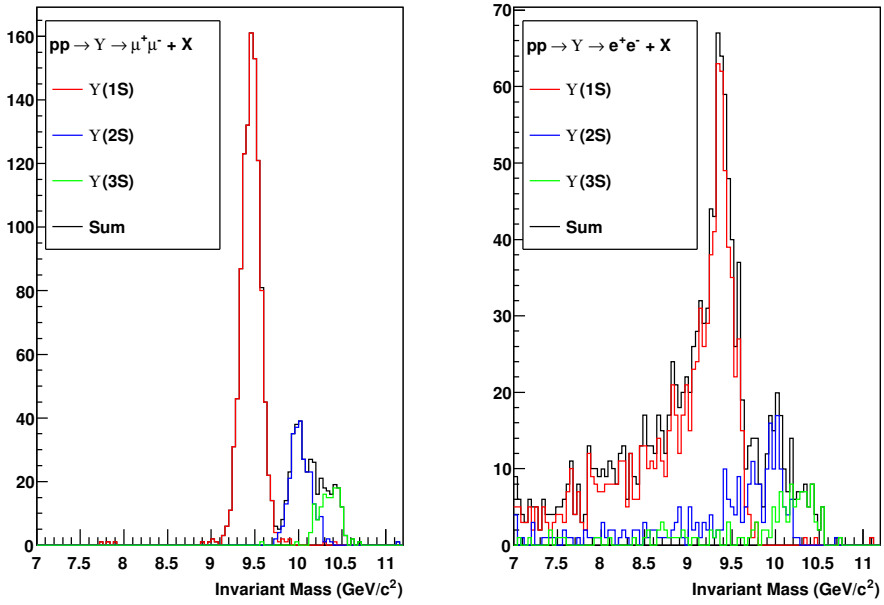

Figure 7.11: GEANT4 and track model evaluation for the Υ state mass resolution in the dimuon decay channel (left) and the dielectron decay channel (right).

electron identification. Full occupancy Au+Au studies are underway. Shown in Figure 7.13 (right) is the energy resolution for single photons.

7.1.3 Technology options for the midrapidity upgrade

Our strawman design calls for two additional layers of silicon tracking at radii of 40 and 60 cm to augment the tracking capabilities of the central silicon vertex tracker (VTX). These two additional tracking planes will improve our momentum resolution for higher momentum tracks, and improve our ability to reject background tracks and identify decays. The concept for an upgraded PHENIX detector would use the VTX as the central part of the vertex finding and tracking system; the addition of two more silicon tracking detectors is a natural extension of the present design. It also provides a basis for specifying a number of important parameters, such as position resolution, segmentation, and so forth for simulation studies of the physics requirements of the overall detector. However, when actually implementing such a device, one must not only consider the required spatial resolution and segmentation needed at the larger radii, but also other factors, such as the material budget, electronic readout requirements and cost. We are therefore also considering other tracking detector technologies that could meet our requirements.

One such technology is that of micropattern detectors, which includes Gas Electron Multipliers (GEMs), Micromegas and other types of gas detectors. These devices have been used in many particle physics experiments [86, 234, 83], can provide excellent spatial resolution ($\sim$50–100 μm), and have very high rate capabilities. In addition, they consist

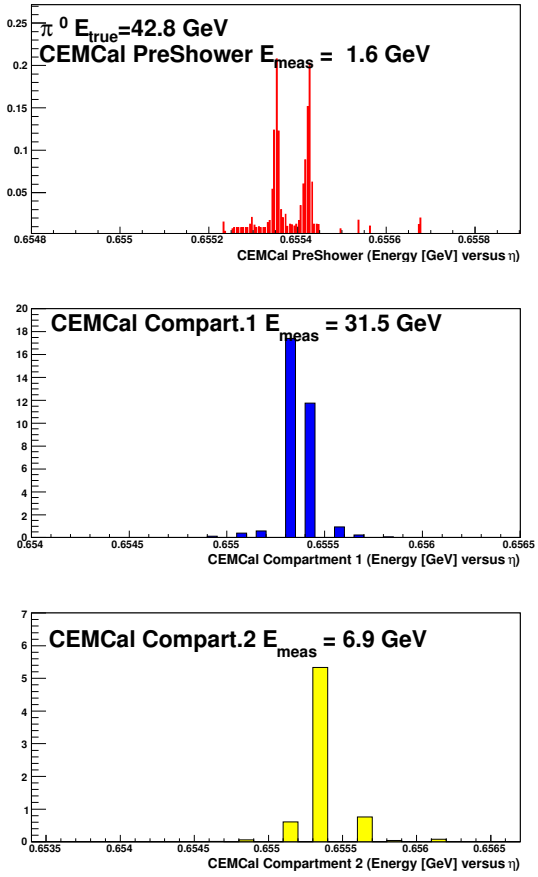

Figure 7.12: GEANT4 example compact EMCal shower profile for a single π^0 event.

mainly of low mass materials and add relatively little radiation length, which is crucial for preserving good momentum resolution for measuring the upsilon. For example, the radiation length of a single layer of GEM tracker would be ∼0.8%, including the readout board and electronics. They also offer the possibility of reducing the number of readout channels by the use of various types of charge sharing techniques to interpolate between larger size readout pads in order to obtain good position resolution with fewer readout channels [321]. The same type of readout electronics could be used for either GEMs or silicon, so the total cost would therefore be less due to the lower channel count. The cost of the GEM foils, which are currently produced mainly at CERN at a cost of ∼\$5K/m^2, is expected to come down considerably as the technology for producing them is transferred to industry [297, 159].

The PHENIX group has considerable experience with GEMs—they were used in the Hadron Blind Detector (HBD) that just completed its final data taking during run-10 at RHIC [319]. The use of GEMs in this particular detector was much more challenging than in a straightforward tracking detector, as it involved the use of a cesium iodide photocathode to detect single photoelectrons, a very high purity CF_4 gas radiator that was also

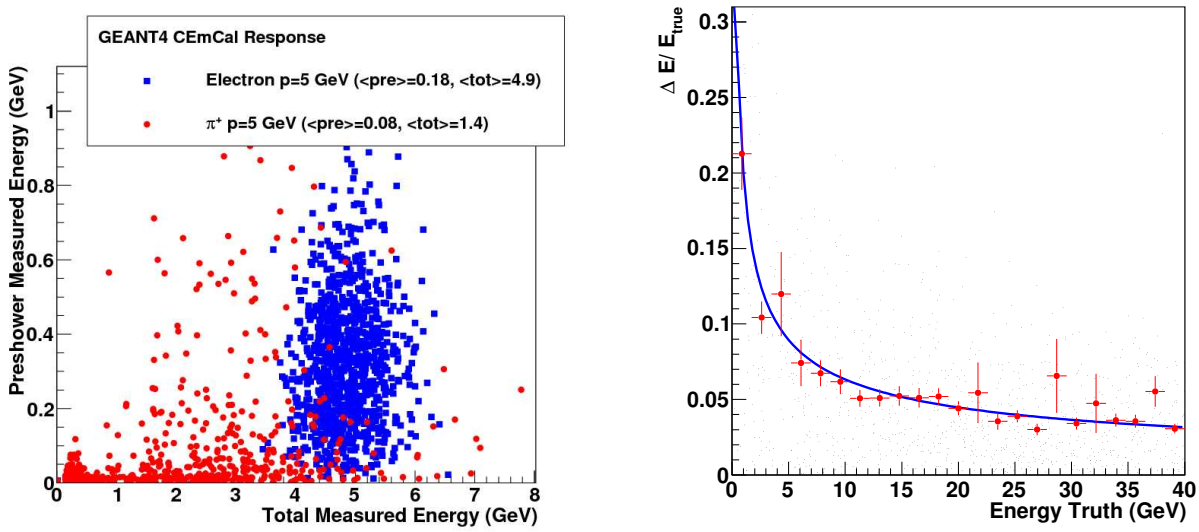

Figure 7.13: GEANT4 simulation examining the electron to π^- separation for momentum = 5 GeV particles (left). GEANT4 simulation for single photon response in the compact electromagnetic calorimeter. With the default sampling in this configuration, the resolution is approximately $20\%/\sqrt{E}$ (right).

used for the operating gas for the GEMs, and the requirement that it be essentially blind to hadrons. The requirements for building and operating a GEM tracking detector for PHENIX would be much less demanding, and would be similar to the design of other GEM trackers that have now been successfully operated for many years [86]. Figure 7.14 shows a three-stage GEM detector providing a gas gain $\sim 10^3$–10^4 with simple readout strips that could be used as a tracking detector. More complex readout structures are possible that could provide two dimensional information with a minimal number of readout channels.

The STAR Collaboration is constructing their Forward GEM Tracker using GEM detectors in a very similar application at RHIC [296]. They plan to acquire GEM foils from an industrial manufacturer (Tech Etch [297]) and have adapted the COMPASS readout electronics to work with the STAR data acquisition system. The experience gained in the design, construction and operation of this detector will be of benefit for the future development of a GEM tracker for PHENIX, and we identify this as one specific area of R&D that we would like to pursue. This would involve studying various two dimensional readout structures in order to optimize the spatial resolution with minimal channel count, constructing larger scale prototype detectors, and developing readout electronics that would be compatible with an upgraded PHENIX data acquisition system.

One other possibility offered by a low cost gas tracking detector would be to increase the radius of the solenoid magnet (e.g., to ~1.0–1.5 m) and placing the tracking detectors at a larger radius. This could not only improve our momentum resolution, but might also

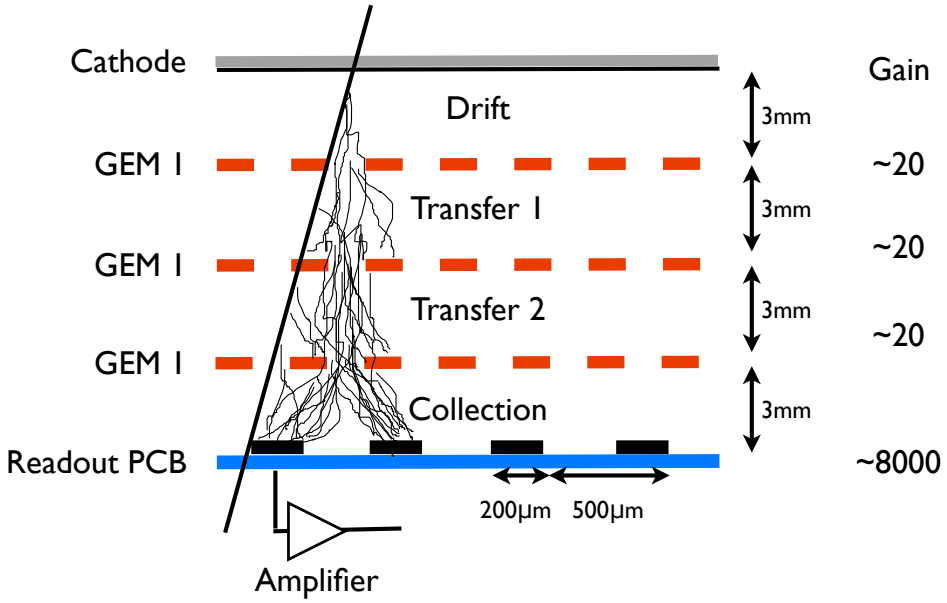

Figure 7.14: Three-stage GEM detector configured as a tracking detector using simple readout strips.

provide room for some form of particle identification (e.g., a Čerenkov counter or high resolution time-of-flight) inside the magnet, as discussed below. However, the implication of a larger magnet needs to be studied in terms of its impact on the magnet cost, as well as the cost and design of the EM and hadronic calorimeters and other components of the detector.

Compact EMCal

The design of the compact electromagnetic calorimeter is driven by the relatively small solenoidal magnet that forms the basis of the magnetic spectrometer and the desire to keep the overall detector small in order to minimize costs. The requirement on the energy resolution is rather modest ($\sim 15\%/\sqrt{E}$), but with an inner radius of 60 cm, the particle density on the face of the calorimeter will be quite high in heavy ion collisions, and it is therefore important to have a calorimeter with high segmentation and a small Molière radius in order to resolve individual showers. In addition, since we are interested in measuring jets, it is important to achieve a high level of hermiticity, which means that the calorimeter should be free of cracks or large uninstrumented regions. This implies that the calorimeter should have a pointing geometry which places some constraints on the choice of detector materials and readout devices.

The strawman detector which uses tungsten as the primary absorber and silicon sensors would have a Molière radius of $\sim$2 cm, which should provide adequate transverse shower

containment for measuring total energy. The spatial resolution requirements are highest for the preshower detector, and it is most likely that silicon strips will be required to achieve good two-shower separation up to ∼50 GeV. For the remainder of the calorimeter, the spatial resolution requirements are less demanding, and other sensor materials could be considered. For a sampling calorimeter, tungsten would still be the best choice for the absorber material due to its short radiation length and Molière radius. However, one could use plastic scintillator as the sensor material with an optical readout, which would still preserve the small Molière radius, but would reduce the cost and complexity of the silicon sensors in the rear portion of the calorimeter. This would mean having to combine two different technologies for different parts of the detector. One possibility would be a scintillator accordion design, similar to the liquid argon accordion used in ATLAS [11], but with plastic scintillator used in place of liquid argon. A prototype design constructed of lead is shown in Figure 7.1.3. In this configuration, layers of plastic scintillator are interspersed between tungsten plates and read out at the back with wavelength shifting fibers. One potential challenge with this design would be forming the tungsten plates into an accordion shape, which may require special machining or joining of multiple plates. However, a new technology that uses a tungsten composite with a density very similar to pure tungsten ($\rho = 17.5\,\mathrm{g/cm^3}$) would allow forming accordion shaped plates and is also being considered [301]. These shaped plates of tungsten and scintillator would be arrayed cylindrically around the beam to form the EMCal as shown in Figure 7.16.

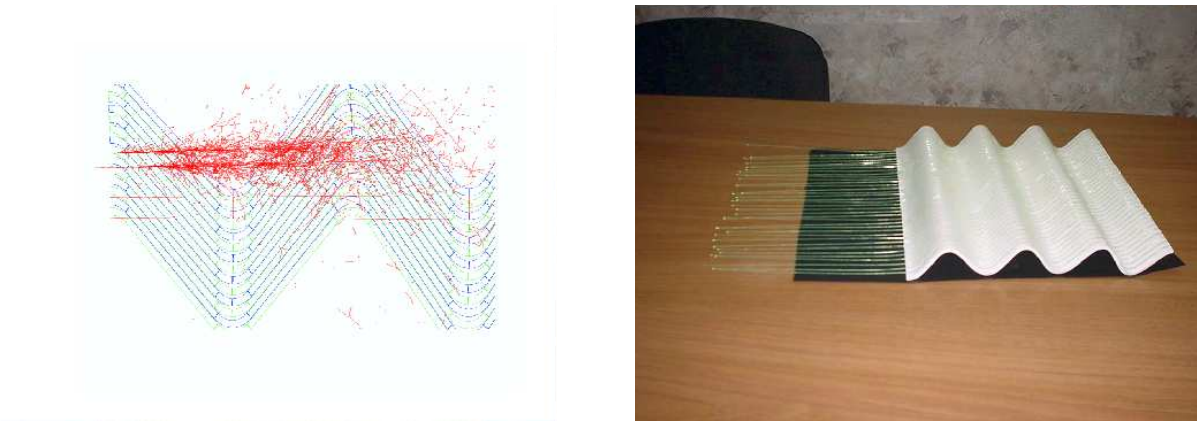

Figure 7.15: Prototype design of a scintillator accordion calorimeter with layers of plastic scintillator read out with wavelength shifting fibers interspersed between heavy metal absorber plates.

Another possibility would be to have a projective shashlik type design using tungsten plates to form trapezoidal shaped modules with interspersed layers of plastic scintillator and wavelength shifting fibers passing through which are read out at the back as shown in Figure 7.17. One other possibility would be to use high density scintillating crystals, such as lead tungstate, which also has a Moliere radius of ∼2 cm, but this would probably be a more expensive than any of the tungsten scintillator designs.

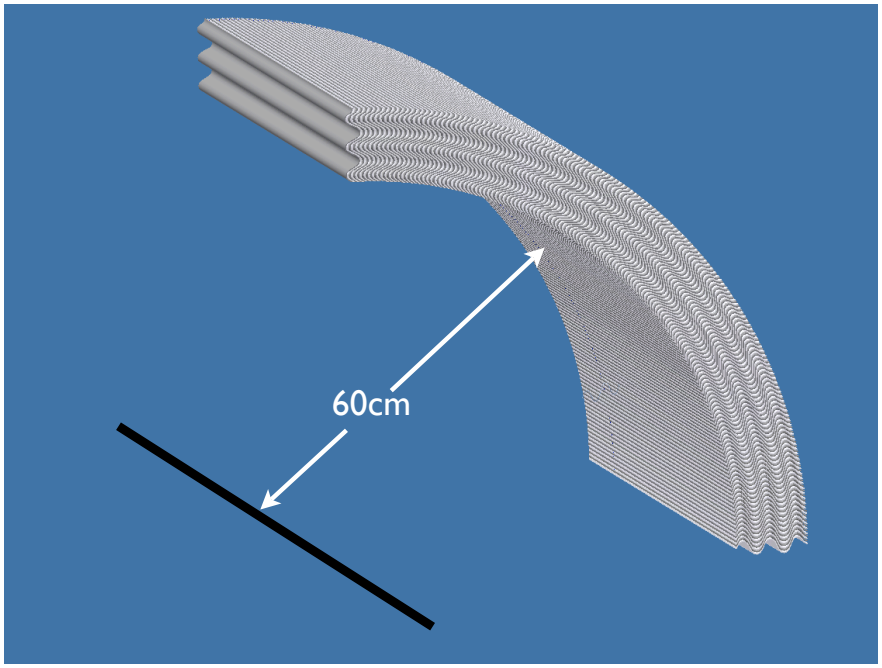

Figure 7.16: Schematic diagram of a one-quarter azimuth portion of a possible W-Sc accordion EM calorimeter. The front face of the EMCal sits at a radius of 60 cm from the beam.

If the entire calorimeter sits in the magnet field, one would have to use a readout device that could work in that environment. The likely choices would be either avalanche photodiodes or silicon photomultipliers. These are small, compact devices that are well suited to fiber readout detectors, as well as crystals. It is likely that such devices would also be used even if the back portion of the calorimeter was outside the magnetic field simply because of their compact size relative to photo-tubes.

We have not estimated the cost of using tungsten and scintillator for the back portion of the calorimeter, but we expect that it would result in a considerable cost savings compared to tungsten plus silicon. This is due to the lower cost of the scintillator relative to silicon, and also because the readout system could in principle be much simpler, having fewer readout channels only at the back. However, the design of a tungsten scintillator calorimeter would have to be studied in more detail, and a realistic cost estimate would have to be developed. We identify this as another R&D area that we would like to pursue. In particular, we would like to study both the scintillator accordion and projective shashlik designs in order to determine their performance, energy resolution, and to study the various mechanical issues involved in their construction. This would involve a program of simulation, design, fabrication and testing of various prototypes of both types of detectors.

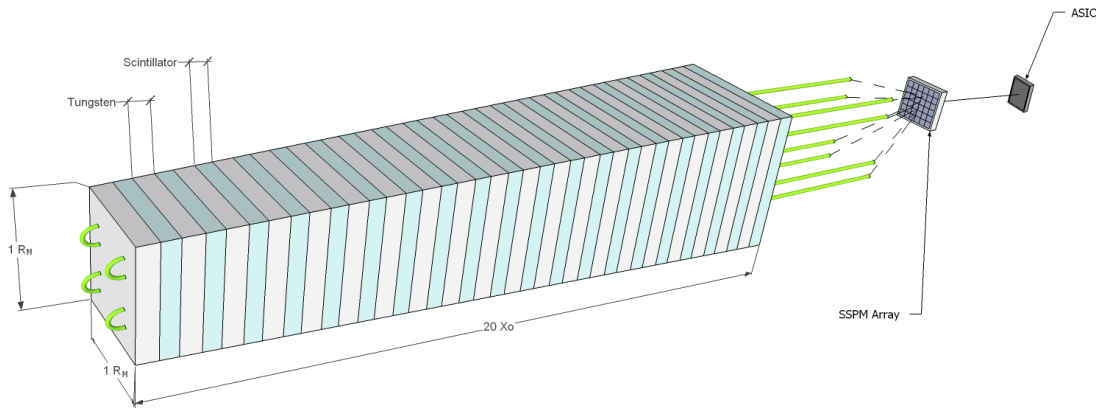

Figure 7.17: Projective shashlik type calorimeter using scintillator plates and wavelength shifting fibers read out with silicon photomultipliers.

Hadronic Calorimetry

The conceptual design of the hadron calorimeter is at an early stage, but we can nonetheless identify certain key design requirements. We need a high degree of hermiticity. This is particularly important for jet measurements. We also need a compact design, implying a calorimeter with high density and a short hadronic absorption length. Our requirements for energy resolution ($\sim 50\%/\sqrt{E}$) and segmentation ($\Delta\eta = \Delta\phi = 0.1$) are not particularly demanding. We feel that all of these requirements can be met with calorimeter designs that are available today.

One promising design uses scintillating tiles with wavelength shifting fibers and is similar to both the ATLAS barrel and CMS hadron calorimeters [11] [153]. These detectors are both hermetic and have been constructed on a very large scale, and a calorimeter of the size needed for the PHENIX upgrade would not require any significant new development. Another option is a design using scintillating fibers—this has been used in previous experiments [100, 186]. Finally, one could consider a combination of scintillating and Čerenkov fibers [317], which would provide excellent energy resolution and a very uniform electron-hadron response. The enhanced performance of a dual fiber calorimeter may not be required, and the overall hermiticity of such a design would have to be studied. We therefore plan to investigate these options as we move forward on the hadronic calorimeter design.

Magnet

The D0 solenoid magnet is an existence proof of a small, thin, superconducting solenoid magnet. The cryostat of the D0 magnet has an inner bore of diameter 1.067 m, a length of 2.729 m, a central field of 2.0 T, and a thickness of 0.9 X_0 at 90° [14]. The D0 solenoid was built by Toshiba and delivered to the D0 experiment in 1997. The D0 solenoid provides a useful baseline for discussion of a solenoid designed specifically for PHENIX.

We have had preliminary discussions with the Superconducting Magnet Division at BNL about possible designs of a suitable solenoid. It would most likely be based on conventional low temperature superconducting cable, although a high temperature superconducting (HTS) magnet may become cost effective in the next few years. The D0 solenoid was constructed in about two years, and a similar construction period could be anticipated for a similar solenoid for PHENIX.

Table 7.2: A schematic of a solenoidal magnet with the dimensions being considered in the strawman design. The table shows the field integral along lines of constant η.

η	θ (degrees)	$\int \boldsymbol{B}\,\boldsymbol{dl}$ (T-m)
0.0	90.0	1.506
1.0	40.4	1.322
2.0	15.4	0.387
3.0	5.7	0.140
4.0	2.1	0.052

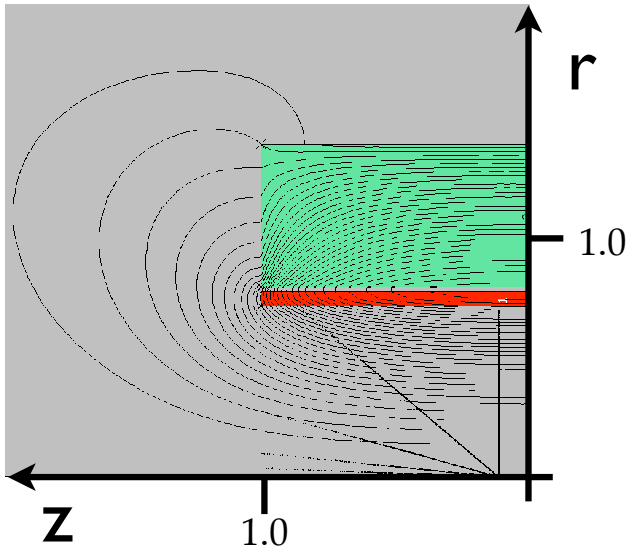

Particle Identification

The strawman design has excellent particle identification for γ, π^0, η, and electrons with the Compact Electromagnetic Calorimeter. Lessons from RHIC have shown that identification and differentiation of suppression, flow, and in the future fragmentation patterns for baryons (in contrast to mesons) contain key information. In the compact configuration this presents a major challenge. We have π, K, p identification via dE/dx in the silicon detectors, but with a range limited to hundreds of MeV. One can also identify Λ and K_S, though this is limited in p_T reach due to the quickly decreasing probability to decay within the range of the tracking detectors (particularly if the inner radius of the CEMCal

is of order 50–60 cm). We are exploring novel technology options that might be feasible, and may influence design decisions including moving the inner radius of the CEMCal to a somewhat larger distance.

A key question is in the future, how interesting is baryon versus meson identification for $p_T < 5$ GeV, as PHENIX has had over the past decade. This might be achievable within the compact design if one moved the radius out to 1 meters with 10 ps TOF. However, if one is measuring jets with $p_T = 40$ GeV, does the physics interest lead one to want to measure leading meson and baryons in which case one needs some baryon (e.g. (anti) proton or (anti) Λ) identification for $p_T > 20$ GeV or more. This measurement challenge is one we are pursuing, but without a clear current solution. Below, we present a possible technological path forward for performing charged particle identification in the former case.

High Resolution Time of Flight The field of high resolution timing for PID has recently seen progress after a long period during which typical resolutions hovered around 100 ps. One significant advance is the development of multigap Resistive Plate Chambers (mRPC) which have made it possible to build large area, high performance timing detectors. This technology is being used successfully in the PHENIX, STAR and ALICE experiments. Research is underway to improve the timing performance of these detectors by increasing the number of gaps and making the gaps smaller, so that it might be possible in a few years to achieve 30 ps timing resolution. An mRPC placed at a radius of $\sim$1.5 m would then be able to perform π, K separation out to a momentum of $\sim$2.5 GeV/c and K, p separation out to $\sim$4 GeV/c.

Another trend in fast timing has been the development of photodetectors with transit time spreads of less than 50 ps, such as Multi-Channel Plate PMTs (MCP-PMT) and Hybrid Photodetectors (HPD). These new photodetectors enable one to build TOF detectors that could achieve better than 10 ps resolution. A detector configuration would consist of a Čerenkov radiator to generate from a charged particle many prompt photons which are then detected with the very fast photodetector. With 10 ps resolution, one would be able to build a TOF wall at a radius of 60 cm, consistent with the compact requirements of the current strawman design, and still have the desired PID performance. The high cost of these photodetectors currently prohibits covering the large area required in the PHENIX upgrade, but research in the field is underway aimed at reducing the cost of MCP-PMTs, and in two years time one might be able to consider using the MCP-PMTs for large area coverage if these development efforts are successful.

The current strawman design does not include a detector for PID based on fast timing, but we are tracking the technology and are engaged in some related R&D. In fact, a proposal for a small area, large solid angle acceptance TOF wall using MCP-PMTs is being developed, which would provide much of the expertise and concepts needed to build the large acceptance central barrel TOF wall.

7.2 Forward Upgrades

In the second half of the decade the focus of the spin physics program will be on physics observables in polarized p+p collisions, which will require a detector with high acceptance at forward rapidity $1 < \eta < 4.0$ (see Chapter 6). Such a forward spectrometer added to PHENIX would not only allow measurements of A_N^{DY} at forward rapidity to test the QCD prediction that the analyzing power for the Sivers function in Drell-Yan and SIDIS is opposite, but would also allow the unique possibility to detect the scattered lepton in e+p/e+A collisions in the era of an eRHIC to virtualities $Q^2 \sim 0.1$ GeV^2, opening a whole new physics frontier (see Chapter 8). To realize these physics goals it is necessary to upgrade significantly the current PHENIX detector. The strawman design for the central barrel has already been described; in this section we describe a concept for the forward detectors.

Figure 7.18 shows the forward detectors of the strawman design, which consist of a RICH, a preshower, an EMCal, and a HCal, and additional tracking detectors to provide good momentum definition of the particles going forward. This combination of detectors is motivated in Section 6.1.1. For both Drell-Yan and the e+p/e+A physics the emphasis is on detecting electrons with high efficiency and purity.

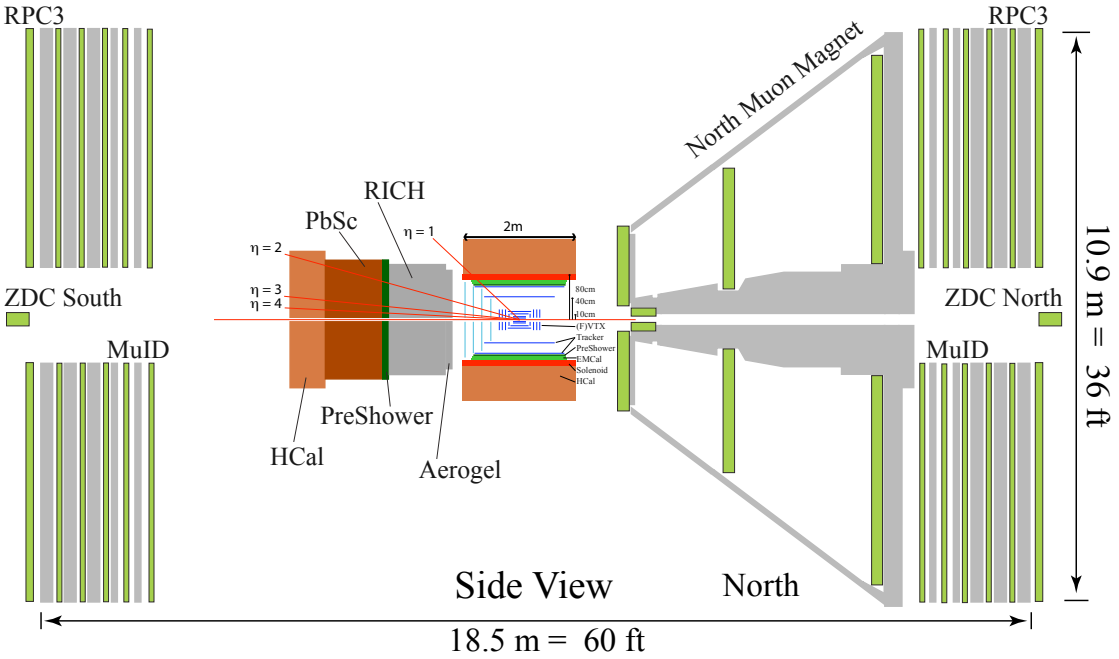

Figure 7.18: Schematic drawing of the new PHENIX detector.

The detector designed for these measurement requires excellent electron identification to reject hadron and photon backgrounds. In order to study various scenarios for achieving the required rejection, we have implemented a fast detector simulation consistent with

our proposed forward spectrometer upgrade. The spectrometer consists of a tracking detector (TRACK) in a magnetic field, a ring imaging Čerenkov counter (RICH), an electromagnetic calorimeter (EMCal), and an hadronic calorimeter (HCAL). The following conservative assumptions in terms of parameterized performance have been made.

- TRACK has a momentum resolution of $\Delta p/p \approx 2\%$.
- RICH has an electron efficiency of 94% for $p > 10$ GeV/c.
- EMCal has the resolution of the current PHENIX PbGl: $5.95\%/\sqrt{E} + 0.76\%$
- HCAL has the resolution: $50\%/\sqrt{E} + 5\%$ (similar to CMS or LHCb)

We have shown PYTHIA studies through a fast simulator in Chapter 6. We are currently pursuing a full GEANT4 implementation. Below we discuss the various technology options and R&D required to arrive at a full detector design.

7.2.1 Technology Options

Tracking Detectors

There are important tracking requirements for the $p+p$ spin program as detailed in Chapter 6, but also for detecting electrons and carry out a precision DIS physics program. It is important to keep the integrated radiation length at a minimum to keep bremsstrahlung as low as possible. As many of the tracks will be at small angles ($> 2^\circ$) the tracking system should also provide good position resolution as the bending in a solenoid close to the axis is minimal.

A modern collider detector should include a vertex detector that can track over a wide range of pseudorapidity, down to the lowest p_T allowed by the detector geometry, and be capable of reconstructing displaced vertexes from heavy flavor decays. Such detectors are typically implemented in two separate parts: a "barrel" layer that detects tracks out to $|\eta| \sim 2$ and an end cap composed of disks that extend the acceptance down to smaller polar angles (larger η). To achieve the performance needed to resolve displaced vertices from the primary vertex down to a separation of less than 100 μm, the barrel and end cap will need at least three sensitive layers providing two-dimensional measurement of particle positions with resolutions better than 10 μm in both directions. The usual technology choice for vertex detectors designed to measure heavy flavor decays is silicon hybrid pixel detectors. Such detectors have been used successfully at the Tevatron and are an integral part of the tracking systems for the ATLAS and CMS detectors. However, these detectors typically contain 100–300 μm of silicon and significantly more material in the separate readout chips resulting in typically 3–10% radiation length of material per layer, and this renders them unsuitable for applications like Drell-Yan and $e+p/e+$A physics, at least

in the forward (electron direction) end cap detectors where the constraints on material budget necessary to limit electron bremsstrahlung are the most severe.

In the last decade there has been significant progress in the development of Monolithic Active Pixel Sensors (MAPS) in which the active detector, analog signal shaping, and digital conversion take place in a single silicon chip (i.e. on a single substrate) (see [190] and references therein). These devices built using CMOS technology use an epitaxial layer as the active sensing element. Ionization deposited in the epitaxial layer is collected by N+ wells embedded in the epitaxial layer. The "pixel" pitch is determined by the location of the N wells so there is no need for actual segmentation of the detector as is done with traditional hybrid pixel detectors. As a result, CMOS pixel detectors can be built with high segmentation, limited primarily by the space required for additional shaping and digital conversion elements.

The key advantage of CMOS MAPS detectors is the reduced material required for the detector and the (on substrate) on-detector electronics. Such detectors have been fabricated and extensively tested (see e.g. [207]) with thicknesses of about 50 μm corresponding to 0.05% of a radiation length. The charge collection N+ wells are coupled to transistors that provide a first amplification stage and the incorporation of additional amplification and discrimination stages in the same substrate has been successfully demonstrated [173]. As a result, the MAPS pixel chips can directly drive digital signals to off-detector data collection electronics. The lack of separate read-out chips and associated bonding reduces both the material budget of the detector and the complexity of detector assembly. The reduced ionization electron yield of CMOS detectors compared to thicker hybrid detectors is offset by the on-board amplification of the signal and the reduction in noise due to the thin, low-depletion active layer. As a result, the detectors can be operated with a signal-to-noise ratio of 20–30 at temperatures as high as 40°C [190]. The CMOS MAPS detectors operate with low power dissipation.

There has been extensive development of the CMOS MAPS detector technology by Winter's group at Strasbourg (see [2] for an overview of the Strasbourg group's efforts), and ladders fabricated with sensors of similar geometry and functionality that might be required for the barrel part of a vertex detector are already being produced by that group.

For the endcap detector, nontrivial R&D may need to be done on fabrication of large sensors satisfying both geometric and material constraints. The most natural way to segment the disks in the end caps in would be to divide them up into ϕ-segments with each segment consisting of a single sensor. By not dividing the wedges radially, the need for detector overlap and the corresponding increase in material would be obviated. Assuming that the extent of the disks in the radial direction would be at least 10 cm, sensors capable of covering a complete ϕ-segment would be larger than the typical reticule (photo mask) used at foundries. However, through a process called stitching it is possible to join reticules to fabricate larger devices. Such a procedure was developed by industry for CMOS light imagers, in particular for space applications, but has never been used for CMOS charged particle detectors, and demonstrating the use of the technology for

CMOS MAPS sensors would help in the design of a vertex endcap detector capable of meeting the severe material constraints as in electron-ion/proton collisions. There is a proposed R&D project between BNL-Columbia and Strasbourg, which proposes for the forward disk-shape detectors to demonstrate a proof of principle of the stitching process, assuming a forward disk inner radius of 8 cm and an outer radius between 16 and 24 cm. The disk surface needs to be subdivided in as few as possible separate sensors in order to keep the material budget as low as possible. A rather natural set of dimensions of the sensitive area would be typically 2 cm width in its inner part and 4 to 6 cm width at its outer edge. Its radial extension would be in the range 8–16 cm. Such a surface is much larger than a typical reticule surface (about $2 \times 2\,\mathrm{cm}^2$) and thus would require stitching to produce. CMOS sensors are fabricated within standard mass production chip manufacturing processes, where the chip photolithography is realized over an exposure field (reticule) of about $2 \times 2\,\mathrm{cm}^2$. A stepper allows replication of these reticules over the full wafer surface. By default, the chip die is therefore limited to the reticule size. The limitation imposed by the exposure field of lithography steppers may be overcome with the stitching technology, which allows the physical merger of multiple design structures onto a wafer during the photolithography process. This opens the door to fabricating sensors composed of millions or tens of millions of pixels and featuring dimensions similar to those of a complete 8″ wafer. As it was never tried for charged particle pixel sensors, it is crucial to achieve the proof of principle of stitching within the proposed project. The plan is to extend the area of an existing chip from $1 \times 2\,\mathrm{cm}^2$ to a surface of about $5 \times 5\,\mathrm{cm}^2$ (10M pixels with 16 μm pitch). Their binary, zero-suppressed, read-out translates into a spatial resolution of about 3–3.5 μm. The expected read-out time is of the order of 300 μs. There are some challenges related to the stitching prototyping:

- the precision of the stitching technique, which manifests itself at the reticule boundaries, should match the accuracy of the pixel and read-out circuitry design without introducing design discontinuities;
- the sensor performance should be uniform over the complete sensitive area;
- the fabrication process and the stitching technique should allow for a high yield;
- capacitive and resistive effects consecutive to several-centimeter-long traces implemented in the sensor should not dilute its noise and read-out speed performances;
- the read-out architecture adapted to a sensor of 10M pixels needs to be validated.

If this project is successful it will be an option for the forward tracking of PHENIX in the next half of the decade. For the larger-angle tracking in the forward direction GEM detectors as described in Section 7.1.3 are the perfect solution. They provide good position resolution ($\sim 100\,\mu$m) and low material density.

Calorimetry

This section describes first ideas on technical solutions based on existing technology for the EMCal, HCal and Preshower in the forward spectrometer.

Electromagnetic Calorimetry The current plan is to re-use the lead glass and lead scintillator electromagnetic calorimeters from the present central detector and re-stack the modules so they fit in the geometrical requirements. As the particles have very high longitudinal momentum in the forward direction it is important to choose a material with a very small Molière radius. The goal should be to resolve the clusters of the photons from π^0 decays as high as possible—60 GeV is required and up to 80 GeV would be desirable for measurements of A_N at high x_F. The PbSc has a Molière radius of 3 cm with a tower size of $5.5 \times 5.5\,\mathrm{cm}^2$; the lead-glass has a Molière radius of 3.7 cm with a tower size of $4 \times 4\,\mathrm{cm}^2$ [114]. We are working to understand the relative advantages of reusing one type of module or the other as a forward EM calorimeter. An alternative would be an electromagnetic calorimeter made of $PbWO_4$ crystals. The advantages of such a calorimeter would be a significantly smaller Molière radius of 2 cm and a factor of two better energy resolution and higher radiation hardness than lead-glass. As it is planned to have calorimetry down to a rapidity of 4, it might be important to increase the lifetime of the PbSc-calorimeter to construct it in a way that it can be opened to the left and right during beam set up and injections. The experience from the forward meson spectrometer at STAR shows that this is a efficient method to protect the calorimeter from radiation damage. Before taking a decision on the EMCal detector material more studies on potential radiation damage need to be done.

Hadronic Calorimetry As the requirements for jet reconstruction in the forward direction are the same as for jets in the central detector, the same technology can be chosen (compare Section 7.1.3). After more detailed simulations it might turn out that keeping muon identification in the south arm in addition to the North Muon Arm might be beneficial. If this becomes an requirement it might turn out that following design ideas as presented for the CALICE HCAL and TCMT design [1] might provide a good technical solution combining hadronic calorimetry and muon identification.

Preshower If the final solution is to re-use the PbSc for the electromagnetic calorimeter it is essential to have a high resolution preshower, similar to the one discussed for the central detector in Section 7.1.3. There is one difference in the requirements for the forward one. For single spin asymmetries A_N in the forward direction it would be desirable to resolve photons from π^0 and η decays up to 80 GeV to ensure that the highest x_F are covered. A preshower based on the FOCAL technology (Section C.2.5) would be good solution. As in the case for the HCal, R&D and design of the forward and central detector preshower can be done together.

The latest information about the developments on RICH detectors can be found at [6, 7]. For our application we need a RICH detector which can identify particles over a wide range of momenta, preferably up to 60–80 GeV/c. This can normally not be reached by single-radiator RICH; the solution is to go for a dual-radiator RICH, the same way HERMES [**?**] and LHCb [3] did successfully.

The two radiators should have different refractive indices, such that one radiator distinguishes responses to particles at low momentum and the other at higher momentum. For the last several years aerogel has been the chosen radiator for RICH detectors, which cover lower momentum particles (1–10 GeV/c). LHCb chose aerogel from the Budker Institute of Nuclear Physics in Novosibirsk with a refractive index of $n = 1.03$. Matsushita together with university institutes in Japan is also producing high quality aerogel. They have tiles with refractive indices up to 1.22, and for the standard tiles with $n = 1.03$ the light output has more than doubled for a 50 mm thick tile between 2001 and new production as of 2005.

The aerogel radiator in combination with a gas radiator like C_4F_{10} ($n = 1.00137$) will allow separation of particles up to 60 GeV/c, which would be a nice solution for the forward RICH for PHENIX. LHCb has chosen exactly this design and added another RICH based on CF_4 to identify particles up to 100 GeV/c. Figure 7.19 (left) shows the detection thresholds for the different particle species in the three Čerenkov media, and the right plot shows the estimated performance of the particle identification based on simulation studies including effects from the quantum efficiency of the photo-detectors.

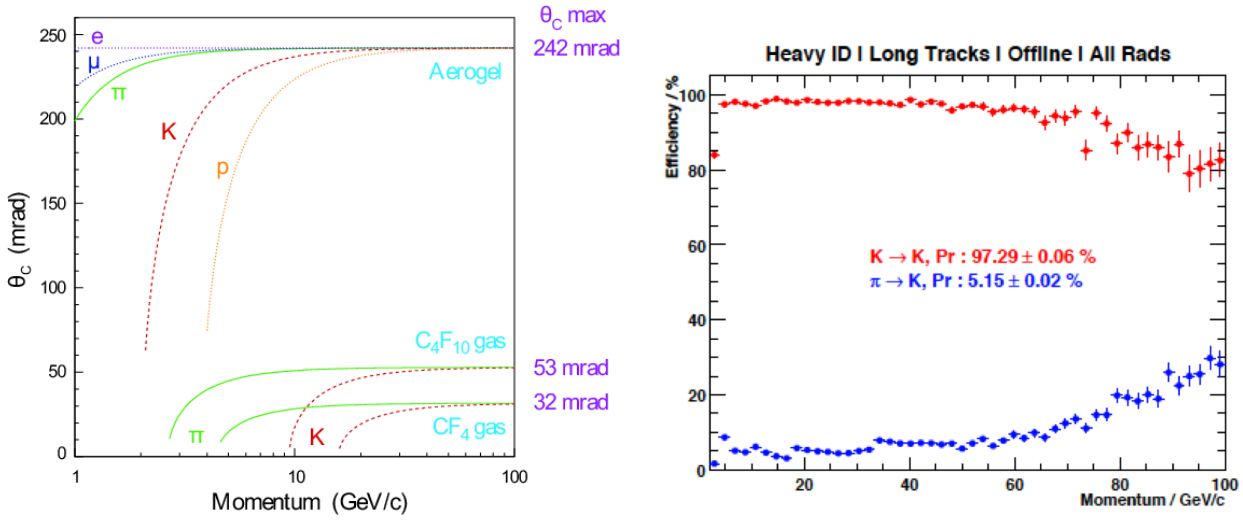

Figure 7.19: Left: Detection thresholds for the different particle species in the three Čerenkov media. Right: Estimated performance of the particle identification based on simulation studies including effects from the quantum efficiency of the photo-detectors

Another critical part of a RICH detector is the mirrors, which need to be lightweight as they are in the path of particles and yield to photon conversions and straggling. There are several solutions. LHCb uses glass-coated beryllium and carbon-fiber lightweight spherical mirrors, which have less than 2% of a radiation length. This would not cause any problems for PHENIX as the RICH would be situated behind all tracking detectors.

Lastly, we address the question of what technology to choose for the photon detector. The technology depends strongly on the wavelength spectrum of the radiators, the angular resolution needed to separate multiple rings and the anticipated rates and backgrounds in the detector. Experience shows that photon detectors based on conventional PMT technologies work best, but they have the disadvantage of being expensive and do not always have the pixel size needed for the angular resolution. Many other technologies have been used, LHCb uses custom-built pixel Hybrid Photon Detectors [253]. The latest trend is moving toward GEMs as photon detectors. PHENIX already has experience from the HBD with GEM detectors as part of a Čerenkov detector. It will require some R&D to understand what the best and most cost effective solution for a PHENIX RICH is.

The performance of the new PHENIX detector with respect to acceptance for $e+p/e+$A collisions is discussed in Chapter 8.

Chapter 8

ePHENIX Physics Plan for the Electron Ion Collider

The PHENIX detector upgrades referred to as sPHENIX and discussed in Chapter 7 are driven by p+p, p+A, A+A physics. This detector upgrade also provides an excellent opportunity to carry out an e+p and e+A physics program, referred to as ePHENIX. In this Chapter, we show that the upgraded PHENIX is well suited for:

- Inclusive e+p physics to measure polarized and unpolarized structure functions. For the polarized case, these measurements will significantly advance our knowledge of the contributions of quarks and gluons to the proton spin.

- Inclusive e+A physics to measure unpolarized structure functions and derive nuclear parton distribution functions nPDFs. These measurements are particularly relevant to studies of gluon saturation effects.

- Elastic diffractive physics, i.e. elastic vector meson production and deeply virtual Compton scattering (DVCS). In e+p a tomographic picture of the proton will become possible, while diffractive e+A pins down the initial state for heavy ion collisions. Most of the measurements require the addition of "Roman pot" detectors.

With completion of sPHENIX prior to turn on of eRHIC, these measurements will be available at the start of the eRHIC program. It is important to stress that during the eRHIC era, the capabilities for running p+p, p+A, A+A are kept fully intact—which is why we refer to this time period as the SuperQCD Era in Figure 1 of the Executive Summary.

8.1 eRHIC Machine Design

The future "QCD factory" eRHIC would provide for the first time ever collisions between polarized electrons and: longitudinally and transversely polarized protons in a beam energy range of 50-250 GeV (up to 325 GeV if the DX magnets are replaced); light ions (*d*,Si,Cu); heavy ions (Au, U) with beam energies of 50-100 GeV/u (and up to 130 GeV/u if the DX magnets are replaced); and longitudinally and transversely polarized He^3 at 215 GeV/u. In the current eRHIC design the electrons undergo multiple passes through recirculating linacs (energy recovery linacs, ERLs) sited within the existing RHIC tunnel. Figure 8.1 shows the recirculating linacs and lattice of the multipass arcs in the RHIC tunnel. The current eRHIC staging will sequentially increase the electron energy from 5 to 20 (or possibly 30) GeV as the superconducting cavities are built and installed. There is also the possibility of having a positron beam at the top energy.

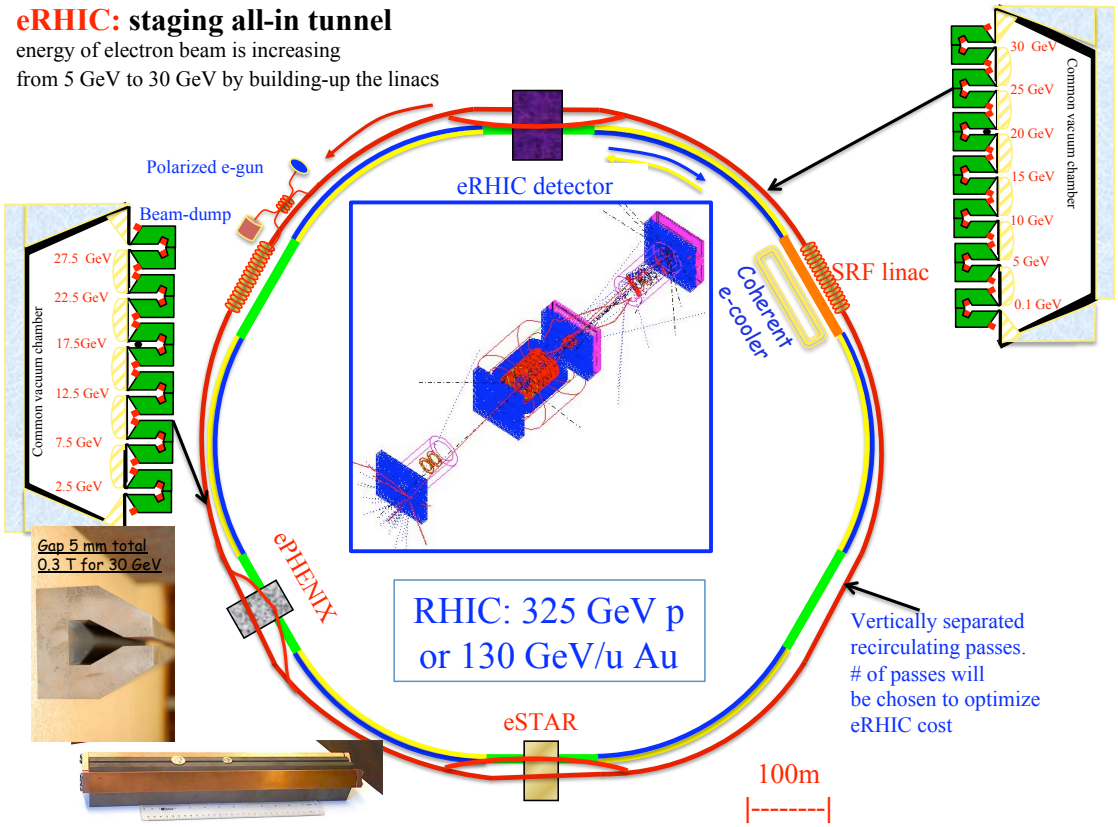

Figure 8.1: New eRHIC layout with two linacs inside of the RHIC tunnel. Inserts show the magnets and recirculating arcs.

As already indicated, the staging of eRHIC is not expected to require additional civil-engineering construction. The recirculating linacs and arcs will be placed inside the existing RHIC tunnel. The noncolliding electron beams will bypass the two existing large detectors four to six times, although the technical details of the bypass still need to be

determined. It is assumed that the present large detectors can be changed to accommodate electron-ion collisions. Another dedicated eRHIC detector will be placed at the large RHIC interaction region at the 12 o'clock position. Two recirculating linear accelerators (RLAs) will be installed in the straight sections of the IRs at 10 and 2 o'clock.

The details and constraints of the eRHIC IR design for electron-ion collisions as implemented for the PHENIX IR still needs to be worked out, and will require more details on the upgraded PHENIX detector design. One of the major changes compared to what is discussed above might be the distance between the IP and the first focusing quadrupoles. This distance is currently 4.5 m; increasing it at a specific IR leads to a lower luminosity. The current plan foresees the electron beam going in the same direction as the yellow hadron beam, while using the blue ring for the hadron beam only. We stress here that none of the changes discussed above will compromise RHIC's capabilities for hadron-hadron collisions.

8.2 Deep-Inelastic Scattering and ePHENIX

Deep-inelastic scattering (DIS) and hadron-hadron scattering have advantages and disadvantages in studying QCD and nuclear structure. Figure 8.2 shows the neutral-current (NC) and charged-current (CC) cross sections measured by ZEUS and H1 over a wide range in Q^2. The figure shows that the NC DIS process is dominated by electromagnetic interactions up to $Q^2 \sim M_W^2$.

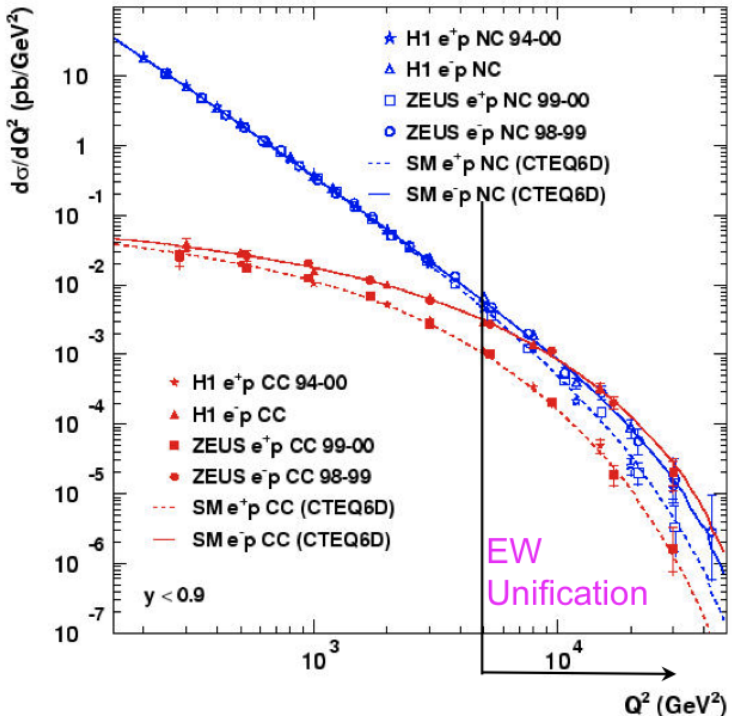

Figure 8.2: Cross sections for (blue) neutral and (red) charged currents measured by ZEUS and H1. Electroweak unification is easily observed at $Q^2 \sim M_W^2$.

In contrast to hadron-hadron interactions, DIS is governed by a probe with a simple structure, which does not disturb or interfere with the partons in the nucleons. Having a photon as the dominant exchange boson leads to one of the major differences between DIS and hadron-hadron scattering: access to the gluonic structure of nuclei is indirect, via the Q^2 scaling violation of the structure functions [13] unless processes such as photon-gluon fusion (PGF) or QCD-Compton (QCDC) are tagged. The Feynman diagrams for both of these processes are shown together with the one for DIS in Figure 8.3.

The biggest difference between DIS and hadron-hadron interactions is that for processes in which the scattered lepton is detected, the parton kinematics can be accessed by measuring the scaling variable Bjorken-x (x_B), which in LO is directly related to the momentum fraction x of partons on the light cone [291]. Diffractive processes constitute another important class of processes in lepton-nucleon scattering [104]. The Feynman diagrams

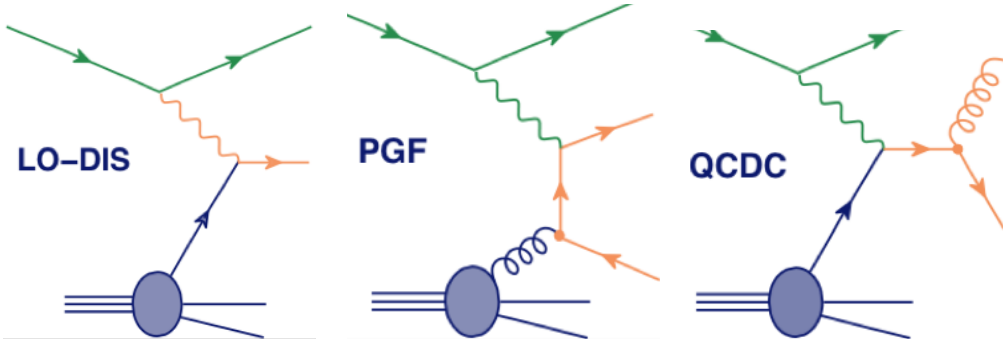

Figure 8.3: Feynman diagrams for leading order (left) deep inelastic scattering, (middle) photon-gluon fusion and (right) QCD-Compton.

for elastic, single, and double diffraction are shown in Figure 8.4. To tag these processes it is either necessary to detect the complete final state including the scattered beam proton or to use the so-called rapidity gap method, which requires an absence of activity in the detector between the outgoing proton beam and the final state coming from the virtual photon.

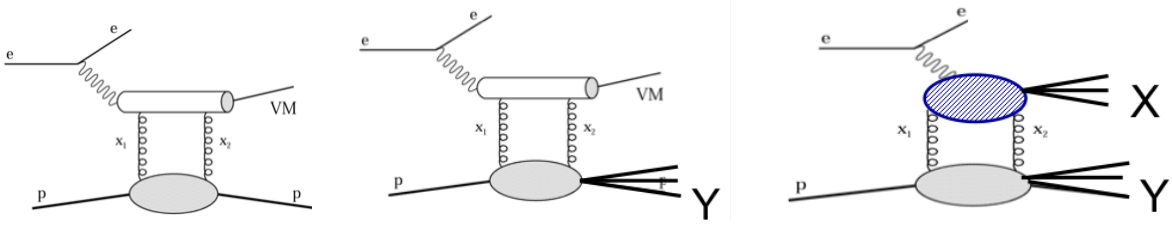

Figure 8.4: Feynman diagrams for (left) elastic, (middle) single, and (right) double diffraction.

Figure 8.5 shows that eRHIC will extend the current kinematic coverage in lepton-nucleus scattering significantly, since all prior e+A experiments having used fixed targets. A similar increase in kinematic reach will be provided in polarized lepton-nucleon scattering.

Figure 8.6 shows the pseudorapidity coverage of the current and strawman sPHENIX detectors. With the upgraded central detector and, more importantly, with the new forward spectrometer, PHENIX will have electromagnetic and tracking coverage from $1 < \eta < -4$; therefore, PHENIX will have a large acceptance for the scattered lepton at all stages (5×50 GeV^2 to 30×325 GeV^2) of eRHIC.

Figures 8.7–8.10 show kinematic plots for the different stages of eRHIC. The kinematic definitions follow the conventions used at HERA. Positive z is defined by the hadron beam direction, with positive pseudorapidity and a θ of 0°. The lepton beam goes in the opposite direction, with negative z and pseudorapidity and a θ of 180°. All plots require a minimum Q^2 of 0.1 GeV^2 and the inelasticity y between 0.05 and 0.93.

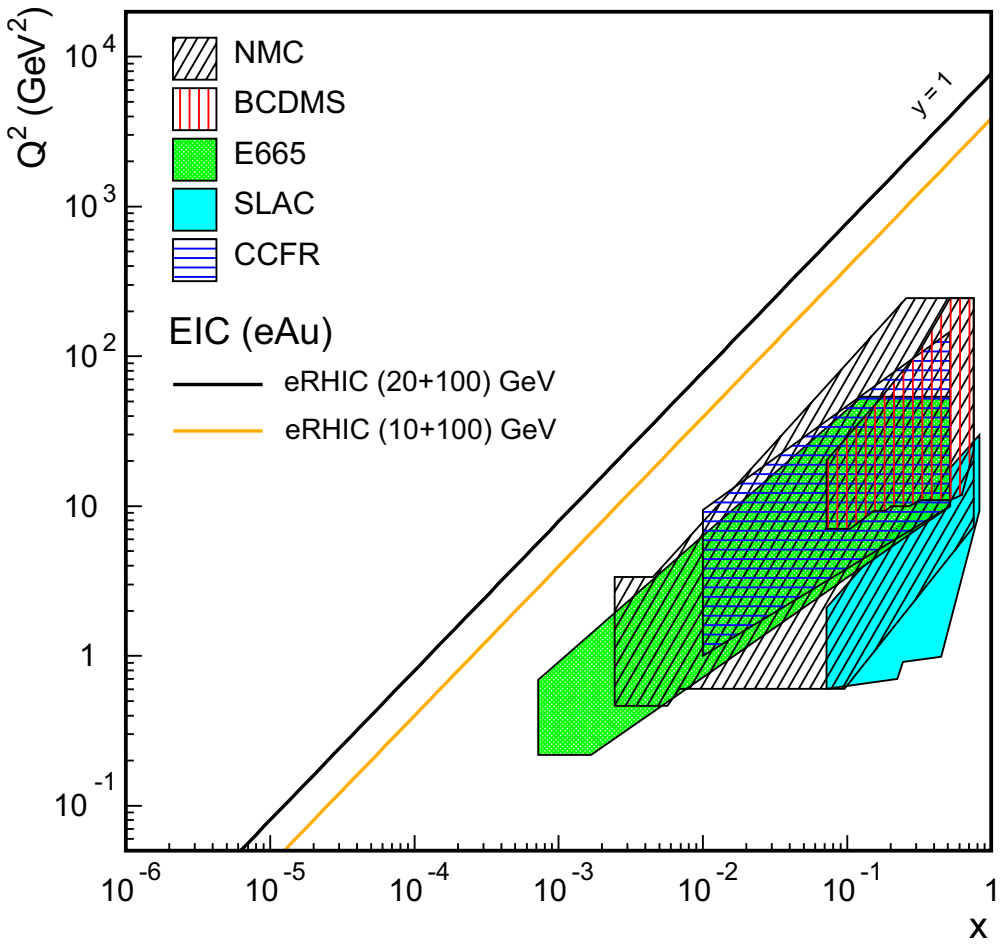

Figure 8.5: The $x - Q^2$ coverage of eRHIC for two beam-energy combinations compared to different fixed-target experiments.

Figure 8.7 shows the pseudorapidity of the scattered lepton as a function of Q^2 for varying lepton and hadron beam energies. The two black lines give the bounds of the acceptance in pseudorapidity of the current PHENIX central detector. It is evident that with the current PHENIX detector the detection of the scattered lepton is only possible at very high Q^2 for the low electron beam energy stage of eRHIC.

Figure 8.8 shows z (=E_π/ν) for pions for DIS as a function of rapidity. Even for the newly upgraded PHENIX it will be difficult to make significant measurements that require the detection of at least one identified hadron in coincidence with the scattered lepton. The majority of hadrons have a rapidity > 1, and therefore miss the central detector and go into the muon arm (see Figure 8.6). This measurement is complicated by the fact that currently no PID is foreseen in the central detector. (The acceptance of the new central and forward sPHENIX detector is indicated by the black lines.)

As pointed out above there is another important class of processes in lepton-nucleon scattering, diffractive processes, such as elastic vector meson production or deeply virtual

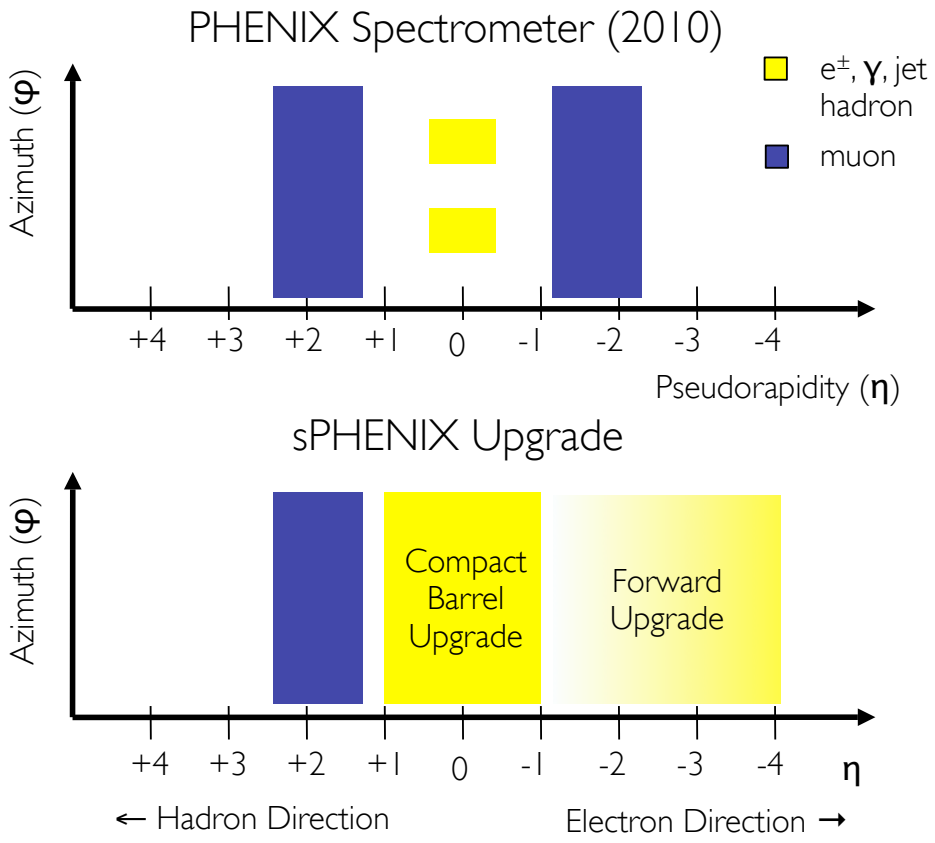

Figure 8.6: Rapidity coverage of the current PHENIX detector compared to the strawman sPHENIX detector. The central barrel detector covers $|\eta| < 1.0$; the forward detector has tracking coverage for $1 < \eta < 4$, with full EMCal and HCAL coverage for 1.5–2.0 $< \eta <$ 4.0, with the exact range dependent on the final design configuration

Compton scattering (DVCS). Figure 8.9 shows the rapidity distribution of pions coming from exclusively produced vector mesons like the ρ^0. The same distribution is obtained for the decay products of the J/ψ. The new PHENIX detector will be perfectly designed to measure the decay products of exclusively produced ρ^0's and J/ψ's. There is only one caveat to this statement: to ensure that the final state is exclusive it is important to measure the scattered beam proton. Figure 8.10 shows the scattering angle for the proton as a function of the Mandelstam variable t, the momentum transfer to the proton. It is obvious from these plots that the proton can only be detected in "Roman Pot" detectors very near the beam line. It might be highly desirable for PHENIX, especially because of the importance of these reactions for e+A collisions, to install "Roman Pot" detectors for the eRHIC era.

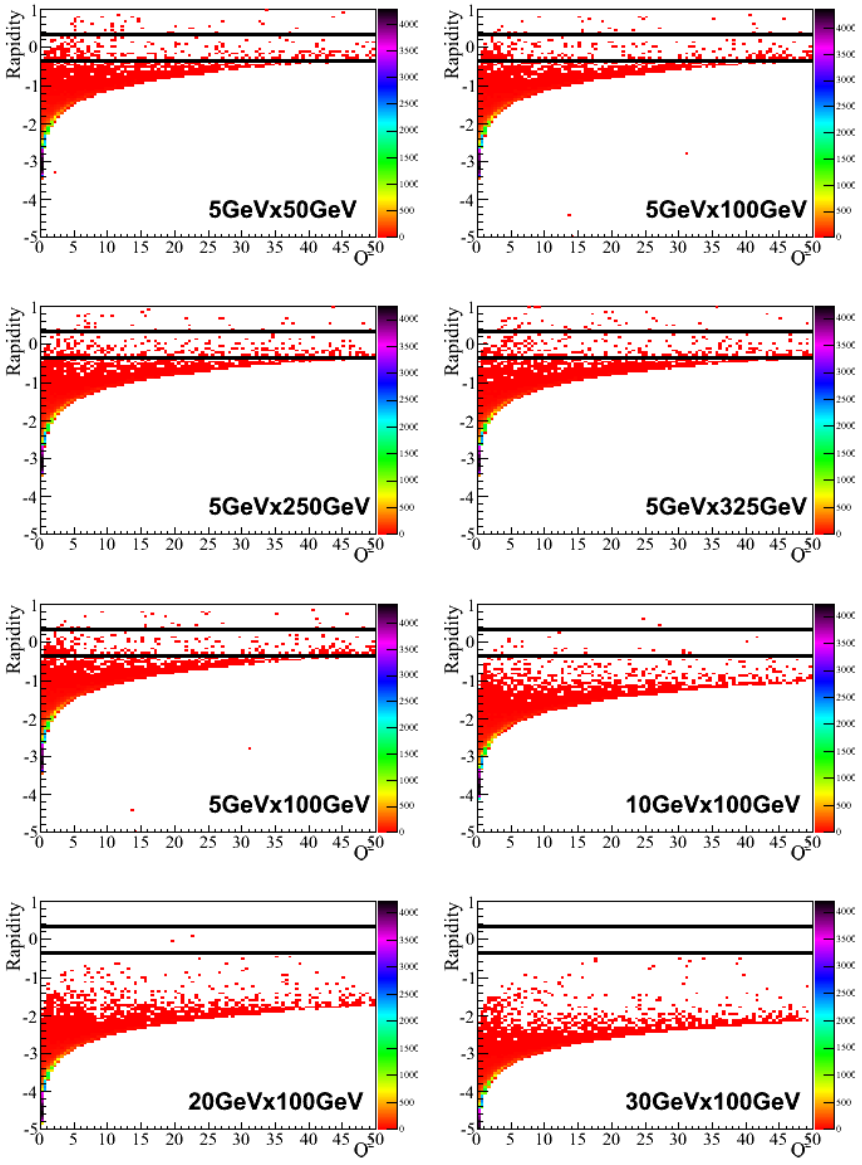

Figure 8.7: Scattered lepton pseudorapidity as a function of Q^2 for different beam energy combinations.

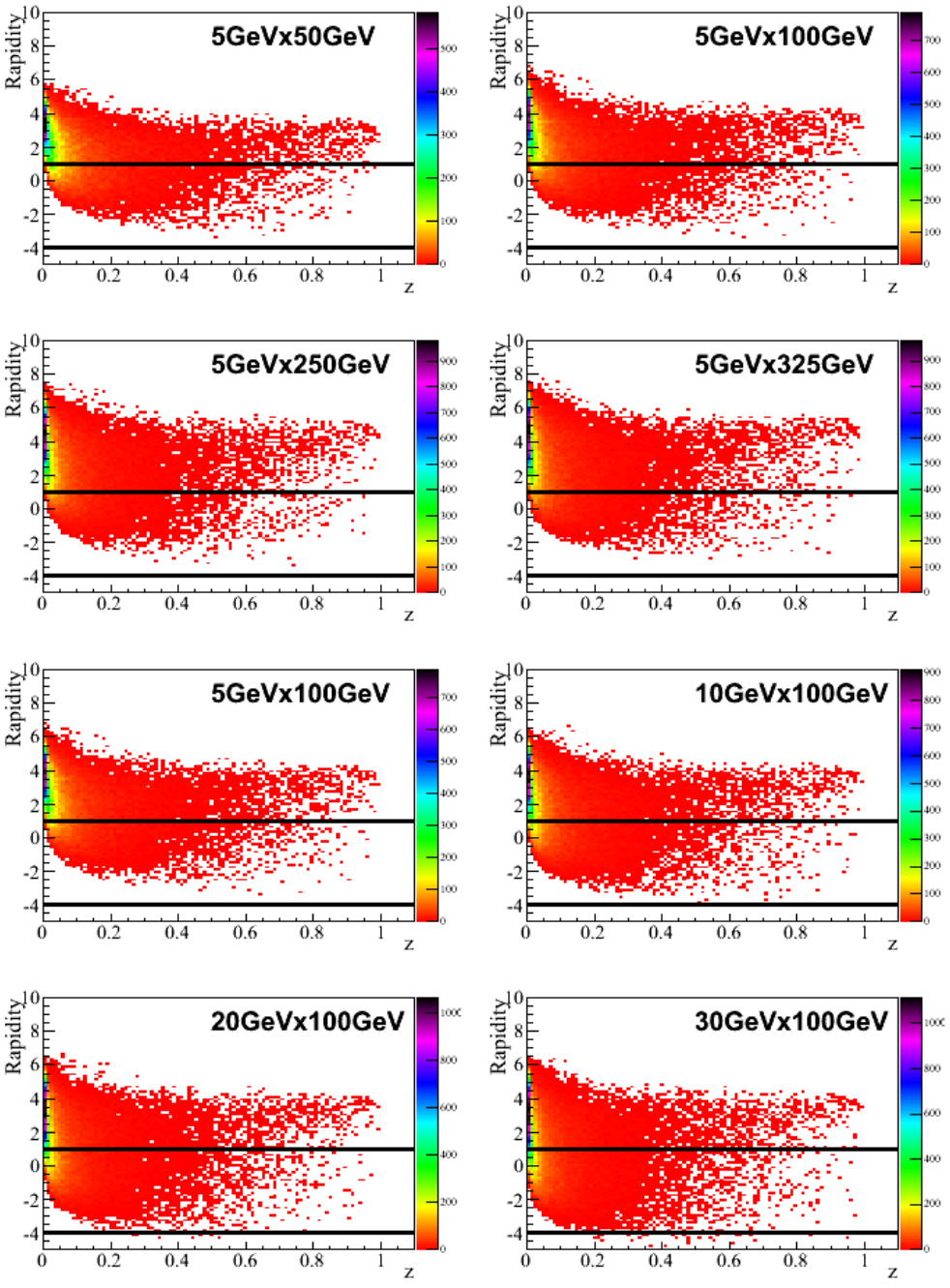

Figure 8.8: Pion z ($=E_\pi/\nu$) as a function of pseudorapidity for different beam energy combinations for nonexclusive processes. For these plots the Q^2 cut was raised to 1 GeV^2. The black lines bound the acceptance for hadrons in the new PHENIX detector.

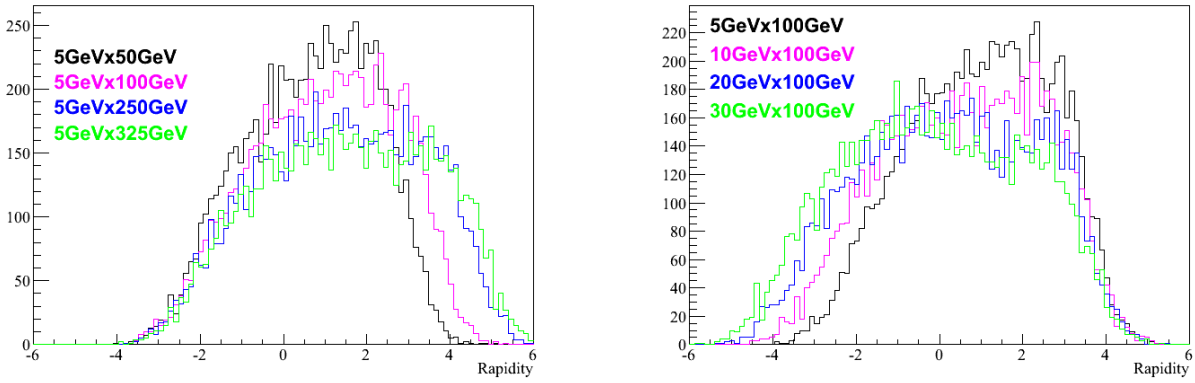

Figure 8.9: Rapidity distribution for pions coming from exclusively produced vector mesons such as the ρ^0 for different beam energy combinations. The decay products of the J/ψ have the same distributions.

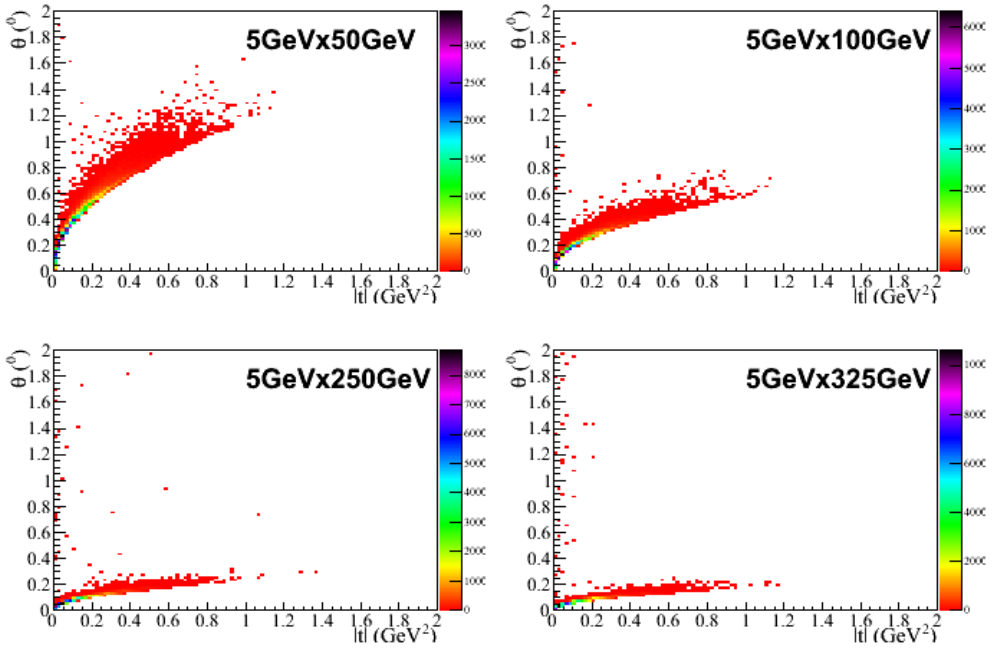

Figure 8.10: The angle of the scattered beam proton as a function of the variable t for elastic diffractive processes with different beam energy combinations.

8.3 e+A Physics with ePHENIX

Electron-nucleus (e+A) collisions at RHIC will provide essential data for and/or insight on physics problems critical to the understanding of RHIC nuclear collision results. An extensive analysis of the physics opportunities presented by e+A measurements at a collider such as eRHIC is presented in [60]. Here we highlight the key points and demonstrate where e+A measurements using the upgraded PHENIX detector can significantly advance the program described in [60]. In particular PHENIX can contribute critical measurements addressing the following topics:

- Improving knowledge of nuclear parton distributions (nPDFs).
- Testing the hypothesis that nuclear parton distributions are saturated at low x.
- Investigating nuclear generalized parton distributions.

Measurements corresponding to these items will both provide valuable "baseline" data for the RHIC program including the precision hard physics program discussed in Section. 3.1 and will advance the understanding of the partonic structure of nuclei.

8.3.1 Nuclear parton distributions

The current status of uncertainties in nuclear parton distributions has been discussed previously in Section 1.2. To further elucidate those uncertainties we show in Figure 8.11 results from a recent NLO extraction of parton distribution functions in Pb nuclei [184]. The bands in the figure indicate the uncertainties in the Pb PDFs resulting from errors in the input experimental data. Even in the context of this pQCD calculation relying on DGLAP evolution, there are large uncertainties at low x due to the limited range in both x and Q^2 of existing nuclear DIS data shown in Figure 8.5.

Inclusive measurements of deep inelastic scattering at eRHIC will provide new data that will improve the knowledge of nuclear parton distributions in heavy nuclei at both intermediate and low x. The neutral current deep inelastic $e^{\pm} + p$ scattering cross section is given by a linear combination of generalized structure functions. For unpolarized beams it can be expressed as

$$\sigma^{\pm}_{r,\mathrm{NC}} = \frac{\mathrm{d}^2\sigma^{e^{\pm}p}_{\mathrm{NC}}}{\mathrm{d}x\mathrm{d}Q^2} \cdot \frac{Q^4 x}{2\pi\alpha^2 Y_+} = \tilde{F}_2 \mp \frac{Y_-}{Y_+} x\tilde{F}_3 - \frac{y^2}{Y_+}\tilde{F}_L \,, \tag{8.1}$$

where the electromagnetic coupling constant α, the photon propagator and a helicity factor are absorbed in the definition of the reduced cross section $\sigma^{\pm}_{r,\mathrm{NC}}$, and $Y_{\pm} = 1 \pm (1-y)^2$. At the Q^2 values probed at an eRHIC, the contribution of Z exchange can be neglected, therefore $\sigma_{r,\mathrm{NC}}$ simplifies to $F_2 - y^2 F_L / Y_+$. The contribution of the term containing the

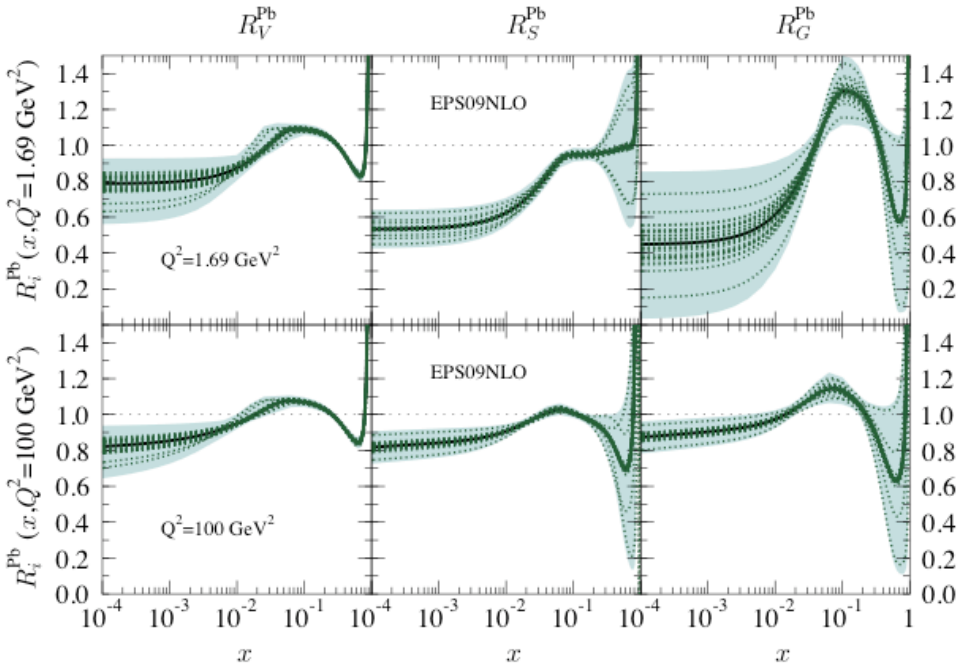

Figure 8.11: Results of EPS09 [184] extraction of parton distribution functions in Pb nuclei for valence quarks (left), sea quarks (middle), and gluons (right) for two different Q^2 values, top: $Q^2 = 1.69$ GeV^2, bottom: $Q^2 = 100$ GeV^2. Results are expressed in terms of the ratio with respect to parton distributions in the nucleon. Bands indicate the uncertainties in extraction of the Pb PDFs.

structure function F_L is significant for large values of y. The structure function F_2 probes the momentum distribution of quarks and anti-quarks in the nucleon and through its scaling violation it gives access to the gluonic structure [13]. F_L on the other hand is directly sensitive to the gluon distribution in the nucleon [148].

Figure 8.12 shows the Q^2 vs. x coverage of the proposed PHENIX upgrade detector for different combinations of nuclear and electron beam energies that will be available as the electron beam energy is increased. With such a combination of energies PHENIX will be able to substantially extend the Q^2 range of existing nuclear DIS measurements for $x > 10^{-3}$ and provide totally new measurements down to $x \sim 10^{-5}$. The extension of the Q^2 range of the nuclear F_2 measurements will improve constraints on the gluon distribution obtained from scaling violations, especially for $x < 10^{-2}$ where data are currently only available for $Q^2 <\sim 3$ GeV^2(see Figure 8.5). For $x = 10^{-3}$, PHENIX could extend the Q^2 range of data from 1 GeV^{2}to 20 GeV^{2}thereby providing a qualitative improvement in the extraction of the nuclear gluon distribution at such low x values.

Inclusive measurements of nuclear $F_2(x, Q^2)$ will be complementary to d+Au measurements that also provide constraints on the nuclear parton distributions, but with poorer control over the parton kinematics. For example, as discussed in Section 3.1, there are predictions for significant initial-state energy loss effects in hadron-nucleus and nucleus-

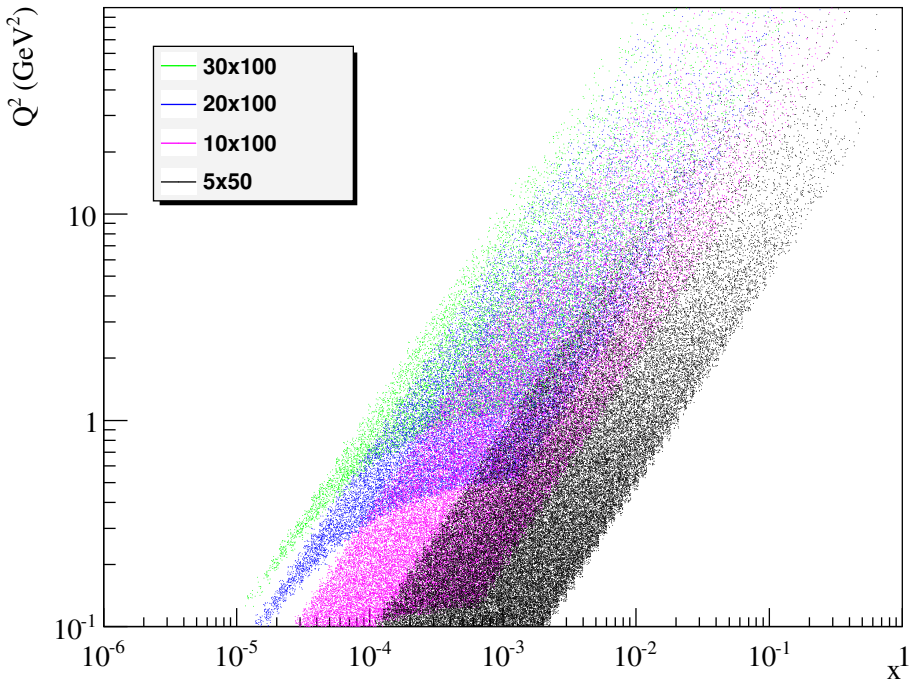

Figure 8.12: Q^2 vs. x coverage of the PHENIX detector for e+A measurements using the successive stages of the eRHIC electron beam. This plot includes cuts on inelasticity, $y < 0.9$ and $y > 0.05$. The kinematic coverage is determined by the requirement that the electron be detected in the PHENIX central detector or the new forward detector, i.e. $-4 \leq y_e \leq 1$.

nucleus collisions at high p_T (x_T) that will not be easily separable from reductions in hard-scattering rates due to EMC suppression of the quark distributions at large x. DIS processes do not suffer initial-state effects and probe only the EMC suppression at large x. In principle, existing data constrain the valence quark EMC suppression, but as shown in Figure 8.11, the EMC modification of the gluon and sea distributions at large x is poorly constrained by existing nuclear DIS data. Precision measurements with extended Q^2 range at moderate to large x will be helpful in reducing those uncertainties from initial-state effects. Also, measurements with Au nuclei will reduce hidden systematic errors resulting from the extrapolation of data from other nuclei to Au. d+Au measurements provide sensitivity to the impact parameter dependence of nuclear modifications – something that is not accessible in inclusive DIS measurements. The combination of precise d+Au measurements with precise constraints on the b-integrated nuclear modifications from e+A DIS measurements provides the best opportunity for separating initial-state energy loss effects in d+Au from nuclear modifications and then providing direct experimental constraints on the impact parameter dependence of nuclear modifications. The results of this program will directly feed into the precision jet measurement program described in this document by reducing theoretical uncertainties in initial-state effects.

One of the most important consequences of measurements with the kinematic coverage indicated in Figure 8.12 is the coverage in the low-x range. This coverage will directly constrain the nuclear gluon distribution in a range where it is almost completely undetermined, and it will resolve the uncertainty in the extent of the shadowing in heavy nuclei at very low x. Not only will the measurements thereby resolve a fundamental problem in nuclear physics, but they will also substantially reduce theoretical uncertainties in pQCD calculations of hard scattering rates involving low-x partons. Examples where that improvement is relevant to the heavy ion physics program include

- Calculations of the rate of quarkonia production, particularly the rapidity dependence.
- Calculations of hard scattering rates in nuclear collisions at the LHC.
- Calculations of forward hadron production in d+Au collisions at RHIC and the LHC, important for testing the role of saturation effects.
- Improved calculations of the rate of mini-jet production in heavy ion collisions at RHIC in hard + soft models such as HIJING.

The flexibility in beam energies at eRHIC will give a unique opportunity to measure F_L in nuclei (F_L^A) via the y-dependence of the reduced cross section. This measurement requires high momentum and angular resolution for the detection of the scattered lepton, as F_L^A is extracted from fitting the slope of the reduced cross section as function of y^2/Y_+.

Another direct probe of the gluon distribution in the nucleus would be provided by measuring the nuclear charm structure function [$F_2^c(x, Q^2)$]. With the electron measurement capabilities of the envisioned forward and central upgrades, PHENIX should be able to measure $F_2^c(x, Q^2)$ over a wide range of x and Q^2 with a semileptonic tag of the outgoing charm quark with little background from bottom. Because the charm content of the nucleus (nucleon) is primarily due to gluon splitting (except possibly at large x [138, 310]), F_2^c may provide a more direct probe than $F_2(x, Q^2)$ of the nuclear gluon distribution. Figure 8.13 shows the rapidity of semileptonic decay electrons from DIS processes involving charm production for different beam energies, requiring $Q^2 > 1$ GeV^2. The p_T of the leptons is for all cases below 1 GeV. More work will be required to demonstrate that the requirement of (e.g.) a displaced vertex in addition to the observation of a lepton will allow measurement of F_2^c with acceptably low background.

8.3.2 Saturation in nuclei at low x

The problem of unitarity and the role of nonlinear evolution of parton distributions at low x, generally referred to as gluon saturation, is one of the key outstanding problems in QCD. A full discussion of saturation physics is beyond the scope of this document. A recent review of saturation physics and references to a large body of other work can

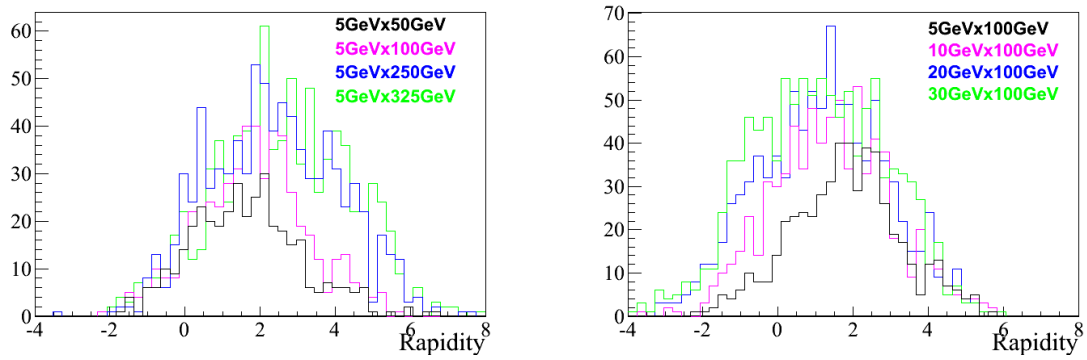

Figure 8.13: Rapidity distribution of leptons coming from charmed mesons in nuclear DIS processes at different beam energies, requiring Q^2 >1GeV^2.

be found in [192]. The most direct experimental support for the presence of nonlinear evolution in the scattering of hadrons at very high energies is provided by HERA electron/positron-proton DIS measurements. The observed geometric scaling in the inclusive DIS measurements at HERA [294] and similar behavior in diffractive data [247] are naturally described in the context of saturation models [294].

The resolution scale at which saturation effects in DIS are expected to become dominant is referred to as the saturation scale, Q_s. When $Q^2 \sim Q_s^2$, linear leading-twist evolution of structure functions is expected to break down. In fact, geometric scaling in saturation models is explicitly tied to the presence of a dimensionful scale such as Q_s whose x dependence controls the x dependence of the physics.

We note that there are alternative explanations for geometric scaling [149] that do not require the nonlinear effects of saturation, although they do not exclude it at low x. Indeed, recent attempts to understand the evolution of HERA F_2 data to low Q^2 and low x indicate deviations from DGLAP evolution [150] that may either indicate the need for resummation of large logarithms at low x or indicate the presence of nonlinear evolution [151]. Thus, while potentially more sensitive probes of the gluon density and saturation exist, a detailed study of the evolution of DIS to Q^2 values large enough compared to Λ^2_{QCD} for the physics to be perturbative but small enough to be at or below Q_s^2 provides sensitivity to saturation physics.

Nevertheless, it can be argued that the best way to test for the presence of nonlinear evolution in DIS is to fix the kinematics and increase the gluon density being probed by (e.g.) a virtual photon. The simplest way to to achieve such an increase is to use a nuclear "target"where at high energies the virtual photon (e.g.) interacts coherently with the entire thickness of the nucleus, and thus, "sees" an increased gluon density. Ideally, departure from proportional growth of nuclear structure functions with A might, then, indicate the presence of saturation effects. Unfortunately, even at leading twist, "nuclear shadowing," seen in Figure 8.11, will modify the nuclear parton distributions producing an effect similar to that expected from saturation, namely a reduction in the nuclear pdf

at low x compared to A times the proton pdf. However, a study similar to that described above for the HERA data evaluating possible deviations from DGLAP evolution with decreasing Q may provide a way to observe the transition from leading-twist shadowing to saturation. There is currently no nuclear DIS data set that allows such a study in an x range relevant for saturation physics. With the x and Q acceptance shown in Figure 8.12, PHENIX would be able to provide the first such data set. While nuclear F_2^A measurements alone will not provide the ultimate test of saturation in nuclei, such measurements will likely provide the first glimpses of saturation and will certainly constrain or test saturation models. Other observables directly sensitive to the gluon distribution in the nuclei are F_L^A and F_2^c; they will be more sensitive to gluon saturation effects.

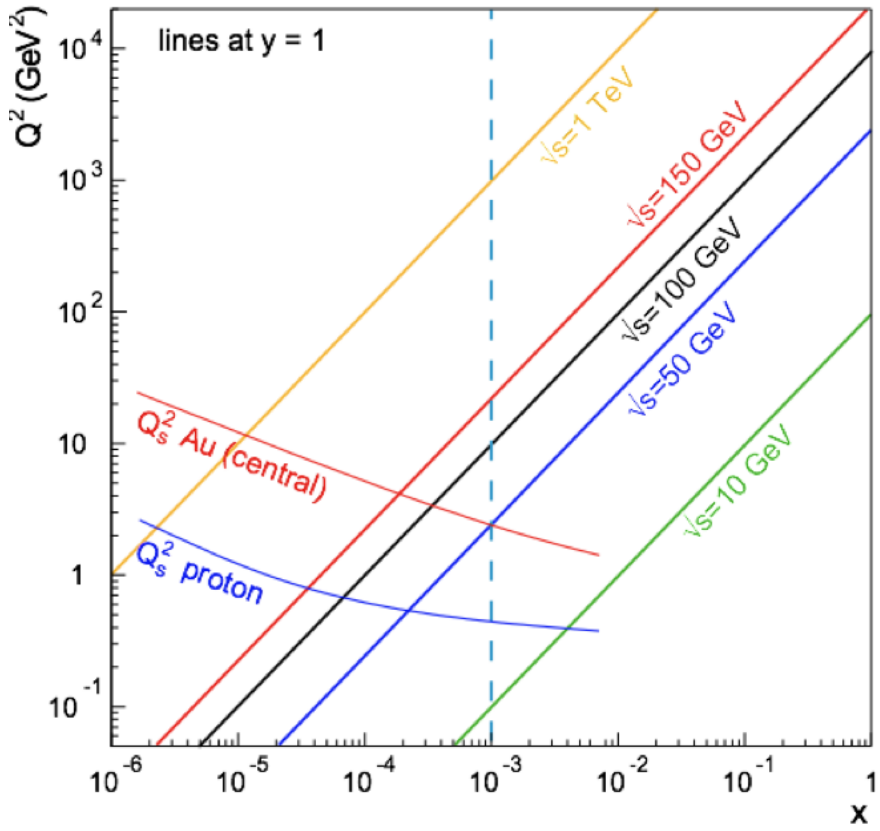

Figure 8.14: The x-Q^2 plot showing lines at $y = 1$ for different $\sqrt{s}$ with lines of the saturation scale Q_s^2 vs. x.

8.3.3 Gluon tomography in nuclei - The initial state

As discussed in Chapter 1 and Chapter 2, uncertainties in the eccentricity of the initial state of a Au+Au collision can lead to a factor of two uncertainty in the value of η/s extracted from v_2 measurements at RHIC. That factor of two can, for example, be the

difference between concluding that the QGP has an η/s consistent with the AdS/CFT bound or a value twice as large which might (e.g.) imply that for part of its evolution the QGP is not strongly coupled. Uncertainties in the initial eccentricity also influence negatively the interpretation of differential quenching measurements ($R_{\rm AA}(\Delta\phi)$) which ostensibly provide direct sensitivity to the path length dependence of medium-induced energy loss. Systematic errors in the relative lengths of the medium in the in-plane and out-of-plane direction will limit the physics conclusions that can be drawn from measured differences in the $R_{\rm AA}$ in the two directions. We note that uncertainties in the geometry of the initial state in $Pb+Pb$ collisions at the LHC may be even greater than at RHIC due to an expected greater impact of saturation on initial particle production at the higher LHC energy.

Measuring the initial state of the sQGP

Knowledge of the initial conditions at RHIC is crucial to interpretation of the experimental data from heavy ion collisions. The density distribution in nuclear matter at rest is well understood from diffraction experiments (see, e.g., [130]), but particle production in heavy ion collisions depends on the distribution of quarks and gluons in the nuclear wave function. Below some value of x, nonlinear QCD evolution effects become important. The (mostly) gluonic initial-state medium at midrapidity at RHIC consists of particles of $x \sim p_T/\sqrt{s_{NN}} \sim 10^{-3}$; in this range the small x phenomena are likely to be relevant, but they are not yet fully understood. Furthermore, theoretical calculations of v_2 are very sensitive to the shape of the edge of the initial nuclear overlap in heavy ion collisions. However, it is just in this region that many of the theoretical tools developed to study small x physics break down. Through diffractive measurements at an electron-ion collider, these fundamental limitations can be addressed. Of key interest are coherent vector meson production and deeply-virtual Compton scattering. Measured diffraction patterns may be inverted to determine the initial gluon and quark densities of the highly boosted nuclei. It turns out that the most sensitive density determination is at the edge of the nucleus, so these measurements will provide key information about the overlap region to which hydrodynamics and energy loss calculations are most sensitive.

The relevant Feynman diagram contributing to coherent vector meson production, in which an electron emits a virtual photon that splits into a $q\bar{q}$ pair that subsequently interacts coherently with the nucleus and forms the vector meson, is shown in Fig. 8.15. To lowest order, the diffraction pattern given a known nuclear thickness function $T_A(b)$ is

$$\frac{d\sigma^{q\bar{q}}_{A_0\to A_0}}{dt} \propto e^{-B_p\cdot\Delta^2}\cdot\left|\int d^2bT_A(b)e^{-i\vec{b}\cdot\vec{\Delta}}\right|^2, \tag{8.2}$$

where B_p is the diffractive slope of the proton and $t=-\vec{\Delta}^2$ [258, 147]. Assuming that the gluonic density is proportional to the Woods-Saxon [318] distribution

$$\rho_{WS}(r) \propto \left[1+\exp\left((r-R)/w\right)\right]^{-1} \tag{8.3}$$

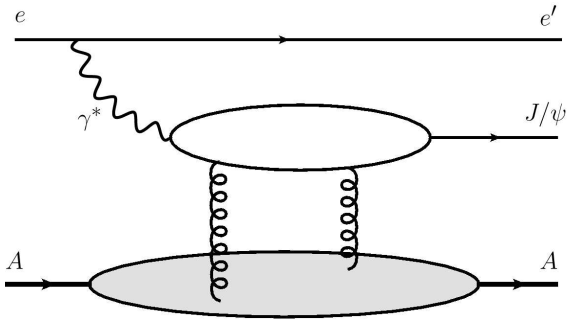

Figure 8.15: Relevant Feynman diagram for vector meson production (in this case the production of a J/ψ). Note that the $q\bar{q}$ dipole probes the gluon density in the nucleus A with *two* gluons: not only can vector meson production probe the mean gluon density in A but also gluon density correlations.

the predicted diffraction pattern is shown in Fig. 8.16 when using 1) the usual parameters for ^{197}Au, $R = R_0 = 6.38$ fm and $w = w_0 = 0.535$ fm, 2) for a density with a slightly smaller radius $R = 0.9R_0 = 5.742$ fm but the same width, $w = w_0$, and 3) for a density with the same radius but a slightly sharper nuclear edge, $R = R_0$ and $w = 0.8w_0 = 0.428$ fm. Also shown in the figure is the dominant contribution to the cross section coming from incoherent scatterings, in which the outgoing nucleus is either broken up or in an excited state. One can readily see from the figure that the measured coherent diffraction pattern is very sensitive to the details of the gluon density. Figure 8.16 also demonstrates, however, that this is a difficult measurement to make: the rejection rate of incoherent vector meson production must be extremely good. While Figure 8.16 does not take into account the finite resolution of a realistic eRHIC detector nor the influence of higher-order effects on the theoretical calculation, the ability to directly measure the gluon density and its fluctuations in an ultra-relativistic nucleus is extremely encouraging and its importance for heavy ion physics, irrespective of small-x physics, is hard to overstate.

eRHIC gives another completely unique possibility to study the gluon distribution impact parameter dependence through DVCS. A more complex t dependence arises in the process $e + A \rightarrow e + A\gamma$, due to the interference between Compton scattering and the Bethe-Heitler process. The interference term, which can e.g. be isolated by changing the lepton beam charge or its helicity, is proportional to the product $F_{em}(t)\mathcal{A}(t)$ of an electromagnetic form factor and the Compton scattering amplitude. If these two functions have their zeroes at slightly different values of t, then the interference term will change sign with increasing t.

The challenge for both of these measurements is to ensure exclusivity, meaning the heavy ion nucleus should not break up. This can be ensured by checking for the neutrons from the breakup in the ZDC and protons in forward detectors like "Roman Pots". The other challenge is to have momentum and energy resolutions for the decay products of the vector mesons and the DVCS γ sufficient to resolve the minima in the diffractive pattern and to see the sign change in the interference term as a function of t. The acceptance for

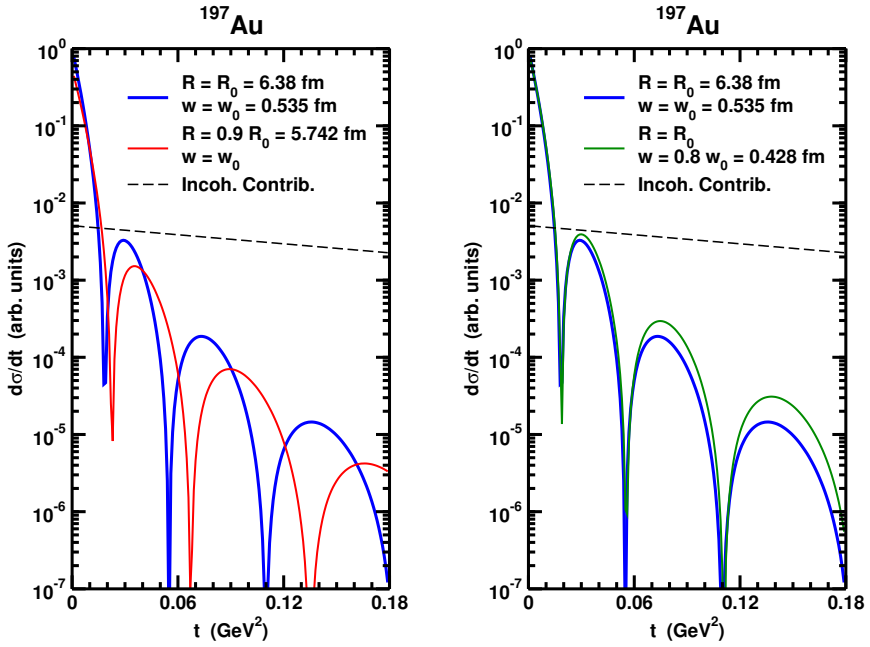

Figure 8.16: Vector meson diffraction patterns for ^{197}Au. (blue curves) Differential cross section when the gluon density is assumed to scale with the Woods-Saxon charge distribution with the usual parameters taken for the radius and width. Shown are comparisons for a Woods-Saxon distribution with a (left) 10% smaller radius and (right) 20% smaller width. As discussed in the text, both plots also show the dominant contribution to the cross section due to incoherent vector meson production.

the vector mesons (e.g. J/ψ) is extremely good for the upgraded PHENIX (see Figure 8.9); while for the DVCS photon the acceptance is limited to $-4 < \eta < 1$.

8.4 Polarized $e+p$ Physics with ePHENIX

Polarized $e+p$ physics with eRHIC is the natural continuation of the RHIC polarized $p+p$ program. eRHIC will advance the study of spin nucleon structure, as HERA did for increased understanding of unpolarized nucleon structure. The high luminosity, kinematic coverage, and flexibility in polarized beams from eRHIC will give us the opportunity to answer some of the overarching questions discussed in Chapter 4. Currently all polarized DIS experiments are fixed-target experiments, which severely limits their x-Q^2 coverage. The anticipated luminosity is 2×10^{34} s^{-1}cm^{-2}, which is a factor 1000 more than the collider luminosity at HERA and a factor 500 more than the luminosity of the HERMES and COMPASS polarized programs. One of the first measurements possible with eRHIC will be the measurement of the inclusive polarized structure function g_1. It will be possible to extend its kinematic coverage with an unprecedented statistical precision. Figure 8.17 shows g_1 plotted as a function of Q^2 for different x_B bins for one combination of beam energies (7 GeV on 150 GeV) and an integrated luminosity of 5 fb^{-1}, compared to the current world data from HERMES, SMC and E155 at SLAC.

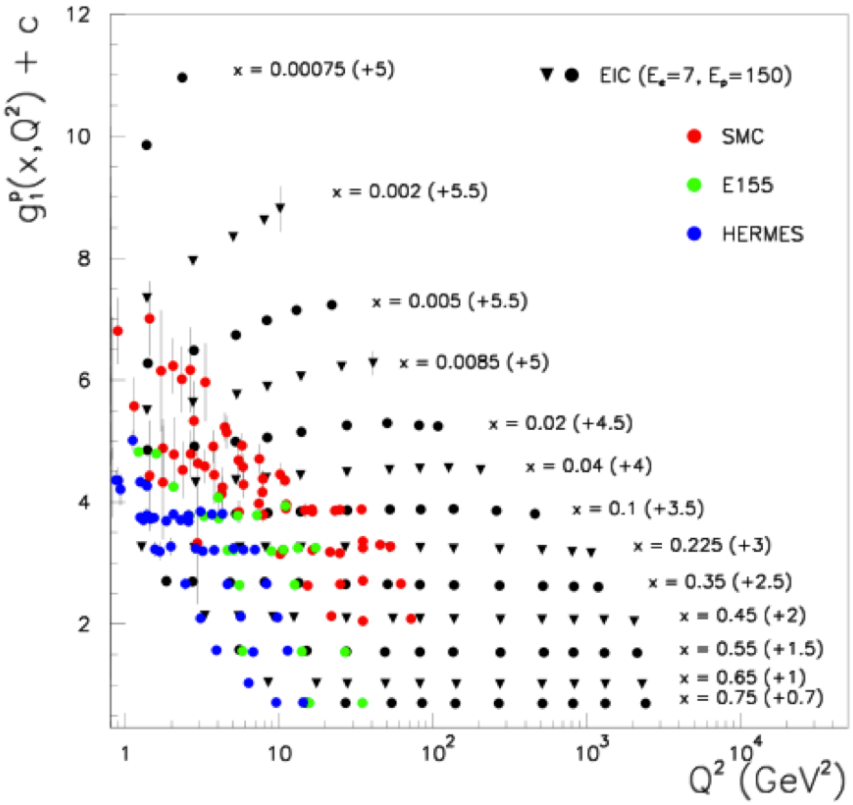

Figure 8.17: The polarized structure function g_1 as a function of Q^2 for different x_B bins indicated. Shown are (black points) the expected coverage for eRHIC with $\sqrt{s}$=65 GeV and an integrated luminosity of 5 fb^{-1} and (colored points) the world data from fixed-target facilities.

An integrated luminosity of 5 fb^{-1} corresponds to 1.5 weeks running time assuming a 50% efficency of the detector and the facility. Repeating the same measurement at higher beam energies, e.g. 20 GeV on 325 GeV, will extend the kinematic coverage in x further to 10^{-5}. Figure 8.18 shows g_1 plotted for individual Q^2-bins as a function of x_B compared to the prediction using different assumptions for the polarized gluon distribution. This plot shows that a measurement of g_1 at eRHIC will allow extraction of the gluon polarization at low x through the scaling violation of g_1 via global pQCD fits such as DSSV [169] and BB-09 [131]. The two figures show capabilities with a ZEUS or H1-type detector, and the upgraded PHENIX detector is qualitatively different. However the ePHENIX acceptance for low x and low Q^2, which provide the heart of the physics program, would be very similar. Furthermore it will be possible to determine the contribution from the quark spins to the spin of the nucleon with even higher precision and two decades more in x than currently done by HERMES and COMPASS [68, 79]. eRHIC will provide not only

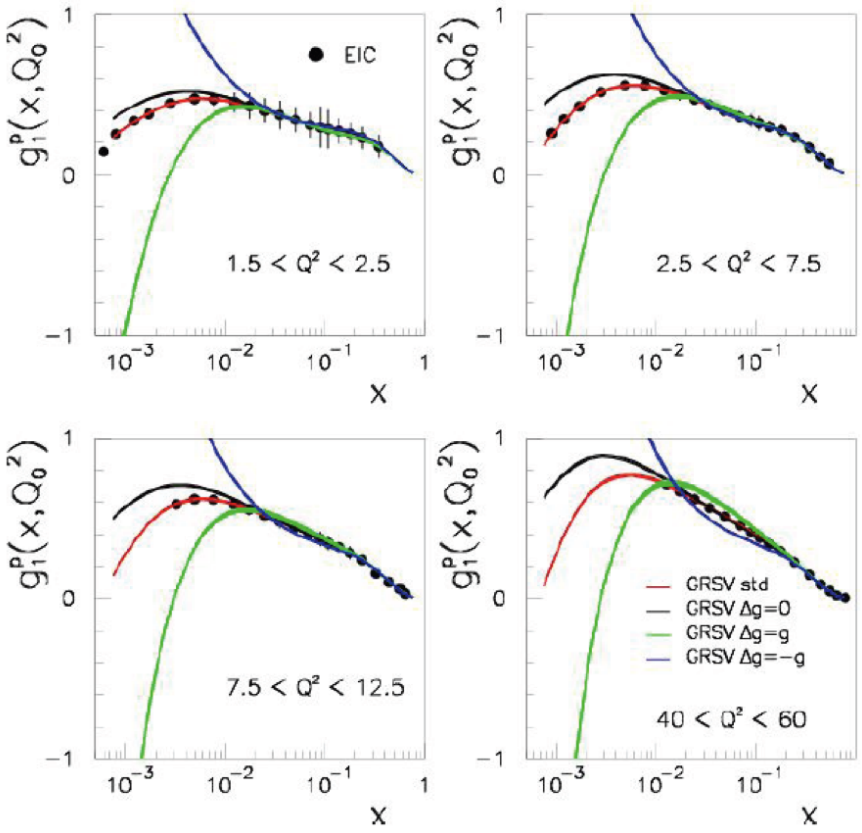

Figure 8.18: The polarized structure function g_1 as a function of x_B for different Q^2 bins. Also plotted are different predictions for g_1 using various assumptions for the polarized gluon distribution [181].

the possibility to run with polarized protons but also with a polarized ^{3}He beams. If it is possible to tag that the scattering occurred on the neutron by detecting the proton remnants from the ^{3}He nucleus, g_1 could be measured for the neutron. As for studies

of elastic diffraction, this measurement would require Roman pots around the detector. With precision measurements of $g_1(x, Q^2)$ on the proton and neutron to low x, a scientific highlight at eRHIC would be a precision test of the Bjorken sum rule [126],

$$\int_0^1 dx \langle g_1^p - g_1^n \rangle (x, Q^2) = 1/6 g_A \langle 1 + \mathcal{O}(\alpha_s) + \mathcal{O}(1/Q^2) \rangle$$

, where g_A is the neutron β-decay constant, and where the schematic terms on the right-hand-side indicate perturbative corrections in the strong coupling α_s and higher-twist contributions, respectively. The Bjorken sum rule is a rare example of a fundamental relationship that is theoretically very well understood within QCD. The perturbative corrections are known through order α_s^3, and we even have a relatively clear picture about the first higher-twist contributions. Thus, apart from being a remarkable relation between DIS structure functions and a low-energy hadronic quantity, the sum rule also offers unique tests of QCD dynamics, and of our ability to quantitatively describe these. This by itself warrants an experimental study, and it is anticipated that a 2% measurement of the sum rule would be possible at eRHIC. At this level, one might actually start to see deviations from the sum rule due to isospin and charge symmetry violations. Relatively little is known about such effects so far, however, so that precision studies of the Bjorken integral also have the potential to provide genuinely new insights.

Running eRHIC with polarized proton and polarized ^{3}He beams with a detector which is able to measure not only the scattered lepton but also one or more identified hadrons over a wide range will allow determination of the quark polarizations and polarized quark distributions for the different quark flavors. As in the case for the inclusive structure function g_1, the x-Q^2-coverage will be significantly extended. This will give the opportunity to test whether the polarized light quark sea is flavor symmetric or asymmetric as in the unpolarized case. It will also provide the opportunity to measure the Δs and $\Delta\bar{s}$ polarized quark distributions and resolve the current puzzle between pQCD fits to g_1 favoring a negative strange quark polarization and to the SIDIS data giving a strange quark polarization consistent with zero. It is additionally interesting to note that the strange quark polarization is one of the biggest uncertainties of the neutralino interaction cross section with matter [182].

eRHIC also offers a unique opportunity to go beyond collinear pQCD at leading twist, because the high luminosity, the wide kinematic coverage and polarized beams make it possible to measure the SIDIS cross section for the first time fully differential in x, Q^2, z, p_T and Φ depending on the spin orientation. Assuming the TMD and the collinear twist-3 formalism have been verified by the planned DY measurements (see Section 6.1.1), eRHIC will be the machine to study unintegrated parton distribution functions and will allow the 3-dimensional momentum structure of the partons in the nucleon to be unraveled. DIS is extremely valuable for this program because contrary to most inclusive measurements of A_N in polarized $p+p$ collisions, SIDIS allows separation of the different underlying subprocesses leading to the single spin asymmetries. This separation is achieved by measuring single spin asymmetries as a function of different modulations of the angle Φ, the

angle between the lepton scattering plane and the hadron production plane, depending for certain measurements on the spin direction of the nucleon. Unfortunately the design of the current and the upgraded PHENIX detector will only allow very restricted kinematic access to semi-inclusive measurements (see Section 8.2).

Similar unique opportunities will exist at eRHIC for exclusive diffractive reactions to constrain GPDs, introduced in Chapter 4. While PDFs are measured in inclusive deep-inelastic scattering, where the proton does not stay intact, GPDs can be accessed in exclusive reactions, in which the proton usually stays intact after the lepton-parton interaction. The difference in the momentum of the proton before and after the scattering took place is the Mandelstam variable t, known from simple two-body kinematics. It accounts for the momentum difference both in the direction of the beam as well as transverse to it. GPDs depend on this variable t and encode the proton substructure in longitudinal momentum space as well as in transverse position space. The Ji relation [211, 213] connects the low $-t$ limit of a certain combination of GPDs and the total angular momentum of a given quark species in the nucleon and is the only quantitative way known today to access total quark angular momentum.

There are multiple ways to access GPDs experimentally. DVCS is currently the theoretically cleanest and simplest way to access information on GPDs. The angular distributions and cross sections of the real photons can be used to retrieve information on GPDs. In Jlab [261, 312] and HERMES [71, 244, 72] kinematic conditions, hard exclusive leptoproduction of real photons is dominated by the Bethe-Heitler (BH) process, the elastic scattering of the incident lepton with the target nucleon, where a photon is produced as bremsstrahlung from the incident or scattered lepton. The DVCS and BH processes interfere, meaning that the scattering amplitude has three separate contributions: one from DVCS, one from BH and one from their interference. In Jlab and HERMES kinematics, the interference is the largest contribution and measurement of it can be used to access information on GPDs most easily. For H1 and ZEUS at HERA the access to GPDs is through the cross section and the angular distributions of the DVCS process directly [12, 154]. There is an enormous amount of data from both experiments on exclusive reactions with different final states ($\rho, \omega, \phi, \mathrm{J}/\psi$), which can constrain different features of GPDs and allow access to either quark or gluon GPDs. The first global fit to the world DVCS data has placed initial constraints on the functional shape and magnitude of GPDs [230, 231], but we remain far from the point of being able to extract orbital angular momenta of quarks and gluons. eRHIC will be able to provide the precision differential data for different final states and observables (cross sections, single spin asymmetries for beam charge, beam polarizations and longitudinal and transverse target polarizations) to finally get a 2+1-dimensional picture of protons and nuclei and to constrain the orbital angular momentum of quarks and gluons.

Making measurements of exclusive diffractive vector meson production and DVCS over a wide range of kinematics and for spin dependent observables will be the golden tool to constrain GPDs. As in the case for heavy nuclei (Section 8.3) measuring the t-distribution of the exclusive diffractive cross section offers the possibility to measure parton distri-

bution functions in impact parameter space depending on their momentum fraction x, enabling us to do parton tomography in the nucleon. Equally exciting is that the second moments of GPDs H and E give the possibility to get a handle on the total angular momentum of quarks J_q and gluons J_g. Combining this with the precise determination of the contribution of quark spin to the spin of the nucleon will give the first chance to determine via the Ji sum rule the orbital angular momentum of quarks in the nucleon [211]. Assuming that by the time eRHIC comes on line the issue with the different helicity sum rules for the proton [208, 211, 155, 156, 313, 314] is resolved, the same should be possible for the angular momentum of gluons. This would finally give a chance to solve the holy grail of nucleon spin physics, the helicity sum rule of quarks and gluons.

As shown in Section 8.2, with the addition of "Roman Pots" in the forward direction, the new PHENIX detector is well suited to make measurements of exclusive diffraction for different final states in $e + p$ collisions. The capabilities for vector meson final states are very good. Studies are underway to determine the feasibility of measuring diffractive processes off of nuclei in a collider geometry. This will require acceptance for the final states of interest, the scattered electron, and the nearly-intact nucleus at very forward angle. We look forward to demonstrating this, as the upgraded PHENIX detector with "Roman Pots" added will have good capability for such measurements.

In order to summarize the physics reach of ePHENIX, we note that the eRHIC goals are broadly distributed along four thrusts. The first is improved determination of the longitudinal nucleon spin structure via inclusive and semi-inclusive deep inelastic scattering in polarized $e + p$. Another pillar of eRHIC is examination of the gluon distribution in nuclei at very low x using inclusive and also diffractive DIS off of nuclei. The third thrust is mapping the three-dimensional landscape of the nucleon through measurement of GPDs, while the fourth is possible electroweak physics, e.g parity violating effects in $e + p$ scattering at high luminosity. The initial eRHIC physics program will focus predominantly upon inclusive measurements accessing low x and relatively low Q^2, as well as some semi-inclusive physics extending to moderate Q^2 (approximately 50-100 GeV^2). These could begin at ePHENIX for both $e + p$ and $e + A$ collisions, providing information of unprecedented range and precision on the nucleon spin and partonic structure of nuclei at low x. The third eRHIC physics goal would be a challenge for the presently planned PHENIX upgrade, due to the absence of extensive particle identification at midrapidity. Electroweak physics at eRHIC will require measurements at large x and large Q^2, which implies a capability to measure the backward scattered electron with high precision. The envisioned PHENIX upgrade does presently not include a path toward such event geometries.

Appendix A

Charge Letter

From: Vigdor, Steven <vigdor@bnl.gov>
Date: Wed, Dec 16, 2009 at 6:44 PM
Subject: Charge for new decadal plans for STAR and PHENIX
To: Barbara Jacak <jacak@skipper.physics.sunysb.edu>, Nu Xu <nxu@lbl.gov>

Dear Barbara and Nu,

As we have discussed in Spokesperson's Meetings, I am herein charging the PHENIX and STAR Collaborations with generating new decadal plans that lay out your proposed science goals and detector upgrade paths for the period 2011-2020. The decadal plans generated in 2003 have been extremely useful for RHIC and both experiments. Now that we have received (or are on the verge of receiving) funding to carry out most of the upgrades described in those earlier reports, it is timely to develop a clear roadmap for what comes next. With current funding profile guidance from DOE, it appears that the STAR Heavy Flavor Tracker may be completed in FY2015, and the suite of significant PHENIX upgrades are likely to be completed sooner. We also anticipate that the various RHIC machine luminosity upgrades under way (six planes of stochastic cooling, 56 MHz SRF rebunching, electron lenses) or contemplated (low-energy electron cooling) will be completed by 2015. Not unexpectedly, then, we are being asked by DOE what plans we have for RHIC beyond 2015.

I am therefore asking you to generate a document for each Collaboration, to be delivered to me by August 1 [October 1], 2010, that provides the following information:

1) A brief summary of the detector upgrades already (or soon to be) in progress, the timelines for completing them, the new science capabilities each adds in combination with upgraded RHIC luminosity, and your best current estimates (informed by the current strawman 5-year run plan for RHIC) of when you will be able to acquire the data that addresses the relevant science goals. This can even be summarized in tabular form, and should be consistent with the latest RHIC Midterm Plan.

2) The compelling science goals you foresee for RHIC A+A, p+p, and d+A collisions that can only be carried out with additional upgrades (or replacements) of detector subsystems or machine ca-

pabilities (e.g., further luminosity or diamond size improvements). For each such goal, provide some explanation of why RHIC is the appropriate facility (e.g., in competition with LHC or FAIR) to pursue that science, and preferably some simulations that demonstrate the need for new detector or machine capabilities to address the compelling questions. If the pursuit of some science goals is conditional on results to be obtained over the next several years, try to outline the decision points you foresee for deciding future paths.

3) Prioritized, or at least time-ordered, lists of the major (above $2M total project cost) and more modest (below $2M total project cost) new detector upgrades your Collaboration foresees, together with R&D milestones that may have to be passed to demonstrate their technical feasibility. Also provide whatever information you have on the indicated timescale concerning probable costs of each upgrade. I understand these will likely be very preliminary in most cases.

4) Any plans or interest your Collaboration has in adapting your detector or detector subsystems (or detector R&D) to study electron-nucleon and electron-ion collisions with an eventual eRHIC upgrade. This is relevant only near the end of the decade addressed here, but will be important for planning purposes. (We may well be forced by financial or environmental considerations, even for a first MeRHIC stage, to consider options in which acceleration of the electron beam is carried out around the RHIC tunnel, requiring some scheme for getting an electron beamline through or around PHENIX and STAR. So it is worth considering if there is some way you could make use of the e-p and e-A collisions if we provided them.)

5) The envisioned evolution of your Collaboration through the decade: institutions that may leave, others that might join, any plans to keep your Collaboration healthy and vibrant as RHIC becomes a .mature. facility.

Having been involved heavily myself in the preparation of the previous decadal plan for STAR, I understand how much work is involved in this exercise. But we also now have an existence proof of how important it can be in providing a future program. Please let me know if you foresee difficulty in meeting the above timeline. I imagine convening a special PAC (or perhaps overlapping "red team") review of the decadal plans after they are prepared, to help advise me on priorities. It continues to be made clear to us by DOE that they want higher standards applied in the internal vetting of the compelling science goals that are actually technically achievable with proposed upgrades.

I know that both of you have already launched the intensive discussions within your Collaborations that are necessary to inform these plans. I will need an update (not necessarily written) from each of you before our annual ONP budget briefing (scheduled for February 10, 2010) of the upgrades and new science goals you already foresee, so that we can intelligently answer questions that we are likely to get regarding the RHIC science program beyond 2015.

Please let me know if you have questions about this charge.
Cheers, Steve

Steve Vigdor
Associate Laboratory Director
Nuclear and Particle Physics
Brookhaven National Laboratory

Appendix B

RHIC Beam Projections & PHENIX Run Plans

A critical component of planning for future physics at RHIC is the projection of available luminosities and polarizations from the Collider Accelerator Division (CA-D). CA-D has provided detailed projections for 2011–2015 that include the full commissioning and utilization of stochastic cooling, electron lenses, and critical RF upgrades. The "RHIC Collider Projections" document is available online [5]. We note that the version used for the calculations included in this document is dated July 20, 2010.

Our current planning uses these projections for the PHENIX 2010–2015 run plans, and then assumes the maximum delivered luminosities with no further improvements beyond 2015. We fully anticipate a "Decadal Plan" from CA-D that may include new ideas and improvements that are not presently available in our planning.

B.1 PHENIX Data-Taking Rate Projections

Using the information in [5], the PHENIX projected luminosities are calculated incorporating a realistic ramp-up time, as detailed in [5], and the mean value of the maximum and minimum luminosity projections for each year's running period. Figure B.1 shows the Au+Au interaction rate at PHENIX within the z-vertex range $|z| < 10$ cm as a function of time in store for the different stages of integrating full stochastic cooling and RF upgrades.

With the 2010 installation of the silicon vertex detector (VTX), for physics topics utilizing the VTX, the usable z-vertex collision range is reduced to $|z| < 10$ cm. However, for topics such as $W \rightarrow \mu$ and π, K, p particle identified tracks in lower energy heavy ion reactions, the larger z-vertex range of $|z| < 30$ cm is usable for physics. Thus, we

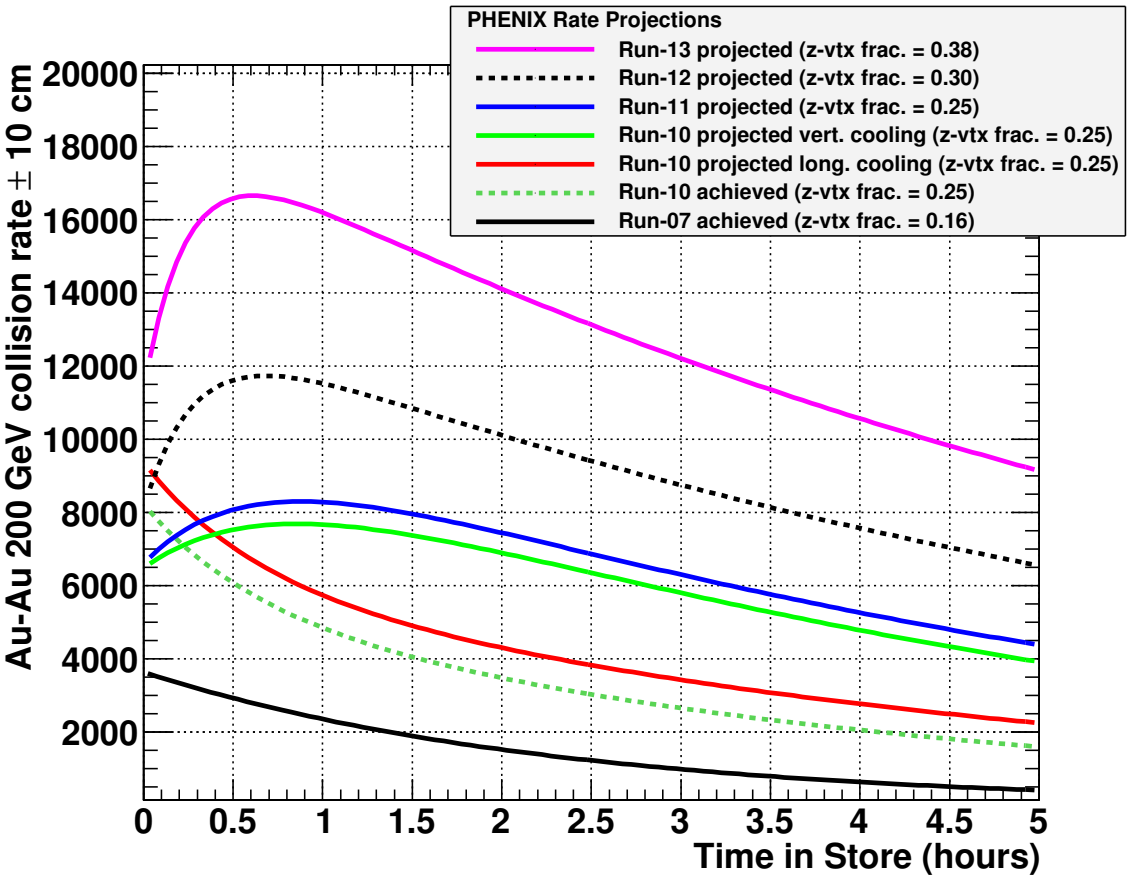

Figure B.1: Projected Au+Au at $\sqrt{s_{NN}} = 200\,\text{GeV}$ interaction rates within $|z| < 10$ cm as a function of time-in-store. The results are measured by PHENIX in run-7 and run-10, and projected by CA-D for future runs with the implementation of stochastic cooling and other accelerator improvements.

quote the integrated luminosity within both z-vertex ranges where relevant. For the p+p and d+Au cases the integrated luminosity is that sampled by our selective physics signal based Level-1 triggers. For the Au+Au case we quote the integrated luminosity as the number of minimum bias events actually recorded. For run-11 and run-12, PHENIX will be commissioning the new silicon detectors (VTX and FVTX), as well as the upgraded data acquisition (DAQTRIG2010), and thus we assume a Au+Au minimum bias archiving bandwidth of 2.5 kHz increasing to the full specified performance of 5 kHz. Ahead of the Au+Au running in run-15, we project a full implementation of the SuperDAQ upgrade which allows an 8 kHz bandwidth. In all these cases, the luminosity sampled by the subset of Level-1 triggers that remain selective in the high multiplicity environment, may allow an increased sampled luminosity of a factor of approximately 1.5–2.0 (relative to the number quoted below). This additional sampling would apply to high $p_T > 4$–5 GeV photons, electrons and jets, as well as for dimuon pairs.

B.2 PHENIX Run Plans

Table B.1 shows the projected run plan for the next five years. For reference, Table B.2 shows the last ten years of PHENIX data taking (2000–2010).

For the next five year run plan we assume 26–30 cryo weeks in each running period. If the available running time is less, priority decisions will be necessary and the overall run plan will be extended in time. We have included the number of physics weeks for each species, and have accounted for cryogenic cool-down and warm-up and RHIC ramp-up periods—though these are not shown in Table B.1. We assume 65% PHENIX uptime while beam is available.

We do not provide a detailed year-by-year run plan beyond these five years, and assume the full implementation and full functionality of the complete suite of CAD proposed accelerator upgrades for that running period. Additional upgrades and innovations in the accelerator performance beyond that are not included (though we expect and encourage a continued and active accelerator development program).

For the heavy ion case, on the time frame where the large scale upgraded detector (sPHENIX) is available for physics data taking, we project being able to record 25 billion Au+Au minimum bias collisions and sample 50 billion Au+Au collisions with rare event triggers in a twenty week running period. This nearly order of magnitude increase in data samples is an important component of the physics program.

Table B.1: PHENIX run plan for the years 2010–2015. Longitudinal polarization is indicated by (L), transverse by (T).

run	Species	$\sqrt{s_{NN}}$	Wks	$\int$ L dt		Pol.	Comments
				$\lvert z\rvert < 30$ cm	$\lvert z\rvert < 10$ cm		
11	p+p	500	10	50 pb^{-1}	20 pb^{-1}	50% (L)	W program + ΔG
	Au+Au	200	8		0.7 nb^{-1}		heavy flavor (VTX)
	Au+Au	18	1.5	5.5 μb^{-1}			energy scan
	U+U	192	1.5		0.03 nb^{-1}		explore geometry
12	p+p	500	8	100 pb^{-1}	35 pb^{-1}	50% (L)	W program + ΔG
	p+p	200	5	13.1 pb^{-1}	4.7 pb^{-1}	60% (T)	HI comparison
	Au+Au	200	7		0.8 nb^{-1}		heavy flavor (F/VTX)
	Au+Au	27	1	5.2 μb^{-1}			energy scan
13	p+p	500	10	200 pb^{-1}	74 pb^{-1}	60% (L)	W program
	U+U	200	5		0.57 nb^{-1}		} geometry
	Cu+Au	200	5		2.4 nb^{-1}		
14	p+p	200	10	34 pb^{-1}	12 pb^{-1}	65% (T)	} HI comp., transv.
	p+p	62	3	0.6 pb^{-1}	0.2 pb^{-1}	60% (T/L)	
	d+Au	200	8	260 nb^{-1}	150 nb^{-1}		} CNM/FOCAL
	d+Au	62	2	6.5 nb^{-1}	3.8 nb^{-1}		
15	Au+Au	200	10		2.8 nb^{-1}		High Bandwidth
	Au+Au	62	4		0.13 nb^{-1}		HF vs $\sqrt{s_{NN}}$
	p+^{3}He	132	5			(T)	Test Run

Table B.2: Table of PHENIX Past 10 Years of running (2000-2010) for $|z|$ <30 cm.

run	Species	$\sqrt{s_{NN}}$	$\int$ L dt	Pol.	Comments
1	Au+Au	130	$1.0\,\mu b^{-1}$	—	first heavy-ion run
2	Au+Au	200	$24\,\mu b^{-1}$	—	first jet quenching + flow results
	p+p	200	$0.15\,pb^{-1}$	(T)	first p+p spin run
3	d+Au	200	$2.7\,nb^{-1}$	—	first CNM run
	p+p	200	$0.35\,pb^{-1}$	(L)	first π^0 ΔG and J/ψ
4	Au+Au	200	$241\,\mu b^{-1}$	—	HI high statistics
	Au+Au	62.4	$9\,\mu b^{-1}$	—	HI energy dependence
5	Cu+Cu	200	$3\,nb^{-1}$	—	HI geometry dependence
	Cu+Cu	62.4	$0.2\,nb^{-1}$	—	} HI geom. + energy dep.
	Cu+Cu	22.5	$2.7\,\mu b^{-1}$	—	
	p+p	200	$3.8\,pb^{-1}$	(L)	spin running
6	p+p	200	$10.7\,pb^{-1}$	(T&L)	high statistics spin run
	p+p	62.4	$0.1\,pb^{-1}$	(L)	HI comparison, spin lower E
7	Au+Au	200	$0.8\,nb^{-1}$	—	HI high statistics II, RXPN detector
8	d+Au	200	$80\,nb^{-1}$	—	high statistics CNM–MPC correlation, J/ψ suppression
	p+p	200	$5.2\,pb^{-1}$	(T)	spin run
9	p+p	500	$14\,pb^{-1}$	(L) 39%	first W spin run
	p+p	200	$16\,pb^{-1}$	(L) 55%	spin run
10	Au+Au	200	$1.3\,nb^{-1}$	—	} HI dilepton HBD runs
	Au+Au	62.4	$0.11\,nb^{-1}$	—	
	Au+Au	39	$40\,\mu b^{-1}$	—	HI lower energy + dileptons
	Au+Au	7.7	$0.26\,\mu b^{-1}$	—	HI lowest energy

Appendix C

Detector Evolution

This Appendix describes the essential configuration of the PHENIX detector over the first decade of running (2000–2010) followed by a summary of the design and status of each of the currently funded PHENIX upgrade projects:

- Hadron Blind Detector (HBD) [Operations 2007–2010]
- Silicon Vertex Tracking Detector (VTX) [Operations start 2011]
- Forward Silicon Vertex Detector (FVTX) [Operations start 2012]
- Muon Trigger Upgrades (MuTrg and RPC) [Operations start 2011]
- Data Acquisition Upgrade (DAQTRIG2010) [Operations start 2011]

An overview is included of two modest scale upgrade proposals that PHENIX is considering for official submission in the next year and a plan for existing detector maintenance and improvements:

- Forward Calorimeter Upgrade (FOCAL) [Projected Operations start 2014]
- Super Data Acquisition Upgrade (SuperDAQ) [Projected Operations start 2013-14]
- Existing Detector Maintenance and Improvements

The projects are tied to specific physics performance enhancements described earlier in the document. The cost scale is $<$ \$2M for the FOCAL and $<$ \$1M for the SuperDAQ, with a goal of implementation by 2014 and 2013–2014, respectively. These upgrades, in addition to critical detector maintenance, are a key part of the next five year physics program and a step towards the larger scale upgrade described in Chapter 7.

C.1 From 1999 to 2010

The baseline PHENIX detector was completed in 2002 coincident with the commissioning and initial operation of the PHENIX Muon spectrometer arms. Figure C.1 shows that the the PHENIX detector evolved from a partial implementation of the central arms in run-1 to a completed installation of the baseline + AEE (Additional Experimental Equipment) systems in run-3.

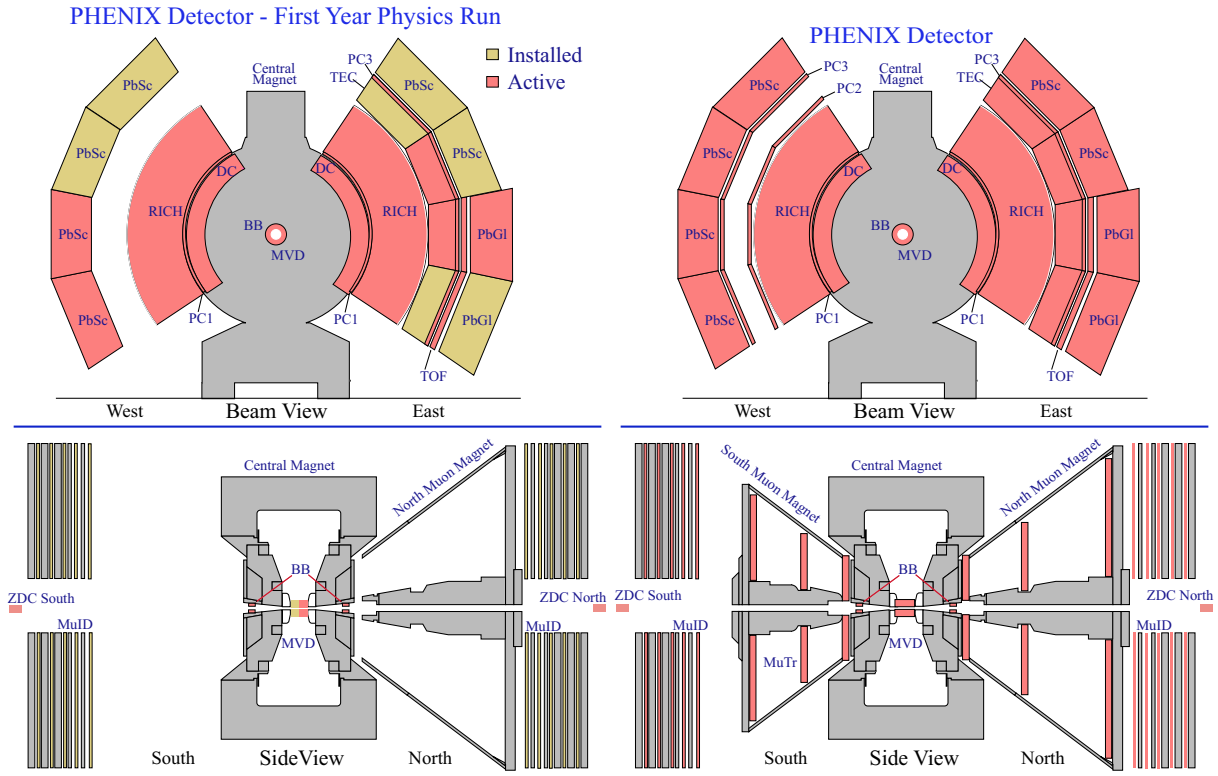

Figure C.1: Installed and active detectors for 2000 (left) and 2003 (right) configurations of the PHENIX experiment.

The collaboration then initiated both a short term detector upgrade program to cover the next 3–5 years and a longer term program that required substantial funding-agency contributions and an implementation plan covering the first decade of RHIC and PHENIX operation. Each of the configurations was capable of using the delivered luminosity from RHIC to explore heavy ion, deuteron + Au, and polarized proton collisions.

The short term upgrade program involved fabrication of new subsystems that could be completed in 1–2 years and generally focused on either one or two physics topics, or enhanced detector capabilities. The short term upgrades included the High-p_T detector, a combined Aerogel Čerenkov counter and mRPC-based Time of Flight wall that extended the PHENIX particle identification capability, especially π/K/p, from 3.5 GeV/c to approximately 8 GeV/c in p_T. The Reaction Plane Detector (RxNP) consisted of two ar-

rays of phi-segmented scintillation counters that enabled a factor of two improvement in the measurement accuracy of the collision geometry in HI collisions. The Muon Piston Calorimeter (MPC) was a pair of arrays of Pb-tungstate crystals ($PbWO_4$) that measured π^0's and jets in a pseudorapidity range previously inaccessible to PHENIX, $3.0 \leq \eta \leq 4.0$.

Figure C.2 shows the configurations for (left) run-5 with the Aerogel and (right) run-9 with the MPC and RxNP installed.

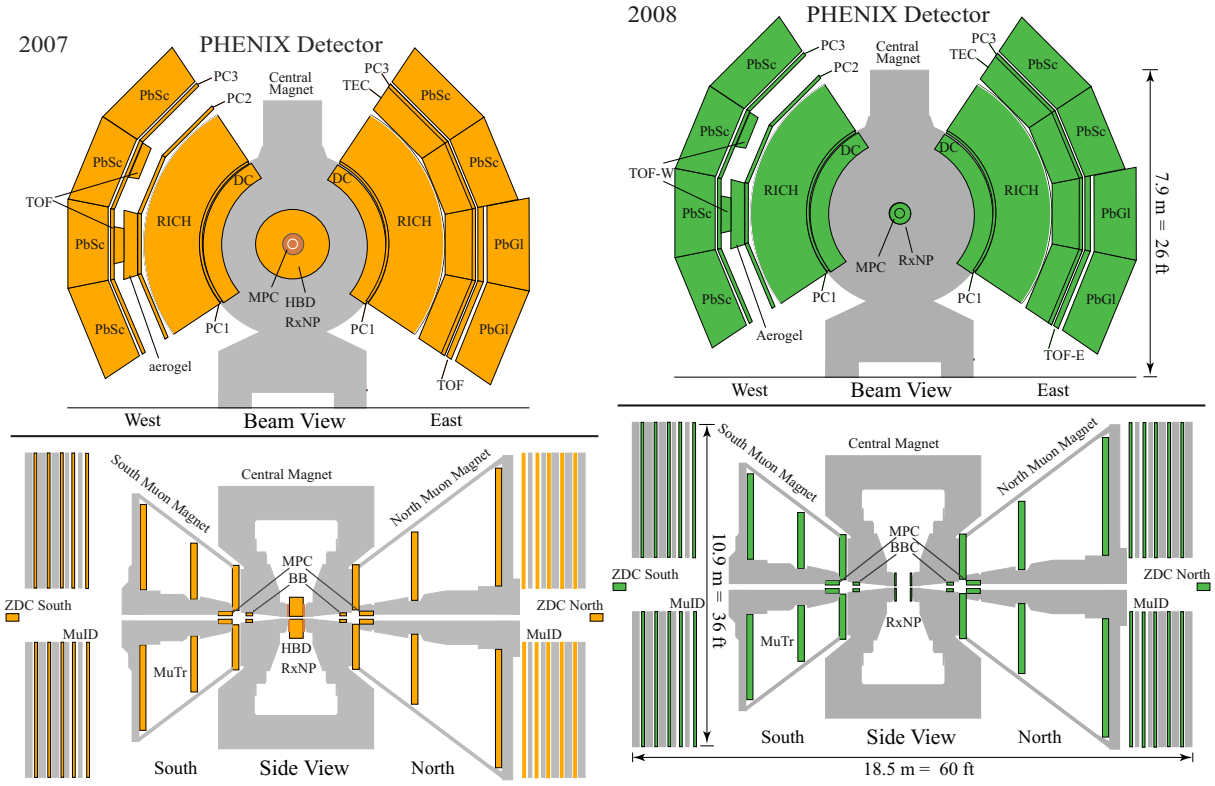

Figure C.2: RHIC run-8 (left) and run-9 (right) configurations of the PHENIX experiment.

The upgrades included in the long term plan were associated with broad physics programs that involved dedicated RHIC physics runs over multiple years. The first of these projects, the Hadron Blind Detector had its first successful data run in 2009, which was RHIC run-9.

C.1.1 HBD

The Hadron Blind Detector is a proximity-focused Čerenkov counter filled with pure CF_4 gas and readout with CsI-doped Gas Electron Multipliers (GEMs). The HBD allows PHENIX to do precise measurements of the electron-pair continuum in both the low mass region from approximately 300 MeV up to the ϕ mass, and also in the Intermediate Mass Region in the range between the ϕ and J/ψ masses. The HBD is located in the PHENIX

central spectrometer covering a radius of 5 cm to 60 cm. The device is configured to be sensitive to electrons and insensitive to other charged particles. Its main purpose is to tag all electrons, enabling the identification of electrons from conversions and Dalitz pairs which allows an offline background subtraction that improves the S/B for the e-pair continuum by a factor of 7–10.

Two fundamental characteristics expected of the dense partonic plasma created in RHIC HI collisions are deconfinement and chiral symmetry restoration. A likely signature of these effects would be a modification to the dielectron continuum at masses below the ϕ meson. Additionally, the thermal radiation emitted by the hot plasma should result in an enhancement of dilepton pairs in the mass range 1–3 GeV. Measurement of the dielectron spectrum in HI collisions is particularly challenging due to the large background from photon conversion and Dalitz decay of π^0's. The HBD is specifically designed to identify and reject these backgrounds.

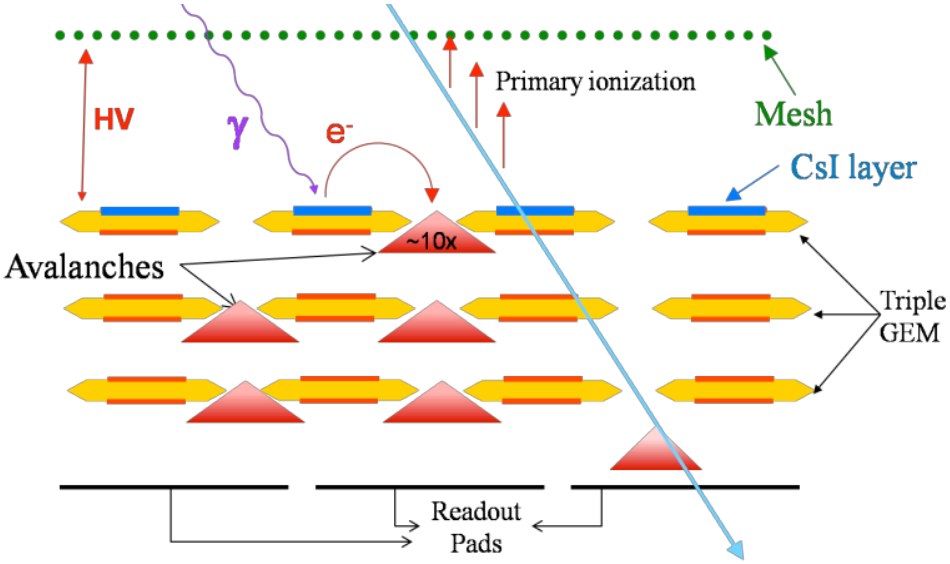

Figure C.3: Configuration of the GEM detectors and CsI photocathodes in the HBD. In *forward bias* mode a larger negative voltage is collected and amplified by the GEM stack. In *reverse bias* mode a lower negative voltage is applied to the mesh and ionization in the gap is collected by the mesh, making the detector essentially *hadron blind*.

The HBD had to satisfy a number of stringent design parameters in order to serve as an effective rejecter of the electron conversion and Dalitz pair background from both p+p and Au+Au collisions at RHIC. The detector had to fit within a relatively small space, maintain a high efficiency for detecting electrons while being blind to all hadrons, be very low mass, able to resolve electron singles from pairs and be insensitive to the high charged particle multiplicities at RHIC. These criteria determined the detector design. The HBD is built as a windowless, mirrorless Čerenkov counter filled with CF_4 gas which serves both as the radiator gas and the operating gas for the GEM readout. Pure CF_4 is well

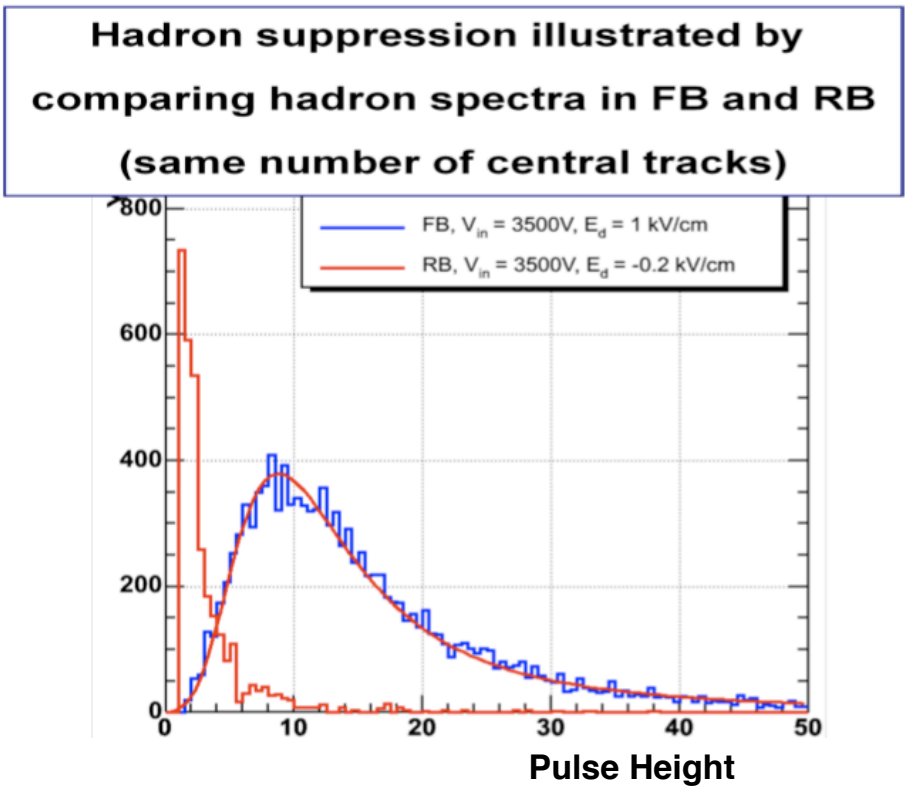

Figure C.4: HBD distribution of the charged hadron signal operating in both *forward bias and reverse bias mode.*

matched to the electron efficiency requirement of the detector as it has a large bandwidth of UV sensitivity (∼6.0–11.5 eV) which results in a very large number of Čerenkov photons available for detection, N_0 = 800 cm^{-1}. The HBD is able to obtain a single electron efficiency of over 90%. An additional benefit of the CF_4 is its relatively low emission rate of scintillation light when transversed by charged particles, which is a critical feature when operating in the high multiplicity environment of HI collisions. Figure C.3 shows the configuration of the HBD GEM modules.

The HBD converts the Čerenkov light generated by the electrons to a signal input to its electronics chain through an array of photosensitive GEMs. The top GEM layer of each triple stack was coated with a 300 nm layer of CsI which acts as a photocathode converting the Čerenkov light to photoelectrons. A cathode mesh above each GEM stack allows the ionization produced in the top GEM to be transported either into the GEM stack, *forward bias mode*, or away from the GEM stack and toward the mesh, *reverse bias mode*. Operating the GEMs in forward bias mode makes them sensitive to all charged particles, whereas operation in reverse bias mode makes the GEMs essentially hadron-blind. When operating in the hadron-blind configuration the photoelectrons produced in the top GEM layer by the Čerenkov light get drawn into the GEM stack, avalanche in the GEM triplet and produce a signal in the cathode readout pads located immediately behind the GEM

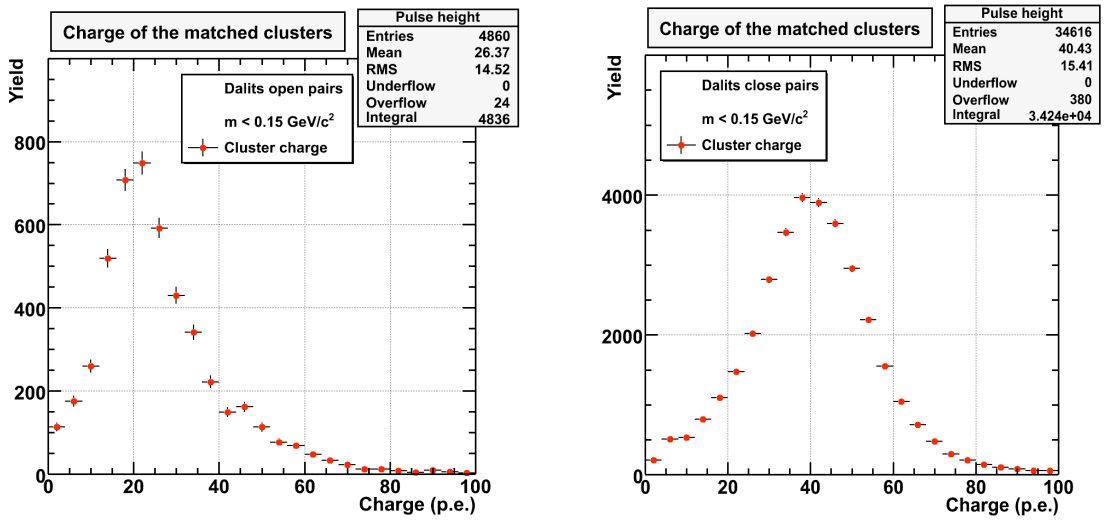

Figure C.5: Photoelectron yield for both single electrons and pairs.

stack.

The HBD was operated in PHENIX for an engineering run in RHIC run-7. After run-7 the detector was removed, refurbished to improve its voltage holding capability and re-installed for run-9. The HBD took a large set of p+p data in run-9 and Au+Au data in run-10. Figure C.4 shows the HBD performance as a hadron-blind device. Figure C.5 shows that the photoelectron yield for both single electrons and pairs met the performance specifications. The measured photo-electron yield is at the theoretical limit from what we expect given the know efficiencies of the detector. Figure C.6 shows the HBD installed in the PHENIX central spectrometer. After RHIC run-10 the HBD was removed, to be replaced by the VTX.

C.2 From 2011 to 2015

RHIC run-11 (2011) is the first physics run for both the silicon vertex barrel (VTX) and one arm of the Muon Trigger (MuTrg). RHIC run-12 (2012) is the first run for the forward silicon detector (FVTX) and the MuTrg operating in both north and south muon arms. Associated with these projects are upgrades to many of the Data Acquisition/Trigger components of PHENIX including the development of the second generation of the Data Collection Module (DCM II), the upgrade of the Event Builder from 1 GBit to 10 GBit Ethernet technology, the revision of the LVL-1 trigger to include new capabilities in muon and vertex triggering and the expansion of data archiving capacity through the upgrade of our data buffer boxes. Figure C.7 shows the configurations for run-10 and run-11.

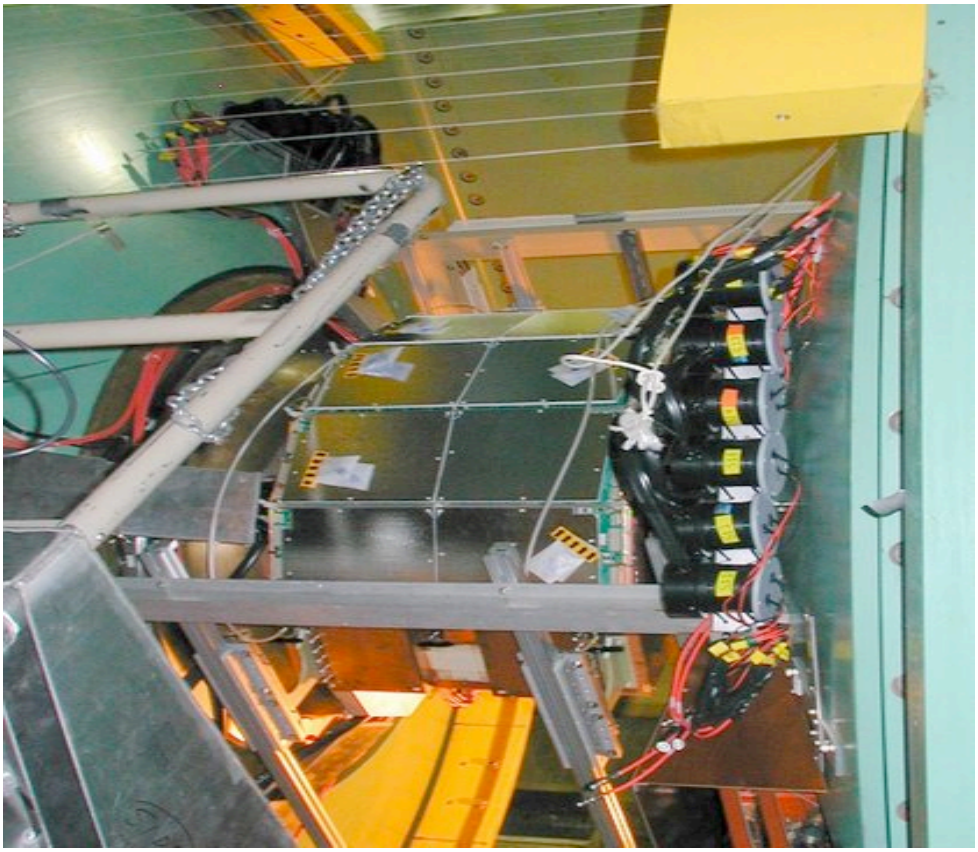

Figure C.6: HBD location in PHENIX central region.

C.2.1 VTX

The Silicon Vertex Tracking Detector (VTX) is a four-layer silicon barrel covering approximately 2π in azimuth and $-1.2 \leq \eta \leq 1.2$ in pseudorapidity located around the beampipe in the PHENIX central spectrometer. In the 2010 RHIC shutdown the HBD was removed from its position near the PHENIX beampipe and the VTX was installed. The inner two silicon layers use pixel sensors based on the design developed for the silicon pixel detector of the LHC's ALICE experiment. The outer silicon layers consist of stripixel sensors developed by the BNL Instrumentation Division which use a serpentine charge-sharing design to enable single-sided silicon to be readout with 2-dimension resolution comparable to that of pixel sensors.

The VTX contributes to the PHENIX physics program in two important ways. The detector has the ability to identify tracks from displaced vertices with an accuracy better than 100 microns. The VTX also significantly increases the solid angle coverage of the PHENIX Central spectrometer. Precise measurements of displaced vertices enable the VTX to identify and separate tracks from decay particles such as charm and bottom mesons. This in turn allows for measurement of charm and bottom $R_{AA}(p_T)$ and $v_2(p_T)$ in Heavy Ion

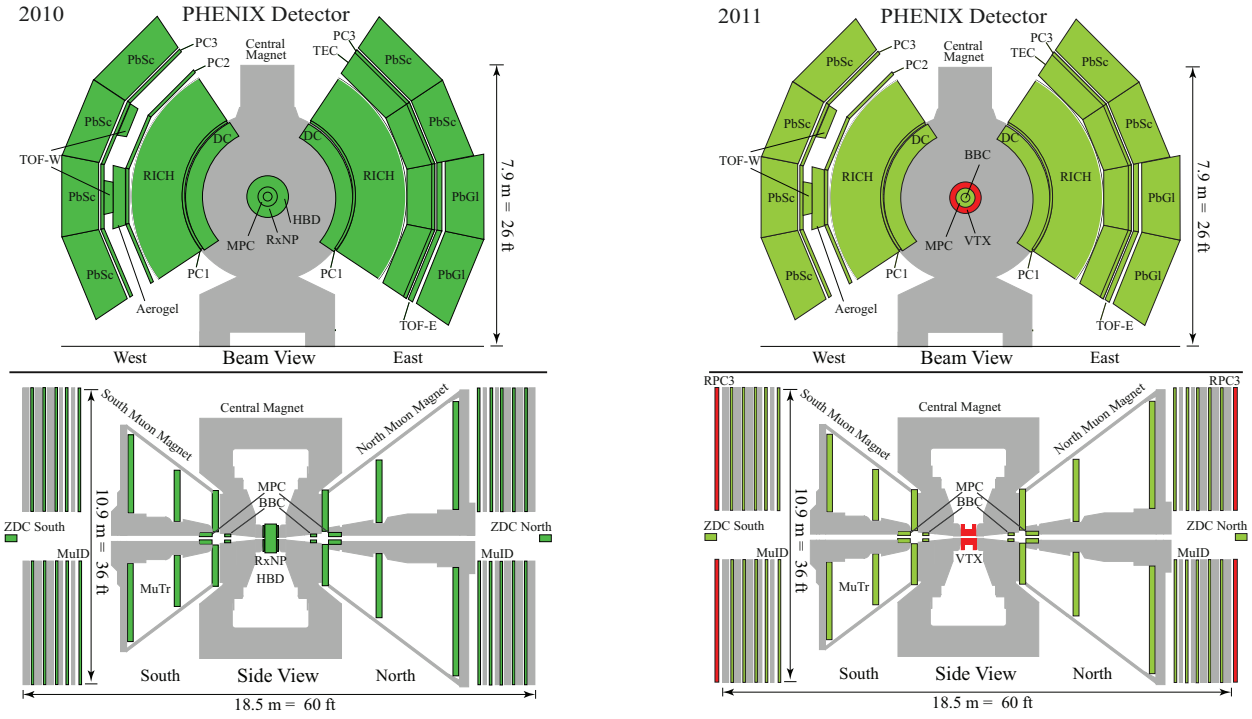

Figure C.7: RHIC run-10 (left) and run-11 (right) configurations of the PHENIX experiment.

collisions. The tagging of c and b decays will also enable the study of charm-hadron correlations in HI collisions and the measurement of A_{LL} through the heavy flavor mesons produced in polarized proton collisions. The significant increase in solid angle coverage that the VTX brings to PHENIX will greatly improve the experiment's capabilities in HI jet tomography through dihadron and γ-hadron correlations. Polarized proton measurements of A_{LL} through the γ-jet channel will also benefit from the larger solid angle coverage.

The VTX pixel sensors are mounted in 30 ladders arranged in two cylindrical layers located at radii of 2.5 and 5 cm from the PHENIX IP. The approximately 4M pixel channels have a pixel size of 50x425 μm^2. The stripixel sensors are fabricated into 40 ladders, also arranged in two cylindrical layers located at radii of 10 and 14 cm. Figure C.9 shows the pixel and a stripixel ladders mounted in the half-barrel structure of the VTX. Each of the 400k stripixel sensor channels has a dimension of 80 μm x 3 cm with a charge-sharing configuration that results in an effective channel size of 80x1000 μm^2. The pixel readout is based on the ALICE1LHCb chip developed at CERN for the ALICE experiment at the LHC. The stripixel readout is based on the SVX4 developed at Fermilab for the CDF and D0 silicon detectors. Both the pixel and stripixel electronics have custom Readout Cards, Front End Electronics modules and various interface cards developed specifically to optimize VTX performance and to interface with the PHENIX Data Acquisition system. The VTX fabrication completes in the fall of 2010 prior to commissioning and first data-taking in RHIC run-11. Figure C.8 shows a cut-away view of the VTX installed in the PHENIX

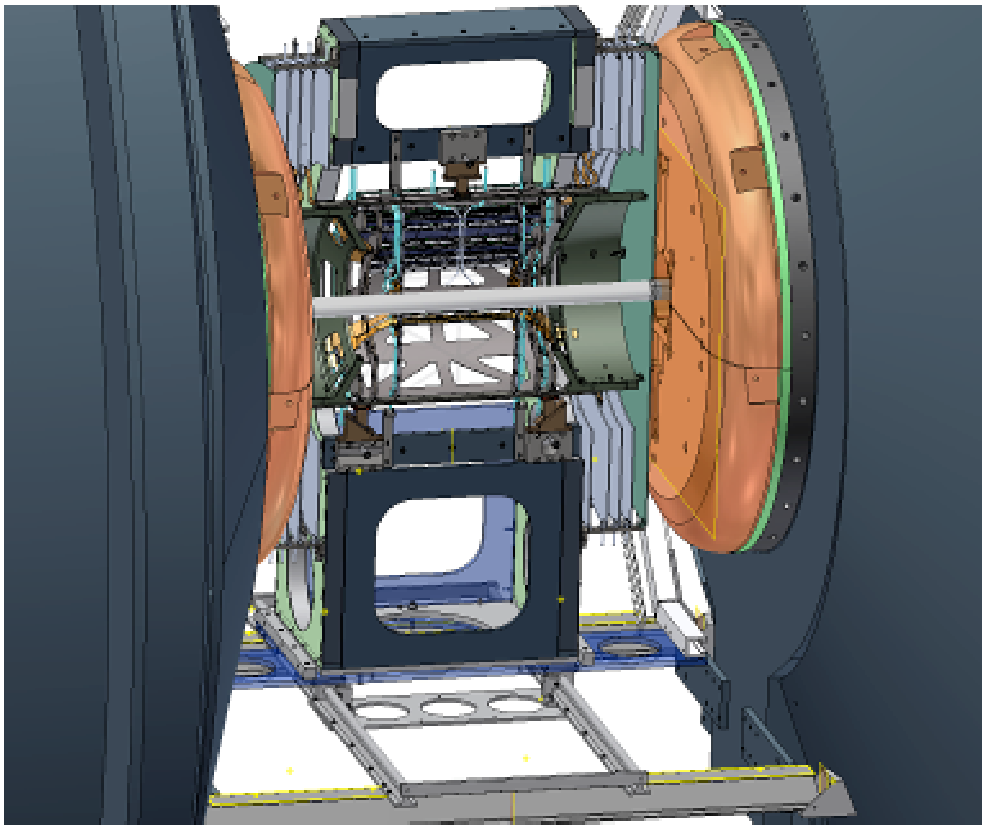

Figure C.8: Engineering drawing for installation of the VTX into the PHENIX central spectrometer.

Central spectrometer

C.2.2 FVTX

The Forward Silicon Vertex Detector (FVTX) is composed of two, four-layer endcaps of silicon mini-strip sensors located on either end of the VTX barrel in the PHENIX central spectrometer. The FVTX covers 2π in azimuth and $1.2 \leq \eta \leq 2.2$ in pseudorapidity. The FVTX endcaps are positioned so as to have an acceptance that almost completely overlaps the PHENIX Muon spectrometer arms.

The FVTX makes a number of significant contributions to the PHENIX physics program. The FVTX will allow for the identification and separation of muons coming from charm and bottom decays. It also improves the momentum resolution of the muon arms. The FVTX can identify tracks from displaced vertices with an accuracy of 200 microns. This enables the separation decay muons from long-lived light mesons (π's and K's) from the muons of charm and bottom decay. Tagging muons from heavy quark decays will allow for the measurement of charm and bottom $R_{AA}(p_T)$ and $v_2(p_T)$ at forward pseudorapidity

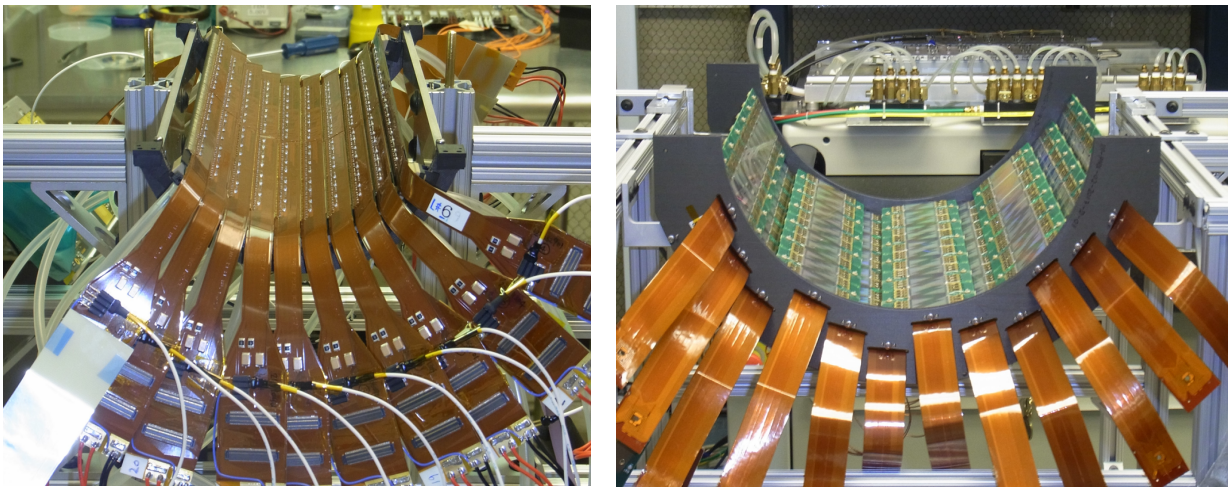

Figure C.9: VTX half barrel prior to final assembly showing the Layer 2 pixel ladders and the Layer 4 stripixel ladders.

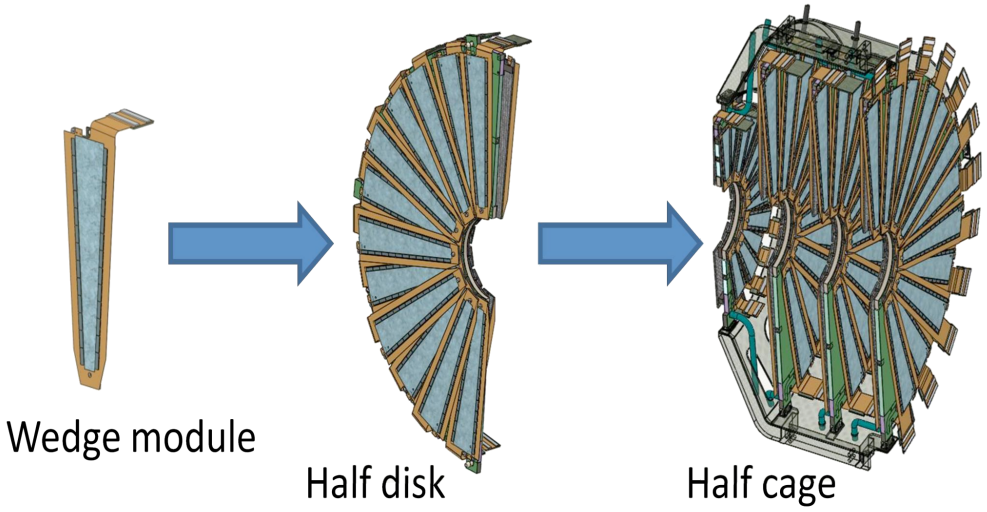

Figure C.10: One half of one FVTX endcap.

in HI collisions. Direct measurements of bottom can be made via the $B \rightarrow J/\psi + X$ channel by tagging J/ψ's coming from displayed vertices. Improvements from the FVTX to the mass resolution of the muon spectrometers will enable the separation of the J/ψ from the ψ' and extraction of Drell-Yan from the dimuon continuum. The FVTX is also expected to improve rejection of the fake high p_T muon background for the polarized proton W measurement.

Each layer of the FVTX is composed of 48 wedges of mini-strips arranged in disks per-

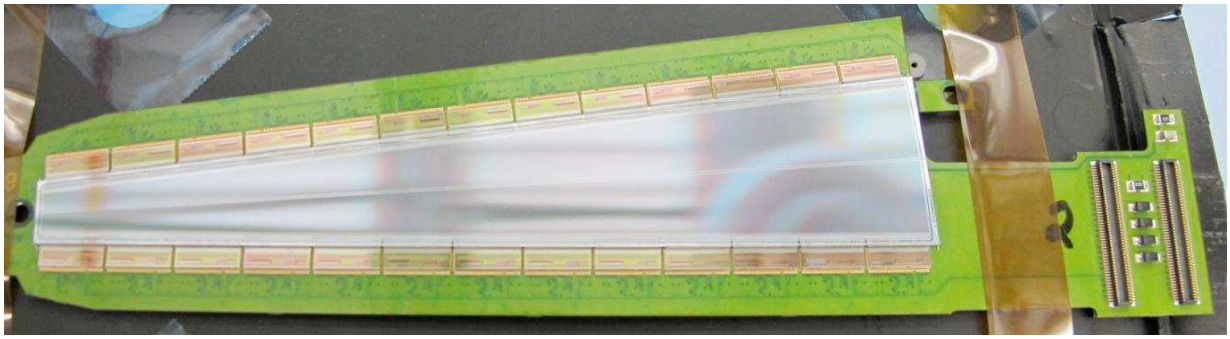

Figure C.11: Fully assembled FVTX wedge.

pendicular to the beampipe. Each sensor channel has a 75 μm pitch in the radial direction and a 3.75^0 segmentation in phi. The FVTX has approximately 1M channels and uses a readout based on an ASIC customized by FNAL engineers for this detector. The FPHX chip is derived from the FPIX2.1 which was originally developed for the BTeV project. In addition the detector has Readout Cards, Front End Electronics modules and various interface cards developed specifically to optimize the FVTX performance and to interface with the PHENIX Data Acquisition system.

The FVTX fabrication is complete in the summer of 2011 prior to commissioning and initial data-taking in RHIC run-12 (2012). Figure C.10 shows a schematic of the components of half of one FVTX endcap.

Figure C.11 shows a fully assembled wedge that includes the silicon sensor, high density interface board and carbon-fiber support structure.

C.2.3 Muon Trigger

The Muon Trigger (MuTrg) is a key element of the 500 GeV polarized p+p program of PHENIX. The MuTrg is composed of a set a detectors plus trigger electronics used to increase the Level-1 trigger rejection for backgrounds to single muons from W decay into the PHENIX Muon spectrometer arms (see Figure C.12). Each of the two Muon spectrometer arms consist of a piston-lampshade magnet instrumented with three muon tracking stations based on cathode-strip chamber (CSC) technology, followed by a Muon Identifier consisting of five planes of Iarocci-tubes interleaved with five layers of steel absorber with thicknesses of 30 cm, 10 cm, 10 cm, 20 cm and 20 cm. The Level-1 trigger rejection for single high p_T muons using only the Muon Identifier is approximately a factor of 200. The MuTrg combines trigger signals from the Muon Identifier with new Level-1 trigger electronics installed on every Muon Tracking station and two new layers of Resistive Plate Chambers (RPCs) in each arm. With the addition of the MuTrg the background rejection for high p_T single muon events increases to 10–20k, an improvement of approximately two orders of magnitude.

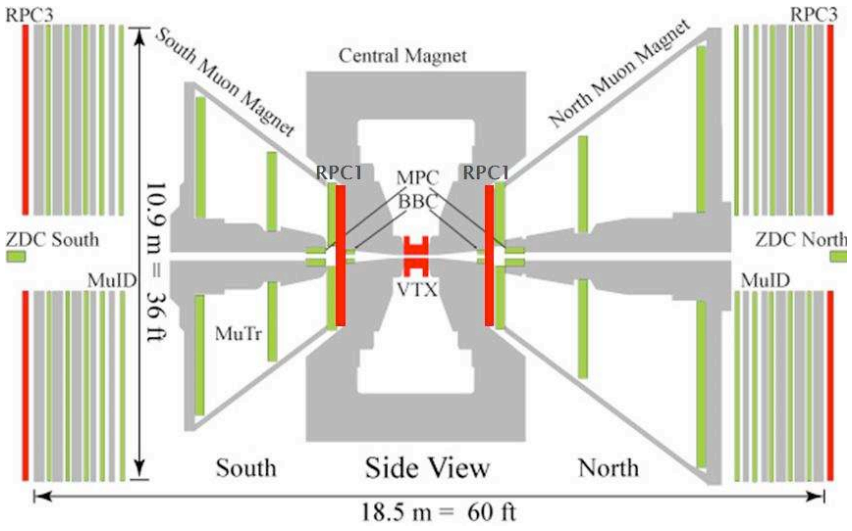

Figure C.12: Schematic of the PHENIX Muon Arms

By measuring the single spin asymmetries, A_L, in $W^{\pm}$ boson production in polarized proton collisions at RHIC it is possible to determine the flavor-identified spin contribution of the sea and valence quarks. The small cross section for W production at RHIC energies requires maximizing statistics for this measurement. The identification and recording of events containing a W in the muon arms must be made as efficient as possible. The MuTrg is necessary to reduce the single muon trigger rate so that all potential W events fit into the available bandwidth of the PHENIX Data Acquisition while also maintaining a high efficiency for recording single muons from W decays.

Each station of Resistive Plate Chambers provides position and timing information for the Level-1 trigger. In the muon arms one RPC Station is located immediately in front of MuTracker St1 on the front face of the muon spectrometer magnet and the other RPC Station is located immediately behind the final layer of the Muon Identifier. The RPCs are built from high rate Bakelite arranged in a configuration nearly identical to the muon trigger RPCs used in the Muon Endcaps of the CMS experiment at CERN. The Bakelite RPC technology was chosen because of its reasonable cost, high rate capability and availability of a significant amount of the production infrastructure that CMS used to produce their trigger RPCs. The RPCs obtain a timing resolution of $\sigma_t < 2$ ns which is needed to reject out of time backgrounds from both beam gas events and cosmic rays.

The MuTrg Level-1 front end electronics (FEE) installed on the Muon Tracker CSCs take a fraction of the signal generated by the CSC cathode readout and uses it generate primitives that are input into the MuTrg local LVL-1 processors. Since the MuTrg FEE directly ties into the Muon Tracker readout electronics chain great care has been taken to minimize any introduction of noise to the Muon Tracker system.

Signals from the RPCs, MuTrg Fee and Muon Identifier are combined in the MuTrg local LVL-1 processor boards to form the high p_T single muon trigger. Information from the

Figure C.13: RPC3 location in the RHIC tunnel.

Muon Identifier tags the muon, position information from the RPCs and MuTrg Fee is used to determine an approximate track momentum and timing information from the RPCs cut out of time background.

The MuTrg FEE installation was completed in 2010 and commissioned during RHIC run-10. The RPC installation started in 2009 and continues into the RHIC 2011 shutdown. The initial physics run for one arm of the MuTrg takes place in RHIC run-11. The MuTrg is completed before the start of RHIC run-12.

Figure C.13 shows the Station-3 RPC installed in the RHIC tunnel behind the north Muon Identifier.

C.2.4 DAQTRIG2010

A major factor in the success of the PHENIX physics program over the past decade is the performance of the data acquisition and trigger system. The system includes a multievent front end electronics buffering that allows for a nearly dead-timeless running up to very near the maximum throughput rates. Figure C.14 shows the data acquisition live time as a function of the Au+Au minimum bias interaction rate recorded with the PHENIX Beam-Beam Counters. As a result of improvements to code run in the Data Collection Modules

(DCM), optimization of the readout timing of the Front End Modules (FEM), use of multi-event buffering in the front end modules, a faster network switch,improvements resulting in faster data logging, and careful attention to zero suppression, the data acquisition system is capable of acquiring minimum bias Au+Au events with greater than 90% livetime at 6 kHz.

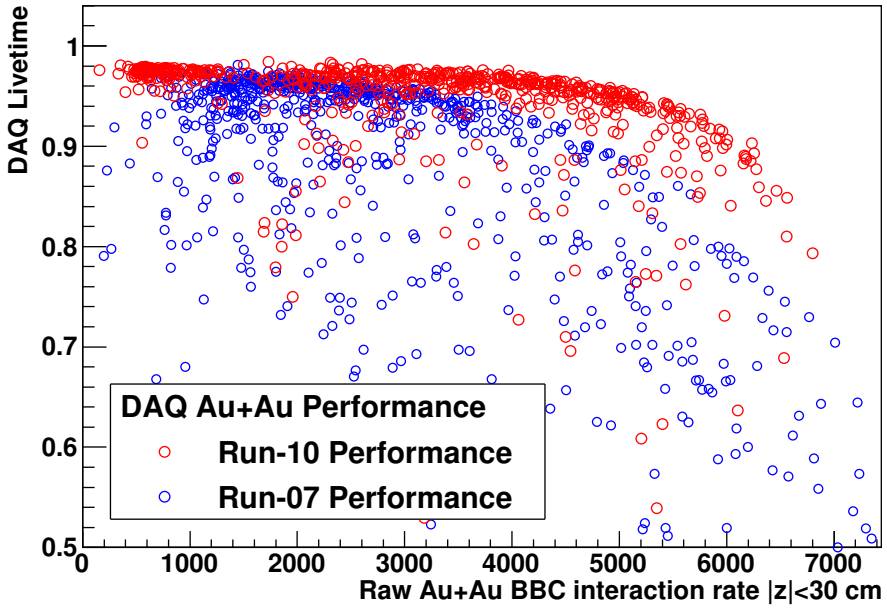

Figure C.14: DAQ Performance—showing livetime up to Au+Au 200 GeV raw rates of greater than 5 kHz.

The readout speed of the detector is ultimately limited by the conversion and readout times of the FEMs, which are presently 40 and 80 μs. The objective is to maintain this high bandwidth, dead-timeless design with the new large data volume silicon detectors (VTX and FVTX) being added to the detector configuration. Thus, a comprehensive set of data acquisition upgrades, called DAQTRIG2010, are being constructed to match this bandwidth goal. These include a new generation of Data Collection Modules II (DCM II), a custom digital electronics board with ALTERA STRATIX FPGAs for data zero suppression, formatting, and transfer. Additional, a set of 10 Gigabit custom electronics (the JSEB II) are designed for high speed transfer from the DCM II crate to a set of commercial computers that serve at the Sub-Event Buffers of the Event Builder. A higher bandwidth (10 Gigabit) commercial network switch for the Event Builder has been purchased to handle the higher total data throughput, in addition to upgrades to the PHENIX Buffer Box array for temporary data writing and storage before final archiving at the RHIC Computing Facility (RCF). These upgrades are partially implemented in the fall of 2010 for reading out the VTX and a full implemented in 2011 with the incorporation of the FVTX readout.

C.2.5 The FOCAL Design: A Tracking Calorimeter

The prime physics motivation of this new detector is to provide precision measurements of direct photons, π^0s and jets over an extended range of rapidity in d+Au collisions. In general terms this upgrade will provide capabilities for the measurement of physics observables that are not currently accessible to PHENIX or that are now available only indirectly and with very limited accuracy. Details of the current FOCAL design, development and R&D is provided in this appendix.

The FOCAL is a highly segmented tracking calorimeter designed to reconstruct and identify electromagnetic signals at intermediate rapidity in close proximity to the production vertex. This detector takes full advantage of the large body of existing data on particle showering in matter to design a total absorption calorimeter that is able to measure the energy and direction of impinging particles and to discriminate between electromagnetic and hadronic showers. FOCAL is composed of an active preshower segment (E0) and two identically structured high density energy sampling segments (E1 and E2). All three segments have an identical number of energy sampling cells: an absorber layer of tungsten followed by pad-structured silicon sensors. Sampling cells 2–5 of the preshower segment also include two strip structured (pitch 500μm) position sensing sensors (at a depths of $\sim 2X_0$ (L0), $\sim 3X_0$ (L1), $\sim 4X_0$ (L2) and $\sim 5X_0$ (L3)). These strip layers will serve to count hits, measure hit-to-hit separation, and estimate the energy sharing between possible contributors to the high energy tracks constructed from clusters seen in the (pad) calorimeter segments. The longitudinal structure of the calorimeter tower is sketched in Figure C.15.

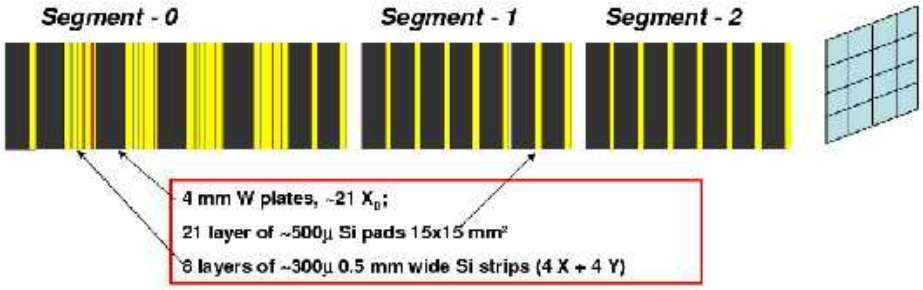

Figure C.15: Longitudinal structure of a single calorimeter supertower (one sensor wide) showing the locations of the three calorimetric segments, S0, S1, and S2, and the high-resolution position sensitive layers.

The FOCAL will be located 44 cm from the nominal collision point, on the poles of the PHENIX central magnet, and limited to a depth of 16 cm. It will be built of tungsten plates (each 4 mm thick) interleaved with silicon readout layers. The readout layers are structured into pads of $15.5 \times 15.5\,\mathrm{mm}^2$ in the calorimetric and strips of $0.5 \times 62\,\mathrm{mm}^2$ in the position sensitive layers. Each segment is $\sim$8 L_{rad} deep. FOCAL adds 24 L_{rad}

or 0.9 L_{abs} to the total absorber depth in the muon spectrometer (the currently installed copper absorber has a depth of $\sim$1.3 L_{abs}). The Molière radius of FOCAL is $\sim$14 mm. The acceptance region covered by the current PHENIX nosecone will be replaced with a support structure and tungsten plates. This, in principle, allows the FOCAL acceptance to fully match the acceptance of the PHENIX muon arms. However, at the present time it is our plan to only instrument a portion of the FOCAL with Si sensors.

Figure C.16 shows a beams-eye view of the FOCAL detector. As described more thoroughly in this section, the detector is comprised of a set of $\sim$6$\times$6 cm detector elements (called "supertowers"). Figure C.16 shows the full mechanical structure of FOCAL with the instrumented towers highlighted in gray. The two rectangular regions on either side of the are beam line made of four 1$\times$4 "bricks" (a collection of towers) and two 1$\times$5 bricks. The inner red line corresponds to $\eta = 1.6$. Between $\eta = 1.6$–2.5 the FOCAL will cover a full 2π in azimuthal angle.

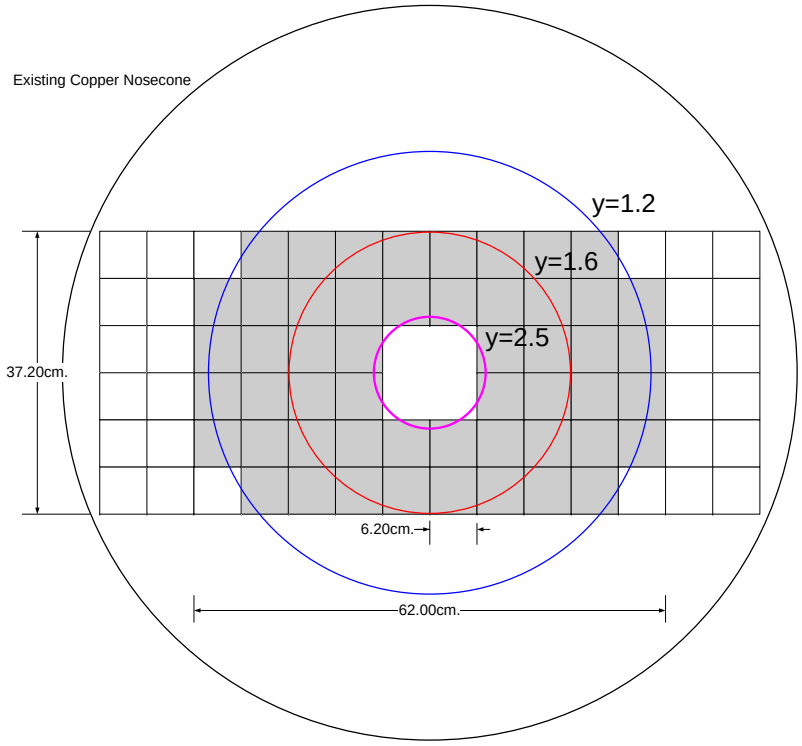

Figure C.16: A beam-view of the FOCAL acceptance superimposed on the existing PHENIX Cu nosecone. The instrumented region of the detector is shown in gray. See text for a complete description.

The acceptance of the FOCAL was optimized to give as wide a rapidity coverage as possible as the rapidity of a direct photon correlates with the x of the gluon in the partonic process. At the highest rapidities, the smallest reachable x, the FOCAL will have 2π azimuthal coverage to allow for γ+jet correlation measurements within its acceptance.

By design, the FOCAL segments are structured into mechanically nonprojective towers. This design feature was prompted by the experience with the PHENIX central calorimeters. There we have particles hitting at angles up to 20° without any noticeable effect on the calorimeter's performance. The sub-towers in the FOCAL (readout towers in individual segments) have an aspect ratio of ∼2 (ratio of the sub-tower depth to its lateral size measured in the diagonal direction) which helps to keep occupancy in the individual segments low—even at the periphery of the detector. The tower cluster multiplicity per track rises by less than 50 % between minimum and maximum impact angles (compared to two-fold increase in the central arm calorimeter). The density of particles hitting the detector decreases towards larger impact angles (smaller rapidities), which minimizes the effect of increased cluster multiplicities on the calorimeter occupancy.

Projectivity together with longitudinal segmentation have a dramatic effect on the FOCAL performance as a particle identification detector, allowing it to effectively reject hadronic showers by comparing the measured longitudinal shower development to the parametrized electromagnetic shower shape.

FOCAL Mechanical Design

A modular design has been developed for the FOCAL to allow for ease of construction and minimization of custom parts. The calorimeter is built of "bricks", three bricks (preshower brick and two energy sampler bricks) are stacked together form a "superbrick" (see Figure C.17). All bricks are a double $6.2 \times 6.2\,\mathrm{cm}^2$ silicon sensor wide. Each brick has a tungsten plate facing upstream and a copper skin enclosing it on all other sides, save one for connections to external electronics.

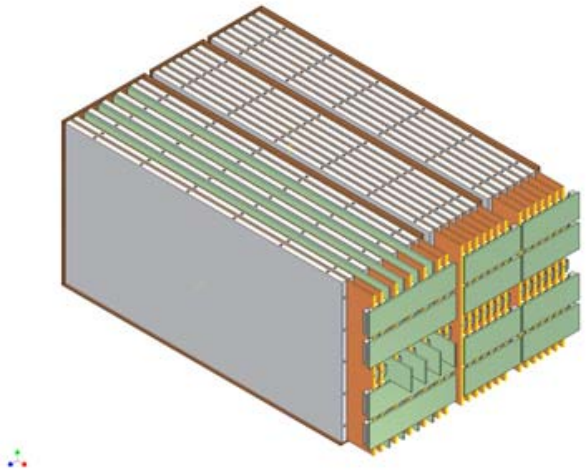

Figure C.17: FOCAL building brick.

When the FOCAL is assembled, the bricks form three segments: one made of preshower bricks, the other two of energy sampling bricks. Small locking pins are used to maintain

the geometry. For mechanical reasons all three segments have identical lateral dimensions. Projective readout on the periphery of detector will be maintained, depopulating detector edges. The nominal design of the external calorimeter support includes two shelves above and below the FOCAL, with front supports of thin, pretensioned braces (strips of stainless steel or Kevlar) that keep the segments from buckling outward.

FOCAL Sensors and Readout

FOCAL active layers (pads and strips) are built following the same modular principle discussed above. The basic element in the readout chain is the micromodule which consists of a silicon sensor (pad or strip structured), an interconnect board hosting passive and/or active readout components, connections to a grounding plane, and ceramic backing tiles which protect sensors and insure micromodule rigidity.

Two kinds of silicon sensors (and two different micromodules) are used in the FOCAL readout: pad structured and strips. The pad size chosen for FOCAL is $\sim 1.55 \times 1.55\,\mathrm{cm}^2$. The strip size for the preshower section is $\sim 0.5 \times 62\,\mathrm{mm}^2$. All silicon detectors in the FOCAL are $6.2 \times 6.2\,\mathrm{cm}^2$ diced either from 4″ or from 6″ wafers 525 μm thick. The FOCAL must reliably maintain its performance specifications while operating in a high radiation environment. The estimates based upon ionization losses of collision related particles produced in $p+p$interactions at $\sqrt{s} = 500\,\mathrm{GeV}$ at a luminosity of $10^{32} cm^{-2} s^{-1}$ result in radiation dose of $\sim$10 Krad/year close to the beampipe. Albedo neutrons from the calorimeter absorber will constitute 3 to 10% of the value of the MIP fluence but will induce $\times 10$ higher damage effectively doubling the radiation dose to $\sim$ 20 Krad/year of operation. In 10 years of running at RHIC luminosity (assuming full stochastic cooling) the sensors in the central region of FOCAL will begin showing signs of radiation damage. To alleviate the possible consequences of exposure all sensors in the FOCAL are used in AC coupled mode (external RC decoupling network) thus allowing the sensors to maintain performance with at least a $\times 10$ increase in the leakage current. In addition, the mechanical design of the readout units allows for replacement of problematic sensors without collateral losses. The design of sensors and the selection of raw material were guided by the experience and work done within the scope of the D0 (FNAL) and ALICE (LHC) projects and recent published data from the R&D in radiation hard silicon technology. In particular, the following simple rules were followed:

- The FOCAL will use *single sided sensors* from established vendors to ensure high yields and less trouble due to the simplicity of the design. In addition, double-sided sensors suffer more radiation damage,

- A *minimal number of different sensor designs* (only two in the FOCAL case). Design to successful completion of the project using a single vendor. The design can be transferred to additional vendors when ready to speed up production,

- *Use short strips* to reduce the number of ghosts hits to avoid creating pattern recognition problems. We use 4″ wafers only,
- *Specially designed guard ring structures*. Such guard rings are important in order to keep breakdown voltages before and after irradiation as high as possible.

Table C.1: FOCAL silicon sensor parameters.

Specification	**Pad-structured sensors**	**Strip sensors**
Wafer thickness	525 μm	300 μm
Depletion voltage	100–120 V	80–100 V
Diode capacitance	25 pF	5 pF
Bias voltage	Full dep. V + 20 V	Full dep. V + 20 V
Leakage current	$<$ 300 nA total, $<$ 20 nA/pad	$<$ 1 nA per strip
Junction breakdown	$>$ 300 V	$>$ 300 V
Implant area	15×15 mm^2	
Al area	15.02×15.02 mm^2	0.45×61 mm^2.
Interpad (strip) capacitance	$<$ 2 pF (pad-pad) or $<$8 pF (pad-all neighbors)	$<$ 1 pF (strip-strip)
Maximum heat dissipation from the bulk material	$<$ 50 mW/sensor	$<$ 50 mW/sensor
Heat dissipation from on-the-sensor electronics	no major heat sources	0.5 W/sensor

Following these recommendations, the silicon sensors for FOCAL are built using single-sided single-metal p+ on n$-$ bulk silicon devices. A short summary of sensor parameters is given in Table C.1.

Both pad and strip sensors have first been prototyped at ELMA (Russia), ON Semiconductor's (Czech Republic) then at ETRI (South Korea). The pad structured silicon layers (21 in total) are built of 6.2×6.2 cm^2 silicon detectors subdivided into 16 identical square cross section pads (diodes). The individual pad-structured sensors are assembled into micromodules consisting of the silicon sensor, a single layer interconnect board, a ceramic spacer and ceramic backing tile all glued together using silicon-based adhesive. An assembled and exploded (for clarity) micromodule is shown in Figure C.18. The strip layers will also be assembled in a similar micromodule format.

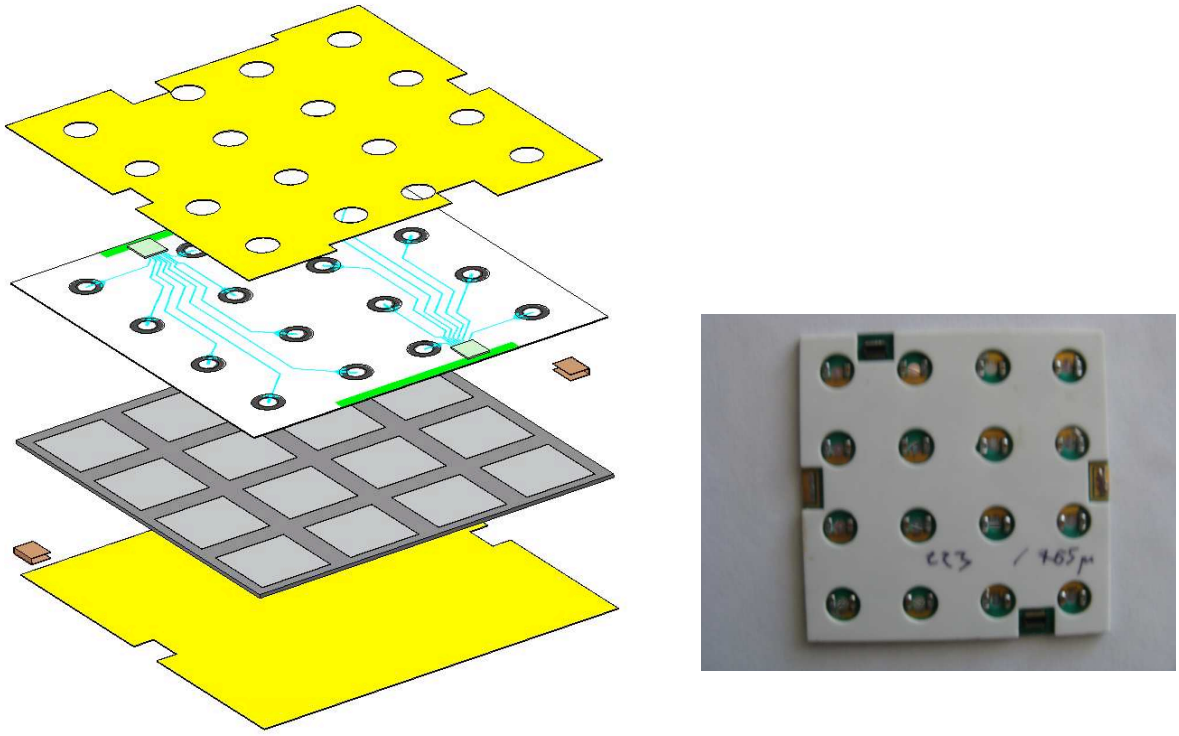

Figure C.18: Pad-sensor micromodule sandwich components. From bottom to top: backing ceramic tile, silicon sensor, interconnect board, and ceramic spacer.

The sensors are first glued to the dielectric side of the laminate of the interconnect board and the ceramic spacer. A silicon based glue is used everywhere so any thermal expansion mismatch effects are alleviated. The bonding pads on the interconnect board are further wire bonded to the aluminized pad centers through 3 mm diameter vias. Low-profile RC-network components are placed on the interconnect board close to the bonding point locations—hidden inside large diameter vias in the ceramic spacer separating the interconnect and carrier boards. Gold plated copper foil is bonded and glued to the aluminum plating on the sensor common side and soldered to the ground pad on the interconnect for the ground connection. Two 20 pin low profile (0.9 mm total height) connectors are installed close to the edges of the interconnect board to connect the sensor stack to traces on the carrier board which is conductively glued (grounded) to the tungsten plate.

The interplate gap reserved for the carrier board with installed micromodules is 2.5 mm wide. 0.5 mm of this space is silicon, $\sim$0.2 mm is FR4 (motherboard), and 0.2 mm is the FR4 interconnect board. 0.9 mm, partially filled with ceramic spacer, is used to accommodate connectors and RC-network distributing bias voltage to individual diodes. 0.4 mm is used by ceramic backing which provides additional protection to the ground side of the silicon sensor. The remaining $\sim$0.3 mm gap is to ensure that no pressure is applied to the surface of the sensors. Such pressure may result in increased noise due to the piezoelectric

effect.

This particular design is developed to ensure an easy repair of the assembled sampling cell. If the sensor fails, the sensor micromodule can be removed from the carrier board and a new micromodule installed. The same approach can be used if repair will ever be needed due to, for example, unplanned beam losses in the area close to the detector location.

A fully assembled prototype superbrick (2x4 sensors) is shown in Figure C.17 In this picture the top skin plate was removed to allow access to the gaps reserved for installation of the strip layers. In June of 2009 the fully assembled and bench tested superbrick was exposed to beams of electrons and hadrons at the CERN PS and SPS. The energy resolution of the device was found to be $21\%/\sqrt{E}$, with a negligible constant term, consistent with simulation results.

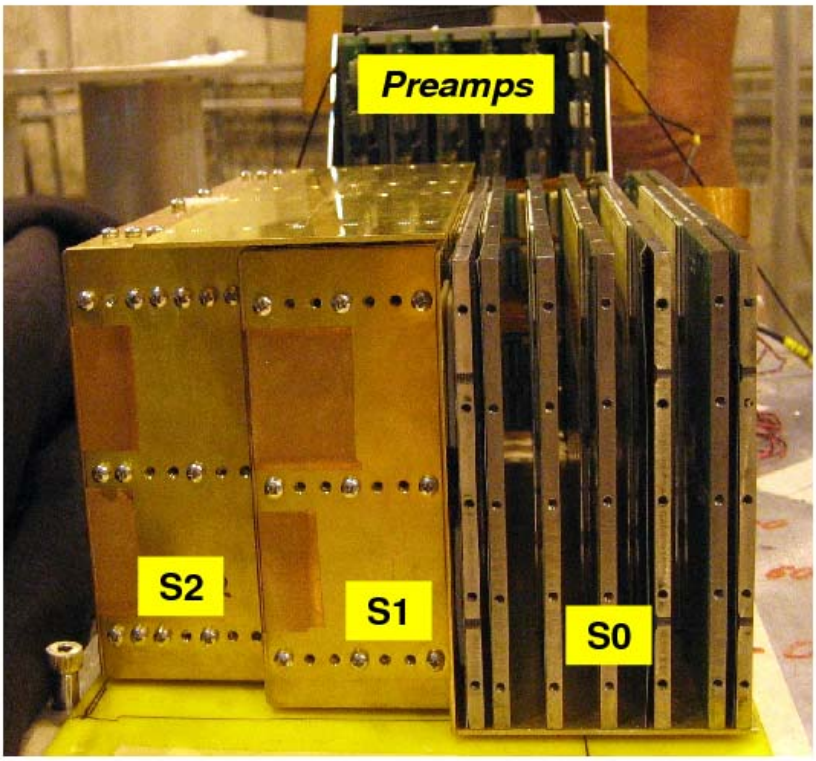

Figure C.19: A fully assembled prototype superbrick.

C.2.6 SuperDAQ

The total bandwidth of the PHENIX data acquisition in Au+Au collisions will remain at approximately 5 kHz after the implementation of the DAQTRIG2010 upgrades. However, those upgrades will allow for a higher bandwidth (approximately 8 kHz) readout of the new larger data volume detectors (i.e. the VTX and FVTX). The bandwidth limitation will be the data size from the existing detector system front-end electronics to the existing original Data Collection Modules (DCM). The DCM modules were designed in the late 1990's using Analog Devices SHARC 40 MHZ (CPU and IO) digital signal processors DSPs.

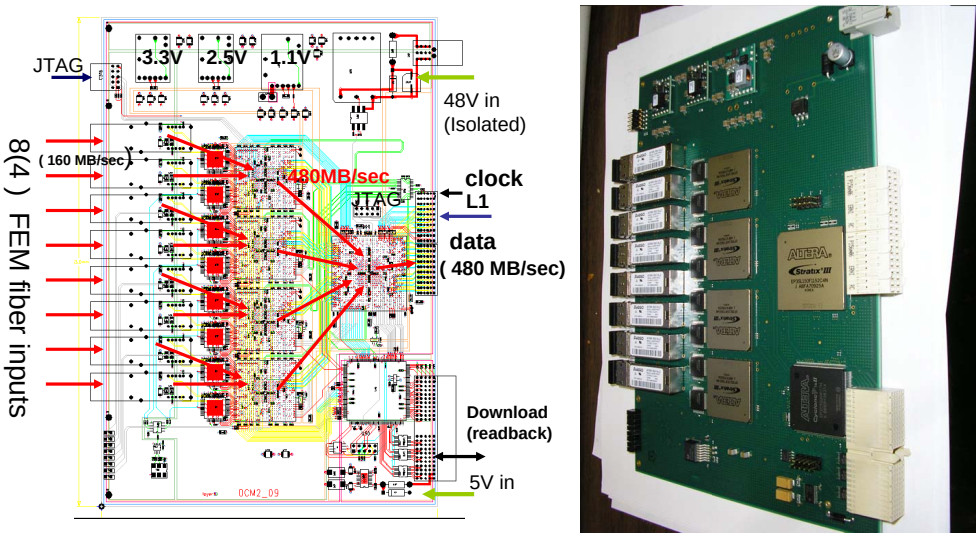

Figure C.20: DCM2 diagram and picture.

A conversion of all the original DCM electronics to the new DCM II boards, as shown in Figure C.20, will bring all systems to the higher bandwidth capability. We are currently implementing DCM II modules for the VTX readout, and once the system is fully working, expect to submit a proposal for the production of additional modules for this SuperDAQ upgrade. Additional engineering for firmware modifications will be needed and also a conversion of fiber transmission encoding. We are also exploring the requirements for the back end of the data acquisition, though the Event Builder switch purchased as part

of DAQTRIG2010 should already have sufficient capacity for this additional increase in bandwidth.

C.2.7 Existing Detector Maintenance and Improvements

In addition to the currently funded mid-term upgrades and the two additional proposals (FOCAL and SuperDAQ), a number of relatively small upgrades to the detector will likely be desirable before 2015 to address the aging of core PHENIX subsystems. These upgrades are briefly detailed for completeness.

Tracking

The PHENIX tracking system is now more than 10 years old, and, as with all systems involving proportional wire chambers, requires a regular program of maintenance and repair in order to keep operating at optimal efficiency. Recent enhanced maintenance of the PHENIX central tracking system includes the replacement of one of the sixteen Pad Chamber 1 (PC1) modules during 2009 shutdown and major servicing to the West Drift Chamber during the 2010 shutdown. Though as of 2010 the central arm tracking system is in good condition for future running, various options are being considered to both maintain a high level of operating efficiency and improve overall tracking performance.

Options involving the utilization of GEM detectors as replacements for existing wire chambers or as possible additions to the PHENIX central tracking system are being studied. Possibilities include building GEMs detector as a replacement for the aging inner pad chambers (PC1 East and West) or adding additional GEM-based tracking layers located at radii between the VTX and the Drift Chamber. The GEMs would provide the same track position information as the present proportional wire chambers, but would be more robust in terms of rates, aging and wire breakage. The actual cathode pad readout structure for the GEMs could be the same as the existing PCs which would allow for little change to existing track finding and reconstruction algorithms, and compatibility with and possible reuse of existing PC readout electronics.

One or two additional GEM-based tracking layers located in the space between the VTX and Drift Chamber could be designed to provide expanded azimuthal coverage (up to 2π) to the PHENIX Central arms, improve momentum resolution by making additional track measurements at larger radii, and help to reject background from nonvertex sources such as albedo, conversions and decays. GEM detectors would be able to provide good spatial resolution (≤ 100 μm) over a large area for a relatively low cost.

An R&D program would need to begin in the near future in order to design, build and install GEM-based tracking detectors into PHENIX within the next five years. An R&D program would build on the experience within the PHENIX collaboration with GEM detectors that was acquired in the construction and operation of the Hadron Blind Detector.

GEMs trackers have far less demanding performance requirements then those of the HBD. Any such intermediate upgrade would be coordinated with the larger scale upgrades and technology choices.

Electromagnetic Calorimeter

Maintenance of calorimeter electronics has been an ongoing effort. Recently, additional tubes and bases have become available for the lead-glass sectors, and it may be necessary to develop and produce new tube bases in the future.

EMCAL Trigger

The present EMCAL-RICH Trigger(ERT) uses signals generated in the EM Calorimeter Front End Module by 12x12 EMCAL super-modules, inputs them to readout cards (ROCs) designed for the PHENIX Muon Identifier (MuID) which then transmit Local Level 1 (LL1) data on every beam-clock to slightly modified versions of the Muon Identifier trigger (LL1) boards. The intermediary MUID ROCs are a suboptimal feature of the ERT because their location in the PHENIX IR makes maintenance and debugging of the trigger difficult, while introducing noise and synchronization problems of their own. Additionally only four signals from each FEM are transmitted to the ROC, which reduces the flexibility of the trigger.

Development of a second generation trigger board has begun which could alleviate some of the problems with the present trigger and enable more sophisticated EMCAL triggers. If the development and testing is successful, eventual deployment of an upgraded trigger will likely require a staged installation to provide adequate testing and comparison with the present trigger.

Muon Tracking

One of the largest sources of data in PHENIX is the muon tracker system. The possibility of relieving the data bottleneck in the Data Collection Modules (DCM) has been discussed elsewhere, but the muon tracker presents a more difficult problem by virtue of the large number (218) of data fibers. Data is translated from a different serial protocol (CLINK) transmitted from the FEM to cards which send data to DCMs on GLINK fibers. These GLINK-CLINK cards could be improved mechanically and electrically to be more reliable, and at the same time could be redesigned to directly transit data to the DCM II, which uses a different and more modern serial protocol and fiber optic technology. Design of an improved card could begin in the very near future.

Appendix D

Collaboration Status 2010

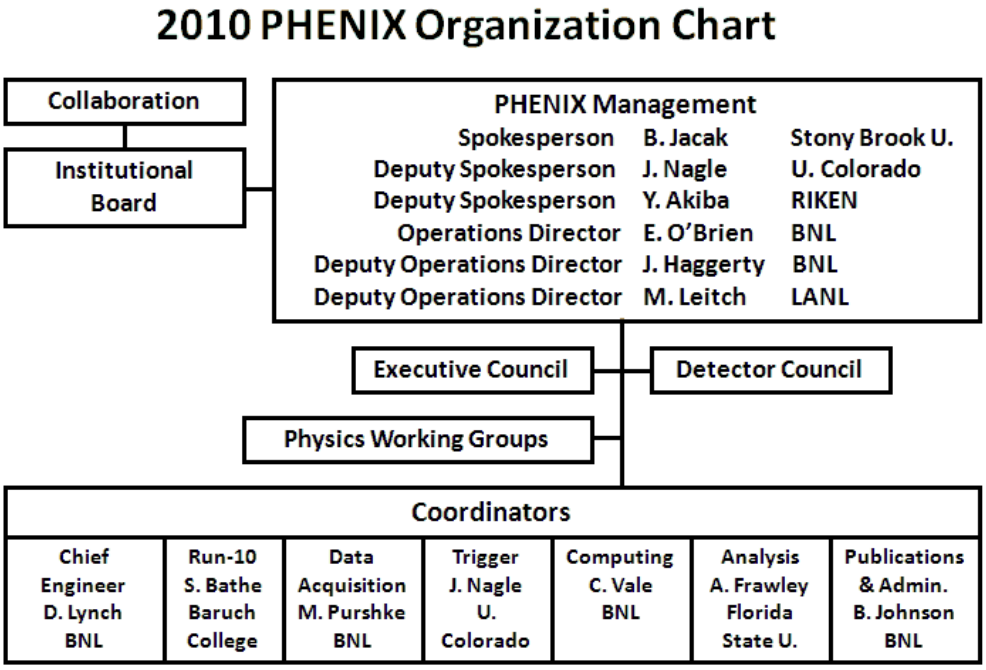

Figure D.1: PHENIX Management Structure as of October 2010

Figure D.1 illustrates the current governance of PHENIX. The six positions in PHENIX Management (PM) are responsible for planning and executing the research, operations, and upgrades of PHENIX, and for managing the collaboration. PM is assisted by the indicated Coordinators who report directly to PM. The Executive Council sets scientific priorities for PHENIX and advises PM on all the scientific issues of the experiment. The Detector Council advises PM on all PHENIX technical, operational, and upgrades issues. The Institutional Board decides issues concerning collaboration governance and elects the Spokesperson and members of the Executive Council. Conveners are appointed by PM to

oversee topical analysis efforts and to conduct weekly Physics Working Group meetings and a weekly joint meeting with PM to assist in managing and coordinating the PHENIX physics analysis and approval of preliminary data for presentation in conferences and the release of final data for publication.

D.1 Growth of the Collaboration

PHENIX is currently a collaboration of over 560 scientists and engineers from 74 institutions in 14 countries. Figure D.2 and Table D.1 show the growth of the collaboration since 1993.

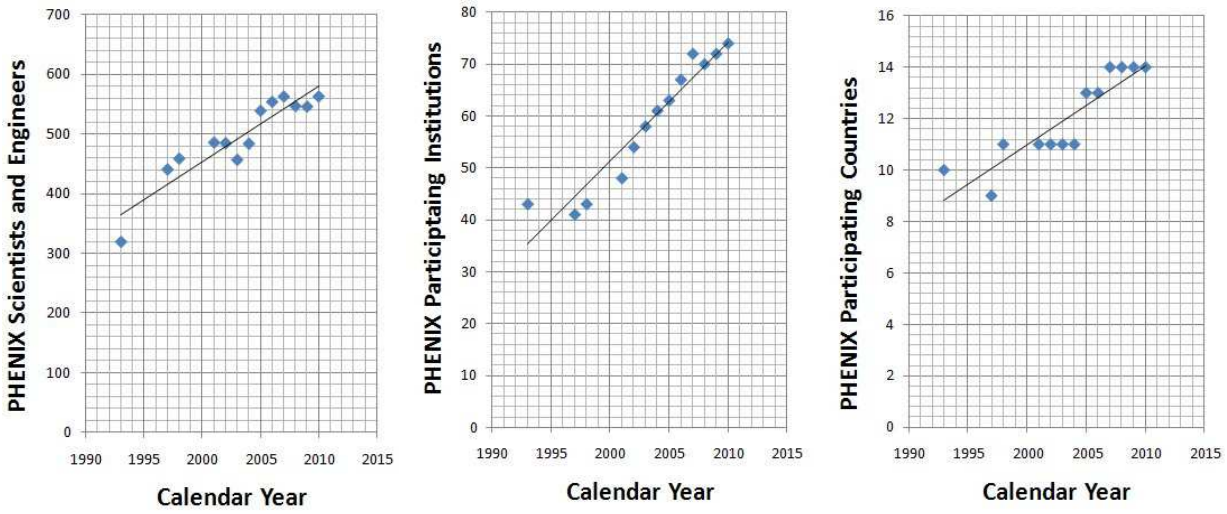

Figure D.2: PHENIX Collaboration Growth in (a) Scientists and Engineers, (b) Participating Institutions, and (c) Participating Countries

Table D.1: Growth of the PHENIX Collaboration from 1993 to present.

	Year												
	'93	**'97**	**'98**	**'01**	**'02**	**'03**	**'04**	**'05**	**'06**	**'07**	**'08**	**'09**	**'10**
Sci. & Engr.	320	441	459	486	485	457	484	539	554	563	547	546	563
Institutions	43	41	43	48	54	58	61	63	67	72	70	72	74
Countries	10	9	11	11	11	11	11	13	13	14	14	14	14

D.2 Institutional Responsibilities and Sources of Funding

The design and construction of PHENIX was administered by PHENIX governing boards, particularly PHENIX Management, Executive Council, Detector Council, and Institutional Board. The roles and responsibilities of these units are specified in the PHENIX Bylaws[8]. In addition, institutional responsibilities are specified through Memoranda of Understanding (MoU) between PHENIX, BNL, and the individual collaborating institutions.

The collaboration is responsible for operating and maintaining the PHENIX experiment and carrying out its physics research program. In addition, the PHENIX collaboration initiates, designs, builds and operates all upgrades to the detector. The collaboration is assisted in these tasks by a dedicated technical support group located at Brookhaven National Laboratory. PHENIX institutions contribute additional technical and engineering support to the experiment, especially in areas directly related to an institution's subsystem or upgrade project responsibilities.

The PHENIX baseline detector and major upgrades were built primarily with funds from the US Office of Nuclear Physics in the Office of Science of the Department of Energy. Significant additional funds are provided from the Japanese Ministry of Education, Culture, Sports, Science, and Technology and the Japan Society for the Promotion of Science. In addition, there are many in-kind contributions of manpower and equipment from numerous PHENIX institutions and their national and international funding agencies.

Institutions that built a PHENIX detector subsystem are responsible for operating and maintaining it. New groups that join PHENIX are strongly encouraged to join service groups that are responsible for subdetectors, DAQ and trigger components, software functions, or upgrade efforts. The outside institutions fill a large pool of experts who are needed to operate PHENIX during both data-taking and data production at the RHIC Computing Facility.

Appendix E

PHENIX Participants – October 2010

Abilene Christian University,
Abilene, Texas 79699, USA
P. Abernathy, M.S. Daugherity, K. Gainey, D. Isenhower, W.S. Lynn, H. Qu, R.S. Towell*, T.S. Watson

Department of Physics, Banaras Hindu University,
Varanasi 221005, India
P. Garg, B.K. Singh, C.P. Singh*, V. Singh, P.K. Srivastava, S. Tarafdar

Bhabha Atomic Research Centre,
Bombay 400 085, India
R.K. Choudhury*, D.K. Mishra, A.K. Mohanty, P.K. Netrakanti, P. Sett, P. Shukla

Baruch College, City University of New York,
New York, New York, 10010 USA
S. Bathe*, J. Bryslawskyj

Collider-Accelerator Department, Brookhaven National Laboratory,
Upton, New York 11973-5000, USA
M. Bai, K.A. Drees, S. Edwards, Y.I. Makdisi*, A. Zelenski

Physics Department, Brookhaven National Laboratory,
Upton, New York 11973-5000, USA
E.C. Aschenauer, B. Azmoun, M.D. Baker, A. Bazilevsky, J.C. Biggs, S. Boose, H. Buesching, M. Chiu, G. David, E.J. Desmond, A. Dion, M. Faulkner, A. Franz, P. Giannotti, J.S. Haggerty, R. Inguanta, J. Jia, B.M. Johnson, K. Jones, H.-J. Kehayias, E. Kistenev, J. LaBounty, T.K. Langin, M. Lenz, W. Lenz, D. Lynch, S. Marino, J.T. Mitchell, D.P. Morrison, R. Nouicer, E. O'Brien, R. Pak, C. Pinkenburg, R.P. Pisani, S. Polizzo, M.L. Purschke, T. Sakaguchi, A. Sickles, I.V. Sourikova, P. Steinberg, S.P. Stoll, A. Sukhanov, M.J. Tannenbaum*, F. Toldo, J. Tradeski, C. Vale, S.N. White, C.L. Woody

University of California - Riverside,
Riverside, California 92521, USA
K.N. Barish*, M. Beaumier, O. Chvala, K.O. Eyser, L. Garcia, T. Hester, R.S. Hollis, A. Iordanova, D. Kleinjan, M. Mendoza, A. Morreale, S.D. Rolnick, K. Sedgwick, R. Seto, W. Usher

Charles University,
Ovocný trh 5, Praha 1, 116 36, Prague, Czech Republic
M. Finger,Jr., M. Finger*, M. Slunecka, V. Sluneckova

Chonbuk National University,
Jeonju, 561-756, Korea
J.B. Choi, E.J. Kim*, K.-B Kim, S.R. Lee

China Institute of Atomic Energy (CIAE),
Beijing, People's Republic of China
X. Bai, S. Hu, X. Li*, B. Sa, L. Ye, H. Zhang, J. Zhou, S. Zhou

Center for Nuclear Study (CNS), Graduate School of Science, University of Tokyo,
7-3-1 Hongo, Bunkyo, Tokyo 113-0033, Japan
R. Akimoto, Y. Aramaki, T. Gunji, H. Hamagaki*, R. Hayano, S. Hayashi, Y. Komatsu, S. Masumoto, K. Ozawa, A. Nukariya, A. Takahara, Y. Tsuchimoto, T. Tsuji, Y.S. Watanabe, Y.L. Yamaguchi

University of Colorado,
Boulder, Colorado 80309, USA
E. Kinney, M. McCumber, J.L. Nagle*, M.R. Stone, M. Wysocki

Columbia University and Nevis Laboratories,
New York, New York 10027 and Irvington, New York 10533, USA
A. Angerami, C.Y. Chi*, B.A. Cole, T. Engelmore, N. Grau, Y.S. Lai, E. Mannel, D. Perepelitsa, F.W. Sippach, E. Vazquez-Zambrano, A. Veicht, D. Winter, W.A. Zajc, L. Zhang

Czech Technical University,
Zikova 4, 166 36 Prague 6, Czech Republic
T. Liska, M. Tomasek, M. Virius*, V. Vrba

Dapnia, CEA Saclay,
F-91191, Gif-sur-Yvette, France
H. Pereira*

Debrecen University,
H-4010 Debrecen, Egyetem tér 1, Hungary
J. Imrek, P. Tarjan*

ELTE, Eötvös Loránd University,
H–1117 Budapest, Pázmány P. s. 1/A, Hungary
M. Csanad, A. Kiss*, M. Vargyas

Ewha Womans University,
Seoul 120-750, Korea
K.I. Hahn, A. Kim, J. Lee*, I.H. Park, J.S. Yoo

Florida State University,
Tallahassee, Florida 32306, USA
A.D. Frawley*, J.R. Hutchins, J. Klatsky, D. McGlinchey

Georgia State University,
Atlanta, Georgia 30303, USA
C. Butler, L. Byrum, X. He*, M. Javani, M. Sarsour, A. Sen, J. Ying

Hanyang University,
Seoul 133-792, Korea
B.H. Kang, J.S. Kang, Y.K. Kim*, M.S. Ryu

Hiroshima University,
Kagamiyama, Higashi-Hiroshima 739-8526, Japan
K. Homma, K.M. Kijima, Y. Nakamiya, M. Nihashi, M. Ouchida, K. Shigaki,
T. Sugitate*, H. Torii, D. Watanabe

IHEP Protvino, State Research Center of Russian Federation,
Institute for High Energy Physics,
Protvino, 142281, Russia
V. Babintsev, V. Bumazhnov, S. Chernichenko, A. Denisov, A. Durum, I. Shein,
A. Soldatov, N. Tyurin*, A. Yanovich

University of Illinois at Urbana-Champaign,
Urbana, Illinois 61801, USA
J. Blackburn, A. Burnap, I.J. Choi, M. GrossePerdekamp, D.S. Jumper, Y.-J. Kim,
J. Koster, M. Leitgab, C. McKinney, B. Meredith, P. Montunega, D. Northacker,
J.-C. Peng*, J. Strack, A. Vossen, S. Williamson, S. Wolin, R. Yang

Institute of Physics, Academy of Sciences of the Czech Republic,
Na Slovance 2, 182 21 Prague 8, Czech Republic
M. Havranek, M. Marcisovsky, J. Popule, P. Sicho, L. Tomasek, M. Tomasek,
V. Vrba*

Iowa State University,
Ames, Iowa 50011, USA
A. Anderson, A. Bergstrom, J. Bowen, L. Ding, M. Eggleston, A. Goers, V. Hanger,
R. Livings, J.C. Hill*, A. Hulsebus, T. Kempel, J.G. Lajoie, A. Lebedev, M. Lockner,

R. McKay, C.A. Ogilvie, H. Pei, J. Perry, M. Rosati, A. Shaver, A. Timilsina, B. Voss, F. Wei, S. Whitaker, P. Wiecki

Advanced Science Research Center (ASCR), Japan Atomic Energy Agency (JAERI),
2-4 Shirakata Shirane, Tokai-mura, Naka-gun, Ibaraki-ken 319-1195, Japan
K. Imai*, T. Maruyama, S. Sato, H. Sako

Joint Institute for Nuclear Research (JINR),
141980 Dubna, Moscow Region, Russia
S. Afanasiev, S. Bazilev, D. Dryablov, A. Isupov, A. Litvinenko*, A. Malakhov, I. Migulina, V. Peresedov, P. Rukoyatkin, I. Slepnev, V. Slepnev, M. Suleimanov, N. Zamyatin, L. Zolin

Helsinki Institute of Physics and University of Jyväskylä,
P.O.Box 35, FI-40014 Jyväskylä, Finland
A. Kaskela, D.J. Kim, J. Kral, F. Krizek, N. Novitzky, J. Rak*, S. Rasanen, J. Viinikainen

KEK, High Energy Accelerator Research Organization,
Tsukuba, Ibaraki 305-0801, Japan
S. Hirota, H. Iinuma, M. Makek, T. Mibe, K. Mikuni, S. Nagamiya, N. Saito, S. Sawada*

KFKI Research Institute for Particle and Nuclear Physics of the Hungarian Academy of Sciences (MTA KFKI RMKI),
H-1525 Budapest 114, POBox 49, Budapest, Hungary
T. Csorgo*, S. Hegyi, M.I. Nagy, A. Ster, J. Sziklai, R. Vertesi

Korea University,
Seoul, 136-701, Korea
B. Hong*, B.I. Kim, C. Kim, K.B. Lee, K.S. Lee, S.K. Park, K.S. Sim

Russian Research Center "Kurchatov Institute",
Moscow, Russia
S.T. Belyaev, D.S. Blau, S.L. Fokin, M.S. Ippolitov, K.V. Karadjev, A.V. Kazantsev, V.A. Lebedev, V.I. Manko*, N.I. Mishustin, T.V. Moukhanova, S.A. Nikolaev, A.S. Nyanin, D.Yu. Peressounko, I.G. Sibiryak, A.A. Tsvetkov, A.A. Vasiliev, A.A. Vinogradov, I.E. Yushmanov

Kyoto University,
Kyoto 606-8502, Japan
H. Asano, S. Dairaku, K. Karatsu, K.R. Nakamura, T. Murakami*, T. Nagae

Laboratoire Leprince-Ringuet, Ecole Polytechnique, CNRS-IN2P3,
Route de Saclay, F-91128, Palaiseau, France
S. Chollet, A. Debraine, O. Drapier, F. Fleuret*, F. Gastaldi, M. Gonin, R. Granier de Cassagnac, L. Kluberg

Lawrence Livermore National Laboratory,
Livermore, California 94550, USA
I. Garishvili, A. Glenn, L.A. LindenLevy, R.A. Soltz*

Los Alamos National Laboratory,
Los Alamos, New Mexico 87545, USA
C. Aidala, M.L. Brooks, L. Guo, X. Jiang, J. Kapustinsky, G.J. Kunde, D.M. Lee, M.J. Leitch, M.X. Liu*, P.L. McGaughey, C.L. Silva, W.E. Sondheim, H.W. vanHecke, Z. You

LPC, Université Blaise Pascal, CNRS-IN2P3,
Clermont-Fd, 63177 Aubiere Cedex, France
G. Roche*

Department of Physics,
Lund University, Box 118, SE-221 00 Lund, Sweden
P. Christiansen, E. Haslum, A. Oskarsson*, L. Osterman, E. Stenlund

University of Maryland,
College Park, Maryland 20742, USA
L. D,Orazio, A.C. Mignerey*, E. Richardson

Department of Physics, University of Massachusetts,
Amherst, Massachusetts 01003-9337, USA
A. Datta, D. Kawall*, M. Stepanov

Morgan State University,
Baltimore, Maryland 21251, USA
C. McLean, W. Powell*

Institut fur Kernphysik, University of Muenster,
D-48149 Muenster, Germany
C. Baumann, N. Heine, R. Luechtenborg, K. Reygers, W. Verhoeven, J. Wessels*

Muhlenberg College,
Allentown, Pennsylvania 18104-5586, USA
J. Ben-Benjamin, G. Benjamin, D. Broxmeyer, A. Caringi, B. Fadem*, C. Harper, J. Herstoff, J. Ide, M. Jacob, P. Lichtenwalner, S. Motschwiller, T. Sodre

Myongji University,
Yongin, Kyonggido 449-728, Korea
K.S. Joo*, H.J. Moon

Nagasaki Institute of Applied Science,
Nagasaki-shi, Nagasaki 851-0193, Japan
T. Fusayasu*, Y. Tanaka

University of New Mexico,
Albuquerque, New Mexico 87131, USA
A. Barron, B. Bassalleck, S. Butsyk, D.E. Fields*, M. Hoefferkamp, M. Phillips, T.L. Thomas, I. Younus

New Mexico State University,
Las Cruces, New Mexico 88003, USA
H. Al-Bataineh, H. Al-Taani, K.V. Dharmawardane, G.S. Kyle, A. Meles, V. Papavassiliou, S.F. Pate*, E. Tennant, X.R. Wang

Department of Physics and Astronomy, Ohio University,
Athens, OH 45701, USA
X. Bing, J.E. Frantz*, D. Kotchetkov

Oak Ridge National Laboratory,
Oak Ridge, Tennessee 37831, USA
T.C. Awes, M. Bobrek, C.L. Britton,Jr., V. Cianciolo, Y.V. Efremenko, A. Enokizono, K.F. Read, D. Silvermyr, P.W. Stankus*

IPN-Orsay, Universite Paris Sud, CNRS-IN2P3,
BP1, F-91406, Orsay, France
D. Jouan*

Peking University,
Beijing, People's Republic of China
R. Han, Y. Liang, Y. Mao*, Y. Ye

PNPI, Petersburg Nuclear Physics Institute,
Gatchina, Leningrad region, 188300, Russia
V. Baublis, D. Ivanischev, V. Ivanov, A. Khanzadeev, L. Kochenda, B. Komkov, P. Kravtsov, V. Riabov, Y. Riabov, E. Roschin, V. Samsonov*, V. Trofimov, E. Vznuzdaev, M. Zhalov

RIKEN Nishina Center for Accelerator-Based Science,
Wako, Saitama 351-0198, JAPAN
Y. Akiba, K. Aoki, H. Asano, S. Baumgart, S. Dairaku, H. Enyo, Y. Fukao, Y. Goto, K. Hashimoto, T. Ichihara, M. Ishihara, K. Karatsu, K.R. Nakamura, K. Kurita, M. Kurosawa, Y. Mao, Y. Miyachi, S. Miyasaka, T. Murakami, J. Murata, I. Nakagawa, T. Nakamura, K. Nakano, N. Ogawa, J. Onishi, R. Seidl, T.-A. Shibata, K. Shoji, A. Taketani, K. Watanabe, Y. Watanabe*, S. Yokkaichi

RIKEN BNL Research Center,
Brookhaven National Laboratory, Upton, New York 11973-5000, USA
Y. Akiba*, K. Boyle, A. Deshpande, H. Enyo, Y. Goto, T. Ichihara, I. Nakagawa, R. Nouicer, K. Okada, R. Seidl, A. Taketani, K. Tanida, M. Togawa, Y. Watanabe, S. Yokkaichi

Physics Department, Rikkyo University,
3-34-1 Nishi-Ikebukuro, Toshima, Tokyo 171-8501, Japan
K. Hashimoto, K. Kurita*, J. Murata, N. Ogawa, J. Onishi, K. Watanabe

Saint Petersburg State Polytechnic University,
St. Petersburg, Russia
A. Berdnikov, Y. Berdnikov*, D. Kotov

Universidade de São Paulo, Instituto de Física,
Caixa Postal 66318, São Paulo CEP05315-970, Brazil
O. Dietzsch*, M. Donadelli, M. Kuriyama, M.A.L. Leite, R. Menegasso, E.M. Takagui

Department of Physics and Astronomy, Seoul National University,
Seoul, Korea
S. Choi, K. Tanida*

Skobeltsyn Institute of Nuclear Physics, Lomonosov Moscow State University,
Vorob'evy Gory, Moscow 119992, Russia
P.F. Ermolov, M. Merkin*

Chemistry Department, Stony Brook University, SUNY,
Stony Brook, New York 11794-3400, USA
N.N. Ajitanand, J. Alexander, J. Jia, R. Lacey*, A. Mwai, M. Nomura, R. Reynolds, A. Taranenko, R. Wei

Department of Physics and Astronomy, Stony Brook University, SUNY,
Stony Brook, New York 11794-3400, USA
N. Apadula, E.T. Atomssa, B. Bannier, C.-H. Chen, Z. Citron, M. Connors, A. Deshpande, A. Dotsenko, A. Drees, J.M. Durham, C. Faroughy, C. Gal, J. Hanks, T.K. Hemmick*, B.V. Jacak, J. Kamin, S. Kaneti, P. Kline, S.H. Lee, R. Lefferts, B. Lewis, A. Lipski, A. Manion, C. Pancake, R. Petti, B. Sahlmueller, M. Savastio, E. Shafto, J. Sun, S. Taneja

University of Tennessee,
Knoxville, Tennessee 37996, USA
A. Garishvili, C. Nattrass, K.F. Read, S.P. Sorensen*, E. Tennant

Department of Physics, Tokyo Institute of Technology,
Oh-okayama, Meguro, Tokyo 152-8551, Japan
Y. Miyachi, S. Miyasaka, K. Nakano, T.-A. Shibata*

Institute of Physics, University of Tsukuba,
Tsukuba, Ibaraki 305, Japan
T. Chujo, S. Esumi*, R. Funato, E. Hamada, T. Horaguchi, S. Horiuchi, Y. Ikeda, M. Inaba, M. Kajigaya, M. Kimura, Y. Miake, S. Mizuno, D. Sakata, M. Sano, H. Sekine, M. Shimomura, T. Takeuchi, T. Todoroki, K. Watanabe, H. Yokoyama

Vanderbilt University,
Nashville, Tennessee 37235, USA
R. Belmont, S.V. Greene*, S. Huang, M. Issah, B. Love, C.F. Maguire, D. Roach, B. Schaefer, J. Velkovska

Weizmann Institute,
Rehovot 76100, Israel
M. Makek, A. Milov, I. Ravinovich, D. Sharma, I. Tserruya*

Yonsei University, IPAP
Seoul 120-749, Korea
J.H Do, J.H. Kang*, H.J. Kim, Y. Kwon, S.H. Lim, M. Song

*PHENIX Institutional Board member

Spokesperson	Barbara Jacak *Stony Brook University*
Deputy Spokesperson	Jamie Nagle *University of Colorado*
Deputy Spokesperson	Yasuyuki Akiba *RIKEN Nishina Center for Accelerator-Based Science*
Operations Director	Ed O'Brien *Brookhaven National Laboratory*
Deputy Operations Director for Upgrades	Mike Leitch *Los Alamos National Laboratory*
Deputy Operations Director for Operations	John Haggerty *Brookhaven National Laboratory*

Bibliography

[1] CALICE at the ILC [online]. Available from: https://twiki.cern.ch/twiki/bin/view/CALICE/WebHome. 7.2.1

[2] CMOS & ILC [online]. Available from: http://www.iphc.cnrs.fr/-CMOS-ILC-.html. 7.2.1

[3] LHCb RICH [online]. Available from: https://twiki.cern.ch/twiki/bin/view/LHCb/LHCbRICH. 7.2.1

[4] PHENIX Decadal Plan: 2004–2013 [online]. Available from: http://www.phenix.bnl.gov/phenix/WWW/docs/decadal/2003/PHENIXDecadalPlan.pdf. 2.1, 2.2

[5] RHIC Beam Projections [online]. Available from: http://www.rhichome.bnl.gov/RHIC/Runs/RhicProjections.pdf. 6.1.1, B, B.1

[6] RICH 2007 [online]. Available from: http://rich2007.ts.infn.it. 7.2.1

[7] RICH 2010 [online]. Available from: http://rich2010.in2p3.fr. 7.2.1

[8] The PHENIX Bylaws [online]. Available from: http://www.phenix.bnl.gov/WWW/publish/jacak/sp/bylaws/by-laws.htm. D.2

[9] Report to the Nuclear Science Advisory Committee by the Subcommittee on Performance Milestones [online]. 2008. Available from: http://www.er.doe.gov/np/nsac/docs/PerfMeasEvalFinal.pdf. 6.1.1

[10] **COMPASS Collaboration**. COMPASS-II Proposal [online]. 2010. Available from: http://wwwcompass.cern.ch/compass/proposal/compass-II_proposal/compass-II_proposal.pdf. 4.4, 6.1.1

[11] G. Aad *et al*. The ATLAS experiment at CERN. *Journal of Instrumentation*, 3, 2008. doi:10.1088/1748-0221/3/08/S08003. 7.1.3, 7.1.3

[12] **H1 Collaboration**, F. Aaron *et al*. Deeply Virtual Compton Scattering and its Beam Charge Asymmetry in $e^{\pm}p$ Collisions at HERA. *Phys. Lett.*, B681:391–399, 2009. arXiv:0907.5289, doi:10.1016/j.physletb.2009.10.035. 8.4

[13] **H1 Collaboration**, F. Aaron *et al*. Combined measurement and QCD analysis of the inclusive ep scattering cross sections at HERA. *JHEP*, 01:109, 2010. arXiv:0911.0884, doi:10.1007/JHEP01(2010)109. 4, 8.2, 8.3.1

[14] **D0 Collaboration**, V. Abazov *et al*. The Upgraded D0 Detector. *Nucl. Instrum. Meth.*, A565:463–537, 2006. arXiv:physics/0507191, doi:10.1016/j.nima.2006.05.248. 7.1, 7.1.3

[15] **D0 Collaboration**, V. Abazov *et al*. b-Jet Identification in the D0 Experiment. *Nucl. Instrum. Meth.*, A620:490–517, 2010. arXiv:1002.4224, doi:10.1016/j.nima.2010.03.118. 3.2.2

[16] **E143 Collaboration**, K. Abe *et al*. Measurements of the proton and deuteron spin structure function g_2 and asymmetry A_2. *Phys. Rev. Lett.*, 76:587–591, 1996. arXiv:hep-ex/9511013, doi:10.1103/PhysRevLett.76.587. 4.1

[17] **Belle Collaboration**, K. Abe *et al*. Measurement of azimuthal asymmetries in inclusive production of hadron pairs in e^+e^- annihilation at Belle. *Phys. Rev. Lett.*, 96:232002, 2006. arXiv:hep-ex/0507063, doi:10.1103/PhysRevLett.96.232002. 4.2

[18] **STAR Collaboration**, B. Abelev *et al*. Longitudinal double-spin asymmetry and cross section for inclusive jet production in polarized proton collisions at $\sqrt{s} = 200$ GeV. *Phys. Rev. Lett.*, 97:252001, 2006. arXiv:hep-ex/0608030, doi:10.1103/PhysRevLett.97.252001. 4.1, 7.1

[19] **STAR Collaboration**, B. Abelev *et al*. Forward neutral pion transverse single spin asymmetries in p+p collisions at $\sqrt{s} = 200\,\text{GeV}$. *Phys. Rev. Lett.*, 101:222001, 2008. arXiv:0801.2990, doi:10.1103/PhysRevLett.101.222001. 4.2, 6.1.1

[20] **STAR Collaboration**, B. Abelev *et al*. J/ψ production at high transverse momentum in p+p and Cu+Cu collisions at $\sqrt{s_{NN}} = 200\,\text{GeV}$. *Phys. Rev.*, C80:041902, 2009. arXiv:0904.0439, doi:10.1103/PhysRevC.80.041902. 3.4, 3.4

[21] **CDF Collaboration**, D. Acosta *et al*. Υ production and polarization in $p\overline{p}$ collisions at $\sqrt{s} = 1.8\,\text{TeV}$. *Phys. Rev. Lett.*, 88:161802, 2002. doi:10.1103/PhysRevLett.88.161802. 3.4, 7.1.2

[22] **E704 Collaboration**, D. Adams *et al*. Analyzing power in inclusive π^+ and π^- production at high x_F with a 200 GeV polarized proton beam. *Phys. Lett.*, B264:462–466, 1991. doi:10.1016/0370-2693(91)90378-4. 4.2, 6.1.1

[23] **E581 Collaboration**, D. Adams *et al*. Comparison of spin asymmetries and cross-sections in π^0 production by 200 GeV polarized anti-protons and protons. *Phys. Lett.*, B261:201–206, 1991. doi:10.1016/0370-2693(91)91351-U. 4.2, 4.9, 6.1.1

[24] **STAR Collaboration**, J. Adams *et al*. Cross sections and transverse single-spin asymmetries in forward neutral pion production from proton collisions at $\sqrt{s} = 200\,\text{GeV}$. *Phys. Rev. Lett.*, 92:171801, 2004. arXiv:hep-ex/0310058, doi:10.1103/PhysRevLett.92.171801. 4.2, 4.9, 4.11, 6.1.1

[25] **STAR Collaboration**, J. Adams *et al*. Experimental and theoretical challenges in the search for the quark gluon plasma: The STAR collaboration's critical assessment of the evidence from RHIC collisions. *Nucl. Phys.*, A757:102–183, 2005. arXiv:nucl-ex/0501009, doi:10.1016/j.nuclphysa.2005.03.085. 1

[26] **E665 Collaboration**, M. Adams *et al*. Shadowing in inelastic scattering of muons on carbon, calcium and lead at low x_{Bj}. *Z. Phys.*, C67:403–410, 1995. arXiv:hep-ex/9505006, doi:10.1007/BF01624583. 3.6

[27] A. Adare, S. Afanasiev, C. Aidala, N. N. Ajitanand, Y. Akiba, *et al*. Cross Section and Parity Violating Spin Asymmetries of $W^{\pm}$ Boson Production in Polarized p+p Collisions at $\sqrt{s} = 500\,\text{GeV}$. 2010. arXiv:1009.0505. 4.1, 4.7, 4.8, 5.1

[28] A. Adare, S. Afanasiev, C. Aidala, N. N. Ajitanand, Y. Akiba, *et al*. Measurement of transverse single-spin asymmetries for J/ψ production in polarized p+p collisions at $\sqrt{s} = 200\,\text{GeV}$. 2010. arXiv:1009.4864. 4.3, 4.15

[29] **PHENIX Collaboration**, A. Adare *et al*. Measurement of high-p_T single electrons from heavy- flavor decays in p+p collisions at $\sqrt{s} = 200\,\text{GeV}$. *Phys. Rev. Lett.*, 97:252002, 2006. arXiv:hep-ex/0609010, doi:10.1103/PhysRevLett.97.252002. 2.4.1

[30] **PHENIX Collaboration**, A. Adare *et al*. Energy loss and flow of heavy quarks in Au+Au collisions at $\sqrt{s_{NN}} = 200\,\text{GeV}$. *Phys. Rev. Lett.*, 98:172301, 2007. arXiv:nucl-ex/0611018, doi:10.1103/PhysRevLett.98.172301. 1.1, 2.2

[31] **PHENIX Collaboration**, A. Adare *et al*. J/Ψ production versus transverse momentum and rapidity in $p + p$ collisions at $\sqrt{s}$ = 200 GeV. *Phys. Rev. Lett.*, 98:232002, 2007. arXiv:hep-ex/0611020, doi:10.1103/PhysRevLett.98.232002. 3.4

[32] **PHENIX Collaboration**, A. Adare *et al*. J/ψ production vs centrality, transverse momentum, and rapidity in Au+Au collisions at $\sqrt{s_{NN}} = 200\,\text{GeV}$. *Phys. Rev. Lett.*, 98:232301, 2007. arXiv:nucl-ex/0611020, doi:10.1103/PhysRevLett.98.232301. 1.2, 3.4

[33] **PHENIX Collaboration**, A. Adare *et al*. Scaling properties of azimuthal anisotropy in Au+Au and Cu+Cu collisions at $\sqrt{s_{NN}} = 200\,\text{GeV}$. *Phys. Rev. Lett.*, 98:162301, 2007. arXiv:nucl-ex/0608033, doi:10.1103/PhysRevLett.98.162301. 1.6

[34] **PHENIX Collaboration**, A. Adare *et al*. Cold Nuclear Matter Effects on J/ψ as Constrained by Deuteron-Gold Measurements at $\sqrt{s_{NN}} = 200\,\text{GeV}$. *Phys. Rev.*, C77:024912, 2008. arXiv:0711.3917, doi:10.1103/PhysRevC.77.024912. 1.3, 3.4

[35] **PHENIX Collaboration**, A. Adare *et al*. J/ψ Production in $\sqrt{s_{NN}} = 200\,\mathrm{GeV}$ Cu+Cu Collisions. *Phys. Rev. Lett.*, 101:122301, 2008. arXiv:0801.0220, doi:10.1103/PhysRevLett.101.122301. 1.2, 3.4

[36] **PHENIX Collaboration**, A. Adare *et al*. Quantitative Constraints on the Opacity of Hot Partonic Matter from Semi-Inclusive Single High Transverse Momentum Pion Suppression in Au+Au collisions at $\sqrt{s_{NN}} = 200\,\mathrm{GeV}$. *Phys. Rev.*, C77:064907, 2008. arXiv:0801.1665, doi:10.1103/PhysRevC.77.064907. 3.1

[37] **PHENIX Collaboration**, A. Adare *et al*. Inclusive cross section and double helicity asymmetry for π^0 production in p+p collisions at $\sqrt{s} = 62.4\,\mathrm{GeV}$. *Phys. Rev.*, D79:012003, 2009. arXiv:0810.0701, doi:10.1103/PhysRevD.79.012003. 4.1

[38] **PHENIX Collaboration**, A. Adare *et al*. Measurement of bottom versus charm as a function of transverse momentum with electron-hadron correlations in p+p collisions at $\sqrt{s} = 200\,\mathrm{GeV}$. *Phys. Rev. Lett.*, 103:082002, 2009. arXiv:0903.4851, doi:10.1103/PhysRevLett.103.082002. 2.2

[39] **PHENIX Collaboration**, A. Adare *et al*. Measurement of bottom versus charm as a function of transverse momentum with electron-hadron correlations in p+p collisions at $\sqrt{s} = 200\,\mathrm{GeV}$. *Phys. Rev. Lett.*, 103:082002, 2009. arXiv:0903.4851, doi:10.1103/PhysRevLett.103.082002. 3.2

[40] **PHENIX Collaboration**, A. Adare *et al*. The polarized gluon contribution to the proton spin from the double helicity asymmetry in inclusive π^0 production in polarized p+p collisions at $\sqrt{s} = 200$ GeV. *Phys. Rev. Lett.*, 103:012003, 2009. arXiv:0810.0694, doi:10.1103/PhysRevLett.103.012003. 4.1, 5.2

[41] **PHENIX Collaboration**, A. Adare *et al*. Detailed measurement of the e^+e^- pair continuum in p+p and Au+Au collisions at $\sqrt{s_{NN}} = 200\,\mathrm{GeV}$ and implications for direct photon production. *Phys. Rev.*, C81:034911, 2010. arXiv:0912.0244, doi:10.1103/PhysRevC.81.034911. 1.1, 1.2, 1.7

[42] **PHENIX Collaboration**, A. Adare *et al*. Elliptic and hexadecapole flow of charged hadrons in Au+Au collisions at $\sqrt{s_{NN}} = 200\,\mathrm{GeV}$. *Phys. Rev. Lett.*, 105:062301, 2010. arXiv:1003.5586, doi:10.1103/PhysRevLett.105.062301. 1.1

[43] **PHENIX Collaboration**, A. Adare *et al*. Enhanced production of direct photons in Au+Au collisions at $\sqrt{s_{NN}} = 200\,\mathrm{GeV}$ and implications for the initial temperature. *Phys. Rev. Lett.*, 104:132301, 2010. arXiv:0804.4168, doi:10.1103/PhysRevLett.104.132301. 1.1, 3.5

[44] **PHENIX Collaboration**, A. Adare *et al*. Heavy quark production in p+p and energy loss and flow of heavy quarks in Au+Au collisions at $\sqrt{s_{NN}} = 200\,\mathrm{GeV}$. 2010. arXiv:1005.1627. 2.2

[45] **PHENIX Collaboration**, A. Adare *et al*. High p_T direct photon and π^0 triggered azimuthal jet correlations in $\sqrt{s} = 200\,\text{GeV}$ p+p collisions. 2010. arXiv:arXiv:1006.1347. 6.2

[46] **PHENIX Collaboration**, A. Adare *et al*. Trends in yield and azimuthal shape modification in dihadron correlations in relativistic heavy ion collisions. *Phys. Rev. Lett.*, 104:252301, 2010. arXiv:1002.1077, doi:10.1103/PhysRevLett.104.252301. 1.2, 1.2, 1.11

[47] **PHENIX Collaboration**, K. Adcox *et al*. Suppression of hadrons with large transverse momentum in central Au+Au collisions at $\sqrt{s_{NN}} = 130\,\text{GeV}$. *Phys. Rev. Lett.*, 88:022301, 2002. arXiv:nucl-ex/0109003, doi:10.1103/PhysRevLett.88.022301. 3.1

[48] **PHENIX Collaboration**, K. Adcox *et al*. Formation of dense partonic matter in relativistic nucleus nucleus collisions at RHIC: Experimental evaluation by the PHENIX collaboration. *Nucl. Phys.*, A757:184–283, 2005. arXiv:nucl-ex/0410003, doi:10.1016/j.nuclphysa.2005.03.086. 1

[49] **SMC Collaboration**, B. Adeva *et al*. Erratum: Spin asymmetries A_1 of the proton and the deuteron in the low x and low Q^2 region from polarized high energy muon scattering. *Phys. Rev.*, D62:079902, 2000. doi:10.1103/PhysRevD.62.079902. 4.1

[50] A. Adil and M. Gyulassy. 3-D jet tomography: A probe of the hydrodynamic initial state in heavy ion collisions. *Nucl. Phys.*, A783:523–526, 2007. doi:10.1016/j.nuclphysa.2006.11.108. 3.5, 3.33

[51] A. Adil, M. Gyulassy, and T. Hirano. 3D jet tomography and the twisted color glass condensate. *Nucl. Phys.*, A774:593–596, 2006. doi:10.1016/j.nuclphysa.2006.06.094. 3.5, 3.33

[52] A. Adil and I. Vitev. Collisional dissociation of heavy mesons in dense QCD matter. *Physics Letters B*, 649(2-3):139–146, 2007. doi:10.1016/j.physletb.2007.03.050. 2.2

[53] **PHENIX Collaboration**, S. Adler *et al*. Measurement of transverse single-spin asymmetries for mid-rapidity production of neutral pions and charged hadrons in polarized p+p collisions at $\sqrt{s} = 200\,\text{GeV}$. *Phys. Rev. Lett.*, 95:202001, 2005. arXiv:hep-ex/0507073, doi:10.1103/PhysRevLett.95.202001. 4.3

[54] **PHENIX Collaboration**, S. Adler *et al*. Systematic studies of the centrality and $\sqrt{s_{NN}}$ dependence of $dE_T/d\eta$ and $dN_{ch}/d\eta$ in heavy ion collisions at mid-rapidity. *Phys. Rev.*, C71:034908, 2005. arXiv:nucl-ex/0409015, doi:10.1103/PhysRevC.71.034908. 1.1

[55] **PHENIX Collaboration**, S. Adler *et al*. Evidence for a long-range component in the pion emission source in Au+Au collisions at $\sqrt{s_{NN}} = 200\,\text{GeV}$. *Phys. Rev. Lett.*,

98:132301, 2007. arXiv:nucl-ex/0605032, doi:10.1103/PhysRevLett.98.132301. 2.3

[56] **PHENIX Collaboration**, S. Adler *et al*. Measurement of single muons at forward rapidity in p+p collisions at $\sqrt{s} = 200\,\text{GeV}$ and implications for charm production. *Phys. Rev.*, D76:092002, 2007. arXiv:hep-ex/0609032, doi:10.1103/PhysRevD.76.092002. 2.4.1

[57] **PHENIX Collaboration**, S. Afanasiev *et al*. Enhancement of the dielectron continuum in $\sqrt{s_{NN}} = 200\,\text{GeV}$ Au+Au collisions, 2007. arXiv:0706.3034. 2.1

[58] **CERES Collaboration**, G. Agakichiev *et al*. e^+e^--pair production in Pb-Au collisions at 158 GeV per nucleon. *Eur. Phys. J.*, C41:475–513, 2005. arXiv:nucl-ex/0506002, doi:10.1140/epjc/s2005-02272-3. 2.1

[59] **COMPASS Collaboration**, E. Ageev *et al*. A new measurement of the Collins and Sivers asymmetries on a transversely polarised deuteron target. *Nucl. Phys.*, B765:31–70, 2007. arXiv:hep-ex/0610068, doi:10.1016/j.nuclphysb.2006.10.027. 4.2, 6.1.1

[60] **EIC Collaboration**, C. Aidala *et al*. Physics Opportunities with e+A Collisions at an Electron Ion Collider [online]. White Paper Prepared for the 2007 NSAC LRP. Available from: http://www.eic.bnl.gov/docs/PositionPaper_eA.pdf. 8.3

[61] **HERMES Collaboration**, A. Airapetian *et al*. Observation of a single-spin azimuthal asymmetry in semi-inclusive pion electro-production. *Phys. Rev. Lett.*, 84:4047–4051, 2000. arXiv:hep-ex/9910062, doi:10.1103/PhysRevLett.84.4047. 6.1.1

[62] **HERMES Collaboration**, A. Airapetian *et al*. Single-spin azimuthal asymmetries in electroproduction of neutral pions in semi-inclusive deep-inelastic scattering. *Phys. Rev.*, D64:097101, 2001. arXiv:hep-ex/0104005, doi:10.1103/PhysRevD.64.097101. 6.1.1

[63] **HERMES Collaboration**, A. Airapetian *et al*. Measurement of single-spin azimuthal asymmetries in semi-inclusive electroproduction of pions and kaons on a longitudinally polarised deuterium target. *Phys. Lett.*, B562:182–192, 2003. arXiv:hep-ex/0212039, doi:10.1016/S0370-2693(03)00566-5. 6.1.1

[64] **HERMES Collaboration**, A. Airapetian *et al*. Quark fragmentation to $\pi^{\pm}$, π^0, $K^{\pm}$, p and $\overline{p}$ in the nuclear environment. *Phys. Lett.*, B577:37–46, 2003. arXiv:hep-ex/0307023, doi:10.1016/j.physletb.2003.10.026. 1.3

[65] **HERMES Collaboration**, A. Airapetian *et al*. Quark helicity distributions in the nucleon for up, down, and strange quarks from semi-inclusive deep-inelastic scattering. *Phys. Rev.*, D71:012003, 2005. arXiv:hep-ex/0407032, doi:10.1103/PhysRevD.71.012003. 4.1

[66] **HERMES Collaboration**, A. Airapetian *et al*. Single-spin asymmetries in semi-inclusive deep-inelastic scattering on a transversely polarized hydrogen target. *Phys. Rev. Lett.*, 94:012002, 2005. arXiv:hep-ex/0408013, doi:10.1103/PhysRevLett.94.012002. 4.2, 6.1.1

[67] **HERMES Collaboration**, A. Airapetian *et al*. Subleading-twist effects in single-spin asymmetries in semi-inclusive deep-inelastic scattering on a longitudinally polarized hydrogen target. *Phys. Lett.*, B622:14–22, 2005. arXiv:hep-ex/0505042, doi:10.1016/j.physletb.2005.06.067. 6.1.1

[68] **HERMES Collaboration**, A. Airapetian *et al*. Precise determination of the spin structure function g_1 of the proton, deuteron and neutron. *Phys. Rev.*, D75:012007, 2007. arXiv:hep-ex/0609039, doi:10.1103/PhysRevD.75.012007. 4.1, 8.4

[69] **HERMES Collaboration**, A. Airapetian *et al*. Evidence for a Transverse Single-Spin Asymmetry in Leptoproduction of $\pi^+\pi^-$ Pairs. *JHEP*, 06:017, 2008. arXiv:0803.2367, doi:10.1088/1126-6708/2008/06/017. 4.2, 5.3

[70] **HERMES Collaboration**, A. Airapetian *et al*. Observation of the naive-T-odd Sivers effect in deep-inelastic scattering. *Phys. Rev. Lett.*, 103:152002, 2009. arXiv:0906.3918, doi:10.1103/PhysRevLett.103.152002. 4.2, 6.1.1

[71] **HERMES Collaboration**, A. Airapetian *et al*. Separation of contributions from deeply virtual Compton scattering and its interference with the Bethe-Heitler process in measurements on a hydrogen target. *JHEP*, 11:083, 2009. arXiv:0909.3587, doi:10.1088/1126-6708/2009/11/083. 8.4

[72] **HERMES Collaboration**, A. Airapetian *et al*. Nuclear-mass dependence of azimuthal beam-helicity and beam-charge asymmetries in deeply virtual Compton scattering. *Phys. Rev.*, C81:035202, 2010. arXiv:0911.0091, doi:10.1103/PhysRevC.81.035202. 8.4

[73] **HERMES Collaboration**, A. Airapetian *et al*. Transverse momentum broadening of hadrons produced in semi-inclusive deep-inelastic scattering on nuclei. *Phys. Lett.*, B684:114–118, 2010. arXiv:0906.2478, doi:10.1016/j.physletb.2010.01.020. 1.3

[74] J. Albacete and C. Marquet. Single Inclusive Hadron Production at RHIC and the LHC from the Color Glass Condensate. *Phys. Lett.*, B687:174–179, 2010. arXiv:1001.1378, doi:10.1016/j.physletb.2010.02.073. 3.3, 3.23

[75] D. Alde *et al*. Nuclear dependence of dimuon production at 800 GeV. FNAL- 772 experiment. *Phys. Rev. Lett.*, 64:2479–2482, 1990. doi:10.1103/PhysRevLett.64.2479. 1.3, 3.6

[76] D. Alde *et al*. Nuclear dependence of the production of Υ resonances at 800 GeV. *Phys. Rev. Lett.*, 66:2285–2288, 1991. doi:10.1103/PhysRevLett.66.2285. 3.35

[77] **COMPASS Collaboration**, M. Alekseev *et al*. Collins and Sivers asymmetries for pions and kaons in muon-deuteron DIS. *Phys. Lett.*, B673:127–135, 2009. arXiv:0802.2160, doi:10.1016/j.physletb.2009.01.060. 4.2, 6.1.1

[78] **COMPASS Collaboration**, M. Alekseev *et al*. Measurement of the Collins and Sivers asymmetries on transversely polarised protons. *Phys. Lett.*, B692:240–246, 2010. arXiv:1005.5609, doi:10.1016/j.physletb.2010.08.001. 4.2

[79] **COMPASS Collaboration**, M. Alekseev *et al*. The spin-dependent structure function of the proton g_1^p and a test of the Bjorken sum rule. *Phys. Lett.*, B690:466–472, 2010. arXiv:1001.4654, doi:10.1016/j.physletb.2010.05.069. 4.1, 8.4

[80] **COMPASS Collaboration**, M.G. Alekseev. Quark helicity distributions from longitudinal spin asymmetries in muon-proton and muon-deuteron scattering, 2010. arXiv:1007.4061, doi:10.1016/j.physletb.2010.08.034. 4.1

[81] **NA50 Collaboration**, B. Alessandro *et al*. A new measurement of J/ψ suppression in Pb-Pb collisions at 158 GeV per nucleon. *Eur. Phys. J.*, C39:335–345, 2005. arXiv:hep-ex/0412036, doi:10.1140/epjc/s2004-02107-9. 3.4

[82] **COMPASS Collaboration**, V. Yu. Alexakhin *et al*. First measurement of the transverse spin asymmetries of the deuteron in semi-inclusive deep inelastic scattering. *Phys. Rev. Lett.*, 94:202002, 2005. arXiv:hep-ex/0503002, doi:10.1103/PhysRevLett.94.202002. 4.2, 6.1.1

[83] M. Alfonsi *et al*. Fast triggering of high-rate charged particles with a triple-GEM detector. *Nucl. Instrum. Meth.*, A535:319–323, 2004. doi:10.1016/j.nima.2004.07.139. 7.1.3

[84] C. Allgower *et al*. Measurement of analyzing powers of π^+ and π^- produced on a hydrogen and a carbon target with a 22 GeV/c incident polarized proton beam. *Phys. Rev.*, D65:092008, 2002. doi:10.1103/PhysRevD.65.092008. 4.2, 6.1.1

[85] G. Altarelli, R. Ellis, M. Greco, and G. Martinelli. Vector Boson Production at Colliders: A Theoretical Reappraisal. *Nucl. Phys.*, B246:12, 1984. doi:10.1016/0550-3213(84)90112-3. 6.1.1

[86] M. Altunbas *et al*. Construction, test and commissioning of the triple-GEM tracking detector for COMPASS. *Nucl. Instrum. Meth.*, A490:177–203, 2002. doi:10.1016/S0168-9002(02)00910-5. 7.1.3

[87] B. Alver and G. Roland. Collision geometry fluctuations and triangular flow in heavy-ion collisions. *Phys. Rev.*, C81:054905, 2010. arXiv:1003.0194, doi:10.1103/PhysRevC.81.054905. 1.2

[88] **Particle Data Group Collaboration**, C. Amsler *et al*. Review of particle physics. *Phys. Lett.*, B667:1, 2008. doi:10.1016/j.physletb.2008.07.018. 1.12, 3.18

[89] M. Anselmino, M. Boglione, U. D'Alesio, E. Leader, S. Melis, *et al*. Sivers and Collins effects in polarized pp scattering processes. 2008. arXiv:0809.3743. 6.1.1

[90] M. Anselmino, M. Boglione, U. D'Alesio, E. Leader, and F. Murgia. Accessing Sivers gluon distribution via transverse single spin asymmetries in $p\uparrow\ p \to DX$ processes at RHIC. *Phys. Rev.*, D70:074025, 2004. arXiv:hep-ph/0407100, doi:10.1103/PhysRevD.70.074025. 5.3

[91] M. Anselmino, U. D'Alesio, S. Melis, and F. Murgia. Constraints on the gluon Sivers distribution via transverse single spin asymmetries at mid-rapidity in $p\uparrow\ p \to \pi^0 X$ processes at RHIC. *Phys. Rev.*, D74:094011, 2006. doi:10.1103/PhysRevD.74.094011. 4.3

[92] M. Anselmino *et al*. Extracting the Sivers function from polarized SIDIS data and making predictions. *Phys. Rev.*, D72:094007, 2005. arXiv:hep-ph/0507181, doi:10.1103/PhysRevD.72.094007. 4.14

[93] M. Anselmino *et al*. Transversity and Collins functions from SIDIS and e^+e^- data. *Phys. Rev.*, D75:054032, 2007. arXiv:hep-ph/0701006, doi:10.1103/PhysRevD.75.054032. 4.2, 4.12, 4.13, 6.1.1

[94] M. Anselmino *et al*. Sivers effect for pion and kaon production in semi-inclusive deep inelastic scattering. *Eur. Phys. J.*, A39:89–100, 2009. arXiv:0805.2677, doi:10.1140/epja/i2008-10697-y. 4.3, 4.14, 6.1.1

[95] M. Anselmino *et al*. Sivers effect in Drell-Yan processes. *Phys. Rev.*, D79:054010, 2009. arXiv:0901.3078, doi:10.1103/PhysRevD.79.054010. 6.1.1

[96] **E155 Collaboration**, P.L. Anthony *et al*. Precision measurement of the proton and deuteron spin structure functions g_2 and asymmetries A_2. *Phys. Lett.*, B553:18–24, 2003. arXiv:hep-ex/0204028, doi:10.1016/S0370-2693(02)03015-0. 4.1

[97] J. Antille *et al*. Spin dependence of the inclusive reaction $p + p(\text{polarized}) \to \pi^0 + X$ at 24 GeV/c for high-p_T π^0 produced in the central region. *Phys. Lett.*, B94:523, 1980. doi:10.1016/0370-2693(80)90933-8. 4.2

[98] N. Armesto, N. Borghini, S. Jeon, U. Wiedemann, S. Abreu, *et al.*, editors. *Heavy Ion Collisions at the LHC—Last Call for Predictions*, volume G35, 2008. arXiv:0711.0974, doi:10.1088/0954-3899/35/5/054001. 3.3, 7.1

[99] N. Armesto, L. Cunqueiro, and C. Salgado. Q-PYTHIA: A Medium-modified implementation of final state radiation. *Eur. Phys. J.*, C63:679–690, 2009. arXiv:0907.1014, doi:10.1140/epjc/s10052-009-1133-9. 3.1.2

[100] T. Armstrong *et al*. The E864 lead-scintillating fiber hadronic calorimeter. *Nucl. Instrum. Meth.*, A406:227–258, 1998. doi:10.1016/S0168-9002(98)91984-2. 7.1.3

[101] R. Arnaldi. J/ψ suppression and polarization results at SPS [online]. 2009. Talk at "Heavy Quarkonia Production in Heavy-Ion Collisions", ECT*, Trento, Italy. Available from: http://www.ect.it/Meetings/ConfsWksAndCollMeetings/ConfWksDocument/2009/Talks/WORKSHOP_25May09/arnaldi.ppt. 3.4

[102] **NA60 Collaboration**, R. Arnaldi *et al*. First measurement of the rho spectral function in high- energy nuclear collisions. *Phys. Rev. Lett.*, 96:162302, 2006. arXiv:nucl-ex/0605007, doi:10.1103/PhysRevLett.96.162302. 2.1

[103] **NA60 Collaboration**, R. Arnaldi *et al*. J/ψ production in proton-nucleus collisions at 158 and 400 GeV. 2010. arXiv:1004.5523. 3.4

[104] M. Arneodo and M. Diehl. Diffraction for non-believers. 2005. arXiv:hep-ph/0511047. 8.2

[105] **BRAHMS Collaboration**, I. Arsene *et al*. Quark Gluon Plasma an Color Glass Condensate at RHIC? The perspective from the BRAHMS experiment. *Nucl. Phys.*, A757:1–27, 2005. arXiv:nucl-ex/0410020, doi:10.1016/j.nuclphysa.2005.02.130. 1

[106] **BRAHMS Collaboration**, I. Arsene *et al*. Single Transverse Spin Asymmetries of Identified Charged Hadrons in Polarized p+p Collisions at $\sqrt{s} = 62.4$ GeV. *Phys. Rev. Lett.*, 101:042001, 2008. arXiv:0801.1078, doi:10.1103/PhysRevLett.101.042001. 4.2, 4.9, 6.1.1

[107] M. Asakawa, S. Bass, and B. Muller. Anomalous transport processes in turbulent non-Abelian plasmas. 2010. arXiv:1008.3496. 3.5

[108] **European Muon Collaboration**, J. Ashman *et al*. An investigation of the spin structure of the proton in deep inelastic scattering of polarized muons on polarized protons. *Nucl. Phys.*, B328:1, 1989. doi:10.1016/0550-3213(89)90089-8. 5.2

[109] **European Muon Collaboration**, J. Ashman *et al*. An investigation of the spin structure of the proton in deep inelastic scattering of polarised muons on polarised protons. *Nucl. Phys.*, B328(1):1–35, 1989. Available from: http://www.sciencedirect.com/science/article/B6TVC-4718HPM-1D/2/90f2211007806eff5140860403780944, doi:10.1016/0550-3213(89)90089-8. 4.1

[110] ATLAS. Heavy Ion Physics with the ATLAS Detector, LoI. *CERN/LHCC*, 2004-009, 2004. Available from: http://cdsweb.cern.ch/record/721909. 7.1

[111] **E598 Collaboration**, J. Aubert *et al*. Experimental observation of a heavy particle J. *Phys. Rev. Lett.*, 33:1404–1406, 1974. doi:10.1103/PhysRevLett.33.1404. 1.1

[112] **SLAC-SP-017 Collaboration**, J. Augustin *et al*. Discovery of a Narrow Resonance in e^+e^- Annihilation. *Phys. Rev. Lett.*, 33:1406–1408, 1974. doi:10.1103/PhysRevLett.33.1406. 1.1

[113] H. Avakian, S. Brodsky, A. Deur, and F. Yuan. Effect of orbital angular momentum on valence-quark helicity distributions. *Phys. Rev. Lett.*, 99:082001, 2007. arXiv:0705.1553, doi:10.1103/PhysRevLett.99.082001. 5.1

[114] T.C. Awes, A. Bazilevsky, S. Bathe, D. Bucher, H. Buesching, *et al*. High-energy beam test of the PHENIX lead scintillator EM calorimeter. *Nucl. Instrum. Meth. A*, 2002. arXiv:nucl-ex/0202009. 7.2.1

[115] A. Bacchetta, C. Bomhof, U. D'Alesio, P. Mulders, and F. Murgia. The Sivers single-spin asymmetry in photon-jet production. *Phys. Rev. Lett.*, 99:212002, 2007. arXiv:hep-ph/0703153, doi:10.1103/PhysRevLett.99.212002. 6.9

[116] **PHOBOS Collaboration**, B. Back *et al*. The PHOBOS perspective on discoveries at RHIC. *Nucl. Phys.*, A757:28–101, 2005. arXiv:nucl-ex/0410022, doi:10.1016/j.nuclphysa.2005.03.084. 1

[117] R. Baier. Probing the sQGP in A-A collisions by measuring energetic low-mass dileptons [online]. 2009. Talk at: "From Particles and Partons to Nuclei and Fields", October 23-25, Columbia University, New York, NY. Available from: http://indico.cern.ch/contributionDisplay.py?contribId=24&confId=72423. 3.5

[118] R. Baier and Y. Mehtar-Tani. Jet quenching and broadening: The Transport coefficient $\hat{q}$ in an anisotropic plasma. *Phys. Rev.*, C78:064906, 2008. arXiv:0806.0954, doi:10.1103/PhysRevC.78.064906. 3.5

[119] S. Bass *et al*. Systematic Comparison of Jet Energy-Loss Schemes in a realistic hydrodynamic medium. *Phys. Rev.*, C79:024901, 2009. arXiv:0808.0908, doi:10.1103/PhysRevC.79.024901. 3.1

[120] S. Bass, B. Muller, and D. Srivastava. Intensity interferometry of direct photons emitted in Au+Au collisions. *Phys. Rev. Lett.*, 93:162301, 2004. arXiv:nucl-th/0404050, doi:10.1103/PhysRevLett.93.162301. 3.5

[121] G. Baum *et al*. A new measurement of deep inelastic *ep* asymmetries. *Phys. Rev. Lett.*, 51:1135, 1983. doi:10.1103/PhysRevLett.51.1135. 5.2

[122] A. Bazavov, T. Bhattacharya, M. Cheng, N.H. Christ, C. DeTar, *et al*. Equation of state and QCD transition at finite temperature. *Phys. Rev.*, D80:014504, 2009. arXiv:0903.4379, doi:10.1103/PhysRevD.80.014504. 3.20

[123] E. Berger and F. Coester. Nuclear effects in deep inelastic lepton scattering. *Ann. Rev. Nucl. Part. Sci.*, 37(1):463–491, 1987. doi:10.1146/annurev.ns.37.120187.002335. 1.3

[124] M. Betemps and M. Gay Ducati. Dilepton low p_T suppression as an evidence of the color glass condensate. *Phys. Rev.*, D70:116005, 2004. arXiv:hep-ph/0408097, doi:10.1103/PhysRevD.70.116005. 3.6

[125] A. Bhatti and D. Lincoln. Jet Physics at the Tevatron. 2010. arXiv:1002.1708. 3.1.2

[126] J. D. Bjorken. Asymptotic Sum Rules at Infinite Momentum. *Phys. Rev.*, 179:1547–1553, 1969. doi:10.1103/PhysRev.179.1547. 8.4

[127] L. Bland. Transverse spin and RHIC. pages 77–87, 2006. arXiv:hep-ex/0602012. 4.2, 4.11

[128] L. Bland *et al*. Transverse-spin Drell-Yan physics at RHIC [online]. Available from: http://spin.riken.bnl.gov/rsc/write-up/dy-final.pdf. 6.1.1

[129] L. Bland *et al*. Future of low-x forward physics at RHIC. *Eur. Phys. J.*, C43:427–435, 2005. arXiv:hep-ex/0502040, doi:10.1140/epjc/s2005-02334-6. 2.4.2

[130] G. Blanpied *et al*. Elastic scattering of 0.8 GeV protons from ^{12}C, ^{58}Ni, and ^{208}Pb. *Phys. Rev. Lett.*, 39:1447–1450, 1977. doi:10.1103/PhysRevLett.39.1447. 8.3.3

[131] J. Blümlein and H. Böttcher. QCD analysis of polarized deep inelastic scattering data. *Nucl. Phys.*, B841:205–230, 2010. arXiv:1005.3113, doi:10.1016/j.nuclphysb.2010.08.005. 4.1, 8.4

[132] M. Boglione, U. D'Alesio, and F. Murgia. Single spin asymmetries in inclusive hadron production from SIDIS to hadronic collisions: universality and phenomenology. *Phys. Rev.*, D77:051502, 2008. arXiv:0712.4240, doi:10.1103/PhysRevD.77.051502. 6.1.1

[133] B. Bonner *et al*. Analyzing Power Measurement in Inclusive π^0 Production at High x_F. *Phys. Rev. Lett.*, 61:1918, 1988. doi:10.1103/PhysRevLett.61.1918. 6.1.1

[134] B. Bonner *et al*. Analyzing power of inclusive production of π^+, π^-, and K_s^0 by polarized protons at 13.3 GeV/c and 18.5 GeV/c. *Phys. Rev.*, D41:13–16, 1990. doi:10.1103/PhysRevD.41.13. 6.1.1

[135] N. Borghini and F. Gelis. Distribution of multiple scatterings in proton-nucleus collisions at high energy. *Phys. Rev.*, D74:054025, 2006. arXiv:hep-ph/0607098, doi:10.1103/PhysRevD.74.054025. 2.4.2

[136] **LHPC Collaboration**, J. Bratt *et al*. Nucleon structure from mixed action calculations using 2+1 flavors of asqtad sea and domain wall valence fermions. 2010. arXiv:1001.3620. 4.3

[137] **E704 Collaboration**, A. Bravar *et al*. Single-spin asymmetries in inclusive charged pion production by transversely polarized antiprotons. *Phys. Rev. Lett.*, 77:2626–2629, 1996. doi:10.1103/PhysRevLett.77.2626. 6.1.1

[138] S. Brodsky, P. Hoyer, C. Peterson, and N. Sakai. The Intrinsic Charm of the Proton. *Phys. Lett.*, B93:451–455, 1980. doi:10.1016/0370-2693(80)90364-0. 8.3.1

[139] S. Brodsky, D. Hwang, and I. Schmidt. Final-state interactions and single-spin asymmetries in semi-inclusive deep inelastic scattering. *Phys. Lett.*, B530:99–107, 2002. arXiv:hep-ph/0201296, doi:10.1016/S0370-2693(02)01320-5. 6.1.1

[140] S. Brodsky and J. Lansberg. Heavy-Quarkonium Production in High Energy Proton-Proton Collisions at RHIC. *Phys. Rev.*, D81:051502, 2010. arXiv:0908.0754, doi:10.1103/PhysRevD.81.051502. 3.6, 3.37

[141] W. Brooks. Physics with nuclei at an Electron Ion Collider. 2010. arXiv:1008.0131. 1.3

[142] W. Brooks and H. Hakobyan. Experimental studies of hadronization and parton propagation in the space-time domain. *Nucl. Phys.*, A830:361c–368c, 2009. arXiv:0907.4606, doi:10.1016/j.nuclphysa.2009.10.031. 1.3

[143] M. Burkardt. Impact parameter dependent parton distributions and transverse single spin asymmetries. *Phys. Rev.*, D66:114005, 2002. arXiv:hep-ph/0209179, doi:10.1103/PhysRevD.66.114005. 4.3

[144] M. Burkardt. Chromodynamic lensing and transverse single spin asymmetries. *Nucl. Phys.*, A735:185–199, 2004. arXiv:hep-ph/0302144, doi:10.1016/j.nuclphysa.2004.02.008. 6.1.1

[145] M. Burkardt and B. Hikmat. Angular momentum decomposition for an electron. *Phys. Rev.*, D79:071501, 2009. arXiv:0812.1605, doi:10.1103/PhysRevD.79.071501. 4.1

[146] M. Cacciari. private communication. 3.16, 3.2.2

[147] A. Caldwell and H. Kowalski. Investigating the gluonic structure of nuclei via j/ψ scattering. *Phys. Rev.*, C81:025203, 2010. doi:10.1103/PhysRevC.81.025203. 8.3.3

[148] C. Callan, Jr. and D. Gross. High-energy electroproduction and the constitution of the electric current. *Phys. Rev. Lett.*, 22:156–159, 1969. doi:10.1103/PhysRevLett.22.156. 8.3.1

[149] F. Caola and S. Forte. Geometric scaling from DGLAP evolution. *Phys. Rev. Lett.*, 101:022001, 2008. arXiv:0802.1878, doi:10.1103/PhysRevLett.101.022001. 8.3.2

[150] F. Caola, S. Forte, and J. Rojo. Deviations from NLO QCD evolution in inclusive HERA data. *Phys. Lett.*, B686:127–135, 2010. arXiv:0910.3143, doi:10.1016/j.physletb.2010.02.043. 8.3.2

[151] F. Caola, S. Forte, and J. Rojo. HERA data and DGLAP evolution: Theory and phenomenology. *Nucl. Phys. A*, 2010. arXiv:1007.5405. 8.3.2

[152] F. Ceccopieri, M. Radici, and A. Bacchetta. Evolution equations for extended dihadron fragmentation functions. *Phys. Lett.*, B650:81–89, 2007. arXiv:hep-ph/0703265, doi:10.1016/j.physletb.2007.04.065. 5.3

[153] S. Chatrchyan *et al*. The CMS experiment at CERN. *Journal of Instrumentation*, 3, 2008. doi:10.1088/1748-0221/3/08/S08004. 7.1.3

[154] **ZEUS Collaboration**, S. Chekanov *et al*. A measurement of the Q^2, W and t dependences of deeply virtual Compton scattering at HERA. *JHEP*, 05:108, 2009. arXiv:0812.2517, doi:10.1088/1126-6708/2009/05/108. 8.4

[155] X. Chen, X. Lu, W. Sun, F. Wang, and T. Goldman. Spin and orbital angular momentum in gauge theories: Nucleon spin structure and multipole radiation revisited. *Phys. Rev. Lett.*, 100:232002, 2008. arXiv:0806.3166, doi:10.1103/PhysRevLett.100.232002. 4.1, 8.4

[156] X. Chen, W. Sun, X. Lu, F. Wang, and T. Goldman. Do gluons carry half of the nucleon momentum? *Phys. Rev. Lett.*, 103:062001, 2009. arXiv:0904.0321, doi:10.1103/PhysRevLett.103.062001. 4.1, 8.4

[157] P. Chesler and L. Yaffe. The wake of a quark moving through a strongly-coupled plasma. *Phys. Rev. Lett.*, 99:152001, 2007. arXiv:0706.0368, doi:10.1103/PhysRevLett.99.152001. 1.10, 1.2

[158] **PHENIX Collaboration**, M. Chiu. Single spin transverse asymmetries of neutral pions at forward rapidities in $\sqrt{s} = 62.4\,\text{GeV}$ polarized proton collisions in PHENIX. *AIP Conf. Proc.*, 915:539–542, 2007. arXiv:nucl-ex/0701031, doi:10.1063/1.2750838. 4.9

[159] CIREA. Commercial supplier of Micromega detectors. Cholet, France. 7.1.3

[160] J. Collins. Fragmentation of transversely polarized quarks probed in transverse momentum distributions. *Nucl. Phys.*, B396:161–182, 1993. arXiv:hep-ph/9208213, doi:10.1016/0550-3213(93)90262-N. 4.2, 6.1.1, 6.1.2

[161] J. Collins. Leading-twist single-transverse-spin asymmetries: Drell-Yan and deep-inelastic scattering. *Phys. Lett.*, B536:43–48, 2002. arXiv:hep-ph/0204004, doi:10.1016/S0370-2693(02)01819-1. 4.3

[162] J. Collins, S. Heppelmann, and G. Ladinsky. Measuring transversity densities in singly polarized hadron-hadron and lepton-hadron collisions. *Nucl. Phys.*, B420:565–582, 1994. arXiv:hep-ph/9305309, doi:10.1016/0550-3213(94)90078-7. 4.2, 5.3

[163] J. Collins, D. Soper, and G. Sterman. Transverse Momentum Distribution in Drell-Yan Pair and W and Z Boson Production. *Nucl. Phys.*, B250:199, 1985. doi:10.1016/0550-3213(85)90479-1. 6.1.1

[164] **PHENIX Collaboration**, M. Connors. Direct photon-hadron correlations measured with PHENIX. *Nucl. Phys.*, A830:447C–450C, 2009. arXiv:0907.4571, doi:10.1016/j.nuclphysa.2009.10.038. 1.2, 1.11

[165] L. Csernai, J. Kapusta, and L. McLerran. On the strongly-interacting low-viscosity matter created in relativistic nuclear collisions. *Phys. Rev. Lett.*, 97:152303, 2006. arXiv:nucl-th/0604032, doi:10.1103/PhysRevLett.97.152303. 2.3

[166] **PHENIX Collaboration**, C. da Silva. Quarkonia measurement in p+p and d+Au collisions at $\sqrt{s} = 200$ GeV by PHENIX Detector. *Nucl. Phys.*, A830:227c–230c, 2009. arXiv:0907.4696, doi:10.1016/j.nuclphysa.2009.10.017. 3.4

[167] D. Das, G. Lin, S. Chattopadhyay, A. Chikanian, E. Finch, *et al*. Preliminary results on direct photon-photon HBT measurements in $\sqrt{s_{NN}} = 62.4$ GeV and 200 GeV Au+Au collisions at RHIC. *Nukleonika*, 51:55–58, 2006. arXiv:nucl-ex/0511055. 3.5

[168] D. de Florian, R. Sassot, and M. Stratmann. Global analysis of fragmentation functions for pions and kaons and their uncertainties. *Phys. Rev.*, D75:114010, 2007. arXiv:hep-ph/0703242, doi:10.1103/PhysRevD.75.114010. 4.1

[169] D. de Florian, R. Sassot, M. Stratmann, and W. Vogelsang. Global analysis of helicity parton densities and their uncertainties. *Phys. Rev. Lett.*, 101:072001, 2008. arXiv:0804.0422, doi:10.1103/PhysRevLett.101.072001. 4.1, 4.6, 5.1, 5.1, 5.3, 5.2, 8.4

[170] D. de Florian, R. Sassot, M. Stratmann, and W. Vogelsang. Extraction of Spin-Dependent Parton Densities and Their Uncertainties. *Phys. Rev.*, D80:034030, 2009. arXiv:0904.3821, doi:10.1103/PhysRevD.80.034030. 5.1, 5.1, 5.3, 5.2, 6.2

[171] D. de Florian and W. Vogelsang. Helicity parton distributions from spin asymmetries in W- boson production at RHIC. *Phys. Rev.*, D81:094020, 2010. arXiv:1003.4533, doi:10.1103/PhysRevD.81.094020. 4.7

[172] D. d'Enterria. Jet quenching in QCD matter: From RHIC to LHC. *Nucl. Phys.*, A827:356C–364C, 2009. arXiv:0902.2488, doi:10.1016/j.nuclphysa.2009.05.078. 3.3

[173] G. Deptuch *et al*. Monolithic active pixel sensors with on-pixel amplification and double sampling operation. *NIM*, A512:299, 2003. doi:10.1016/S0168-9002(03)01907-7. 7.2.1

[174] S. Digal, P. Petreczky, and H. Satz. Quarkonium feed down and sequential suppression. *Phys. Rev.*, D64:094015, 2001. arXiv:hep-ph/0106017, doi:10.1103/PhysRevD.64.094015. 3.4

[175] M. Djordjevic, M. Gyulassy, R. Vogt, and S. Wicks. Influence of bottom quark jet quenching on single electron tomography of Au+Au. *Phys. Lett.*, B632:81–86, 2006. arXiv:nucl-th/0507019, doi:10.1016/j.physletb.2005.09.087. 2.2

[176] Y. Dokshitzer and D. Kharzeev. Heavy quark colorimetry of QCD matter. *Phys. Lett.*, B519:199–206, 2001. arXiv:hep-ph/0106202, doi:10.1016/S0370-2693(01)01130-3. 3.2

[177] F. Dominguez, B. Xiao, and F. Yuan. k_t-factorization for hard processes in nuclei. 2010. arXiv:1009.2141. 3.6

[178] W. Dragoset *et al*. Asymmetries in inclusive proton-nucleon scattering at 11.75 GeV/c. *Phys. Rev.*, D18:3939–3954, 1978. doi:10.1103/PhysRevD.18.3939. 6.1.1

[179] H.-J. Drescher, A. Dumitru, A. Hayashigaki, and Y. Nara. The eccentricity in heavy-ion collisions from color glass condensate initial conditions. *Phys. Rev.*, C74:044905, 2006. arXiv:nucl-th/0605012, doi:10.1103/PhysRevC.74.044905. 2.4.2

[180] K. Dusling, F. Gelis, T. Lappi, and R. Venugopalan. Long range two-particle rapidity correlations in A+A collisions from high energy QCD evolution. *Nucl. Phys.*, A836:159–182, 2010. arXiv:0911.2720, doi:10.1016/j.nuclphysa.2009.12.044. 3.5

[181] EIC Working Group. A High Luminosity, High Energy Electron-Ion Collider [online]. 2007. Available from: http://web.mit.edu/eicc/documentation.html. 8.18

[182] J. Ellis, K. Olive, and C. Savage. Hadronic uncertainties in the elastic scattering of supersymmetric dark matter. *Phys. Rev.*, D77:065026, 2008. arXiv:0801.3656, doi:10.1103/PhysRevD.77.065026. 8.4

[183] S. Ellis, J. Huston, K. Hatakeyama, P. Loch, and M. Tonnesmann. Jets in hadron-hadron collisions. *Prog. Part. Nucl. Phys.*, 60:484–551, 2008. arXiv:arXiv:0712.2447, doi:10.1016/j.ppnp.2007.12.002. 7.1

[184] K. Eskola, H. Paukkunen, and C. Salgado. EPS09: a new generation of NLO and LO nuclear parton distribution functions. *JHEP*, 04:065, 2009. arXiv:0902.4154, doi:10.1088/1126-6708/2009/04/065. 1.3, 1.13, 3.3, 3.4, 8.3.1, 8.11

[185] K. Eskola, H. Paukkunen, and C. Salgado. EPS09: Nuclear PDFs and their uncertainties at NLO. *Nucl. Phys.*, A830:599c–602c, 2009. arXiv:0906.4231, doi:10.1016/j.nuclphysa.2009.10.054. 2.4.2

[186] **CHORUS Collaboration**, E. Eskut *et al*. The CHORUS experiment to search for $\nu_\mu \rightarrow \nu_\tau$ oscillation. *Nucl. Instrum. Meth.*, A401:7–44, 1997. doi:10.1016/S0168-9002(97)00931-5. 7.1.3

[187] A. Frawley. Update* on J/ψ cold nuclear matter R_{AA} estimates from fits to dAu R_{CP} data [online]. 2009. Talk at "Quarkonium in Hot Media: from QCD to Experiment" Workshop at the INT, Seattle, WA. Available from: http://www.int.washington.edu/talks/WorkShops/int_09_42W/People/Frawley_A/Frawley.pdf. 3.4, 3.24

[188] A. Frawley, T. Ullrich, and R. Vogt. Heavy flavor in heavy-ion collisions at RHIC and RHIC II. *Phys. Rept.*, 462:125–175, 2008. arXiv:0806.1013, doi:10.1016/j.physrep.2008.04.002. 3.4

[189] R. Fries, T. Kunihiro, B. Muller, A. Ohnishi, and A. Schafer. From 0 to 5000 in 2×10^{-24} seconds: Entropy production in relativistic heavy-ion collisions. *Nucl. Phys.*, A830:519c–522c, 2009. arXiv:0906.5293, doi:10.1016/j.nuclphysa.2009.09.041. 3.5, 3.5

[190] G. Gaycken *et al*. Monolithic active pixel sensors for fast and high resolution vertex detectors. *Nucl. Instrum. Meth.*, A560:44–48, 2006. doi:10.1016/j.nima.2005.11.233. 7.2.1

[191] D. Geesaman, K. Saito, and A. Thomas. The nuclear EMC effect. *Ann. Rev. Nucl. Part. Sci.*, 45:337–390, 1995. doi:10.1146/annurev.ns.45.120195.002005. 1.3

[192] F. Gelis, E. Iancu, J. Jalilian-Marian, and R. Venugopalan. The color glass condensate. 2010. arXiv:1002.0333. 1.3, 3.6, 8.3.2

[193] K. Golec-Biernat, E. Lewandowska, and A. Stasto. Drell-Yan process at forward rapidity at the LHC. 2010. arXiv:1008.2652. 3.6

[194] L. Gribov, E. Levin, and M. Ryskin. Semihard processes in QCD. *Physics Reports*, 100(1-2):1–150, 1983. doi:10.1016/0370-1573(83)90022-4. 3.6

[195] S. Gubser, S. Pufu, F. Rocha, and A. Yarom. Energy loss in a strongly coupled thermal medium and the gauge-string duality. 2009. arXiv:0902.4041. 3.1.1

[196] T. Gunji. Quarkonia production in high-energy heavy-ion collisions at the RHIC. *J. Phys.*, G35:104137, 2008. 3.4

[197] M. Gyulassy and X. Wang. HIJING 1.0: A Monte Carlo program for parton and particle production in high-energy hadronic and nuclear collisions. *Comput. Phys. Commun.*, 83:307, 1994. arXiv:nucl-th/9502021, doi:10.1016/0010-4655(94)90057-4. 3.1.3

[198] R. Hagedorn. Statistical thermodynamics of strong interactions at high-energies. *Nuovo Cim. Suppl.*, 3:147–186, 1965. 1.1

[199] Y. Hama *et al*. 3D relativistic hydrodynamic computations using lattice-QCD inspired equations of state. *Nucl. Phys.*, A774:169–178, 2006. arXiv:hep-ph/0510096, doi:10.1016/j.nuclphysa.2006.06.024. 3.5

[200] Y. Hatta, E. Iancu, and A. Mueller. Jet evolution in the N=4 SYM plasma at strong coupling. *JHEP*, 05:037, 2008. arXiv:0803.2481, doi:10.1088/1126-6708/2008/05/037. 3.1.1, 3.1.2, 3.5

[201] Y. Hidaka and R. Pisarski. Suppression of the Shear Viscosity in a "semi" Quark Gluon Plasma. *Phys. Rev.*, D78:071501, 2008. arXiv:0803.0453, doi:10.1103/PhysRevD.78.071501. 3.3

[202] T. Hirano. private communication. 1.1, 1.3

[203] T. Hirano, U. Heinz, D. Kharzeev, R. Lacey, and Y. Nara. Hadronic dissipative effects on elliptic flow in ultrarelativistic heavy-ion collisions. *Phys. Lett.*, B636:299–304, 2006. arXiv:nucl-th/0511046, doi:10.1016/j.physletb.2006.03.060. 3.5

[204] W. Horowitz. private communication (adapted from diagram). 3.3

[205] W. Horowitz and M. Gyulassy. Heavy quark jet tomography of Pb+Pb at LHC: AdS/CFT drag or pQCD energy loss? *Phys. Lett.*, B666:320–323, 2008. arXiv:0706.2336, doi:10.1016/j.physletb.2008.04.065. 3.2

[206] W.A. Horowitz. Ratio of charm to bottom R_{AA} as a test of pQCD versus AdS/CFT energy loss. 2007. arXiv:0710.0595. 3.1.1

[207] C. Hu-Guo *et al*. CMOS pixel sensor development: a fast read-out architecture with integrated zero suppression. *JINST*, 4:P04012, 2009. doi:10.1088/1748-0221/4/04/P04012. 7.2.1

[208] R. Jaffe and A. Manohar. The g_1 problem: Fact and fantasy on the spin of the proton. *Nucl. Phys.*, B337:509–546, 1990. doi:10.1016/0550-3213(90)90506-9. 4.1, 8.4

[209] R. Jakob. Spin-dependent fragmentation functions. *Nucl. Phys.*, A711:35–40, 2002. arXiv:hep-ph/0206271, doi:10.1016/S0375-9474(02)01189-2. 6.1.2

[210] J. Jalilian-Marian. Saturation physics and angular correlations at RHIC and LHC. *Eur. Phys. J.*, C61:789–792, 2009. arXiv:0808.2769, doi:10.1140/epjc/s10052-008-0853-6. 2.4.2

[211] X. Ji. Deeply-virtual Compton scattering. *Phys. Rev.*, D55:7114–7125, 1997. arXiv:hep-ph/9609381, doi:10.1103/PhysRevD.55.7114. 4.1, 4.3, 8.4

[212] X. Ji, J. Ma, and F. Yuan. QCD factorization for spin-dependent cross sections in DIS and Drell-Yan processes at low transverse momentum. *Phys. Lett.*, B597:299–308, 2004. arXiv:hep-ph/0405085, doi:10.1016/j.physletb.2004.07.026. 6.1.1

[213] X. Ji, J. Qiu, W. Vogelsang, and F. Yuan. A unified picture for single transverse-spin asymmetries in hard processes. *Phys. Rev. Lett.*, 97:082002, 2006. arXiv:hep-ph/0602239, doi:10.1103/PhysRevLett.97.082002. 4.3, 4.3, 6.1.1, 8.4

[214] G. Kane, J. Pumplin, and W. Repko. Transverse Quark Polarization in Large p_T Reactions, e^+e^- Jets, and Leptoproduction: A Test of QCD. *Phys. Rev. Lett.*, 41:1689, 1978. doi:10.1103/PhysRevLett.41.1689. 4.2, 6.1.1

[215] Z. Kang. Talk at the Iowa RHIC Spin Collaboration meeting [online]. 2010. Available from: http://course.physastro.iastate.edu/rsc_meeting/Iowa_kang.pdf. 6.3

[216] Z. Kang and J. Qiu. Single transverse spin asymmetry of dilepton production near Z^0 pole. *Phys. Rev.*, D81:054020, 2010. arXiv:0912.1319, doi:10.1103/PhysRevD.81.054020. 6.1.1

[217] D. Kharzeev, E. Levin, and L. McLerran. Jet azimuthal correlations and parton saturation in the color glass condensate. *Nucl. Phys.*, A748:627–640, 2005. arXiv:hep-ph/0403271, doi:10.1016/j.nuclphysa.2004.10.031. 2.4.2

[218] D. Kharzeev and K. Tuchin. Signatures of the color glass condensate in J/ψ production off nuclear targets. *Nucl. Phys. A*, 770:40–56, Oct 2006. arXiv:hep-ph/0510358, doi:10.1016/j.nuclphysa.2006.01.017. 3.4

[219] M. Klein and R. Yoshida. Collider physics at HERA. *Prog. Part. Nucl. Phys.*, 61:343–393, 2008. arXiv:0805.3334, doi:10.1016/j.ppnp.2008.05.002. 4

[220] R. Klem *et al*. Measurement of Asymmetries of Inclusive Pion Production in Proton Proton Interactions at 6-GeV/c and 11.8-GeV/c. *Phys. Rev. Lett.*, 36:929–931, 1976. doi:10.1103/PhysRevLett.36.929. 4.2, 6.1.1

[221] P. Kolb and U. Heinz. Hydrodynamic description of ultrarelativistic heavy ion collisions. 2003. Invited review for 'Quark Gluon Plasma 3'. Editors: R.C. Hwa and X.N. Wang, World Scientific, Singapore. arXiv:nucl-th/0305084. 3.5

[222] B. Kopeliovich, E. Levin, I. Potashnikova, and I. Schmidt. Unitarity bound for gluon shadowing. *Phys. Rev.*, C79:064906, 2009. arXiv:0811.2210, doi:10.1103/PhysRevC.79.064906. 1.3

[223] B. Kopeliovich, J. Nemchik, I. Potashnikova, and I. Schmidt. Gluon Shadowing in DIS off Nuclei. *J. Phys.*, G35:115010, 2008. arXiv:0805.4613, doi:10.1088/0954-3899/35/11/115010. 3.6, 3.34

[224] B. Kopeliovich, I. Potashnikova, and Ivan Schmidt. Measuring the saturation scale in nuclei. *Phys. Rev.*, C81:035204, 2010. arXiv:1001.4281, doi:10.1103/PhysRevC.81.035204. 3.6

[225] B.Z. Kopeliovich. Puzzles of J/ψ production off nuclei. 2010. arXiv:1007.4513. 3.4

[226] C. Kouvaris, J. Qiu, W. Vogelsang, and F. Yuan. Single transverse-spin asymmetry in high transverse momentum pion production in pp collisions. *Phys. Rev.*, D74:114013, 2006. arXiv:hep-ph/0609238, doi:10.1103/PhysRevD.74.114013. 6.1.2

[227] P. Kovtun, D. Son, and A. Starinets. Viscosity in strongly interacting quantum field theories from black hole physics. *Phys. Rev. Lett.*, 94:111601, 2005. arXiv:hep-th/0405231, doi:10.1103/PhysRevLett.94.111601. 1.1, 1.4

[228] H. Kowalski and D. Teaney. An impact parameter dipole saturation model. *Phys. Rev.*, D68:114005, 2003. arXiv:hep-ph/0304189, doi:10.1103/PhysRevD.68.114005. 2.4.2

[229] K. Krueger *et al*. Large analyzing power in inclusive $\pi^{\pm}$ production at high x_F with a 22 GeV/c polarized proton beam. *Phys. Lett.*, B459:412–416, 1999. doi:10.1016/S0370-2693(99)00677-2. 6.1.1

[230] K. Kumericki and D. Mueller. Towards a global analysis of generalized parton distributions. 2010. arXiv:1008.2762. 8.4

[231] K. Kumericki, D. Mueller, and K. Passek-Kumericki. Towards a fitting procedure for deeply virtual Compton scattering at next-to-leading order and beyond. *Nucl. Phys.*, B794:244–323, 2008. arXiv:hep-ph/0703179, doi:10.1016/j.nuclphysb.2007.10.029. 8.4

[232] T. Kunihiro, B. Muller, A. Ohnishi, and A. Schafer. Towards a Theory of Entropy Production in the Little and Big Bang. *Prog. Theor. Phys.*, 121:555–575, 2009. arXiv:0809.4831, doi:10.1143/PTP.121.555. 3.5

[233] **PHENIX Collaboration**, Y. Lai. Direct jet reconstruction in p+p and Cu+Cu at PHENIX. 2009. arXiv:0911.3399. 3.12

[234] S. Lami *et al*. First test results of the TOTEM T2 Telescope. *IEEE Nuclear Science Symposium Conference Record*, pages 2880–2882, 2009. doi:10.1109/NSSMIC.2009.5402054. 7.1.3

[235] **E866/NuSea Collaboration**, M. Leitch *et al*. Measurement of J/psi and psi' suppression in p A collisions at 800-GeV/c. *Phys. Rev. Lett.*, 84:3256–3260, 2000. arXiv:nucl-ex/9909007, doi:10.1103/PhysRevLett.84.3256. 2.4.1

[236] E. Levin and A. Rezaeian. Hadron multiplicity in pp and AA collisions at LHC from the Color Glass Condensate. *Phys. Rev.*, D82:054003, 2010. arXiv:1007.2430, doi:10.1103/PhysRevD.82.054003. 3.6

[237] Z. Liang, X. Wang, and J. Zhou. The Transverse-momentum-dependent Parton Distribution Function and Jet Transport in Medium. *Phys. Rev.*, D77:125010, 2008. arXiv:0801.0434, doi:10.1103/PhysRevD.77.125010. 3.6

[238] L. Linden-Levy, J. Nagle, C. Rosen, and P. Steinberg. Quasi-Particle Degrees of Freedom versus the Perfect Fluid as Descriptors of the Quark-Gluon Plasma. *Phys. Rev.*, C78:044905, 2008. arXiv:0709.3105, doi:10.1103/PhysRevC.78.044905. 1.1

[239] F. Liu, T. Hirano, K. Werner, and Y. Zhu. Elliptic flow of thermal photons at midrapidity in Au+Au collisions at $\sqrt{s_{NN}} = 200\,\text{GeV}$. *Nucl. Phys.*, A830:587C–590C, 2009. arXiv:0906.3566, doi:10.1016/j.nuclphysa.2009.09.049. 3.5, 3.31

[240] H. Liu, K. Rajagopal, and U. Wiedemann. Calculating the jet quenching parameter from AdS/CFT. *Phys. Rev. Lett.*, 97:182301, 2006. arXiv:hep-ph/0605178, doi:10.1103/PhysRevLett.97.182301. 3.1.1

[241] H. Liu, K. Rajagopal, and U. Wiedemann. An AdS/CFT calculation of screening in a hot wind. *Phys. Rev. Lett.*, 98:182301, 2007. arXiv:hep-ph/0607062, doi:10.1103/PhysRevLett.98.182301. 3.4

[242] **CMS Collaboration**, I. Lokhtin. Jet Physics in Heavy Ion Collisions with Compact Muon Solenoid detector at the LHC. *J. Phys. Conf. Ser.*, 50:385–388, 2006. arXiv:hep-ph/0503089, doi:10.1088/1742-6596/50/1/053. 7.1

[243] M. Luzum and P. Romatschke. Conformal relativistic viscous hydrodynamics: Applications to RHIC results at $\sqrt{s_{NN}} = 200\,\text{GeV}$. *Phys. Rev.*, C78:034915, 2008. arXiv:0804.4015, doi:10.1103/PhysRevC.78.034915. 1.1, 1.5, 3.5

[244] **HERMES Collaboration**, D. Mahon. An overview of recent deeply virtual Compton scattering results at HERMES. *AIP Conf. Proc.*, 1182, 2009. doi:10.1063/1.3293946. 8.4

[245] A. Majumder, B. Muller, and S. Bass. Longitudinal broadening of quenched jets in turbulent color fields. *Phys. Rev. Lett.*, 99:042301, 2007. arXiv:hep-ph/0611135, doi:10.1103/PhysRevLett.99.042301. 3.1

[246] A. Majumder and M. Van Leeuwen. The theory and phenomenology of perturbative QCD based jet quenching. 2010. arXiv:1002.2206. 3.1

[247] C. Marquet and L. Schoeffel. Geometric scaling in diffractive deep inelastic scattering. *Phys. Lett.*, B639:471–477, 2006. arXiv:hep-ph/0606079, doi:10.1016/j.physletb.2006.07.004. 8.3.2

[248] T. Matsui and H. Satz. J/ψ Suppression by Quark-Gluon Plasma Formation. *Phys. Lett.*, B178:416, 1986. doi:10.1016/0370-2693(86)91404-8. 3.4

[249] L. McLerran and R. Venugopalan. Computing quark and gluon distribution functions for very large nuclei. *Phys. Rev.*, D49:2233–2241, 1994. arXiv:hep-ph/9309289, doi:10.1103/PhysRevD.49.2233. 2.4.2

[250] L. McLerran and R. Venugopalan. Gluon distribution functions for very large nuclei at small transverse momentum. *Phys. Rev.*, D49:3352–3355, 1994. arXiv:hep-ph/9311205, doi:10.1103/PhysRevD.49.3352. 2.4.2

[251] L. McLerran and R. Venugopalan. Green's functions in the color field of a large nucleus. *Phys. Rev.*, D50:2225–2233, 1994. arXiv:hep-ph/9402335, doi:10.1103/PhysRevD.50.2225. 2.4.2

[252] D. Molnar and M. Gyulassy. Saturation of elliptic flow and the transport opacity of the gluon plasma at RHIC. *Nucl. Phys.*, A697:495–520, 2002. arXiv:nucl-th/0104073, doi:10.1016/S0375-9474(01)01224-6. 3.5

[253] M. Moritz *et al*. Performance study of new pixel hybrid photon detector prototypes for the LHCb RICH counters. *IEEE Trans. Nucl. Sci.*, 51:1060–1066, 2004. doi:10.1109/TNS.2004.829450. 7.2.1

[254] S. Mrowczynski. Color filamentation in ultrarelativistic heavy ion collisions. *Phys. Lett.*, B393:26–30, 1997. arXiv:hep-ph/9606442, doi:10.1016/S0370-2693(96)01621-8. 3.5

[255] A. Mueller and J. Qiu. Gluon recombination and shadowing at small values of x. *Nuclear Physics B*, 268(2):427–452, 1986. doi:10.1016/0550-3213(86)90164-1. 3.6

[256] D. Mueller, D. Robaschik, B. Geyer, F. Dittes, and J. Horejsi. Wave functions, evolution equations and evolution kernels from light-ray operators of QCD. *Fortschr. Phys.*, 42:101, 1994. arXiv:hep-ph/9812448. 4.3

[257] P. Mulders and R. Tangerman. The complete tree-level result up to order $1/Q$ for polarized deep-inelastic leptoproduction. *Nucl. Phys.*, B461:197–237, 1996. arXiv:hep-ph/9510301, doi:10.1016/0550-3213(95)00632-X. 6.1.2

[258] S. Munier, A. Stasto, and A. Mueller. Impact parameter dependent S-matrix for dipole proton scattering from diffractive meson electroproduction. *Nucl. Phys.*, B603:427–445, 2001. arXiv:hep-ph/0102291, doi:10.1016/S0550-3213(01)00168-7. 8.3.3

[259] P. Nadolsky and C. Yuan. Single spin asymmetries with weak bosons at RHIC. *Nucl. Phys.*, B666:31–55, 2003. arXiv:hep-ph/0304002, doi:10.1016/S0550-3213(03)00455-3. 4.7

[260] **PHENIX Collaboration**, Y. Nakamiya. Systematic measurements of light vector mesons at RHIC–PHENIX. *J. Phys.*, G35:104158, 2008. doi:10.1088/0954-3899/35/10/104158. 1.8

[261] **CLAS Collaboration**, S. Niccolai. Deeply virtual Compton scattering at CLAS. Prepared for 16th International Workshop on Deep Inelastic Scattering and Related Subjects (DIS 2008), London, England, 7-11 Apr 2008. doi:10.3360/dis.2008.93. 8.4

[262] N. Nicolaev and V. Zakharov. Parton model and deep inelastic scattering on nuclei. *Phys. Lett. B*, 55(4):397–399, 1975. doi:10.1016/0370-2693(75)90368-8. 1.3

[263] C. Nonaka and S. Bass. Space-time evolution of bulk QCD matter. *Phys. Rev.*, C75:014902, 2007. arXiv:nucl-th/0607018, doi:10.1103/PhysRevC.75.014902. 3.5

[264] J. Peng, P. McGaughey, and J. Moss. Dilepton production at Fermilab and RHIC. 1999. arXiv:hep-ph/9905447. 3.35

[265] M. Ploskon. Jet reconstruction with STAR [online]. 2010. Talk at the INT Workshop "Quantifying the Properties of Hot QCD Matter". Available from: http://www.int.washington.edu/talks/WorkShops/int_10_2a/People/Ploskon_M/Ploskon.pdf. 7.1

[266] G. Qin, J. Ruppert, S. Turbide, C. Gale, C. Nonaka, and S. Bass. Radiative jet energy loss in a three-dimensional hydrodynamical medium and high p_T azimuthal asymmetry of π_0 suppression at mid and forward rapidity in au+au collisions at $\sqrt{s_{NN}} = 200$ gev. *Phys. Rev. C*, 76(6):064907, Dec 2007. doi:10.1103/PhysRevC.76.064907. 3.5

[267] J. Qiu and G. Sterman. Single transverse-spin asymmetries in hadronic pion production. *Phys. Rev.*, D59:014004, 1999. arXiv:hep-ph/9806356, doi:10.1103/PhysRevD.59.014004. 6.1.1

[268] J. Qiu and I. Vitev. Coherent QCD multiple scattering in proton nucleus collisions. *Phys. Lett.*, B632:507–511, 2006. arXiv:hep-ph/0405068, doi:10.1016/j.physletb.2005.10.073. 1.3

[269] P. Quiroga-Arias, J. Milhano, and U. Wiedemann. Testing nuclear parton distributions with pA collisions at the TeV scale. *Phys. Rev.*, C82:034903, 2010. arXiv:1002.2537, doi:10.1103/PhysRevC.82.034903. 3.23

[270] A. Radyushkin. Scaling limit of deeply virtual Compton scattering. *Phys. Lett.*, B380:417–425, 1996. arXiv:hep-ph/9604317, doi:10.1016/0370-2693(96)00528-X. 4.3

[271] A. Radyushkin. Nonforward parton distributions. *Phys. Rev.*, D56:5524–5557, 1997. arXiv:hep-ph/9704207, doi:10.1103/PhysRevD.56.5524. 4.3

[272] J. Ralston and D. Soper. Production of dimuons from high-energy polarized proton proton collisions. In *Argonne 1978, Proceedings, High Energy Physics With Polarized Beams and Polarized Targets*, 559-562. 4.2

[273] J. Ralston and D. Soper. Production of Dimuons from High-Energy Polarized Proton Proton Collisions. *Nucl. Phys.*, B152:109, 1979. doi:10.1016/0550-3213(79)90082-8. 6.1.2

[274] R. Rapp. Signatures of thermal dilepton radiation at RHIC. *Phys. Rev.*, C63:054907, 2001. arXiv:hep-ph/0010101, doi:10.1103/PhysRevC.63.054907. 2.1, 2.3

[275] R. Rapp, D. Blaschke, and P. Crochet. Charmonium and bottomonium production in heavy-ion collisions. 2008. arXiv:0807.2470. 3.4, 3.4

[276] A. Rebhan, P. Romatschke, and M. Strickland. Dynamics of quark-gluon plasma instabilities in discretized hard-loop approximation. *JHEP*, 09:041, 2005. arXiv:hep-ph/0505261. 3.1

[277] A. Rebhan, P. Romatschke, and M. Strickland. Hard-loop dynamics of non-Abelian plasma instabilities. *Phys. Rev. Lett.*, 94:102303, 2005. arXiv:hep-ph/0412016, doi:10.1103/PhysRevLett.94.102303. 3.5

[278] P.E. Reimer. Opportunities with Drell-Yan scattering: Probing sea quarks in the nucleon and nuclei. *Eur. Phys. J.*, A31:593–596, 2007. doi:10.1140/epja/i2006-10196-3. 3.6, 3.6

[279] J. Riedl, A. Schafer, and M. Stratmann. Next-to-leading order QCD corrections to heavy quark correlations in longitudinally polarized hadron-hadron collisions. *Phys. Rev.*, D80:114020, 2009. arXiv:0911.2146, doi:10.1103/PhysRevD.80.114020. 5.2

[280] T. Rogers and P. Mulders. No Generalized TMD-Factorization in the Hadro-Production of High Transverse Momentum Hadrons. *Phys. Rev.*, D81:094006, 2010. arXiv:1001.2977, doi:10.1103/PhysRevD.81.094006. 4.3, 5.3, 5.3, 6.1.1, 6.1.2

[281] S. Salur. Full Jet Reconstruction in Heavy Ion Collisions: Prospects and Perils. 2009. arXiv:0910.2081. 3.12

[282] S. Saroff *et al*. Single-spin asymmetry in inclusive reactions $p\uparrow + p \to \pi^+ + X$, $\pi^- + X$, and $p + X$ at 13.3 and 18.5 GeV/c. *Phys. Rev. Lett.*, 64:995, 1990. doi:10.1103/PhysRevLett.64.995. 6.1.1

[283] J. Seely, A. Daniel, D. Gaskell, J. Arrington, N. Fomin, *et al*. New measurements of the EMC effect in very light nuclei. *Phys. Rev. Lett.*, 103:202301, 2009. arXiv:0904.4448, doi:10.1103/PhysRevLett.103.202301. 3.6

[284] R. Sharma, I. Vitev, and B. Zhang. Light-cone wave function approach to open heavy flavor dynamics in QCD matter. *Phys. Rev.*, C80:054902, 2009. arXiv:0904.0032, doi:10.1103/PhysRevC.80.054902. 3.15, 3.2.1, 3.2.2, 3.2.2

[285] E. Shuryak and I. Zahed. Jet quenching in high energy heavy ion collisions by QCD synchrotron-like radiation. *Phys. Rev.*, D67:054025, 2003. arXiv:hep-ph/0207163, doi:10.1103/PhysRevD.67.054025. 3.1

[286] D. Sivers. Single Spin Production Asymmetries from the Hard Scattering of Point-Like Constituents. *Phys. Rev.*, D41:83, 1990. doi:10.1103/PhysRevD.41.83. 4.3, 6.1.1

[287] D. Sivers. Hard scattering scaling laws for single spin production asymmetries. *Phys. Rev.*, D43:261–263, 1991. doi:10.1103/PhysRevD.43.261. 6.1.1

[288] T. Sjostrand, S. Mrenna, and P. Skands. PYTHIA 6.4 physics and manual. *JHEP*, 05:026, 2006. arXiv:hep-ph/0603175. 4.2, 4.11

[289] J. Soffer. Positivity constraints for spin dependent parton distributions. *Phys. Rev. Lett.*, 74:1292–1294, 1995. arXiv:hep-ph/9409254, doi:10.1103/PhysRevLett.74.1292. 4.13

[290] H. Song and U. Heinz. Interplay of shear and bulk viscosity in generating flow in heavy-ion collisions. *Phys. Rev.*, C81:024905, 2010. arXiv:0909.1549, doi:10.1103/PhysRevC.81.024905. 3.5

[291] D. Soper. Lectures at CTEQ—MCnet summer school on QCD phenomenology and Monte Carlo event generators [online]. 2008. Available from: http://www.phys.psu.edu/~cteq/schools/summer08. 8.2

[292] P. Sorensen. Implications of space-momentum correlations and geometric fluctuations in heavy-ion collisions. *J. Phys. G*, G37:094011, 2010. arXiv:1002.4878, doi:10.1088/0954-3899/37/9/094011. 1.2

[293] P. Stankus. Direct photon production in relativistic heavy-ion collisions. *Ann. Rev. Nucl. Part. Sci.*, 55:517–554, 2005. doi:10.1146/annurev.nucl.53.041002.110533. 3.5

[294] A. Stasto, K. Golec-Biernat, and J. Kwiecinski. Geometric scaling for the total $\gamma^* p$ cross-section in the low x region. *Phys. Rev. Lett.*, 86:596–599, 2001. arXiv:hep-ph/0007192, doi:10.1103/PhysRevLett.86.596. 8.3.2

[295] M. Stratmann. Talk at the Iowa RHIC Spin Collaboration meeting [online]. 2010. Available from: http://course.physastro.iastate.edu/rsc_meeting/rsc-iowa-he3-wboson.pptx. 6.3, 6.3

[296] B. Surrow *et al*. The STAR forward GEM tracker. *Nucl. Instrum. Meth.*, A617:196–198, 2010. doi:10.1016/j.nima.2009.09.012. 7.1.3

[297] Tech Etch. Commercial supplier of GEM foils. Plymouth, MA. 7.1.3, 7.1.3

[298] R. Thews. Quarkonium production via recombination. *Nucl. Phys.*, A783:301–308, 2007. arXiv:hep-ph/0609121, doi:10.1016/j.nuclphysa.2006.11.084. 3.4

[299] **E866/NuSea Collaboration**, R. Towell *et al*. Improved measurement of the $\overline{d}/\overline{u}$ asymmetry in the nucleon sea. *Phys. Rev.*, D64:052002, 2001. arXiv:hep-ex/0103030, doi:10.1103/PhysRevD.64.052002. 4

[300] I. Tserruya. Electromagnetic probes. 2009. arXiv:0903.0415. 2.1

[301] Tungsten Heavy Powder, Inc. San Diego, CA. 7.1.3

[302] S. Turbide, C. Gale, and R. Fries. Azimuthal Asymmetry of Direct Photons in High Energy Nuclear Collisions. *Phys. Rev. Lett.*, 96:032303, 2006. arXiv:hep-ph/0508201, doi:10.1103/PhysRevLett.96.032303. 3.5, 3.31

[303] S. Turbide, C. Gale, E. Frodermann, and U. Heinz. Electromagnetic radiation from nuclear collisions at RHIC energies. *Phys. Rev.*, C77:024909, 2008. arXiv:0712.0732, doi:10.1103/PhysRevC.77.024909. 1.7

[304] H. van Hees *et al*. private communication. 2.8, 2.9

[305] **E866 Collaboration**, M. Vasilev *et al*. Parton energy loss limits and shadowing in Drell-Yan dimuon production. *Phys. Rev. Lett.*, 83:2304–2307, 1999. arXiv:hep-ex/9906010, doi:10.1103/PhysRevLett.83.2304. 1.3, 3.6, 3.35

[306] I. Vitev. private communication. 3.22

[307] I. Vitev. Coherent power corrections to structure functions. *AIP Conf. Proc.*, 792:274–278, 2005. arXiv:hep-ph/0506039, doi:10.1063/1.2122035. 3.6, 3.34

[308] I. Vitev and B. Zhang. Jet tomography of high-energy nucleus-nucleus collisions at next-to-leading order. *Phys. Rev. Lett.*, 104:132001, 2010. arXiv:0910.1090, doi:10.1103/PhysRevLett.104.132001. 3.1.2, 3.1.2, 3.7, 3.8, 3.2.2

[309] W. Vogelsang. private communication. 3.1.1, 3.4, 3.1.3

[310] R. Vogt and S. Brodsky. QCD and intrinsic heavy quark predictions for leading charm and beauty hadroproduction. *Nucl. Phys.*, B438:261–277, 1995. arXiv:hep-ph/9405236, doi:10.1016/0550-3213(94)00543-N. 8.3.1

[311] A. Vossen, R. Seidl, M. Grosse-Perdekamp, M. Leitgab, A. Ogawa, *et al*. First Measurement of the Interference Fragmentation Function in e^+e^- at Belle. 2009. arXiv:0912.0353. 5.3, 6.1.2

[312] **Jefferson Lab Hall A, DVCS Collaboration**, E. Voutier. Deeply virtual Compton scattering at JLab Hall A. 2007. arXiv:0709.4328, doi:10.3360/dis.2007.141. 8.4

[313] M. Wakamatsu. Gauge- and frame-independent decomposition of nucleon spin. 2010. arXiv:1007.5355. 4.1, 8.4

[314] M. Wakamatsu. On gauge-invariant decomposition of nucleon spin. *Phys. Rev.*, D81:114010, 2010. arXiv:1004.0268, doi:10.1103/PhysRevD.81.114010. 4.1, 8.4

[315] S. Wicks, W. Horowitz, M. Djordjevic, and M. Gyulassy. Elastic, inelastic, and path length fluctuations in jet tomography. *Nucl. Phys.*, A784:426–442, 2007. arXiv:nucl-th/0512076, doi:10.1016/j.nuclphysa.2006.12.048. 3.1.1

[316] S. Wicks, W. Horowitz, M. Djordjevic, and M. Gyulassy. Heavy quark jet quenching with collisional plus radiative energy loss and path length fluctuations. *Nucl. Phys.*, A783:493–496, 2007. arXiv:nucl-th/0701063, doi:10.1016/j.nuclphysa.2006.11.102. 2.2

[317] R. Wigmans. The DREAM project—Towards the ultimate in calorimetry. *Nucl. Instr. and Meth. A*, 617(1-3):129–133, 2010. 11th Pisa Meeting on Advanced Detectors: Proceedings of the 11th Pisa Meeting on Advanced Detectors. doi:10.1016/j.nima.2009.09.118. 7.1, 7.1.3

[318] R. Woods and D. Saxon. Diffuse surface optical model for nucleon-nuclei scattering. *Phys. Rev.*, 95:577–578, 1954. doi:10.1103/PhysRev.95.577. 8.3.3

[319] C. Woody *et al*. Initial performance of the PHENIX Hadron Blind Detector at RHIC. *IEEE Nuclear Science Symposium Conference Record*, pages 1002–1008, 2009. doi:10.1109/NSSMIC.2009.5402450. 7.1.3

[320] R. Yang, J. Peng, and M. Grosse-Perdekamp. Flavor asymmetry of the nucleon sea and W boson production. *Phys. Lett.*, B680:231–234, 2009. arXiv:0905.3783, doi:10.1016/j.physletb.2009.08.070. 5.1.1

[321] B. Yu, V. Radeka, G. Smith, C. Woody, and N. N. Smirnoff. Study of GEM characteristics for application in a MicroTPC. *IEEE Trans. Nucl. Sci.*, 50:836–841, 2003. doi:10.1109/TNS.2003.814586. 7.1.3

[322] F. Yuan. Single Spin Asymmetry in Inclusive Hadron Production in pp Scattering from Collins Mechanism. *Phys. Lett.*, B666:44–47, 2008. arXiv:0804.3047, doi:10.1016/j.physletb.2008.06.066. 6.1.2

[323] B. Zakharov. Parton energy loss due to synchrotron-like gluon emission. *JETP Lett.*, 88:475–480, 2008. arXiv:0809.0599, doi:10.1134/S0021364008200022. 3.1